RARE-EARTH IONS/ELEMENTAL NANOPARTICLES BASED SILICA COMPOSITES FOR SOLID STATE LIGHTING APPLICATIONS

Thesis Submitted to the University of Calicut for the Award of

Doctor of Philosophy in Physics

By

TESSY PAUL

under the guidance of

DR. ANN MARY K A

Research & Post-Graduate Department of Physics
St. Thomas College (Autonomous), Thrissur
Kerala – 680 001

February 2025

Dedicated to

my appachan.....

ADVANCED MATERIALS RESEARCH DIVISION
DEPARTMENT OF PHYSICS, RESEARCH CENTRE - UNIVERSITY OF CALICUT
ST. THOMAS COLLEGE (Autonomous), THRISSUR, KERALA-680001, INDIA
(Accredited at 'A++' level by NAAC)
www.stthomas.ac.in

Certificate

This is to certify that the thesis entitled **"RARE-EARTH IONS/ELEMENTAL NANOPARTICLES BASED SILICA COMPOSITES FOR SOLID STATE LIGHTING APPLICATIONS"** is an authentic record of precise research work carried out by Ms. Tessy Paul under my guidance and supervision for the partial fulfilment of the award of degree of Doctor of Philosophy in Physics, submitted to University of Calicut and the same has not been submitted elsewhere for the award of any other degree or diploma.

Dr. Ann Mary K A
Assistant Professor & Research Guide
Research & Post-graduate Department of Physics
St Thomas College (Autonomous), Thrissur, Kerala

Declaration

I hereby declare that the work presented in the thesis entitled "**RARE-EARTH IONS/ELEMENTAL NANOPARTICLES BASED SILICA COMPOSITES FOR SOLID STATE LIGHTING APPLICATIONS**" is based on the original work done by me under the guidance of Dr. Ann Mary K A, Assistant Professor, Research & Post graduate Department of Physics, St Thomas College (Autonomous), Thrissur, and has not been included in any other thesis submitted previously for the award of any degree. The contents of the thesis are undergone plagiarism check using iThenticate software at C.H.M.K. Library, University of Calicut, and the similarity index found within the permissible limit. I also declare that the thesis is free from AI generated contents.

Place: Thrissur **Tessy Paul**

Date: 24/02/25

Dr. Ann Mary K A

Assistant Professor & Research Guide

Research & Post-graduate Department of Physics

St. Thomas College (Autonomous), Thrissur, Kerala

Acknowledgements

Voyage of research is nothing but a miniature of life in which I indebted to many people who stood like pillars to reach its destination. At this point, it is great pleasure to convey gratitude to all who motivated and supported me during this journey. This research work would not have been completed without the worthy support, fruitful discussions and endless motivation from my beloved guide ***Dr. Ann Mary K.A****, Assistant Professor, Department of Physics, St. Thomas College (Autonomous), Thrissur. Her meticulous guidance, enthusiastic research efforts, constructive criticism and constant encouragement are always there during the ups and downs. I am truly grateful for the way she triggered and constantly monitored the research work.*

I am extremely thankful to Dr. Anoop K.K., Department of Physics, Cochin University of Science & Technology, Cochin for guiding me during the tenure February 2019 to May 2019 as part of ASPIRE scholarship. His timely suggestions and valuable assistance in the collaborative works are also remembered with deepest gratitude. I extend my sincere thanks towards Dr. Reji Philip, Light and Matter Physics Group, Raman Research Institute, Bangalore for giving me an opportunity to conduct photoluminescence studies in his lab with great pleasure.

Also, I would like to thank Dr. Sunil Thomas for spending his valuable time to nurture the research aptitude in the initial phase of my research. It's my pleasure to convey my deep sense of gratitude to Dr. N V Unnikrishnan, School of Pure and

Applied Physics, Mahatma Gandhi University, Kottayam for valuable assistance and exposure in the research work as collaborator. I would like to thank Ms. Anu Mathew, SAIF, Mahatma Gandhi University, Kottayam for working as a collaborator and a helping hand for performing various characterizations. I convey my heartfelt thanks to Dr. Pranitha Sankar for her valuable assistance in conducting photoluminescence measurements in the research lab, Light and Matter Physics Group, Raman Research Institute, Bangalore.

I owe my profound gratitude to Dr. Nees Paul, Head of Department and former Head of Department Dr. Joe Kizhakooden, P. M. Joy for their constant support during my Ph. D. I would like to sincerely acknowledge Principal and management of St. Thomas College (Autonomous), Thrissur for their timely support for the completion of my research work. My heartiest thanks to all the former and present faculty members of our department. Dr. Anto Johny T, Dr. Vimalkumar T V, Dr. Daison Panengadan, Dr. Johns Naduvath, Mr. Joby Thomas, Dr. Jilmy P Joy and Ms. Sikha Simon K for their encouragement. I also deeply acknowledge the non-teaching faculties especially the physics laboratory staff for providing timely services.

I acknowledge Council of Scientific and Industrial Research (CSIR) for providing the financial assistance in the form of Direct SRF (08/0633(18131)/2024-EMR-I). Also, Iam greatly thankful to Kerala Government for giving financial support as ASPIRE scholarship for completing a small part of my research.

SPAP Mahatma Gandhi University Kottayam, DST-SAIF Mahatma Gandhi University Kottayam, Department of Chemical Sciences Mahatma Gandhi University Kottayam, Department of Botany and Chemistry of St. Thomas College (Autonomous) Thrissur, IUIC- Mahatma Gandhi University Kottayam, CLIF Kerala University Thiruvananthapuram, STIC Kochi, CRF-CeNS Banglore, SAIF-IIT Bombay, PSG Institute of advanced studies Coimbatore, Amala Cancer research Centre Thrissur, CIL Mannuthy are certain key characterization centres that helped

me during the entire research period. At this point I convey my heartiest gratitude towards all these institutions and technical staff for spending their valuable time on my research work. I offer immense gratitude to Library, St. Thomas College (Autonomous) Thrissur for providing services regarding thesis submission and giving a wonderful writing space for completing the thesis.

I would like to express special thanks to my groupmates Anupama K, Jibin P O, Manjusha Rose Jose for keeping a good team spirit filled with positivity. A family like ambience given by my co-researchers Swathy Mohanan, Gadha Menon K, Anitha T V, Shanu A S, Jasmi K K, Greatel Francis Paremel, Reshma Babu played a pivotal role in balancing my research works with family matters. Their sincere criticisms helped a lot in molding myself into a better human being. I am also thankful to all the post graduate and graduate project students who had accompanied me during the research period.

Now it is the time to express deepest affection and gratitude towards my two loving families. Firstly, I thank my lovely father in heaven who is the dream maker and the one who shaped an ambitious mind within me. I convey heartiest gratitude to my mother who stood always there for my goal from the beginning and filled up all the voids of my father in his absence.

I am lifelong thankful to my husband Mr. Deepak Davis for his strong faith in me, genuine support and love. Thank you for being an understanding and lovely partner. Apart from this I am forever indebted to my family members, especially in laws for their care, patience and sincere prayers. Most importantly, I would like to express my great affection and love towards my son Austin who made the tough times of my Ph. D more cooler and tension free.

Above all, I thank the God almighty for being with me all the phases of my work which made me capable to complete my research work.

Tessy Paul

CONTENTS

LIST OF TABLES

LIST OF FIGURES

Abstract

Solid state luminescent materials have garnered considerable attention for the past several years due to their significant role in various fields like optoelectronic devices, sensors, data storage and light emitting applications. The thesis entitled "Rare-Earth Ions/Elemental Nanoparticles Based Silica Composites for Solid State Lighting Applications" describes synthesis and optical investigations on different rare earth (RE) ions/elemental nanoparticles (EN) doped silica composites for solid lighting applications. Discrete sharp green-red luminescence of RE ions (Tb^{3+}, Eu^{3+}) are combined with blue emission of carbon quantum dots (CQDs) to achieve WLE materials with warm to cool tunable correlated color temperatures (CCTs). Obtained composites show a continuous tuning from warm to cool white emission with adjustable CCTs (3508 to 6114 K) under excitation wavelength of 393 nm. Additionally, eco-friendly, biomass derived single component carbon nanoparticles with dual emission bands are synthesized to develop tunable WLE materials. Upon change in the excitation wavelengths from 410 nm to 370 nm, white light emissions are obtained with tunable CCT values from 2648 K to 8980 K respectively. On the other hand, Se- Tb^{3+} doped silica and CQDs-Tb^{3+} doped silica is investigated for its potential in achieving solid state lighting systems. Apart from this, phase dependent optical behaviour for Se-Tb^{3+} doped silica is systematically analyzed for its applications as optical amplifier and optical attenuator. For CQDs- Tb^{3+} doped silica, colour tuning is achieved with a transition from blue (0.1952, 0.2328) to near white (0.2201, 0.3106). Furthermore, nanocarbon doped silica are studied for their tunable structural and optical properties. In accordance with the increase of carbon content in silica, a graphitic to non- graphitic crystalline transitions with a concentration mediated spectral broadening is obtained. Non-graphitic carbon nanoparticles with wide emissions yielded cool white CCTs (> 6000 K) and good CRI value (~80) with favorable CIE coordinates.

Key words: Rare earth (RE) ions, Elemental nanoparticles (EN), Solid state lighting, White light emission, Muticolor emission

സംഗ്രഹം

സോളിഡ് ഫ്ലൂറെസെന്റ് മെറ്റീരിയൽസ്, കഴിഞ്ഞ കുറച്ച് വർഷങ്ങളായി ശാസ്ത്രലോകത്തിന്റെ ശ്രദ്ധയാകർഷിച്ചു വരികയാണ്. സെൻസറുകൾ, ഒപ്റ്റോ ഇലക്ട്രോണിക് ഉപകരണങ്ങൾ, എൽഇഡികൾ എന്നിങ്ങനെ വിവിധങ്ങളായ മേഖലകളിൽ ഇതിനു അപ്ളിക്കേഷനുകൾ ഉണ്ട്.

ഈ പ്രബന്ധം ഇത്തരത്തിലുള്ള സോളിഡ് ഫ്ലൂറെസെന്റ് വസ്തുക്കളെ ആധാരമാക്കിയിട്ടുള്ളതാണ്. ദൃശ്യ പ്രകാശ പരിധിയിൽ വരുന്ന തീവ്രമായ ഫ്ലൂറസെൻസ്, സ്റ്റോക്ക് ആന്റി-സ്റ്റോക്ക് ഷിഫ്റ്റുകൾ, ഫോട്ടോ സ്റ്റെബിലിറ്റി, ദീർഘമായ ഫ്ലൂറസെൻസ് ഡീകെ തുടങ്ങിയ സ്വതസിദ്ധമായ സവിശേഷതകളാൽ റെയർ എർത്ത് അയോണുകൾ സമ്പന്നമാണ്. അതിനാൽതന്നെ ഇവയെ ഉപയോഗപ്പെടുത്തി ധാരാളം ലൈറ്റിംഗ് അപ്ളിക്കേഷനുകൾ ശാസ്ത്രം വികസിപ്പിച്ചെടുത്തിട്ടുണ്ട്. നാനോതലത്തിലുള്ള കാണ്ടം ഡോട്ടുകൾ റെയർ എർത്ത് അയോണുകളോടൊപ്പം സംയോജിപ്പിക്കുന്നതിലൂടെ മികവേറിയ ലൈറ്റിംഗ് പ്ലാറ്റ്ഫോമുകൾ രൂപകൽപന ചെയ്തെടുക്കാവുന്നതാണ്. കാണ്ടം ഡോട്ടുകളുടെ വിസ്തൃതമായ എക്സൈറ്റേഷൻ ബാൻഡുകൾ അതിനുതകുന്നതാണ്. റെയർ എർത്ത് അയോണുകളും മൂലകങ്ങളുടെ നാനോകാണികകളും അധിഷ്ഠിതമാക്കി നിർമിച്ചിട്ടുള്ള കോമ്പോസിറ്റുകൾ മൾട്ടി കളർ അപ്ളിക്കേഷനുകൾക്കും ധവള പ്രകാശോല്പാദനത്തിനും അനുയോജ്യമാണ്. ഉല്പാദന പ്രക്രിയയിൽ മാറ്റം വരുത്തുന്നതിലൂടെ സംയുക്തങ്ങളുടെ ഘടനയും സ്വഭാവ സവിശേഷതകളും ട്യൂൺ ചെയ്തെടുക്കാനും സാധിക്കുന്നുണ്ട്. ഹൈഡ്രോതെർമൽ പ്രക്രിയയിലൂടെ ഉല്പാദിപ്പിച്ചെടുത്തിട്ടുള്ള കാർബൺ കാണ്ടം ഡോട്ടുകളെ റെയർ എർത്ത് (ടെർബിയം, യൂറോപിയം) അയോണുകളുമായി സോൾ ജെൽ പ്രക്രിയയിലൂടെ

സംയോജിപ്പിച്ചെടുത്തിട്ടുണ്ട്. പ്രസ്തുത സിലിക്ക കോമ്പോസിറ്റുകളുടെ പ്രത്യേകതയായ ട്യൂൺ ചെയ്തെടുക്കാനാവുന്ന ധവളപ്രകാശം സോളിഡ് ലൈറ്റിംഗ് അപ്ലിക്കേഷനുകളിലേക്കു വഴി തെളിക്കുന്നു. ജൈവ സ്രോതസ്സുകളിൽ നിന്നും ലളിതമായ, നേരിട്ടുള്ള താപ വിഘടന പ്രക്രിയയിലൂടെ ഡ്യുവൽ എമിസ്സീവ് കാർബൺ നാനോകണികകളെ നിർമിച്ചെടുക്കാനും സാധിച്ചു. അതിനുപുറമെ, സെലീനിയത്തിന്റെയും കാർബണിന്റെയും നാനോ ഘടനകൾ ഉചിതമായ അനീലിങ്ങിലൂടെ പരിവർത്തനങ്ങൾ നേടിയെടുക്കുന്നതായും കാണാം. സെലീനിയത്തിന്റെ ക്യൂബിക്കിൽ നിന്നും അമോർഫസിലേക്കുള്ള ഘടനാമാറ്റം സെലീനിയം-ടെർബിയം സിലിക്ക കോമ്പോസിറ്റുകളുടെ ഒപ്റ്റിക്കൽ സ്വഭാവത്തെ ഗണ്യമായ തോതിൽ തന്നെ സ്വാധീനിക്കുന്നു. സെലീനിയം/ടെർബിയം അയോണുകൾ ഡോപ്പു ചെയ്തിട്ടുള്ള സിലിക്കയിൽ അസാധാരണമായി കാണാൻ സാധിച്ച ഫേസ് ഡിപെൻഡന്റ് സവിശേഷതകൾ ഒപ്റ്റിക്കൽ ആംപ്ലിഫിക്കേഷൻ, ഒപ്റ്റിക്കൽ അറ്റെൻന്യുവേറ്റർ എന്നീ റോളുകളിലേക്കു വിരൽ ചൂണ്ടുന്നു. നാനോകാർബൺ-സിലിക്ക കോമ്പോസിറ്റുകളിൽ കാർബണിന്റെ അളവ് കൂടുന്നതോടെ ഗ്രാഫിറ്റിക്, ക്രിസ്റ്റലൈൻ ഘടനകൾ നോൺ ഗ്രാഫിറ്റിക് പോളിക്രിസ്റ്റലൈൻ ആയി രൂപപ്പെടുന്നുണ്ട്. അതോടൊപ്പം തന്നെ, നീല ഫ്ലൂറസെൻസ് വെള്ളയിലേക്കു ട്യൂൺ ചെയ്യപ്പെടുന്നതായും കാണാം. നിർമിച്ചിട്ടുള്ള ഓരോ കോമ്പോസിറ്റുകളുടെയും ലൈറ്റിംഗ് അപ്ലിക്കേഷൻ തലത്തിലുള്ള സാധ്യതകൾ കളറിമെട്രീയുടെ സഹായത്തോടെ വിശകലനം ചെയ്തു. അനുയോജ്യമായ സി സി ടി, സിആർഐ, സിഐഇ കോർഡിനേറ്റ്സ് ലഭിച്ചിട്ടുള്ള കോമ്പോസിറ്റുകൾ നൂതന ലൈറ്റിംഗ് അപ്ളിക്കേഷനുകൾ രൂപപ്പെടുത്താൻ പ്രാപ്തമാണ്.

Preface

The thesis mainly deals with various combinations of rare earth (RE) ions and elemental nanoparticles (EN) to design multicolor emitting solid state lighting platforms. When RE ions meet elemental nanoparticles in a rigid environment, their individual optical characteristics are modified significantly. Sharp multiple luminescence from RE ions and the nanosized effects of EN are capable in achieving optical platforms with novel fluorescence. Studies on possible energy transfer routes and the role of silica in achieving solid state portable luminescence are presented in between the thesis. In detail, the whole thesis can be divided into eight different chapters and the chapter wise outline is given below.

Chapter 1: General introduction provides a brief note on nanostructures, classification and their significant properties. It outlines different allotropes and diversity in structures particularly, selenium and carbon elements are discussed in detail to understand their unique properties at nano dimensions. Various mechanisms involved in photoluminescence are explained by using Jablonski diagram. Phosphors and their peculiar energy transferring components like sensitizer, activator, host matrix are also discussed. Besides, RE ions, their spectroscopy and applications are briefly detailed. Common synthetic strategies utilized in the preparation of various RE/EN composites are also explained. Different approaches to obtain white light emission and various chromaticity characterization techniques are presented in short.

Chapter 2: Carbon Quantum Dots - Tb^{3+} - Eu^{3+} Doped Silica for Tunable WLE Applications discusses the fabrication of rare earth ions (Eu^{3+}, Tb^{3+}) – CQDs doped silica for white light generation. Structural, optical and cell viability studies of CQDs are explained. Study of spectral stability of CQDs are also presented. Spectroscopic investigations and colorimetric studies of carbon quantum dots -Tb^{3+} - Eu^{3+} doped silica are discussed in detail with possible WLE applications.

Chapter 3: Dual Emitting Carbon Nanoparticles for Tunable WLE Applications depicts the synthesis and characterization of carbon nanoparticles with dual emission bands. The spectroscopic investigations explain energy transfer mechanism between

carbon core and chlorophyl derived porphyrin rings. Tunable white light emission from cool to warm under varying excitations are studied by using chromaticity diagram.

Chapter 4: Se-Tb^{3+} doped Silica for Multicolor Emitting Applications mainly deals with phase dependent structural and optical of studies of Se-Tb^{3+} in silica. While cubic selenium enhances the emission bands of Tb^{3+} ions, the presence of amorphous Se quenches the fluorescence of Tb^{3+} ions.

Chapter 5: Carbon quantum dots-Tb^{3+} doped Silica for Multicolor Emitting Applications studies the influence of CQD fluorescence on green emitting Tb^{3+} ions. The chapter discusses the structure and optical properties of CQDs in detail. Then the impact of CQD fluorescence on Tb^{3+} ions is analyzed with spectroscopic techniques and identified enhanced transitions observed. In addition, excitation wavelength dependence on fluorescence of CQD-Tb^{3+} composite is studied. Colorimetric parameters are found out with the aid of color calculator software and detailed the possibility of CQD-Tb^{3+} composite in solid tunable lighting application.

Chapter 6: Nanocarbon Doped Silica for WLE Applications describes the synthesis of crystalline nano carbon in silica and from phase dependent and concentration dependent fluorescence spectra, chromaticity parameters are calculated. The results illustrate their application in multicolor emitting devices and solid-state concentration dependent emission spectra are also presented. Detailed structural investigations on crystallinity are included. Their excitation dependent and concentration dependent tunable optical behaviour confirms solid state lighting applications with colorimetric spots in distinct color domains.

Chapter 7 summarizes the major conclusions and highlights of the overall work.

Chapter 8 contains the future prospects and possibilities especially in the field of solid-state lighting of both white and multicolor emissions.

Research Papers Published

1. **T. Paul**, K. Anupama, P. O. Jibin et al., Spectroscopic investigations on Se/RE doped sol gel derived silica matrices, *Materials Today: Proceedings*, 33 (2020): 1323-1326.

2. Kuttappan Anupama, **Tessy Paul**, Kakkassery Aippunny Ann Mary., Solid-State Fluorescent Selenium Quantum dots by a Solvothermal Assisted Sol-Gel Route for Curcumin Sensing, *ACS Omega*. 6, no. 33 (2021): 21525-21533.

3. K. A. Ann Mary, **Tessy Paul**, Kuttappan Anupama, P O Jibin, K K Anoop, Dual emitting carbon nanoparticles for tunable white light emission, *Carbon Trends*, 13 (2023)100296.

4. **Tessy Paul**, Joyal Jain Palakulam, N.V. Unnikrishnan, Reji Philip, K.A. Ann Mary, Warm to cool tunable ultra-stable white light emissions from carbon Dots -Tb^{3+} - Eu^{3+} doped silica, *Optical materials*, 138 (2023)113673.

5. **Tessy Paul**, Manjusha Rose Jose, K.A. Ann Mary, Multicolor emissive carbon quantum dots/ Tb^{3+} @SiO_2 lighting applications, *Optics Communications.* 577 (2025) 131444.

Research works presented in National /International Conferences

1. "***Phase dependent energy transfer of selenium quantum dots in sm^{3+} doped silica glasses***" in the national conference on science and applications of functional materials held at St. Joseph's college (autonomous), Irinjalakuda, 7 December 2018.

2. "***Spectroscopic investigations on Se/RE doped sol gel derived silica matrices***" in the International Conference on Photochemistry and Sustainable Energy (ICPSE 2019), 16 -19 October 2019 held at Alappuzha.

3. "***Multicolor Emissive Carbon Quantum Dots/ Tb^{3+} @SiO$_2$ matrices for Solid Lighting Applications"*** in Women in Optics and Photonics in India (WOPI) 2023 at IIT Madras, Chennai, 2-3 January 2024.

4. "***Free standing CQD/Tb^{3+} Nanocomposite Films for Lighting Application***" in international conference on Advances in Material Science (ICAMS), St. Dominic's College, Kanjirapally, Kottayam, Kerala, India, 9-10 January 2025.

1

General Introduction

Chapter 1 *systematically presents a brief outline about nanomaterials, classification and their unique quantum confinement effects. Particularly, elemental allotropism of carbon and selenium with peculiar characteristics are discussed in detail. Different types of photoluminescence along with various mechanisms involved are described with Jablonski diagram. A brief outlook on phosphors and influence of host matrix, sensitizer and activator are clearly mentioned. Lanthanide spectroscopy of RE ions, electronic transition channels and possible energy transfer processes are outlined. Synthesis techniques such as sol gel, solvothermal and pyrolysis methods are also explained. Various chromatic approaches with pictorial illustration, colorimetric parameters for lighting device realization and their prospects are also briefly touched upon. Literature review on CQDs for solid lighting applications, RE-elemental nanoparticle-based composites are also included. Finally, this chapter is concluded with a concise description of organization of the thesis.*

1.1 Nanomaterials

Nanomaterials are superior class of materials having size or at least one-dimension lies below 100 nm [1]. Even the diameter of human hair (100 μm) is one lakh times thicker than one nano meter. By reducing the size of a material to nanoscale, tremendous changes in magnetic, electrical, optical properties are observed from their bulk counterparts. It paves the way to achieve desired materials having peculiar qualities by the precise control of synthetic parameters, precursors and functionalization. In ancient days, nanomaterials are unknowingly utilized in several forms such as hair dyes among Egyptians [2], Lycurgus Cup [3], Asbestos nano fibres [1], [4]. The term 'nano meter' was very first coined in 1914 by Richard Adolf Zsigmondy [1]. But concept of nanoscience was initially introduced in 1959 by Richard Feynman. He put forward this specific concept in his famous speech with title '*There's Plenty of Room at the Bottom*' delivered in the annual meeting of American Physical Society [5]. Nanotechnology involves certain steps like the processing, separation, consolidation, and deformation of materials by single atomic or molecular units [6]. Up to 1980's nanoworld is just an unexplored field of discussion due to the lack of specific spectroscopic techniques for performing in depth investigations. By the invention of scanning tunnelling microscopy (STM) in 1982 [7] and Atomic force microscopy (AFM) in1986 [8],the nanoscale measurements were realized which triggered uncountable researches in nanoworld. Role of nanomaterials in commercial fields are also inevitable. Significant presence of nanomaterials in cosmetics, environmental remediation, sporting products, stain resistant fabrics, paints etcmade our daily life more comfortable. Nanofilms and nanocomposites are seen in every day products like UV blocking films coated on bottles, windows, automobiles etc. [9]. Particularly, when luminescent nano particles encapsulated in solid networks like glasses, polymeric films, it transforms ordinary matrices to highly efficient solid luminescent systems.

1.1.1 Classification

According to the number of dimensions in nano regime, nanomaterials can be categorized into four classes. Zero dimensional (0D), one dimensional (1D), two dimensional (2D), three dimensional (3D) are the various classes in nanoworld (given in Fig. 1.1). Typically, materials with all three spatial dimensions that lies within the nanoscale

comes under zero-dimensional (0D) category [10]. Quantum dot, fullerene are certain examples under 0D class. One dimensional (1D) nano structures such as nanofibers, nanorods and nanotubes have linear geometry with large length to diameter ratio [11]. Two-dimensional (2D) nanomaterials are extremely thin layers of atomic thick with the other two dimensions lies in nanoscale. By the invention of graphene nanosheets with amazing electrical and thermal properties in 2004 [12], 2D nanostructures emerged as key candidates for multifunctional applications. Combined arrangement of 0D, 1D, or 2D materials results in three-dimensional (3D) nano materials. Varying synthetic conditions made 3D nano assemblies with distinct morphology and properties [10].

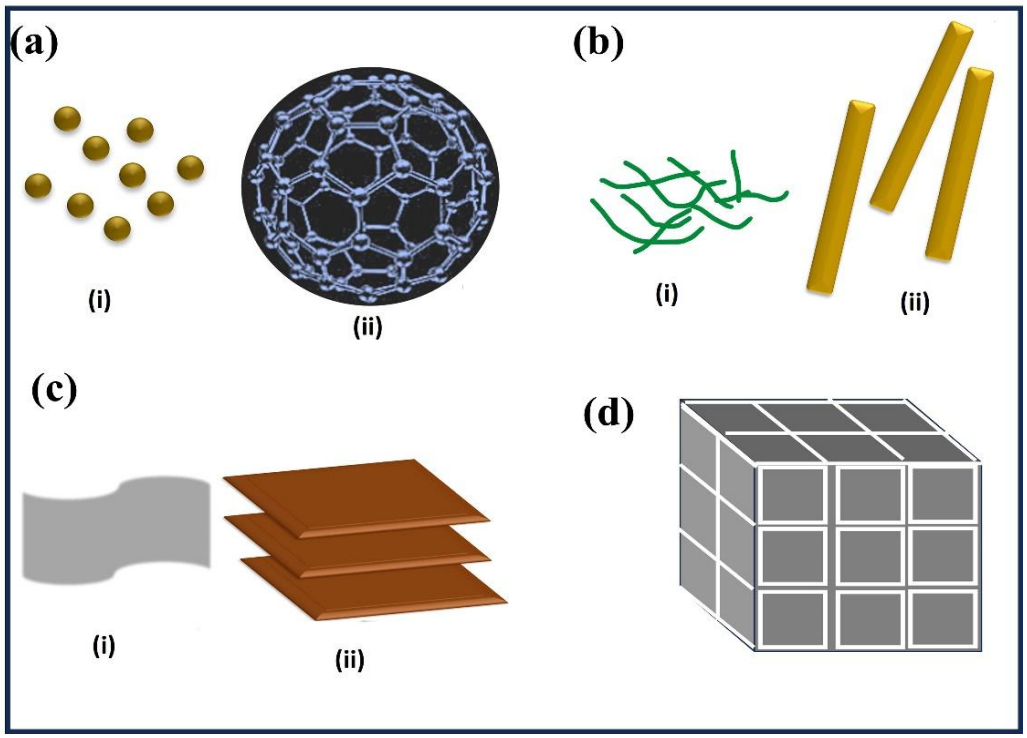

Figure 1.1: Classification of Nanomaterials (a) 0D (if) quantum dots (ii) fullerene, (b) 1D (I) nanofibers (ii) nanorods, (c) 2D (is) films (ii) nanosheets (d) 3D nanomaterials.

Quantum confinement effects: Nanoscale spatial confinement of materials results in altering their entire properties from the respective macroscopic counterparts. Bulk material with large number of atoms have closely lying energy levels which results valence band-conduction band formation. As the particle is confined into nano range, energy levels becomes discrete and thereby the band gap (E_g) will be increased remarkably from the bulk system [13], [14].

Table 1.1: Quantum confined structure classification.

Structures	Quantum confinement	Number of free dimensions
Quantum dots	3	0
Nanorods, Nanofibers	2	1
Thin films, Graphene	1	2
Bulk material	0	3

As the particle size decreases, band gap (E_g) will increase and thereby generating spectral blue shift in absorption and emission (given in Fig.1.2).

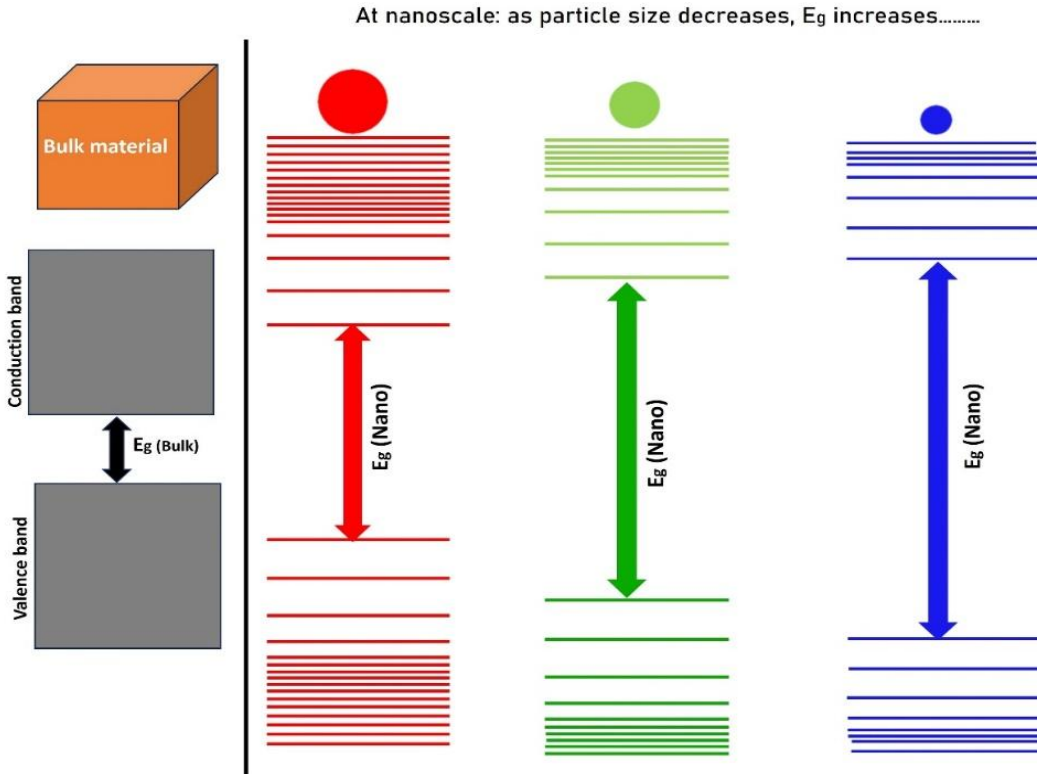

Figure 1.2: Schematic representation of the quantum confinement effects: bandgap increases with decreasing particle size.

1.1.2 Carbon nanostructures

For many years, carbon nanostructures with unique features are reported for their potential applications including sensors, bioimaging, nano medicine, solid state lighting systems. Zero-dimensional (0D) carbon assemblies such as fullerene, carbon dots etc exhibits unique characteristics properties. Fullerenes have a cage-like structure which is capable in stabilizing charged clusters [15]. Accidental discovery of carbon dots in

2004 [16] led to the wide utilization of this non-toxic, easily synthesizable fluorescent nanomaterial with diverse spectral features. Moreover, biocompatible carbon dots are excellent candidates for bioimaging applications [17]. Cylindrical ribbon like carbon nanotubes (CNTs) are formed by wrapping nanosheets of carbon and they exist in both single walled and multiwalled forms. They got enormous attention due to extraordinary tensile strength and remarkable thermal conductivity [18] . Mono layered graphene represents two-dimensional carbon nanostructure of atomic thick and it is well explored as conductive electrodes [15]. It absorbs radiations irrespective of wavelength which enables them for excellent electron transport features [19].

Carbon quantum dots (CQDs): Carbon quantum dots (CQDs) are zero-dimensional (0D) fluorescent nano materials which are extremely nano sized (< 10 nm), dot-like structures (shown in Fig. 1.3). Due to bright luminescence of CQDs, it is also called as carbon nano-lights [20]. In 2004, Xu. et. al, discovered CQDs during the extraction process of CNTs from carbon soot [16]. Intensive scientific investigations were carried out in the last two decades in connection with improving and exploring the characteristics of CQDs. Commonly, CQDs are synthesized from any organic or natural carbon source via both top down and bottom-up synthesis routes.

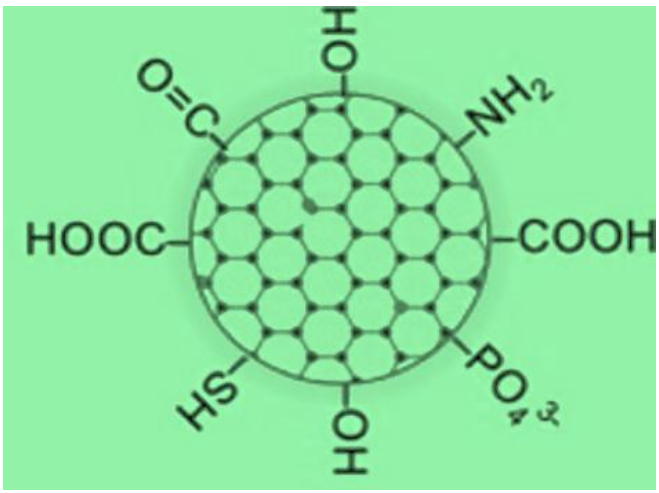

Figure 1.3: Schematic representation of CQDs [21]**.**

High quantum yield, fast-facile synthesis, remarkable water solubility, high photostability, low toxicity, chemical inertness, prolonged fluorescence lifetimes, excitation dependent fluorescence are certain spectacular properties reported for CQDs [22], [23]. So, organic fluorophores and dyes can be undoubtedly replaced with CQDs. Science world intensively utilized CQDs for wide spread applications such as bioimaging,

photovoltaics, targeted drug delivery, lighting platforms, photocatalysis, and potential candidates in other related fields [24]. Usually, CQDs formed via nucleation process which ultimately create a core shell structure. Central carbon core shielded with a self-passivated shell containing various functional groups [25]. Carbon core can exist either in amorphous or graphitic crystalline form and mostly reported core is graphitic form [22]. By varying the precursors and synthetic parameters, both core and surface states may vary that tunes the optical spectrum of CQDs [22], [26]. Usually for CQDs, strong absorption bands are observed in the ultraviolet (UV) region (250–350 nm) and a weak absorption is seen in the visible range. Major contributions in UV absorption bands are π- π^* transitions of core and n- π^* transition of edge or molecular bands. Functional groups of surface states are responsible for feeble visible absorption bands of CQDs. Though PL mechanism of CQDs is not completely understood, it is known that CQD emissions observed are due to quantum confinement effects, functional groups of CQD surface linked to core and molecular states accompanied with fluorescent molecules [22].

1.1.3 Selenium nanostructures

Semiconducting selenium has inherent narrow band gap and occurs in distinct forms that differs in their physical properties. Among different nanostructures, feasible growth mechanism of trigonal selenium (t-Se) nanowires and amorphous selenium (a-Se) nanoparticles have gained enormous interest than other forms [27], [28], [29]. Among various crystalline arrays, trigonal and monoclinic selenium assemblies have got higher stability. Due to low thermodynamic stability of amorphous selenium (a-Se), fast phase transformation from amorphous to trigonal phase were [30]. The transformation energy associated with amorphous to trigonal Se structures is 6.63 kJ/mol. a-Se generally retains spherical geometry to minimize the interfacial free enthalpy. Anisotropic nature of t-Se promotes easy one-dimensional growth as one-dimensional nanowires.

1.2 Allotropy

The concept of allotropy was initially put forward in 1840 by Baron Jons Jakob Berzelius [31]. Elemental allotropism refers to the capability of an element to exist in different forms by retaining in same physical phase. According to the pattern of bonding, allotropic forms of same element show different chemical and physical properties.

Allotropic transitions from unstable to stable forms occur under typical temperature-pressure conditions. So environmental conditions strongly influence the existence of allotropic forms. The term 'allotropy' is exclusively represented for elements, not for compounds. Oxygen, carbon, phosphorous, sulphur, selenium are major examples of elements with allotropism.

1.2.1 Allotropy of carbon

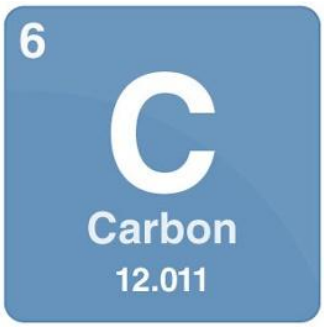

Elemental carbon has several allotropic forms due to its tetravalency. Different types of bonding linked with various hybridizations in carbon nanostructures widens their scope in multi-disciplinary applications. Wide utility of nano carbon in the designing and fabrication of nanoscale devices relies upon its ability to exist in diverse forms. Fullerenes, carbon nanotubes, graphene, graphite, diamond are prominent members in carbon family [32]. Fullerene is a zero-dimensional, sp^2 hybridized carbon allotrope invented in 1985 by Kroto [33]. It contains a group of carbon atoms that exist in the form of a closed cage. Carbon nano tubes are hexagonal network of carbon atoms which have a very high-pressure holding capacity of 24 Gape [34]. Graphene is two-dimensional hexagonal lattice of carbon with interesting applications. Extremely hard sp^3 hybridized diamond is an excellent carbon allotrope that have face centred cubic crystal structure. Multi stacked layers of graphene forms graphite [15], [18].

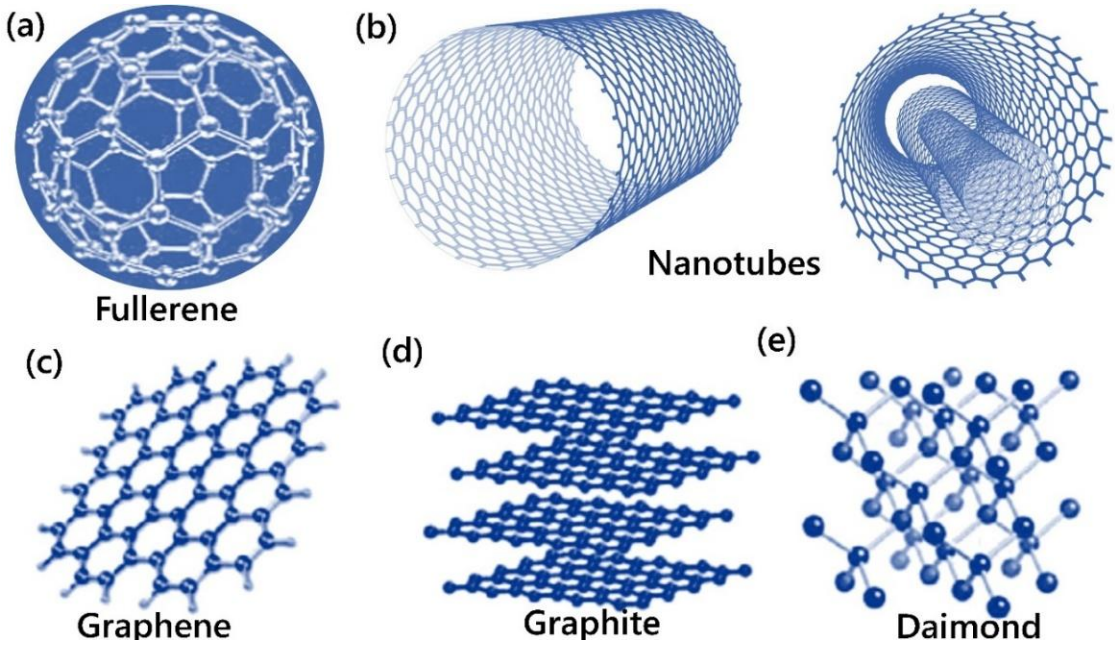

Figure 1.4: Different allotropes of carbon.

1.2.2 Allotropy of selenium

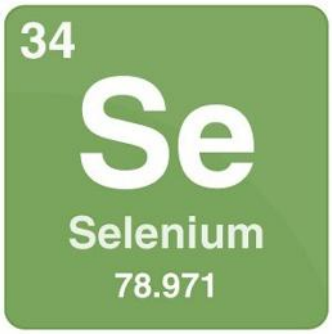

Selenium is a metalloid having metallic and non-metallic behaviours and exist in different allotropic forms with varying properties. Occurrence of allotropism in selenium shows strong analogy to sulphur. Non crystalline and crystalline varieties of elemental selenium are well known for their versatile properties. Crystalline forms of selenium are cubic (α, β, fact), trigonal (metallic grey), hexagonal, orthorhombic and monoclinic (α, β, γ) [35]. Cubic and rhombohedral structures are certain rarely reported crystalline varieties. In non-crystalline category, amorphous and vitreous selenium are the key members. Red amorphous and black amorphous selenium are the two subclasses of amorphous form which contains Se_8 rings and polymeric Se_8 chains respectively. Furthermore, vitreous selenium is a mixture of chains and rings. Unit cell constants of α-cubic and β-cubic selenium are 2.970 Å and 5.755 Å [36]. At normal temperature

scales, phase transformation process became slow and hence selenium retains in its amorphous form.

1.3 Photoluminescence

Luminescence is spontaneous emission process of light from certain materials that are electronically excited. Excited electrons return to ground states via radiative transitions by the release of energy and non-radiative transitions by means of lattice vibrations [37]. According to the nature of transitions, luminescence can be categorized into two classes as fluorescence and phosphorescence. Fluorophores are certain chemical compounds that are capable in generating luminescence after absorbing radiations. Life time (τ) of a fluorophore is the average time spent in the excited state before return to ground state.

1.3.1 Fluorescence and Phosphorescence

Fluorescence occurred within a short span of time (10^{-8} s) and during which singlet to singlet state allowed transitions are associated. Sir John Frederick William Herschel recorded the very first evidence of fluorescence from quinine solution in 1845 which could not describe with the theories of that era [38]. On the other side, phosphorescence involves triplet to singlet state, forbidden transitions and longer life time values of the order of milliseconds to seconds are obtained. It also referred as afterglow luminescence due to the persisting emission obtained even after the removal of excitation source [37].

1.3.2 Jablonski diagram

Jablonski diagram (given in Fig. 1.5) illustrates various energy levels with the possible radiative and non-radiative transitions during photoluminescence. Professor Alexander Jablonski is the one who proposed this diagram in 1933 and he is considered as the father of fluorescence spectroscopy [39]. Major energy levels of molecules are electronic levels in which spin multiplicity is either singlet or triplet states. In singlet states (S_0, S_1, S_2, …), electron spins are antiparallel with zero net spin angular momentum whereas, triplet states (T_1, T_2, T_3, ….) contains unpaired electrons with a net non-zero spin angular momentum. Each electronic levels split into vibrational levels which is further divided into several rotational energy states [37]. Molecules occupied in the ground state absorbs light energy from external light source and getting excited to singlet excited states ($S_0 \rightarrow S_1$). This fast *absorption* process occurs within the order of

Ferm to seconds. Then the excited electrons may undergo rapid relaxation to the lowest vibrational states of S_1 state by means of *internal conversion* process that may take place within picoseconds. Usually, internal conversion process is completed before the much slower process i.e., fluorescence having average fluorescence lifetime of 10^{-8} s. Hence, the transition from lowest vibrational level of S_1 to various vibrational levels of S_0 lead to fluorescence [37].

Sometime, S_1 state molecules may undergo transition to first triplet state T_1 and this spin conversion process is called as *inter system crossing*. Subsequently emission occurs from triplet state T_1 to singlet ground state (S_0) which is known as phosphorescence. Triplet to singlet state transitions are forbidden and hence rate constants for triplet state emissions are negligible as compared to the of singlet state fluorescence transitions [37].

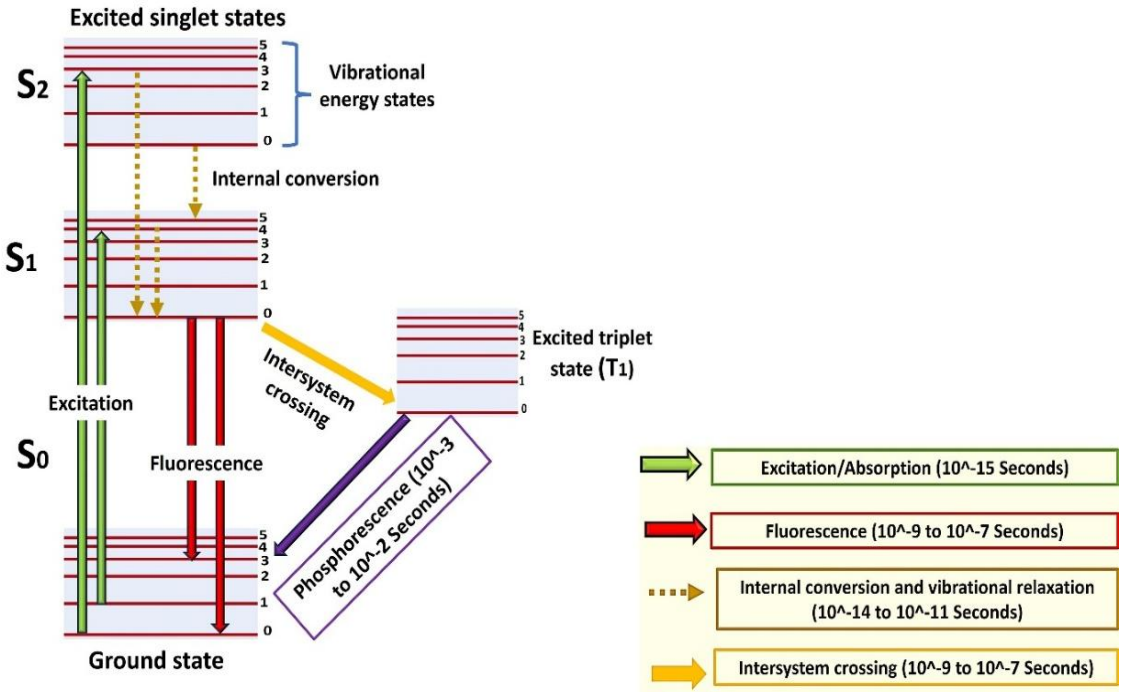

Figure 1.5: Jablonski diagram [37]**.**

1.3.3 Fluorescence lifetime

Generally, photoluminescence spectrum is steady state measuring technique which deals with the relative parameter, i.e., intensity versus wavelength. Fluorescence lifetime gives a dynamic picture of the sample and it does not depend on the concentration of sample. So, it is considered as an absolute measurement method. When a molecule capture photon, a series of photophysical process occurs as given in figure

1.5. Each individual process has its own probability of occurrence which is represented in terms of rate constant k. Average time spent by the molecule in the excited state before return to ground level is called as decay lifetime (τ) and it is the reciprocally related to rate constant k. Mathematically, decay lifetime of a particular photophysical process is the time required to decrease the population (N) in the excited state to N/e (~ 37 %) via energy loss. Fluorescence lifetime values and rate constants are mathematically expressed as is (1.1) where o_r and k_{nr} are rate constants of radiative and non-radiative process. Lifetime values are strongly depending on the processes occurring at molecular levels which make significant changes in k_{nr} value [37], [40] .

$$\mathbf{1/\tau = k_r + k_{nr}}\text{.....(1.1)}$$

Each photophysical process has distinct decay lifetime values ranges from femto to pico, nano, micro, milli scales. Generally, quantum dots havenanosecond lifetime values whereas for RE ions with intra 4f transitions, lengthy lifetimes of the order of 10^{-3} seconds are reported. Moreover,certain phosphorescent materials have τ values in even in seconds. For a typical fluorophore, τ value is an intrinsic feature which does not depend on the measurement method. First order kinetics evolved in fluorescence decay process of a particular excited state to ground state of a molecule can be expressed as eq (1.2) [40]. In many practical cases, due to environmental influences first order kinetics of decay may become multi-exponential in nature.

$$\mathbf{I(t) = I_0 exp\ (-t/\ \tau)}\text{.....(1.2)}$$

Fluorescence lifetime decays are measured via two different methods (i) multi-channel scaling (MCS) (ii) time correlated single photon counting (TCSPC). Among this two, TCSPC is more commonly used and most sensitive digital technique based on Poisson statistics. In this method, arrival of each photon after exciting the samples are counted and excitation pulses are commonly produced from laser sources or LEDs. Many excitation-emission cycles are repeated to obtain the fluorescence curve of a fluorophore. Slope of the decay curve gives the fluorescence lifetime value [40].

1.4 Phosphors

Phosphors are solid materials which exhibit strong luminescence by the irradiation of UV rays or electron beam. By exciting the phosphors, orbital electrons are excited and return to the ground state followed by producing intense emissions in visible window.

Numerous phosphors are already reported for their distinct luminescence characteristics. In general, phosphors are synthesised as a combination of apt host lattice having high band gap and the addition of dopants. These added impurities are termed as activator ions or sensitizer ions. Dopants and host matrix are the key counterparts of phosphors. Phosphors find applications in both scientific and industrial fields including radioluminescence, lighting, cathode ray tubes, white LEDs and scintillation sensors [41], [42].

1.4.1 Silica matrix

Selecting the suitable host matrix is crucial in achieving desired optical features. Generally, host matrix can be any oxides such as vanadate, silicate, aluminate, borate or phosphate [43]. These solid matrices influence the dopant ions and tune the luminescence points. Dopants normally act like activators or sensitizers which are encapsulated within the host matrix. In some case, the introduced host matrix absorbs photons of high energy ($h\nu_1$) and emits low energy photons ($h\nu_2$) in visible region. Certain amount of energy is released by means of lattice vibrations.

Typically, silica matrices are composed of silicon and oxygen which exist in both crystalline and amorphous phases. In crystalline forms, mainly three different polymorphic forms are reported which are quartz, tridymite and cristobalite. But quartz is the most common form of crystalline silica and each polymorphs have low temperature (α) and high temperature (β) forms [44]. Usually, amorphous silica is known as glass which can be transformed into crystalline form via appropriate thermal treatments. Absence of Bragg's reflections from glasses can be ascribed due to the disordered atomic arrangements.

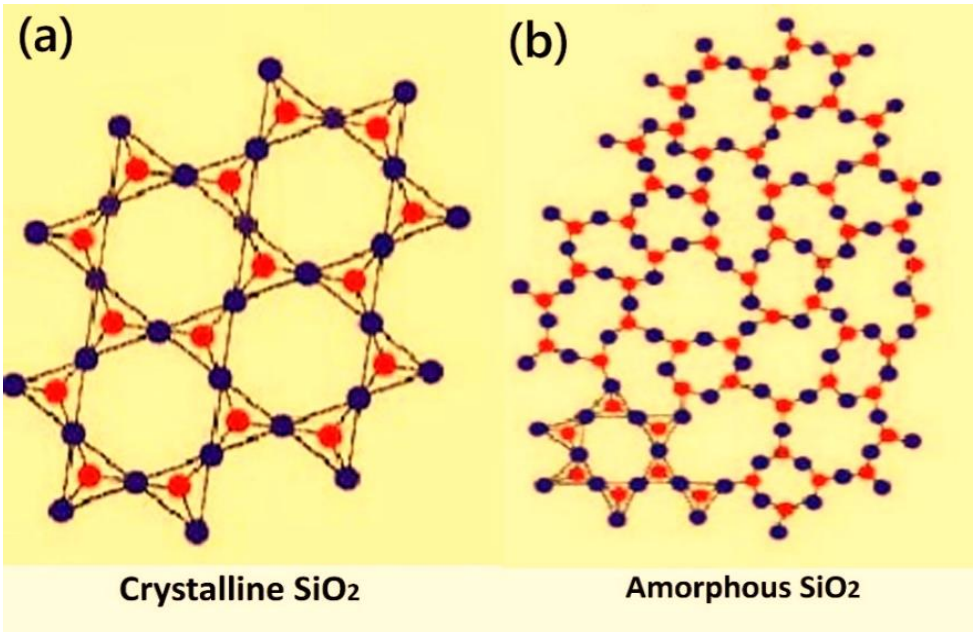

Figure 1.6: Structure of (a) crystalline and (b) amorphous silica [45]**.**

The term silica is originated from the Greek word *'silex'*. In the excited states, presence of four unpaired electrons in silicon forms four bonds that results a tough giant lattice with tetrahedral geometry. Strong network of silica melts only at elevated temperatures and the tetravalent behaviour of silicon is common in most of the compounds. So, (SiO_4) is considered as the fundamental units of all silicate minerals. Each silicon is bonded with four oxygen atoms and reported bond length of Si-O is 0.162 nm [46]. Silica has got wide industrial applications due to its peculiar features given below [47].

(i) Resistive nature towards rapid thermal changes and radioactive exposures.
(ii) Show wide range of spectral transmittance from UV to IR wavelengths.
(iii) Excellent chemical purity and durability.
(iv) Thermal stability at high temperature scales.

1.4.2 Activator

It is the impurity element which is intentionally added in minute quantities to the inorganic host matrix to achieve certain non-homogeneities. During luminescence, only small percentage of atoms are act as emissive centres. Inorganic phosphors are synthesised by adding trace amounts of dopants called as activator to get the desired luminescence characteristics. Activator ions absorbed high energy photons and return to the ground state by emitting radiations [43]. Sometimes, high energy photons ($h\nu_1$) are

absorbed by the host matrix and donate the energy to activator ions and finally, activator ions generate emissions by utilizing the collected energy.

1.4.3 Sensitizer

Owing to the weak absorption channels of activator ions, in some phosphors one more dopant addition occurs named as sensitizer. Sensitizer efficiently transfer the excitation energy to activator ions. Typically, forbidden nature of intra 4f transitions in RE ions mostly prevents direct excitation via absorbing photons which cause urgent requirement of sensitizer ions [48]. It increases the absorption capabilities and transfers the absorbed energy to activator ions. In particular, initially energy is absorbed by sensitizer and then transfer to activator ions having weak absorption. Sensitizer behaves differently in various host lattices [43]. Concentration quenching is another process in as the activator ion concentration crosses a limit value, an accompanied decrease in luminescence intensity occurs. This quenching mechanism can be ascribed due to the energy transfer between neighbouring ions or cross relaxation process [49]. Sensitization is a common process found not only in solids but also in liquid and gas forms.

1.5 Rare earth (RE) ions

Apart from various aromatic compounds, atoms in condensed phase are non-luminescent in nature. But lanthanides are an exceptional category of fluorescent elements among the whole list of elements. In periodic table, $^{139}La_{57}$ to $^{174}Lu_{71}$ are considered as the class of lanthanides which are generally exist in +3 oxidation state with electronic configuration of $[Xe]4f^n$ [50]. Transitions within 4f orbitals which was deeply screened by outer 5s and 5p orbitals made them exceptional from other elements. So, surroundings cannot influence the 4f electrons in significant scale [51]. Carl Auer von Welsbach is a pioneer in finding industrial applications of RE ions in the year 1891 by utilizing CeO_2 for achieving bright white light generating incandescent lamps. Exceptionally, La, Lu are non-luminescent metals in RE category due to the lack of incompletely filled 4f electrons which restricts them to exhibit luminescence as in other RE ions. Forbidden nature of intra 4f transitions in lanthanides cause low absorption coefficients ($< 10\ M^{-1}\ cm^{-1}$) and slow emissive rates which results in prolonged lifetime ranges from 0.5 to 3 ms [37]. Usually, RE ions are excited indirectly via chelated organic ligands. Their remarkable luminescent characteristics provide excellent applications such as immunoassays with remarkable limit of detection, catalytic converters, lasers, faraday rotators,

glass polishing, solid state lighting panels, phosphors, lasers, amplifiers, up conversion devices, scintillators. Certain limitations of RE ions are (i) they requires chelating ligands to get prominent excitations (ii) its applicability in anisotropy measurements is limited due to the lack of polarized emission [37].

1.5.1 Spectroscopy of RE ions

Various electronic energy levels of lanthanides are represented by the Russel-Saunders term symbols $^{(2S+1)}L_J$ where L symbolizes total orbital quantum number, S is the total spin quantum number and J stand for total angular momentum quantum number [41]. Rare earth ions with respective ground states and electronic configurations are given in table 1.2.

Table 1.2: Atomic number, electronic configuration of trivalent oxidation state, ground state, of rare earth elements.

Atomic number	Symbol of RE^{3+} ions	Electronic configuration (RE^{3+})	Ground state
57	La^{3+}	$[Xe]4f^0$	$^1S_0$
58	Ce^{3+}	$[Xe]4f^1$	$^2F_{9/2}$
59	Pr^{3+}	$[Xe]4f^2$	$^3H_4$
60	Nd^{3+}	$[Xe]4f^3$	$^4I_{9/2}$
61	Pm^{3+}	$[Xe]4f^4$	$^5I_4$
62	Sm^{3+}	$[Xe]4f^5$	$^6H_{5/2}$
63	Eu^{3+}	$[Xe]4f^6$	$^7F_0$
64	Gd^{3+}	$[Xe]4f^7$	$^8S_{7/2}$
65	Tb^{3+}	$[Xe]4f^8$	$^7F_6$
66	Dy^{3+}	$[Xe]4f^9$	$^6H_{15/2}$
67	Ho^{3+}	$[Xe]4f^{10}$	$^5I_8$
68	Er^{3+}	$[Xe]4f^{11}$	$^4I_{15/2}$
69	Tm^{3+}	$[Xe]4f^{12}$	$^3H_6$
70	Yb^{3+}	$[Xe]4f^{13}$	$^2F_{7/2}$
71	Lu^{3+}	$[Xe]4f^{14}$	$^1S_0$

Various electronic energy levels and the splitting of vibrational levels within RE ions are given in the Dieke's energy level diagram (Fig. 1.7). Dieke reported specific energy levels of RE ions doped in the $LaCl_3$ matrices.[52].

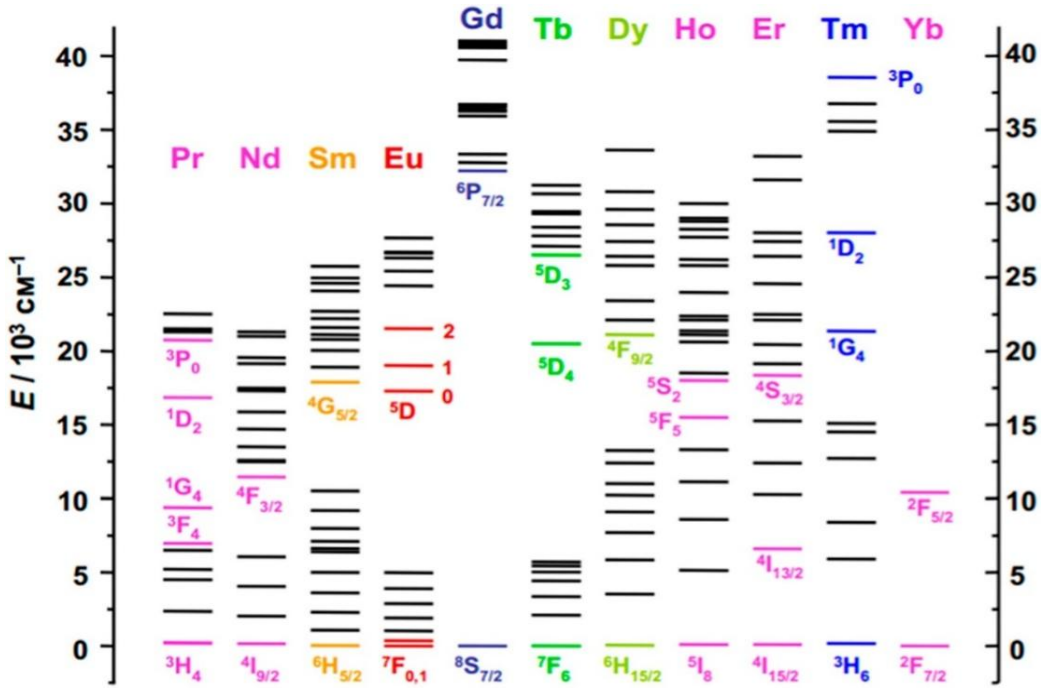

Figure 1.7: Dieke's energy level diagram of lanthanides [52]**.**

1.5.2 Types of transitions in RE ions

Intra 4f transitions, inter-band 4f → 5d transitions and charge transfer transitions are the three major electronic transitions found in RE ions.

(i) ***f-f transitions****:* According to *Laporte's rule*, f-f transitions are parity forbidden. In contrast, when RE ions interact with ligand fields or lattice vibrations, mixed states may raise parity change due to the significant spin orbit coupling. Due to this forbidden nature, f-f transitions result in long lifetime values of the order of milliseconds. The f-f transition is further subdivided into three which are electric dipole transition, electric quadrupole transition and magnetic dipole transitions, [41].

(a) *Electric dipole transition:* This kind of transitions will take place when active interactions between electric field components of radiating source and RE ions are established. Linearly moving charges triggers this transition which are *Laporte* forbidden.

(b) *Electric quadrupole transitions:* Quadrupole nature with zero dipole moment of a charge may cause electric quadrupole transitions. They are weakly intense than other two types of f-f transitions. These are

considered as hypersensitive transitions which are commonly known as pseudo-quadrupole transitions [41].

(c) *Magnetic dipole transitions:* Similar to the previous case, magnetic dipole transitions occur when the RE ions interacts with the vector component of magnetic field of the light source.

(ii) ***$4f^{n-1}$- $5d^1$ transitions:*** In this, 4f electrons transferred to 5d orbitals which are allowed transition and thereby corresponding emissions may be highly intense as compared with spectral lines from f-f transitions. Outer 5d orbitals are strongly interacts with surroundings, ligand field and existing phonons. In most cases, intense emissions from strong f-d transitions are dominant over line like spectra from f-f transitions [53].

(iii) ***Charge-transfer transitions:*** These transitions are Laporte allowed in which transition of electrons from neighbouring anions to 4f orbitals occurs which creates a change in oxidational state of RE ions. Charge transfer reactions are too sensitive to the external environment and hence its influence is significant. Intra 4f transitions produce weak emissions as that of the emissions from charge transfer states [54].

1.6 Energy Transfer in rare earth (RE) Ions

Luminescence enhancements or attenuations are generally explained with energy transfer mechanisms of RE ions with surroundings and dopants. Generally, energy transfer occurs via radiative and non-radiative modes. In first mode, photon absorption occurs from donors which was accepted by acceptors whereas second mode originates from the interaction of dopants with the host lattice vibrations. Donors are capable to release energy which are effectively absorbed by acceptors. Exchange of energy depends on two key factors which are the spectral overlap between emission spectrum of donor with that of absorption spectrum or excitation spectrum of acceptor and also the distance between donor-acceptor (D-A) pairs. Major theoretical concepts developed for explaining the interactions among D-A pairs are namely, Forster's model for condensed media [55], Dexter's concept for solid host lattices [56] and Inokuti and Hirayama's macroscopic model [57].

1.6.1 Non-radiative transition

Non-radiative transition occurs due to the interactions of dopants and the lattice vibrations of host matrix. This type transitions are also called as phonon assisted relaxation. Process differs on the basis of the number of phonons required to cross over the energy band gap and energy of each phonon. Non radiative energy exchange occurs mainly via three mechanisms which are (i) Cross relaxation (ii) Multi phonon relaxation (iii) Co-operative up conversion. Cross relaxation is a non-radiative relaxation occurs at higher dopant concentrations. As the concentration of dopant increases, ions became more closer and strongly interacts with each other. Thereby, donor species exchange its energy to acceptor ions via non radiative mode. In single RE doped ions, cross relaxation occurs between similar ions that results in luminescence quenching whereas in multi doped systems, activator-sensitizer pair may establish [58]. Multi phonon relaxations are also considered as non-radiative process which will occur when multiple phonons are required to achieve the transitions between respective energy levels [59]. Co-operative up conversion deals with two adjacently occupied ions lies in excited states and increase its yield at high concentrations [60], [61].

1.7 Synthesis and growth of nanocrystals

Nanomaterials can be synthesized via numerous methods which can be broadly categorized into two (Fig. 1.8). Top down and bottom up are the two common synthesis approaches employed for nanoscale synthesis. Typically, in top-down method bulk materials can break down into nanoscale structures via different tools and techniques. Ball milling, laser ablation, chemical etching are certain commonly performed methods under this category. This method is also known as destructive approach [62]. In contrast, bottom-up methods are constructive in nature which build up nanostructures via assembling respective atomic or molecular units. Sol gel method, pyrolysis, carbonization and solvothermal method are widely reported bottom- up synthesis techniques [62]. Sol gel process, pyrolysis and solvothermal synthesis are the common techniques employed in the whole research work.

.

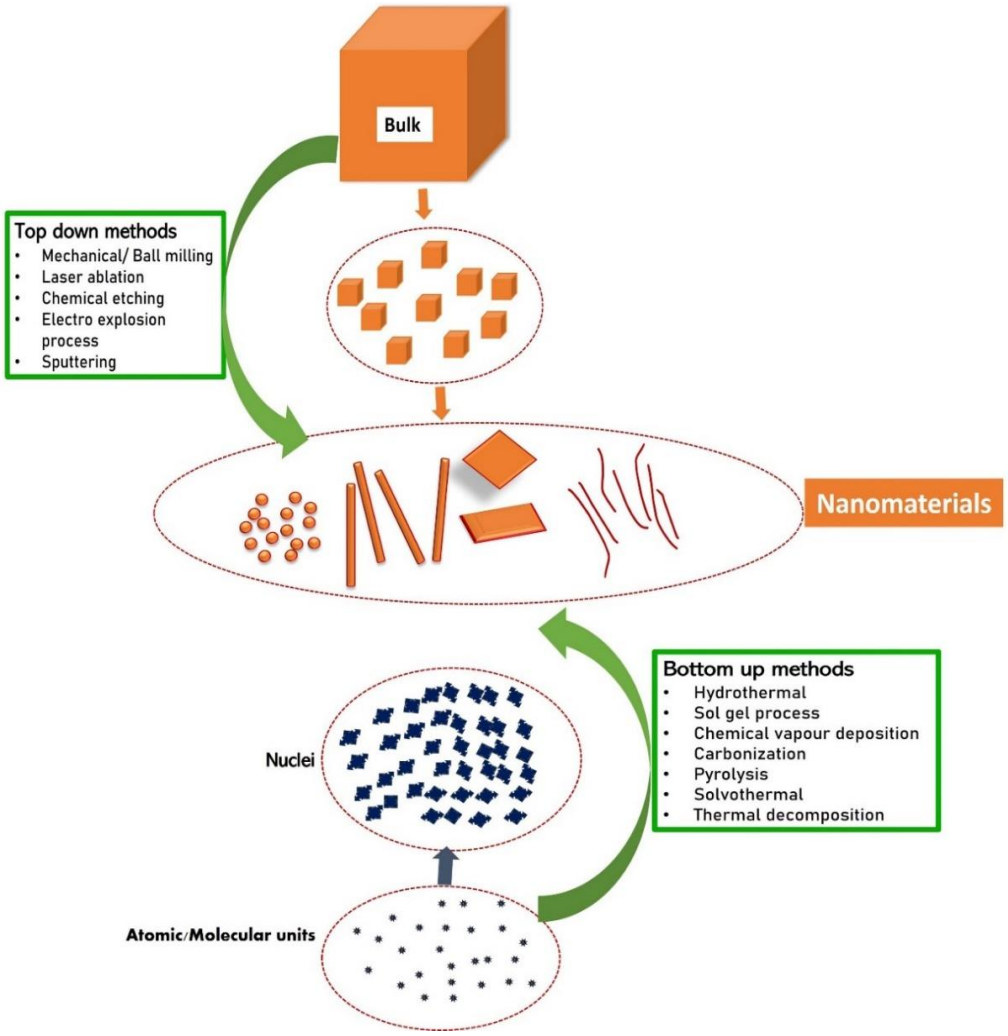

Figure 1.8: Synthesis approaches of nanomaterials.

1.7.1 Sol gel method

Two conventional methods used in glass production are sol gel (at low temperature) and melt quench method (at high temperature). Among this, melt quench is less adopted due to the extreme high melting point of glasses (1983 K) and difficulty in attaining homogeneity while incorporating various dopants. Sol gel process (shown in Fig. 1.9) is a wet chemical technique employed for fabricating high-quality glasses or ceramic materials with remarkable homogeneity. This process performed in open reaction vessels at room temperature and precursor mixing occurs at molecular levels [63]. Hydrolysis of metallic precursors are initiated by the assistance of water, alcohols and acid or base catalysts. Several steps involved in sol gel method are given below [64].

- Mixing: Alkoxide precursors (Si(OR)) are mixed with water, alcohols and acid/base catalysts. The most commonly used precursors for silica are tetra ethyl (TEOS), tetramethyl orthosilicate (TMOS). Water and alcohols are generally

utilized as solvents and molecular level mixing confirms the homogeneity of resultant mixture.

Hydrolysis of the alkoxide precursor:

Where R is alkyl group, R(OH) denotes alcohol.

$Si(OR)_4 + H_2O \rightarrow HO - Si(OR)_3 + R(OH)$

$Si(OR)_4 + 4H_2O \rightarrow Si(OH)_4 + 4R(OH)$

As per the amount of water present, hydrolysis may partially occur or terminated. Via condensation reactions, partially hydrolysed molecules are bonded as given below.

$$(OR)_3\text{-Si-OH} + \text{OH-Si-}(OR)_3 \rightarrow (OR)_3\text{-Si-O-Si-}(OR)_3 + H_2O$$

or

$$(OR)_3\text{-Si-OR} + \text{OH-Si-}(OR)_3 \rightarrow (OR)_3\text{- Si-O-Si-}(OR)_3 + \text{R-OH}$$

The whole process of hydrolysis and condensation can be expressed as below

$$nSi(OR)_4 + 4nH_2O \rightarrow nSi(OH)_4$$

- Casting: Obtained sol was then transferred into certain no adhesive containers.
- Gelation. Colloidal structures in sol were then strongly linked with each other which results in three-dimensional solid gel network. The low viscous sol became highly viscous.
- Aging: Polycondensation continues and the undisturbed gel became thicker, stronger with storage time. Gradual reduction in the porosity made the aged stiff gel more resistive towards cracking.
- Drying: At the drying stage, water and moisture content within the pores of network are removed. As the pore size decreases (< 20 nm) capillary stresses became more dominant. To avoid cracks, moderate drying conditions has to be applied.
- Chemical Stabilization. Porous solids will be produced by the subsequent removal of Si-OH bonds within the network.
- Densification. By treating the porous solids at high temperature scale, minimize the pores which led to densification of porous gels. Surface area, network pores are certain factors which determines the densification temperatures.

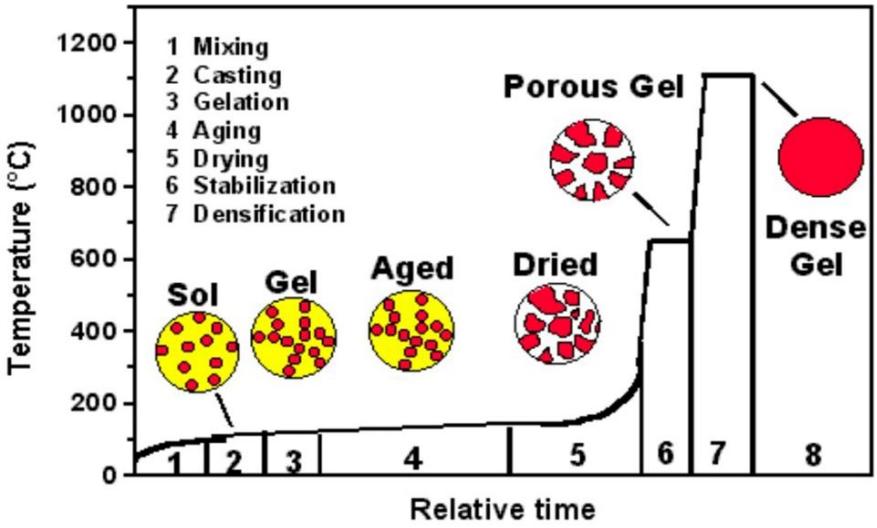

Figure 1.9: Different steps of sol-gel process [65].

Advantages of sol gel method are given below [65]:

1. Economical, with no high-power electricity utilization.
2. Easy, low temperature process to incorporate multiple components
3. Host matrix is capable to encapsulate appreciable dopant concentration
4. Size and shape of matrices can be moulded to different geometry
5. Quality of precursors can be regulated to achieve excellent glasses

1.7.2 Solvothermal method

Hydrothermal synthesis is a single step environmentally benign technique which has got much fame for the processing of advanced nanostructures and novel composite materials. Solvothermal process is exactly similar to hydrothermal route which differs in their medium of reaction from aqueous to non-aqueous [1], [66]. These synthesis methods yield ultra-pure, symmetrical nano structures like nanodots, nanofibers [67], nanosheets [68] through the occurrence of heterogenous reactions at certain harsh temperature-pressure conditions within sealed container [69]. The composition of end product can be tuned by controlling the synthetic parameters. Very first time, K.E. Schafhautl performed hydrothermal synthesis to obtain microscale quartz crystals using a normal pressure cooker [70].

Generally, the container or reaction chamber used for hydrothermal/ solvothermal is termed as autoclave. Pressure, temperature, time duration and the volume of container are the major factors which decides the geometry, composition and properties of end product. Water or the solvent used has also key role in synthesis. Pressure within the container depends on the volume of solution and treating temperature scales.

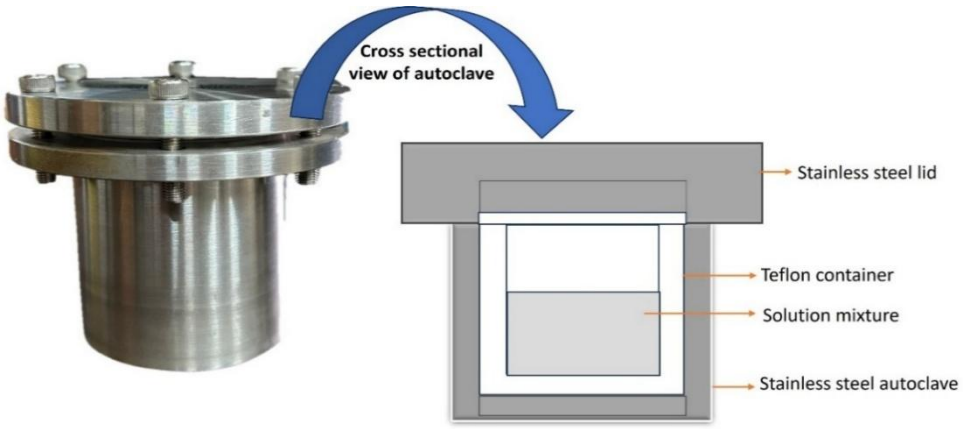

Figure 1.10: Schematic illustration of reaction chamber of solvothermal synthesis.

High temperature, pressure conditions involved in hydrothermal process requires reaction chambers which does not decompose or react with precursors or environment during the entire process. Teflon cup placed within stainless steel shell is often termed as autoclave for hydrothermal synthesis (given in Fig. 1.10). So, the autoclave is specifically designed to withstand in extremely harsh atmospheric conditions. It should not react with chemicals or the solvent used in synthesis. This leak free, ultra stable, corrosion resistant containers do not require further procedures after performing each experiment. Alloys and quartz cylinders are commonly used for this synthesis mode for ensuring the thermal stability. Temperature-difference method, temperature-reduction technique, metastable-phase technique are the three different methods opted in hydrothermal process. Even though it has many merits like compositional control, environmentally benign features, during hydrothermal process the crystal growth cannot be monitored.

1.7.3 Pyrolysis Method

Pyrolysis involves thermal breakdown or fire break down of bulk materials at high temperatures even in the oxygen free atmosphere. Generally, pyrolysis is used to decompose organic materials to obtain carbon rich products. *Pyro* means heat and *lysis* stands for separation which are Greek derived terms combined and obtained the term Pyrolysis. Pyrolysis technique is widely used in large scale production of chemicals such as carbon-based materials [71], ethylene and also employed in petroleum industry [72]. Normally this decomposition method conducted at a temperature scale above the boiling point of the solvent used.

Table 1.3: Different types of pyrolysis and description.

Sl. No.	Types of Pyrolysis	Description
1	Carbonization	Conversion of organic materials or biomass which burnt completely and final residue contains abundant carbon [73], [74].
2	Methane pyrolysis	Process which converts methane into carbon rich residue and hydrogen by appropriate thermal treatments [75].
3	Hydrous pyrolysis.	Pyrolysis is carried out in the presence of pressurized hot water which resulting the release of hydrogen and carbon dioxide.
4	Ceramization	Process which deals with thermal treatment of preceramic polymers held at inert atmosphere [76].
5	Catagenesis	Natural breakdown process which causes conversion of organic kerogens into fossil fuels [77], [78].
6	Flash vacuum pyrolysis	Organic synthesis which involves treating the precursor in harsh thermal conditions [79].

1.8 Solid state light emitting devices

Solid state lighting (SSL) systems are very firstly reported by Henry J Round, while conducting experiments in connection with research in crystal detectors for radio waves [80]. It is an excellent alternative for conventional electrical filaments-based illuminations. These particular solid-state illuminations utilize semiconductor-based LEDs and polymer-based LEDs for lighting. SSL has key characteristic features which differentiate it from other traditional lighting sources. Firstly, they are capable in custom-tailor the light with efficiency of unity. Secondly, spectral quality, chromatic controllability, tailorable compositions are exceptions provided which is not there in fluorescent lamps [80]. Particularly, SSL based lighting systems have inherent benefits which can be listed into three. (i) Highly efficient light generations from SSL minimize the energy consumption and saves huge amount of energy. (ii) Remarkable environment benign SSL features typically, for inorganic semiconductor-based LEDs guarantees the durability and efficiency. (iii) Precise color controlling and the ability to regulate luminescence properties allows it to design efficient lighting platforms [80].

1.8.1 Photoluminescence color tuning (PLCT)

Photoluminescence color tuning (PLCT) is an exciting optical feature of luminescent material which involves tuning of colorimetric point from one color domain to other via various methods. PLCT is generally achieved via various strategies including the compositional control of phosphors, surface modifications. Particularly in carbon quantum dots, varying excitation wavelengths generate tunable luminescence. In some cases, coordination assemblies with different crystal structure are also a reason for acquiring PLCT behaviour. Concentration dependent and excitation dependent PLCT are commonly reported classes of luminescence tuning [81]. PLCT favours multifaceted applications in displays, light emitting diodes (LED), sensors, white light emissions [82].

1.8.2 White light emitting (WLE) approaches

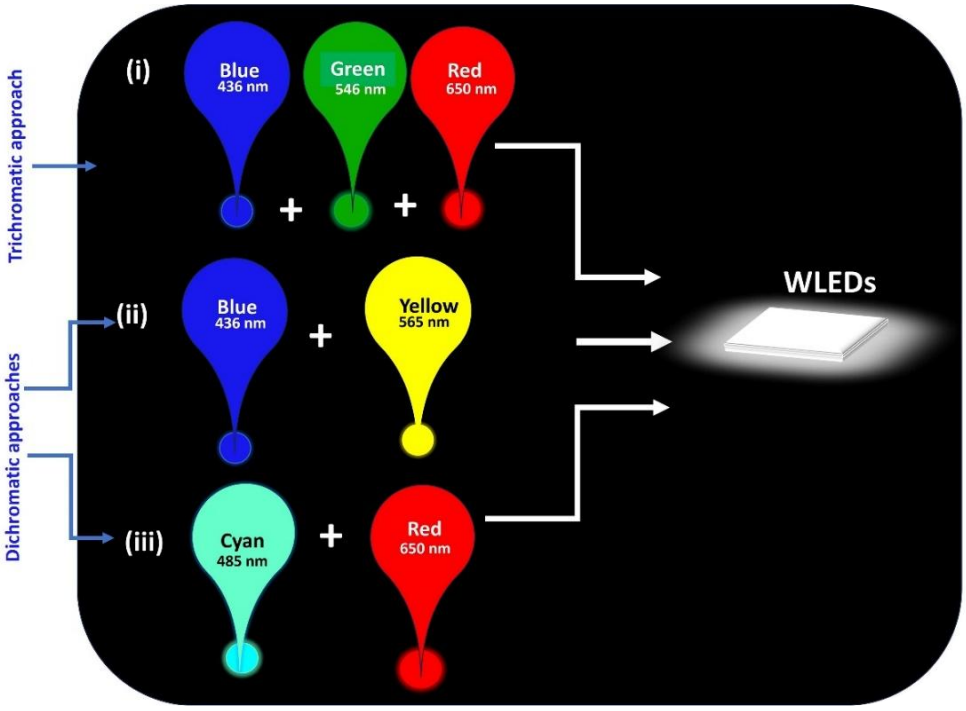

Figure 1.11: Schematic diagram of WLE approaches.

Different white light generating approaches (shown in Fig. 1.11) were reported in various literatures, i.e., dichromatic and trichromatic approaches. Typical methods of white light generation are combining the primary color emitters (red-green-blue) or complementary colors (blue - yellow) or (cyan-red). This process of combining different emissive units is known as additive mixing which primarily strategizes the widening

of spectral distribution of full visible window. On the basis of additive mixing technique, diverse organic-inorganic scaffolds, metal organic frames (MOFs) were built to attain WLE. Integrating UV LED chips with luminescent phosphors are also an important method utilized in WLED fabrication.

1.8.3 Chromaticity characterization techniques

(i) 1931 Commission International de l'Eclairage (CIE) Chromaticity diagram

The CIE system is considered as a key tool of modern colorimetry which deals with color science. It is a color specification technique for evaluating the color purity and spectral quality of testing light source. Generally, color point spotted in the two-dimensional CIE chromaticity chart as (x, y) coordinates whereas ideal white light is assigned with (0.33, 0.33) colorimetric coordinates [83].

(ii) *Color calculator* software

The color calculator is a key software developed by Osram Sylvania for the designing of efficient lighting solutions. It is widely used in LED fabrications due to easy installation, free of cost and user-friendly features. Mainly it has two modes of operation which includes (i) general photometry (ii) design optimization. In the general photometry mode user can select the LED intensities or can directly enter specific spectral data and the software calculates colorimetric parameters like CCT, CRI, CIE indices, LER. In the second mode, user can set the desired photometric parameters and the program calculate the required LED intensity which optimize the design.

(iii) Correlated color temperature (CCT)

The correlated color temperature (CCT) is a measuring tool for checking the spectral quality of white light which is usually measured in Kelvin (K). It can be identified as the temperature at which a black body radiator resembles with the luminescence of testing light source. It quantifies the presence of compositional ratios of high wavelength red, orange lines and the violet-blue regions of low wavelength with the generated white light. CCTs are colorimetric parameter used to distinguish the nature of white light produced. White light with higher CCTs (> 5000 K) contains more bluish content which appears as cool whereas lower CCTs (~ 3000 K) are warm in nature

which carries more orange/red wavelengths. Warm white is more suitable for indoor lighting and cool WLE will be more apt for visual tasks [83].

(iv) Color rendering index (CRI or Ra)

The color rendering index (CRI or Ra) is defined as a measure of comparison between how truthfully colors on a test object revealed under a designed light source under test with that of the standard or reference source. This photometric parameter is introduced due to the significant color difference of objects kept under different light sources. CRI value ranges from 0 to 100 and a light source with CRI equals to 100 indicates that the LED under test revealed all colors on test object as when illuminated under ideal light source. High CRI values are obtained for sources with wide spectral distribution which spans over the entire visible light spectrum. Potential candidates with CRI >= 80 and their adjustable CCTs can be effectively utilized in indoor and outdoor lighting applications [83].

(v) Quantum yield (QY)

$$\text{Quantum yield (QY)} = \frac{Number\ of\ photons\ emitted}{Number\ of\ absorbed\ photons} \quad \ldots\ldots\ldots\ldots\ (1.1)$$

The fluorescence quantum yield (QY) is a measure of how many photons emitted by the light source from the total absorbed photons as given in equation (1.1). QY is an intrinsic parameter which symbolizes radiative transitions linked with luminescence conversion channels [83].

(vi) Luminous efficacy (LER)

$$\text{Luminous efficacy} = = \frac{Total\ luminous\ flux\ (lumens)}{Optical\ ower\ (watts)} \ldots\ldots\ldots\ldots\ (1.2)$$

This photometric parameter is the figure of merit of a light source which can be calculated out from equation (1.2). It always stood contradictory to color rendering properties as for high CRI value with wide spectral distribution which conversely decreases the luminous efficacy significantly from theoretical value of 683 lumen per watt. Luminous efficacy is inversely proportional to the degree of poly chromaticity. As the number of emissive components increases, luminous efficacy decreases [83].

1.9 Literature review

1.9.1 Review on carbon nanostructures for lighting applications

Wide variety of optoelectronic applications are reported for CQDs on account of their unique features like tunable band gap, low toxicity, stable intense fluorescence and broad emission spectrum. Their versatile features are well explored by various researchers in the designing of lighting panels. Cheng and co-workers presented a phosphor based WLED with color point (0.34, 0.35) which is constructed by coating broad yellow emitting CQDs on LED chip made up of GaN [84]. Mostly, due to the lack of red emissive component cool white with CCT > 5000 K are generated which hinders it from warm white applications. In order to ensure the full visible spectral distribution, Siyu Lu and coworkers were synthesised full color emission CQDs on the basis of certain theoretical calculations accompanied with slight modifications in synthetic conditions [85]. Meanwhile, another recent work describes solvothermally synthesised blue green red (B-G-R) CQDs with its high solubility in PVP led to UV - excited lighting devices [86]. Yang et. al, reported color tunable dual emissive CQDs which shows distinct fluorescence in different phases due to the supra molecular cross linking among clusters. Typically, CQDs exhibited significant blue (B) to yellow green (YG) color tuning in liquid form and yellow to orange-red domain spectral tuning in solid form [87]. Similar to this, Fan and his team reported a one pot solvothermal synthesis of multicolor emissive CQDs having unusual double emission which led to potential applications such as solid state luminescence and bio-labelling [88]. Also, Lin and coworkers presented a synthesis approach in which R-CQDs, G-CQDs, B-CQDs were integrated into flexible PVA films which find key applications in LEDs and cellular imaging platforms [89]. To avoid aggregation induced quenching, some researchers incorporated full color emissive CQDs into inorganic host lattices and thereby excellent UV coated LEDs are developed with the aid of InGaN chips [90]. Another interesting work on CQD by the team of Shihe Yang demonstrates solid, ultra broad (FWHM > 200 nm), warm white emitting candidate with excellent CRI value. They employed a peculiar hydrogen bonding mechanism to control the size of nanocarbon which results CCTs ~ 3000 K and CRI of 91 [91].

1.9.2 Review on rare earth (RE) ions/Elemental nanoparticle composites

When rare earth (RE) ions are tailored with elemental nanostructures, their individual merits are combined that widens its spectrum of applications such as indoor-outdoor lighting, white light emitting diodes, display panels. Significant optical enhancement in the luminescence profiles is reported in many RE based nano composites. Typically, Peng et. al. presented a Eu^{3+} ions activated $NaGdF_4$ nanorods for excellent indoor lighting applications. They achieved nanorods with remarkable color purity of 90.5 % in visible red domain [92]. Sol gel derived CdSe/ Eu^{3+}compositions in silica matrix exhibited fluorescence enhancement due to the energy transfer from CdSe to Eu^{3+} ions [93]. Similar to this, for CdS/Tb^{3+} ions composites, fluorescence from Tb^{3+} are significantly increased [94]. Unnikrishnan N V and his co-workers investigated the influence of Ag nanocrystals on the optical performance of Eu^{3+} in SiO_2-TiO_2. They compared results from theoretical and experimental studies for solid state lighting applications [95]. Tho et. al synthesized Eu-doped CdS quantum dots via wet chemical route in which RE concentration varies from 0.5-10 %. Energy transfer between CdS and Eu^{3+} are explained in terms of exchange interactions and the energy transfer efficiency increases with increased RE content [96]. CdTe/Sm^{3+} silica xerogels are also reported in which optical analysis of air annealed composites are well explained using Judd–Ofelt (JO) theory [97]. Junjie et. al constructed a perovskite QD-RE combination in which Eu^{3+} doped with $CsPbBr_3$ quantum dots that shows excellent optical performance for WLEDs [98]. Recently, Hongtao Chu et. al. developed a fluorescent probe for mercury detection by utilizing RE doped CdTe QDs/ CQDs [99]. One of the recent research works by Yuanbing Mao and his team proved the excellency of Sm^{3+}-activated $La_2Hf_2O_7$ nanoparticles in luminescence thermometry, thermographic phosphor and scintillators [100].

1.10 Organisation of thesis

The thesis primarily focused on the structural investigation and optical features of different RE/EN doped silica composites. Detailed investigations are done for their applications in solid-state lighting systems. Particularly, Chapter 1 contains a general introduction on nanostructures, allotropism, energy transfer mechanisms and fundamentals of RE spectroscopy. In addition to that, different approaches to generate white light and

chromaticity characterization techniques are also presented in short. Chapter 2 describes fabrication of carbon quantum dots - Tb^{3+} - Eu^{3+} doped silica and detailed studies on their solid state tunable WLE. Chapter 3 depicts synthesis of dual emitting biomass derived carbon nanoparticles via facile direct thermal decomposition and their in-depth optical investigations. Meanwhile, a phase dependent optical study of Tb^{3+}/Se doped silica for multicolor emitting applications are included in Chapter 4. Chapter 5 comprises fabrication of tunable silica glasses doped with carbon quantum dots and Tb^{3+}ions. Chapter 6 is a study of structural and optical features of nanocarbon doped silica and their promising light emitting applications. Chapter 7 and Chapter 8 contains the overall summary and future scope of the research work respectively.

1.11 Objectives of the research work

- Investigate optical properties and energy transfer mechanism of various RE/EN composites in silica.
- Investigate structural dependence on optical properties of RE/EN based silica composites
- Develop white light emitting RE/EN based silica composites with better CRI and CCT values.
- Examine the possibility of photoluminescence color tunability of RE/EN compositions.

References

[1] N. Baig, I. Kammakakam, and W. Falath, "Nanomaterials: a review of synthesis methods, properties, recent progress, and challenges," *Mater. Adv.*, vol. 2, no. 6, pp. 1821–1871, 2021, doi: 10.1039/D0MA00807A.

[2] P. Walter *et al.*, "Early Use of PbS Nanotechnology for an Ancient Hair Dyeing Formula," *Nano Lett.*, vol. 6, no. 10, pp. 2215–2219, Oct. 2006, doi: 10.1021/nl061493u.

[3] I. Freestone, N. Meeks, M. Sax, and C. Higgitt, "The Lycurgus Cup — A Roman nanotechnology," *Gold Bull.*, vol. 40, no. 4, pp. 270–277, Dec. 2007, doi: 10.1007/BF03215599.

[4] F. J. Heiligtag and M. Niederberger, "The fascinating world of nanoparticle research," *Mater. Today*, vol. 16, no. 7, pp. 262–271, Jul. 2013, doi: 10.1016/j.mattod.2013.07.004.

[5] A. Junk and F. Riess, "From an idea to a vision: There's plenty of room at the bottom," *Am. J. Phys.*, vol. 74, no. 9, pp. 825–830, Sep. 2006, doi: 10.1119/1.2213634.

[6] S. Shanmugam, *Nanotechnology*. MJP Publisher, 2019.

[7] N. Labjar and S. El Hajjaji, "Functionalized Nanocomposites as Corrosion Inhibitors," in *Functionalized Nanomaterials for Corrosion Mitigation: Synthesis, Characterization, and Applications*, vol. 1418, in ACS Symposium Series, no. 1418, vol. 1418. , American Chemical Society, 2022, pp. 141–154. doi: 10.1021/bk-2022-1418.ch006.

[8] P. Parot *et al.*, "Past, present and future of atomic force microscopy in life sciences and medicine," *J. Mol. Recognit.*, vol. 20, no. 6, pp. 418–431, 2007, doi: 10.1002/jmr.857.

[9] R. Jose Varghese, E. hadji M. Sakho, S. Parani, S. Thomas, O. S. Oluwafemi, and J. Wu, "Chapter 3 - Introduction to nanomaterials: synthesis and applications," in *Nanomaterials for Solar Cell Applications*, S. Thomas, E. H. M. Sakho, N. Kalarikkal, S. O. Oluwafemi, and J. Wu, Eds., Elsevier, 2019, pp. 75–95. doi: 10.1016/B978-0-12-813337-8.00003-5.

[10] Paras *et al.*, "A Review on Low-Dimensional Nanomaterials: Nanofabrication, Characterization and Applications," *Nanomaterials*, vol. 13, no. 1, Art. no. 1, Jan. 2023, doi: 10.3390/nano13010160.

[11] B. Su, Y. Wu, and L. Jiang, "The art of aligning one-dimensional (1D) nanostructures," *Chem. Soc. Rev.*, vol. 41, no. 23, pp. 7832–7856, Nov. 2012, doi: 10.1039/C2CS35187K.

[12] M. I. Katsnelson, "Graphene: carbon in two dimensions," *Mater. Today*, vol. 10, no. 1, pp. 20–27, Jan. 2007, doi: 10.1016/S1369-7021(06)71788-6.

[13] M. F. Al-Hakkani, "Biogenic copper nanoparticles and their applications: A review," *SN Appl. Sci.*, vol. 2, no. 3, p. 505, Feb. 2020, doi: 10.1007/s42452-020-2279-1.

[14] L. D. Geoffrion and G. Guisbiers, "Quantum confinement: Size on the grill!," *J. Phys. Chem. Solids*, vol. 140, p. 109320, May 2020, doi: 10.1016/j.jpcs.2019.109320.

[15] H. Liu, L. Zhang, M. Yan, and J. Yu, "Carbon nanostructures in biology and medicine," *J. Mater. Chem. B*, vol. 5, no. 32, pp. 6437–6450, Aug. 2017, doi: 10.1039/C7TB00891K.

[16] X. Xu *et al.*, "Electrophoretic Analysis and Purification of Fluorescent Single-Walled Carbon Nanotube Fragments," *J. Am. Chem. Soc.*, vol. 126, no. 40, pp. 12736–12737, Oct. 2004, doi: 10.1021/ja040082h.

[17] S. Ying Lim, W. Shen, and Z. Gao, "Carbon quantum dots and their applications," *Chem. Soc. Rev.*, vol. 44, no. 1, pp. 362–381, 2015, doi: 10.1039/C4CS00269E.

[18] Y. Hu, O. A. Shenderova, Z. Hu, C. W. Padgett, and D. W. Brenner, "Carbon nanostructures for advanced composites," *Rep. Prog. Phys.*, vol. 69, no. 6, p. 1847, May 2006, doi: 10.1088/0034-4885/69/6/R05.

[19] Geim, A. N. D. R. E., and K. Novoselov, "Graphene calling," *Nat. Mater.*, vol. 6, no. 3, pp. 169–169, Mar. 2007, doi: 10.1038/nmat1858.

[20] Baker, Sheila N., and Gary A. Baker. "Luminescent carbon nanodots: emergent nanolights." *Angewandte Chemie International Edition*, vol. 49, pp. 6726-6744, Aug. 2010, "doi: 10.1002/anie.200906623

[21] K. J. Hong, C. H. Tan, S. T. Tan, and K.-K. Chong, "Chapter 30 - Morphology and topography of quantum dots," in *Graphene, Nanotubes and Quantum Dots-Based Nanotechnology*, Y. Al-Douri, Ed., in Woodhead Publishing Series in Electronic and Optical

Materials. , Woodhead Publishing, 2022, pp. 727–770. doi: 10.1016/B978-0-323-85457-3.00009-8.
[22] P. Kumar, S. Dua, R. Kaur, M. Kumar, and G. Bhatt, "A review on advancements in carbon quantum dots and their application in photovoltaics," *RSC Adv.*, vol. 12, no. 8, pp. 4714–4759, 2022, doi: 10.1039/D1RA08452F.
[23] K. J. Mintz, Y. Zhou, and R. M. Leblanc, "Recent development of carbon quantum dots regarding their optical properties, photoluminescence mechanism, and core structure," *Nanoscale*, vol. 11, no. 11, pp. 4634–4652, 2019, doi: 10.1039/C8NR10059D.
[24] Y. Wang and A. Hu, "Carbon quantum dots: synthesis, properties and applications," *J. Mater. Chem. C*, vol. 2, no. 34, pp. 6921–6939, 2014, doi: 10.1039/C4TC00988F.
[25] L. Tang *et al.*, "Deep Ultraviolet Photoluminescence of Water-Soluble Self-Passivated Graphene Quantum Dots," *ACS Nano*, vol. 6, no. 6, pp. 5102–5110, Jun. 2012, doi: 10.1021/nn300760g.
[26] T. Yu, H. Wang, C. Guo, Y. Zhai, J. Yang, and J. Yuan, "A rapid microwave synthesis of green-emissive carbon dots with solid-state fluorescence and pH-sensitive properties," *R. Soc. Open Sci.*, vol. 5, no. 7, p. 180245, Jul. 2018, doi: 10.1098/rsos.180245.
[27] L. Liu, Q. Peng, and Y. Li, "Preparation of monodisperse Se colloid spheres and Se nanowires using Na2SeSO3 as precursor," *Nano Res.*, vol. 1, no. 5, pp. 403–411, Nov. 2008, doi: 10.1007/s12274-008-8040-5.
[28] Z.-M. Liao, C. Hou, L.-P. Liu, and D.-P. Yu, "Temperature Dependence of Photoelectrical Properties of Single Selenium Nanowires," *Nanoscale Res. Lett.*, vol. 5, no. 6, p. 926, Mar. 2010, doi: 10.1007/s11671-010-9585-2.
[29] J.-M. Song, J.-H. Zhu, and S.-H. Yu, "Crystallization and Shape Evolution of Single Crystalline Selenium Nanorods at Liquid−Liquid Interface: From Monodisperse Amorphous Se Nanospheres toward Se Nanorods," *J. Phys. Chem. B*, vol. 110, no. 47, pp. 23790–23795, Nov. 2006, doi: 10.1021/jp065600k.
[30] H. Chen, D.-W. Shin, J.-G. Nam, K.-W. Kwon, and J.-B. Yoo, "Selenium nanowires and nanotubes synthesized via a facile template-free solution method," *Mater. Res. Bull.*, vol. 45, no. 6, pp. 699–704, Jun. 2010, doi: 10.1016/j.materresbull.2010.02.016.
[31] Jensen, William B W, "The Origin of the Term Allotrope," *Journal of Chemical Education*. vol. 83, no. 6, pp.838, June 2006, /doi: 10.1021/ed083p838
[32] O. Kanoun *et al.*, "Flexible Carbon Nanotube Films for High Performance Strain Sensors," *Sensors*, vol. 14, no. 6, Art. no. 6, Jun. 2014, doi: 10.3390/s140610042.
[33] H. W. Kroto, J. R. Heath, S. C. O'Brien, R. F. Curl, and R. E. Smalley, "C60: Buckminsterfullerene," *Nature*, vol. 318, no. 6042, pp. 162–163, Nov. 1985, doi: 10.1038/318162a0.
[34] S. K. Tiwari, V. Kumar, A. Huczko, R. Oraon, A. D. Adhikari, and G. C. Nayak, "Magical Allotropes of Carbon: Prospects and Applications," *Crit. Rev. Solid State Mater. Sci.*, vol. 41, no. 4, pp. 257–317, Jul. 2016, doi: 10.1080/10408436.2015.1127206.
[35] K. A. A. Mary, N. V. Unnikrishnan, and R. Philip, "Cubic to amorphous transformation of Se in silica with improved ultrafast optical nonlinearity," *RSC Adv.*, vol. 5, no. 18, pp. 14034–14041, Jan. 2015, doi: 10.1039/C4RA14025G.
[36] V. S. Minaev, S. P. Timoshenkov, and V. V. Kalugin, "Structural and phase transformations in condensed selenium". *Journal of Optoelectronics and Advanced Materials,* vol. 7, no. 4, pp.1717, Aug. 2005.
[37] Lakowicz, Joseph R., ed. "Principles of Fluorescence Spectroscopy-Lakowicz, Jr." Springer New York, Sep. 2006. doi.10.1007/978-0-387-46312-4
[38] J. F. W. Herschel, "IV. 'Αμόρφωτα, no. I.— on a case of superficial colour presented by a homogeneous liquid internally colourless," *P*Lakowicz, Joseph R., ed. "Principles of Fluorescence Spectroscopy-Lakowicz, Jr." Springer New York, Sep. 2006. doi.10.1007/978-0-387-46312-4
[39] A. Jabłoński, "Über den Mechanismus der Photolumineszenz von Farbstoffphosphoren," *Z. Für Phys.*, vol. 94, no. 1, pp. 38–46, Jan. 1935, doi: 10.1007/BF01330795.

[40] M. Y. Berezin and S. Achilefu, "Fluorescence Lifetime Measurements and Biological Imaging," *Chem. Rev.*, vol. 110, no. 5, pp. 2641–2684, May 2010, doi: 10.1021/cr900343z.
[41] L. U. Khan and Z. U. Khan, "Rare Earth Luminescence: Electronic Spectroscopy and Applications," in *Handbook of Materials Characterization*, S. K. Sharma, Ed., Cham: Springer International Publishing, 2018, pp. 345–404. doi: 10.1007/978-3-319-92955-2_10.
[42] N. C. George, K. A. Denault, and R. Seshadri, "Phosphors for Solid-State White Lighting," *Annu. Rev. Mater. Res.*, vol. 43, no. Volume 43, 2013, pp. 481–501, Jul. 2013, doi: 10.1146/annurev-matsci-073012-125702.
[43] C.-C. Wu, K.-B. Chen, C.-S. Lee, T.-M. Chen, and B.-M. Cheng, "Synthesis and VUV Photoluminescence Characterization of (Y,Gd)(V,P)O4:Eu3+ as a Potential Red-emitting PDP Phosphor," *Chem. Mater.*, vol. 19, no. 13, pp. 3278–3285, Jun. 2007, doi: 10.1021/cm061042a.
[44] Douglas, Bodie E., and Shih-Ming Ho, "Crystal Structures of Silica and Metal Silicates," in *Structure and Chemistry of Crystalline Solids*, New York, NY: Springer New York, , pp. 233–278. 2006, doi: 10.1007/0-387-36687-3_10.
[45] Zhang, Geoff GZ, and Deliang Zhou. "Crystalline and amorphous solids." *Developing solid oral dosage forms*. Academic Press, pp. 23-57, 2017, doi:10.1016/B978-0-12-802447-8.00002-9
[46] K. K. Unger, Ed., "Chapter 1 General chemistry of silica," in *Journal of Chromatography Library*, vol. 16, Elsevier, 1979, pp. 1–14. doi: 10.1016/S0301-4770(08)60805-2.
[47] I. Fanderlik, *Silica Glass and Its Application*. Elsevier, Oct. 2013.
[48] G. Zucchi, O. Maury, P. Thuéry, F. Gumy, J.-C. G. Bünzli, and M. Ephritikhine, "2,2′-Bipyrimidine as Efficient Sensitizer of the Solid-State Luminescence of Lanthanide and Uranyl Ions from Visible to Near-Infrared," *Chem. – Eur. J.*, vol. 15, no. 38, pp. 9686–9696, 2009, doi: 10.1002/chem.200901517.
[49] M. Cesaria, "Chapter 3 - Physics of inorganic upconverting nanophosphors and their relevance in applications," in *Upconversion Nanophosphors*, S. Thomas, K. Upadhyay, R. K. Tamrakar, and N. Kalarikkal, Eds., in Micro and Nano Technologies. , Elsevier, 2022, pp. 49–102. doi: 10.1016/B978-0-12-822842-5.00012-1.
[50] T. Cheisson and E. J. Schelter, "Rare earth elements: Mendeleev's bane, modern marvels," *Science*, vol. 363, no. 6426, pp. 489–493, Feb. 2019, doi: 10.1126/science.aau7628.
[51] A. N. Carneiro Neto and R. T. Moura Jr., "Overlap integrals and excitation energies calculations in trivalent lanthanides 4*f* orbitals in pairs Ln-L (L = Ln, N, O, F, P, S, Cl, Se, Br, and I)," *Chem. Phys. Lett.*, vol. 757, p. 137884, Oct. 2020, doi: 10.1016/j.cplett.2020.137884.
[52] N. S. Kariaka, A. Lipa, A. N. Carneiro Neto, O. L. Malta, P. Gawryszewska, and V. M. Amirkhanov, "Eu^{3+} and Tb3+ coordination compounds with phenyl-containing carbacylamidophosphates: comparison with selected Ln3+ β-diketonates," *Front. Chem.*, vol. 11, May 2023, doi: 10.3389/fchem.2023.1188314.
[53] J. Solé, L. Bausa, and D. Jaque, *An Introduction to the Optical Spectroscopy of Inorganic Solids*. John Wiley & Sons, 2005.
[54] R. S. Mulliken, "Intensities of Electronic Transitions in Molecular Spectra II. Charge-Transfer Spectra," *J. Chem. Phys.*, vol. 7, no. 1, pp. 20–34, Jan. 1939, doi: 10.1063/1.1750319.
[55] W. Adam, *Chemical and Biological Generation of Excited States*. Elsevier, Dec. 2012.
[56] D. L. Dexter, "A Theory of Sensitized Luminescence in Solids," *J. Chem. Phys.*, vol. 21, no. 5, pp. 836–850, May 1953, doi: 10.1063/1.1699044.
[57] M. Inokuti and F. Hirayama, "Influence of Energy Transfer by the Exchange Mechanism on Donor Luminescence," *J. Chem. Phys.*, vol. 43, no. 6, pp. 1978–1989, Sep. 1965, doi: 10.1063/1.1697063.

[58] S. D. Jackson, "Cross relaxation and energy transfer upconversion processes relevant to the functioning of 2 μm Tm^{3+} -doped silica fibre lasers," *Opt. Commun.*, vol. 230, no. 1, pp. 197–203, Jan. 2004, doi: 10.1016/j.optcom.2003.11.045.
[59] F. Auzel, "Multiphonon-assisted anti-Stokes and Stokes fluorescence of triply ionized rare-earth ions," *Phys. Rev. B*, vol. 13, no. 7, pp. 2809–2817, Apr. 1976, doi: 10.1103/PhysRevB.13.2809.
[60] S. Prucnal, L. Rebohle, and W. Skorupa, "Blue electroluminescence of ytterbium clusters in SiO_2 by co-operative up-conversion," *Appl. Phys. B*, vol. 98, no. 2, pp. 451–454, Feb. 2010, doi: 10.1007/s00340-009-3751-1.
[61] F. E. Auzel, "Up-conversion in rare-earth-doped systems: past, present and future," in *XI Feofilov Symposium on Spectroscopy of Crystals Activated by Rare-Earth and Transition Metal Ions*, SPIE, Jul. 2002, pp. 179–190. doi: 10.1117/12.475333.
[62] S. A. M. Ealia and M. P. Saravanakumar, "A review on the classification, characterisation, synthesis of nanoparticles and their application," *IOP Conf. Ser. Mater. Sci. Eng.*, vol. 263, no. 3, p. 032019, Nov. 2017, doi: 10.1088/1757-899X/263/3/032019.
[63] J. Livage, "Sol-gel processes," *Curr. Opin. Solid State Mater. Sci.*, vol. 2, no. 2, pp. 132–138, Apr. 1997, doi: 10.1016/S1359-0286(97)80057-5.
[64] C. J. Brinker and G. W. Scherer, *Sol-gel science: the physics and chemistry of sol-gel processing*. Gulf Professional Publishing, Apr. 1990. doi: 10.1016/C2009-0-22386-5
[65] S. Rai and A. L. Fanai, "Optical properties of Ho3 + in sol-gel silica glass co-doped with Aluminium," *J. Non-Cryst. Solids*, vol. 449, pp. 113–118, Oct. 2016, doi: 10.1016/j.jnoncrysol.2016.07.023.
[66] K. Byrappa and T. Adschiri, "Hydrothermal technology for nanotechnology," *Prog. Cryst. Growth Charact. Mater.*, vol. 53, no. 2, pp. 117–166, Jun. 2007, doi: 10.1016/j.pcrysgrow.2007.04.001.
[67] S. Cao, C. Zhao, T. Han, and L. Peng, "Hydrothermal synthesis, characterization and gas sensing properties of the WO_3 nanofibers," *Mater. Lett.*, vol. 169, pp. 17–20, Apr. 2016, doi: 10.1016/j.matlet.2016.01.053.
[68] B. Chai, M. Xu, J. Yan, and Z. Ren, "Remarkably enhanced photocatalytic hydrogen evolution over MoS_2 nanosheets loaded on uniform CdS nanospheres," *Appl. Surf. Sci.*, vol. 430, pp. 523–530, Feb. 2018, doi: 10.1016/j.apsusc.2017.07.292.
[69] Jayatissa, Yong X. Gan Ahalapitiya H,"Hydrothermal Synthesis of Nanomaterials " *Journal of Nanomaterials*, vol. 2019, Mar. 2020, doi: 10.1155/2020/8917013
[70] A. Rabenau, "The Role of Hydrothermal Synthesis in Preparative Chemistry," *Angew. Chem. Int. Ed. Engl.*, vol. 24, no. 12, pp. 1026–1040, 1985, doi: 10.1002/anie.198510261.
[71] Q. Chen *et al.*, "Biomass-derived porous graphitic carbon materials for energy and environmental applications," *J. Mater. Chem. A*, vol. 8, no. 12, pp. 5773–5811, Mar. 2020, doi: 10.1039/C9TA11618D.
[72] P. Torregrosa-Rodríguez, M. Martínez-Escandell, F. Rodríguez-Reinoso, H. Marsh, C. G. de Salazar, and E. R. Palazón, "Pyrolysis of petroleum residues: II. Chemistry of pyrolysis," *Carbon*, vol. 38, no. 4, pp. 535–546, Jan. 2000, doi: 10.1016/S0008-6223(99)00133-5.
[73] S. Chen, Z. Liu, S. Jiang, and H. Hou, "Carbonization: A feasible route for reutilization of plastic wastes," *Sci. Total Environ.*, vol. 710, p. 136250, Mar. 2020, doi: 10.1016/j.scitotenv.2019.136250.
[74] I. C. Lewis, "Chemistry of carbonization," *Carbon*, vol. 20, no. 6, pp. 519–529, Jan. 1982, doi: 10.1016/0008-6223(82)90089-6.
[75] M. R. G. Pangestu, Z. Malaibari, A. Muhammad, F. N. Al-Rowaili, and U. Zahid, "Comprehensive Review on Methane Pyrolysis for Sustainable Hydrogen Production," *Energy Fuels*, vol. 38, no. 15, pp. 13514–13538, Aug. 2024, doi: 10.1021/acs.energyfuels.4c01551.
[76] X. Wang, F. Schmidt, D. Hanaor, P. H. Kamm, S. Li, and A. Gurlo, "Additive manufacturing of ceramics from preceramic polymers: A versatile stereolithographic approach

assisted by thiol-ene click chemistry," *Addit. Manuf.*, vol. 27, pp. 80–90, May 2019, doi: 10.1016/j.addma.2019.02.012.

[77] Y. V. Kissin, "Catagenesis and composition of petroleum: Origin of *n*-alkanes and isoalkanes in petroleum crudes," *Geochim. Cosmochim. Acta*, vol. 51, no. 9, pp. 2445–2457, Sep. 1987, doi: 10.1016/0016-7037(87)90296-1.

[78] B. Horsfield and J. Rullkotter, "Diagenesis, Catagenesis, and Metagenesis of Organic Matter: Chapter 10: Part III. Processes", Jan. 1994, doi: 10.1306/M60585C10

[79] C. Wentrup, "Flash Vacuum Pyrolysis: Techniques and Reactions," *Angew. Chem. Int. Ed.*, vol. 56, no. 47, pp. 14808–14835, 2017, doi: 10.1002/anie.201705118.

[80] E. F. Schubert, J. K. Kim, H. Luo, and J.-Q. Xi, "Solid-state lighting—a benevolent technology," *Rep. Prog. Phys.*, vol. 69, no. 12, p. 3069, Nov. 2006, doi: 10.1088/0034-4885/69/12/R01.

[81] M. Pan, W.-M. Liao, S.-Y. Yin, S.-S. Sun, and C.-Y. Su, "Single-Phase White-Light-Emitting and Photoluminescent Color-Tuning Coordination Assemblies," *Chem. Rev.*, vol. 118, no. 18, pp. 8889–8935, Sep. 2018, doi: 10.1021/acs.chemrev.8b00222.

[82] R. L. I. Ayscue, C. P. Verwiel, J. A. Bertke, and K. E. Knope, "Excitation-Dependent Photoluminescence Color Tuning in Lanthanide-Organic Hybrid Materials," *Inorg. Chem.*, vol. 59, no. 11, pp. 7539–7552, Jun. 2020, doi: 10.1021/acs.inorgchem.0c00405.

[83] M. Shang, C. Li, and J. Lin, "How to produce white light in a single-phase host?," *Chem. Soc. Rev.*, vol. 43, no. 5, pp. 1372–1386, Feb. 2014, doi: 10.1039/C3CS60314H.

[84] Q.-L. Chen, C.-F. Wang, and S. Chen, "One-step synthesis of yellow-emitting carbogenic dots toward white light-emitting diodes," *J. Mater. Sci.*, vol. 48, no. 6, pp. 2352–2357, Mar. 2013, doi: 10.1007/s10853-012-7016-8.

[85] B. Wang *et al.*, "Rational Design of Multi-Color-Emissive Carbon Dots in a Single Reaction System by Hydrothermal," *Adv. Sci.*, vol. 8, no. 1, p. 2001453, 2021, doi: 10.1002/advs.202001453.

[86] W. Cai *et al.*, "Full color carbon dots through surface engineering for constructing white light-emitting diodes," *J. Mater. Chem. C*, vol. 7, no. 8, pp. 2212–2218, Feb. 2019, doi: 10.1039/C9TC00274J.

[87] T. Feng *et al.*, "Color-Tunable Carbon Dots Possessing Solid-State Emission for Full-Color Light-Emitting Diodes Applications," *ACS Photonics*, vol. 5, no. 2, pp. 502–510, Feb. 2018, doi: 10.1021/acsphotonics.7b01010.

[88] D. Gao *et al.*, "Exploring of multicolor emissive carbon dots with novel double emission mechanism," *Sens. Actuators B Chem.*, vol. 277, pp. 373–380, Dec. 2018, doi: 10.1016/j.snb.2018.09.031.

[89] K. Jiang *et al.*, "Red, Green, and Blue Luminescence by Carbon Dots: Full-Color Emission Tuning and Multicolor Cellular Imaging," *Angew. Chem.*, vol. 127, no. 18, pp. 5450–5453, 2015, doi: 10.1002/ange.201501193.

[90] Z. Tian *et al.*, "Full-Color Inorganic Carbon Dot Phosphors for White-Light-Emitting Diodes," *Adv. Opt. Mater.*, vol. 5, no. 19, p. 1700416, 2017, doi: 10.1002/adom.201700416.

[91] T. Meng, T. Yuan, X. Li, Y. Li, L. Fan, and S. Yang, "Ultrabroad-band, red sufficient, solid white emission from carbon quantum dot aggregation for single component warm white light emitting diodes with a 91 high color rendering index," *Chem. Commun.*, vol. 55, no. 46, pp. 6531–6534, Jun. 2019, doi: 10.1039/C9CC01794A.

[92] P. Du, W. Ran, Y. Hou, L. Luo, and W. Li, "Eu^{3+} -Activated $NaGdF_4$ Nanorods for Near-Ultraviolet Light-Triggered Indoor Illumination," *ACS Appl. Nano Mater.*, vol. 2, no. 7, pp. 4275–4285, Jul. 2019, doi: 10.1021/acsanm.9b00743.

[93] G. Jose, G. Jose, V. Thomas, C. Joseph, M. A. Ittyachen, and N. V. Unnikrishnan, "Fluorescence enhancement from Eu^{3+} ions in CdSe nanocrystal containing silica matrix hosts," *Mater. Lett.*, vol. 57, no. 5, pp. 1051–1055, Jan. 2003, doi: 10.1016/S0167-577X(02)00923-0.

[94] P. V. Jyothy, K. A. Amrutha, J. Gijo, and N. V. Unnikrishnan, "Fluorescence Enhancement in Tb^{3+}/CdS Nanoparticles Doped Silica Xerogels," *J. Fluoresc.*, vol. 19, no. 1, pp. 165–168, Jan. 2009, doi: 10.1007/s10895-008-0398-y.

[95] K. V. A. Kumar, K. P. Revathy, V. Prathibha, T. Sunil, P. R. Biju, and N. V. Unnikrishnan, "Structural and luminescence enhancement properties of Eu3+/Ag nanocrystallites doped SiO_2-TiO_2 matrices," *J. Rare Earths*, vol. 31, no. 5, pp. 441–448, May 2013, doi: 10.1016/S1002-0721(12)60301-9.

[96] P. M. Tan *et al.*, "New insights on the energy transfer mechanisms of Eu-doped CdS quantum dots," *Phys. Chem. Chem. Phys.*, vol. 22, no. 11, pp. 6266–6274, Mar. 2020, doi: 10.1039/C9CP06778G.

[97] S. Mathew, P. R. Rejikumar, A. K. Adiyodi, P. V. Jyothy, and N. V. Unnikrishnan, "Structural and optical characterization of oxygenated CdTe/ Sm^{3+} in sol–gel silica glasses," *Mater. Chem. Phys.*, vol. 112, no. 3, pp. 1061–1064, Dec. 2008, doi: 10.1016/j.matchemphys.2008.07.024.

[98] P. Li *et al.*, "Nanocrystalline structure control and tunable luminescence mechanism of Eu-doped $CsPbBr_3$ quantum dot glass for WLEDs," *Nanoscale*, vol. 12, no. 12, pp. 6630–6636, Mar. 2020, doi: 10.1039/D0NR01207F.

[99] H. Chu, D. Yao, J. Chen, M. Yu, and L. Su, "Detection of Hg^{2+} by a Dual-Fluorescence Ratio Probe Constructed with Rare-Earth-Element-Doped Cadmium Telluride Quantum Dots and Fluorescent Carbon Dots," *ACS Omega*, vol. 6, no. 16, pp. 10735–10744, Apr. 2021, doi: 10.1021/acsomega.1c00263.

[100] S. K. Gupta, M. Abdou, J. P. Zuniga, A. A. Puretzky, and Y. Mao, "Samarium-Activated $La2Hf_2O_7$ Nanoparticles as Multifunctional Phosphors," *ACS Omega*, vol. 4, no. 19, pp. 17956–17966, Nov. 2019, doi: 10.1021/acsomega.9b01318.

2

Carbon Quantum Dots -Tb^{3+} - Eu^{3+} Doped Silica for Tunable WLE Applications

Development of ultra-stable, solid-state, cost-effective phosphors for white light emitting devices with high color rendition is in high demand. In this work, we prepared carbon quantum dots (CQDs) by a hydrothermal method with an average size ranging from 2-8 nm which exhibits low toxicity. Optical analysis confirmed the influence of both Cu^{2+} and Fe^{3+} ions and the excitation-dependent fluorescence of CQDs are effectively quenched by addition of Fe^{3+} ions. The excitation dependent emission property of CQDs and degradation resistant blue emission of CQDs-silica are utilized to construct CQDs-Europium-Terbium doped silica for stable multicolor emissions upon different excitation wavelengths. Optimized composition of CQDs with Terbium and Europium ions produced white light emissions under UV exposure of 370-393 nm. Continuous tuning from warm white emission to cool white emission with moderate CRI is achieved by varying the concentration of CQDs. The ultra-stable white emissions which last long for a year, reveals the potential WLED applications of these solid-state luminescent materials.

Graphical abstract

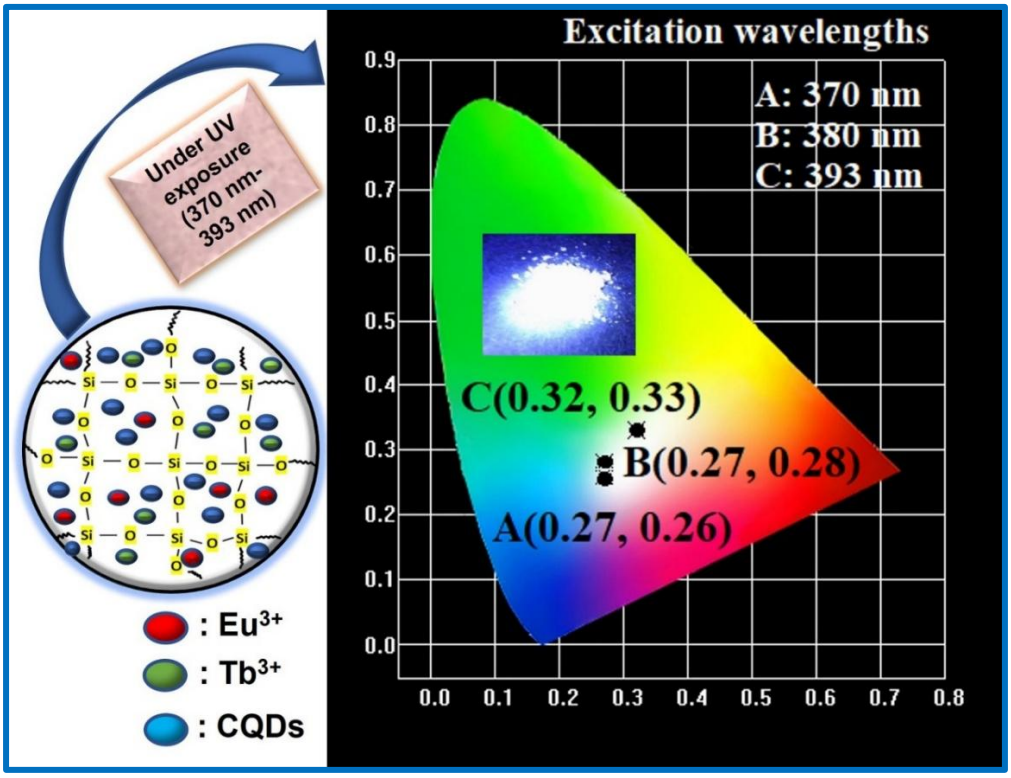

2.1 Introduction

For the past several years considerable efforts have been made on exploring luminescent materials for traditional light emitting devices (LEDs) to achieve minimal power consumptions, long operational life, quick response and compact size [1], [2], [3], [4]. Usually, white emissions are generated by the integration of blue LEDs with a color conversion layer of yellow or red-green luminescence materials [5]. Though they exhibit high luminous efficiencies, unequal RGB distributions with least FWHM generate near white light emission of minimal spectral grade and low color rendering index (CRI). Typical trichromatic RGB (red-green-blue) emitting quantum dots based WLEDs exhibit excellent CRI, high luminous and good efficiency. But these semiconductor dots and organic luminescent materials are Cd, Pb, selenides or tellurides based toxic compounds which restrict their wide applications. Moreover, self-aggregation of QDs and their degradation due to surface oxidation severely limits their applicability for achieving highly stable QD based WLEDs.

In recent years, carbon quantum dots (CQDs) are undoubtedly explored due to its versatile multi-disciplinary profiles which sometimes cross over the limits of toxic semiconducting quantum dots [6]. Luminescent carbon quantum dots (CQDs) have potential applications in various fields like metal-ion sensing, optical limiting, bio imaging and drug delivery etc [7], [8], [9], [10]. CQDs with excellent optical properties are obtained from a long list of non-toxic, green, natural precursors through numerous techniques [11]. Generally, CQDs are known to have strong blue fluorescence which is further tuned by tailoring surface groups and doping. Due to excitation dependent fluorescence and water-soluble nature blue emitting CQDs (B-CQDs) could be integrated with yellow or green-red fluorophore to get the trichromatic luminescence towards white emissions. Though various CQDs based WLEDs have attracted tremendous attention, integration of yellow emitting CQDs on blue light emitting diode chips could give only low CRI value. To yield high CRI values, with least energy losses, traditional lanthanide phosphors can be tailored with the B-CQDs. Many researchers have already put a great deal of effort into developing WLE glassy systems by exploiting the abundant energy levels and narrow emission spectral lines of RE ions [12], [13], [14]. Among RE ions, Tb^{3+} and Eu^{3+}dopants can emit discrete sharp green-red regions. To date, some recent studies have developed WLEDs based on Eu^{3+}/Tb^{3+}/

CQDs by adjusting the amount of CQDs and Ln^{3+} in nanocomposite solution to achieve white light emission [15], [16]. However, considering their low stability in complex solutions, it is necessary to fabricate RE – CQDs solid matrices to enhance mechanical toughness and optical stability for their practical applications in lighting systems.

In solid-state, white emissions from different RGB mixtures exhibit gradual fading and reduction in spectral quality due to self-absorption losses and the time induced degradation. Uniform dispersion of CQDs in solid frames like polymer, silica, gelatine and starch could prevent the aggregation caused quenching (ACQ) yielding high device efficiency and long shelf-lifetimes [17], [18]. Even though tunable CIE chromaticity coordinates are achieved in $Ca_{19}Mg_2(PO_4)_{14}$: Ln^{3+} (Ln^{3+} = Eu^{3+} and/or Tb^{3+}) nano crystalline phosphors, the urge for RE–CQDs solid composites with good CRI values remains [3]. Here, CQDs-silica solid composites with more than one year shelf life are synthesised using hydrothermal assisted sol gel method. RE–CQDs co-doped silica with good optical stability are prepared and color tunable emission ranging from warm to cool white light was achieved by varying nano phosphor concentration. Moreover, the excitation dependent fluorescence observed for CQDs was effectively utilized to obtain excitation dependent multicolor emission ranging from blue to white light.

2.1.1 Aloe vera

Figure 2.1: Photograph of Aloe Vera.

Aloe vera belongs to the genus Aloe which lies within the *Liliaceae* family [19]. But gradually, it spread to Mediterranean regions and now it exists in numerous countries worldwide. Green colored, thick aloe vera leaves containing a list of bioactive

compounds like lignans, phytosterols, polyphenols, anthraquinones, C-glycosides and anthrones [20]. These phytochemicals with remarkable bioactivity have been utilized for a wide spectrum of applications in connection with healthcare products, cosmetics and food processing industries [21]. Leaves have a yellow latex portion with inner jelly part and both were exploited for commercialization. The jelly, whitish inner portion of the leaves is highly nutritious containing 99% water and the remaining filled with major amino acids, minerals, lipids, essential vitamins, polysaccharides, proteins and antioxidants [22]. Role of Aloe vera products in both commercial and medicinal fields are inevitable. Aloe vera usage in multiple forms like nanoparticles, nanofibers, nanocomposites, hydrogels and bio-sponges led specifically to its potential applications in tissue engineering and drug delivery [19].

2.1.2 Hydrothermal carbonization

Generally, hydrothermal synthesis is a technique through which crystallizing a substance take place at high temperature scales by maintaining high vapour pressure. A series of chemical reactions occurred in the sealed container results in the desired nano assemblies. Typically, hydrothermal carbonization (HTC) is a cost efficient, environmentally benign, non-toxic synthesis technique capable of producing novel nanocarbon structures from multi varieties of carbonaceous precursors and crude biomass content [9]. In the process, dissolved solutions of precursors were kept in a hydrothermal reactor which underwent cascades of chemical transformations within the reactor. HTC is a very common technique performed for the CQD synthesis. Carbon nano assemblies were developed by utilizing many precursors such as citric acid [23], glucose [24], banana juice [25], ginger [26], orange [27], beetroot [28] and many other cheap natural sources. Easy availability of precursors, economical and facile preparation steps made it a widely acceptable synthesis process for achieving nanomaterials. Numerous carbonaceous structures with distinct dimension, morphology, and surface groups are already developed with this technique. Intense luminescence with spectral tunability of non-toxic, biocompatible carbon nano systems have miscellaneous applications in bioimaging, solid state lighting and sensing platforms [8], [9].

2.1.3 Terbium ion

Terbium is the ninth member of the lanthanide series with atomic number 65. It is a fairly electropositive rare earth metal which appears in silvery white color. Under UV excitations, intense green emissions from terbium ions are generated. Strong visible luminescence guarantees its potential applications in fluorescent lamps and advanced lighting systems. Fluorescence of Tb^{3+} ions mainly originated from $^5D_3$ and $^5D_4$ levels. Particularly, most of Tb^{3+}activated phosphors exhibit green fluorescence due to the $^5D_4 \rightarrow {}^7F_5$ transition. According to literatures, when Tb^{3+} ions getting excited under UV radiations, multiple emissions with a dominant green luminescence are reported. Typically, emission bands at 488 nm, 543 nm, 584 nm, 620 nm are arisen due to the spectral transitions from the level $^5D_4$ to distinct ^7F_J multiplets ($^5D_4 \rightarrow {}^7F_J$ (with J = 6, 5, 4, 3). Importantly, the most intense green emission at 543 nm is related to the $^5D_4 \rightarrow {}^7F_5$ magnetic dipole transitions [29], [30]. From previous studies, excitation bands of Tb^{3+} ions for the most intense emission band at 543 nm ($^5D_4 \rightarrow {}^7F_5$) are located at 303, 318, 340, 351, 377, 483 nm and associated transitions spectral transitions [31], [32] are shown in table 2.1.

Table 2.1: Excitation bands of Tb^{3+} ions for λ_{em} = 543 nm with corresponding transitions.

Sl. No	Peak positions (in nm)	Corresponding transitions
1	303	$^7F_6 \rightarrow {}^5H_5, {}^5H_6$
2	318	$^7F_6 \rightarrow {}^5H_7, {}^5D_1$
3	340	$^7F_6 \rightarrow {}^5L_{7,8}, {}^5G_3$
4	350	$^7F_6 \rightarrow {}^5L_9, {}^5D_2, {}^5G_5$
5	377	$^7F_6 \rightarrow {}^5L_{10}, {}^5D_3, {}^5G_6$
6	483	$^7F_6 \rightarrow {}^5D_4$

Terbium can also be found in X-ray machines, dopants in lasers and color television tubes. Also, it is alloyed with different metals for multifunctional applications. Terbium in combination with other red blue phosphors, generates efficient white light illuminations for indoor lighting applications. Luminescence channels of Tb^{3+} ions were depicted in Figure 2.2.

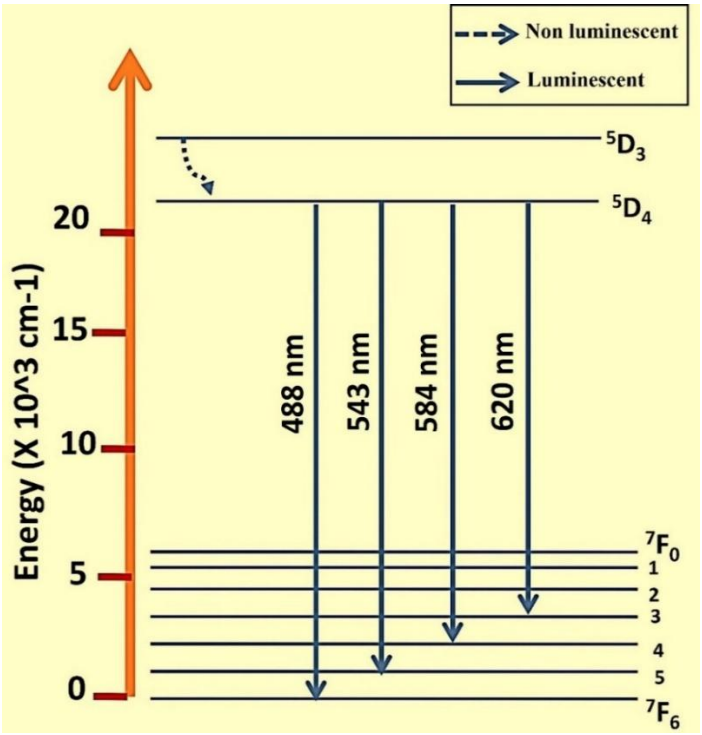

Figure 2.2: Luminescence channels of Tb^{3+} ions.

2.1.4 Europium ion

Europium is one of the most reactive rare earth elements having partially filled 4f-electron shell. Generally, europium exists in two stable valencies as Eu(II) and Eu(III). But mostly europium exists as a trivalent ion with ionic radius 0.121 nm. Strong visible luminescence of Eu^{3+} is generated due to the intra $4f^6$ transitions (S=3, L=3 and J=0) which were utilized in the optoelectronic applications. Lasing applications were successfully achieved by dispersing Eu^{3+} ions within an insulating host to avoid concentration quenching and minimize the energy transfer channels. Commercial production of Eu based laser materials and phosphors was commonly fabricated from Eu_2O_3 source [33]. Possible fluorescence pathways of Eu^{3+} ions were depicted in Figure 2.3. As per reports, prominent emission of Eu^{3+} obtained at 590 nm, 616 nm, 651 nm, 698 nm which are related to the transitions $^5D_0 \rightarrow {}^7F_J$ (with J = 1, 2, 3, 4). Excitation bands of Eu^{3+} ions for the most intense emission band at 616 nm ($^5D_0 \rightarrow {}^7F_2$) are located at 361, 376, 382, 393, 414, 463, 525 and 531 nm and corresponding spectral transitions are given in table 2.2. Most prominent excitation band at 393 nm can be assigned to the spectral transition $^7F_0 \rightarrow {}^5L_6$ [34].

Table 2.2: Excitation bands of Eu^{3+} ions for λ_{em} = 616 nm with corresponding transitions.

Sl. No	Peak positions (in nm)	Corresponding transitions
1	361	$^7F_0 \rightarrow {}^5D_4$
2	376	$^7F_0 \rightarrow {}^5G_2$
3	382	$^7F_1 \rightarrow {}^5L_7$
4	393	$^7F_0 \rightarrow {}^5L_6$
5	414	$^7F_1 \rightarrow {}^5D_3$
6	463	$^7F_0 \rightarrow {}^5D_2$
7	525	$^7F_1 \rightarrow {}^5D_1$
8	531	$^7F_1 \rightarrow {}^5D_0$

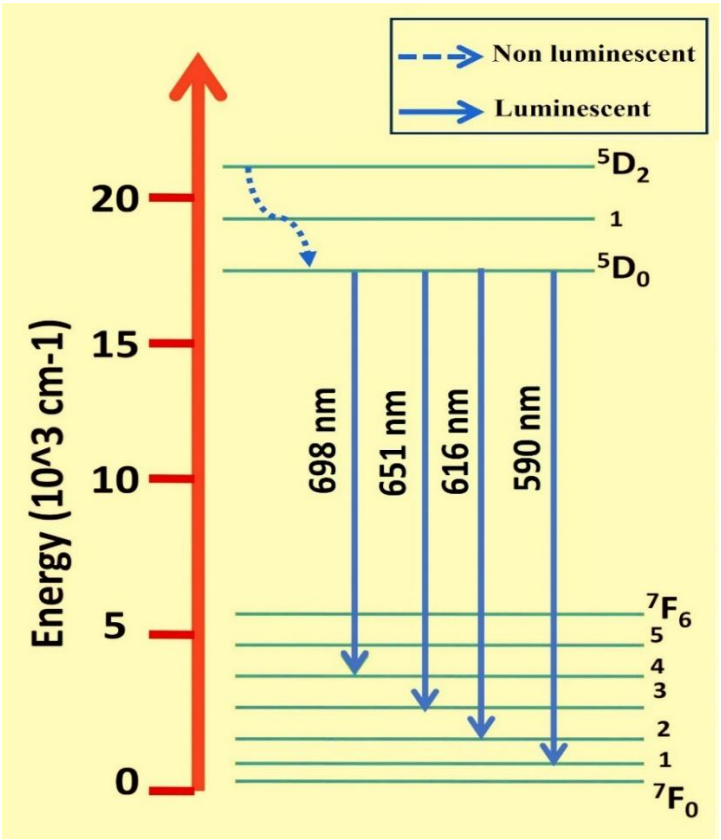

Figure 2.3: Luminescence channels of Eu^{3+} ions.

2.1.5 Review on RE/CQD composites

As a part of improving the spectral qualities of RE doped materials, fluorescent CQDs derived from various synthesis routes are combined via various linkages. Many attempts were reported regarding the preparation and effective applications of RE/CQD hybrids. RE-CQD composites have novel luminescence bands with unusual energy

transfer pathways which made it applicable for exciting applications such as solid-state lighting, phosphor based luminescence [16], fluorescent probes [35] , anticounterfeiting and bioimaging [36]. Among the long list of RE ions, Eu^{3+} and Tb^{3+} are mostly tailored with CQDs due to their inherent red and green luminescence. In some cases, Tb^{3+}, Eu^{3+} are integrated with blue emitting CQDs to achieve white emitting devices and tunable luminescent materials [3], [16], [37]. Typically, in some cases CQDs act like a sensitizer which triggers the energy transfer and thereby photoluminescence color tuning [3]. In a similar work, Eu^{3+}doped LaF_3/CQD nanocomposites are prepared and a particular energy transfer through the sensitizing effect of CQDs are included. Zhao and coworkers studied the quenching effect and the impact of europium ions on the fluorescence lifetime of CQDs. They demonstrated a possible energy transfer mechanism within the RE-CQD composition [38]. Meanwhile, Xu et. al. synthesised $NaYF_4$:Yb, Er(Tm)@CDs composites via sol gel route in which they achieved an impressive enhancement in red emissions and the NIR upcoversion related luminescence. There the integrated CQDs stood like a mediating channel for energy transfer process that results in remarkable optical enhancement in the composites [39]. One of the very recent research attempts by Pratap et. al. presents a CQD-Tb combination in which the CQDs are prepared from *plumeria* leaves and the terbium ions plays the role of a surface passivator. They also prepared CQD phosphor based films for lighting applications [40]. Interestingly, Claus Feldmann and his coworkers prepared extremely nanosized CQDs (3-5 nm) by simple thermal treatment of polyols. Through very simple heating method, they got CQDs with excellent blue, geen bands with remarkable quantum yield. By introducing RE ions into the CQDs, QY values increased to 85 % [41]. Yanzhi Zhao et. al. prepared a novel Gd/Yb@CQDs via one step hydrothermal route which shows applications in diagnostic techniques such as MRI/FI/CT [42].

2.2 Experimental section

2.2.1 Synthesis of carbon quantum dots (CQDs)

The CQDs were prepared by hydrothermal treatment of fresh aloe gel in water similar to previous chemical methods with slightly different reaction conditions [43]. In a typical procedure, aloe gel was extracted, chopped and well ground in a mortar to make into a juicy form. 15 g of the aloe gel was mixed thoroughly with 25 ml of distilled

water, and kept in a 50 ml Teflon-lined autoclave at 180°C. After 24 hours, the autoclave was allowed to cool naturally to room temperature. The brown solution obtained was filtered to remove the unreacted organic moieties. Finally, the light brown aqueous solution was collected for further characterization and use.

2.2.2 Preparation of metal ion solutions

Stock solutions of different metal ions (Fe^{3+}, Cd^{2+}, Mn^{2+}, Cu^{2+}, Zn^{2+}, Pb^{2+}, Co^{2+}) each with 10 mM concentration were prepared in distilled water using the corresponding precursors. Known volumes of stock solutions of metal ions were added into the CQDs solution and corresponding emission and absorption spectra were recorded. All fluorescence spectra were measured at an excitation wavelength of 370 nm.

2.2.3 Fabrication of CQDs-terbium-europium incorporated silica

RE-CQDs co-doped silica [2 wt% Tb^{3+} and 2 wt% Eu^{3+} in 2 g of silica] were prepared via sol gel route at room temperature. Appropriate amount of ethanolic solutions of terbium (III) nitrate pentahydrate and europium (III) nitrate pentahydrate was added to 7.4 ml tetraethyl orthosilicate (TEOS). The mixture was continuously stirred for 1 h after adding aqueous solution of 9.76 mg of CQDs to obtain a homogeneous solution. The molar ratio of TEOS – water − ethanol was taken as 1:2:2. Two drops of concentrated nitric acid were added as a catalyst. The final clear solution obtained was poured into polypropylene containers, sealed using paraffin wax and kept for about a month to form a stiff gel. Samples were then heated in the hot air oven at 60 ^{0}C for 2 days to eliminate water and other organics present [44]. Similar synthesis route was repeated for preparing CQDs (9.76 mg) doped silica and with lower CQDs concentration (1.5 mg). Obtained samples were annealed at 150 ^{0}C in muffle furnace for 2 h to get two sets of samples named as A (9.76 mg CQDs in 2 g of silica), A1 (9.76 mg CQDs, 2 wt% Tb^{3+} and 2 wt% Eu^{3+} in 2 g of silica) and A2 (1.5 mg CQDs, 2 wt% Tb^{3+} and 2 wt% Eu^{3+} in 2 g of silica). All samples were finally ground to fine powder using an agate mortar and stored in vials at room temperature. The solid-state fluorescence spectra of A, A1 and A2 were recorded and re-measured after a period of 1 year. All the measurements were performed at room temperature.

2.2.4 Optical and morphological characterization

The morphology and crystallinity of carbon quantum dots was examined using Transmission Electron Microscopy (TEM) data using JEM 2100 transmission electron microscope operated at 200 kV. The optical absorption spectrum of CQDs was recorded using UV-Visible spectrophotometer, (Shimadzu UV-2600) and fluorescence emission spectra were obtained using Fluoromax Spectro Fluorometer (Horiba Jobin Yvon, USA). Fourier transform infrared (FTIR) spectrum in the region 4000 cm^{-1}- 500 cm^{-1} was measured from FTIR spectrometer (Perkin Elmer, Singapore) with attenuated total reflectance (ATR) and diamond crystal. All the measurements were performed at room temperature.

2.3 Results and discussions

Hydrothermal treatment of aloe vera gel undergoes aromatization and carbonization through the cycloaddition reactions as well as condensation. CQDs are formed as a result of a possible nuclear burst within these aromatic rings [25], [45], [46], [47], [48], [49], [50], [51]. Sufficient number of carboxylic moieties on the CQDs surfaces is responsible for the easy dispersion in water with excellent biocompatibility [52].

2.3.1 Fourier transform infrared spectroscopy (FTIR)

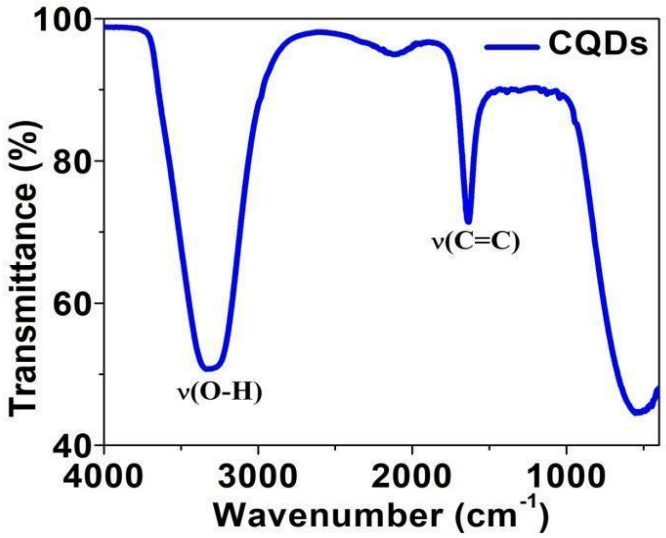

Figure 2.4: FT-IR spectrum of CQDs.

Furthermore, FTIR spectral assay was used to analyse the presence of different functional groups on CQDs surface. The FTIR spectrum of CQDs exhibits vibrational bands (Fig. 2.4) at 3332 cm^{-1} for O-H stretching and 1634 cm^{-1} for C=C stretching respectively [53]. Due to excellent surface functionalization with hydroxyl groups, CQDs have shown high solubility in water [25].

2.3.2 Transmission electron microscopy (TEM)

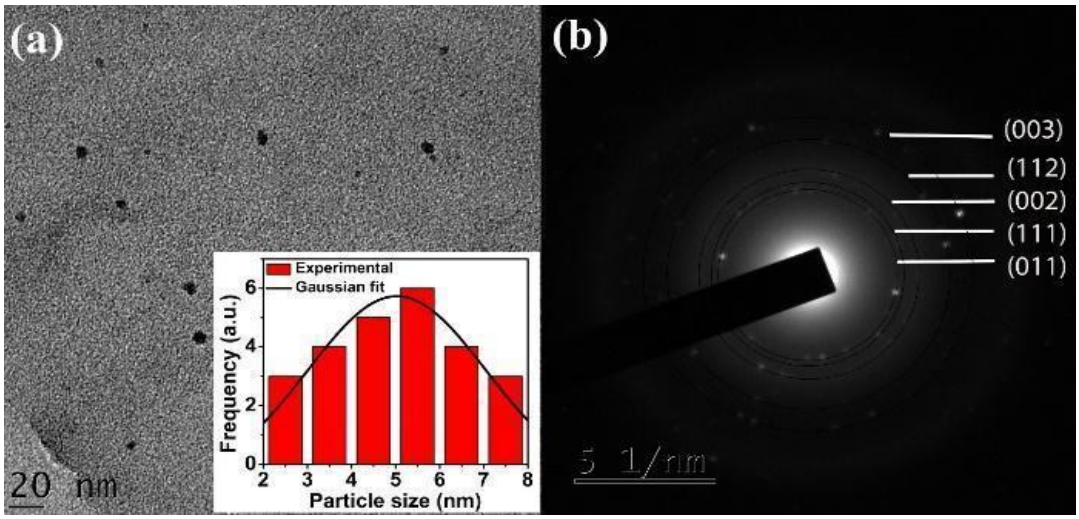

Figure 2.5: (a) TEM image and (b) SAED image of CQDs. [inset of (a) shows particle size distribution profiles of CQDs].

The morphology and crystallinity of the prepared CQDs was studied from TEM images as shown in figure 2.5. CQDs are well separated, and have a quasi-spherical morphology. The particle size ranges 2-8 nm (inset of Fig. 2.5 (a)). The existence of multiple rings in SAED pattern (Fig. 2.5 (b)) indicates the excellent polycrystalline nature of the CQDs. Obtained inter atomic spacing d-values of 0.17 nm, 0.20 nm, 0.26 nm, 0.29 nm, 0.33 nm are closer to the reported values of polycrystalline carbon dot systems [54] and can be indexed to (003), (112), (002), (111) and (011) lattice planes of cubic carbon (C_{20}) respectively (ICSD No-185973) [55]. Extreme thermal conditions with controlled carbonization produced self-assembled crystalline carbon dot structures.

2.3.3 Cell viability assay

Cell viability studies were carried out in rat spleen cells by applying trypan blue exclusion method (Fig. 2.6).

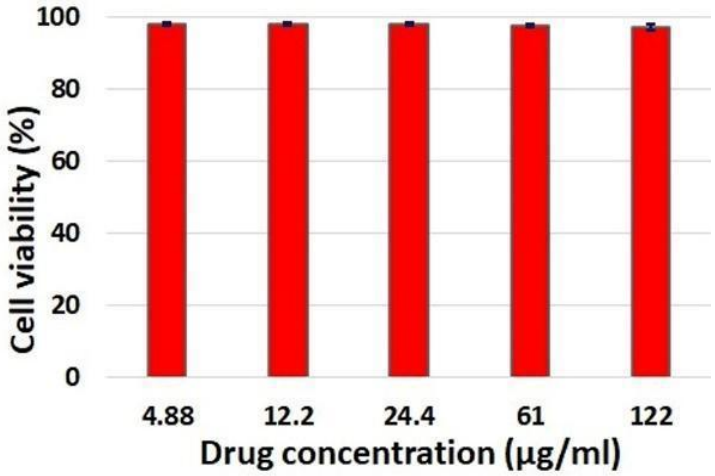

Figure 2.6: Effect of CQDs on cell viability of rat spleen cells using dye exclusion method.

Viable cell suspension ($1x10^6$ cells in 0.1 ml) was added to the tubes containing different concentrations of the CQDs and made up to 1 ml. After an incubation period of 3 hours at 37 ^{0}C, 0.1 ml 1% trypan blue was added to it and kept for 2-3 minutes. Trypan blue gave blue color for dead cells and the living cells were colorless, so that it could be counted separately to calculate the percentage of cytotoxicity. Toxicity for normal cells was found to be around 3% which remains constant even with higher drug concentration. Extremely low cytotoxicity percentage of normal cells reveals high biocompatibility of CQDs which can be ascribed due to the highly oxygenated nanosized nature of carbon dots. Non-toxic carbon dots with tunable emissions can be employed for bioimaging and biosensing applications.

2.3.4 UV-Visible absorption spectra

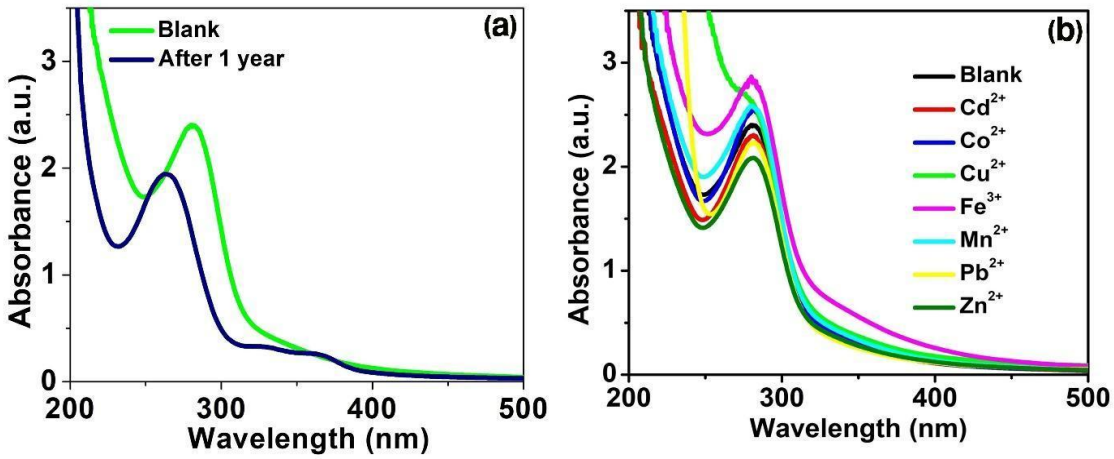

Figure 2.7: UV-visible absorption spectra of CQDs solution (a) as synthesized and after one year (b) in the presence and absence of different metal ions.

From UV-visible absorption spectrum (Fig. 2.7(a)), it can be inferred that CQDs have an absorption edge around 240 nm, 290 nm and 400 nm which can be assigned to π→π* transition of C=C bonds, n→π* transitions of C=N and C=O respectively [56]. Functional groups containing oxygen- and nitrogen- groups are located at surfaces capable of producing multiple impurity levels within the band structure of CQDs. UV visible absorption spectrum of CQDs measured after an interval of 365 days shows similar absorption bands. Slight increase in absorption band around 450 nm wavelength can be ascribed to surface oxidation and degradation upon storage [57].

By the addition of metal ions, absorbance spectra of CQDs remain almost same except for $Cu^{2+}$and Fe^{3+} ions (Fig. 2.7(b)). Considerable change in absorption is observed below 300 nm wavelength with addition of Fe^{3+} ions and 400 nm wavelength upon addition of Cu^{2+} ions [26], [28], [58], [59], [60]. This can be ascribed to the complex formation among surface functional groups of CQDs with ions which agrees well with fluorescence quenching results.

2.3.5 Photoluminescence spectra

(i) Photoluminescence of CQDs

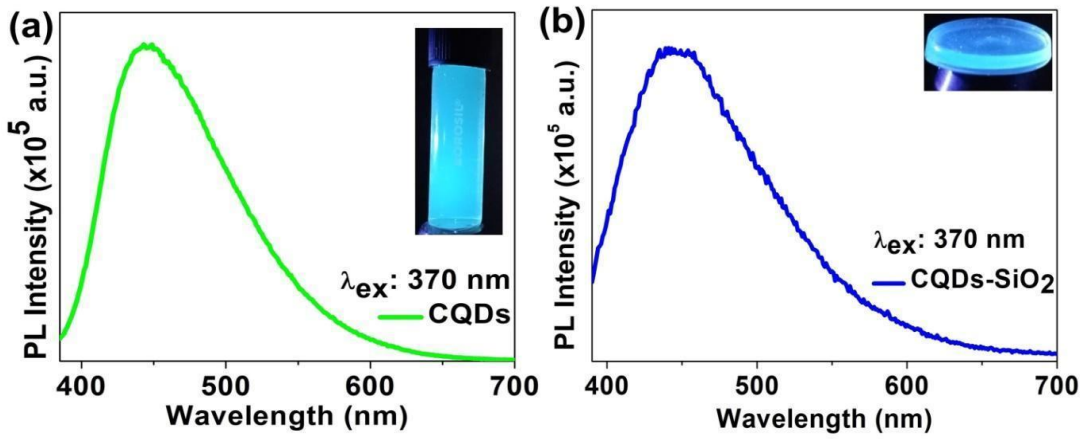

Figure 2.8: PL spectra of (a) aqueous solution of CQDs [inset of (a) shows optical image of CQDs under UV light] (b) CQDs doped silica. [inset of (b) shows optical image of CQDs doped silica under UV light].

The fluorescence spectrum of CQDs observed at 370 nm excitation wavelength is shown in Fig. 2.8(a). The blue emission of CQDs can be attributed to both the presence of oxygenated surface groups with sufficient sp^2 carbon cores and the radiative recombination of excitons [52], [61]. For practical optoelectronic applications, CQDs

in solid state are inevitable but it often suffers from fluorescence quenching induced by aggregation. To overcome this, self-quenching resistant solid-state fluorescence was achieved in CQDs doped silica glasses (Fig. 2.8(b)). The presence of silica networks could hinder the CQDs from surface oxidation, degradation and agglomeration which helps to retain its optical quality.

(ii) Excitation dependent luminescence of CQDs

To examine the excitation dependent emission of CQDs, fluorescence spectra were recorded for excitation wavelengths ranging from 350 nm to 450 nm (Fig. 1.9 (a)).

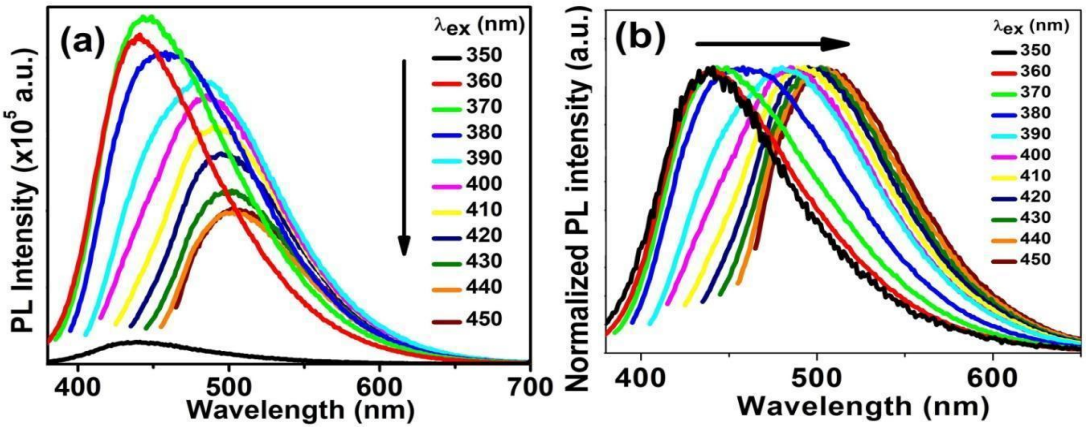

Figure 2.9: PL spectra of CQDs (a) at different excitation wavelengths (b) with normalized PL intensity.

Excitation wavelength dependent photoluminescence of CQDs (given in Fig. 2.9) can be observed with a prominent red shift and reaches a maximum intensity for the wavelength of 370 nm. This behaviour mainly originated from the CQDs surface traps due to their exclusive activation for specific excitation wavelengths [58], [62], [63], [64]. Multiple emissive states within the CQDs surfaces were also responsible for the excitation wavelength dependent luminescence. Fig. 2.9 (b) shows normalized fluorescence spectra which clearly indicate that different emission centres are dominant at different excitation wavelengths. This property is widely reported [64] which can be exploited to design excitation dependent multicolor emitting devices.

(iii) Optical response towards metal ions

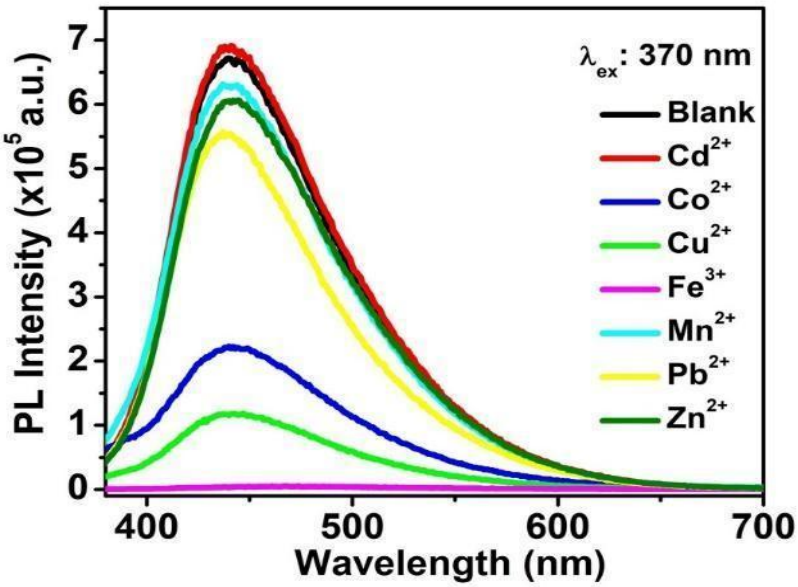

Figure 2.10: PL spectra of CQDs obtained in the presence and absence of different metal ions.

Fluorescence responses of CQDs towards different metal ions the (Cd^{2+}, Co^{2+}, Cu^{2+}, Fe^{3+}, Mn^{2+}, Pb^{2+}, Zn^{2+}, etc.) of same concentration (10mM) on the fluorescent intensity of the CQDs was examined (Fig. 2.10). Distinct optical response of CQDs in the presence of various ions can be ascribed due to their selective interactions among the entangled bonds of CQDs. Obvious fluorescence quenching produced by various ions with a maximum quenching for Fe^{3+} and Cu^{2+}. Among the different cations, Fe^{3+} is more electron deficient with higher affinity towards electron rich groups such as -OR, -OH present in the CQDs surfaces. So, compared with other metal ions, Fe^{3+} electron donating group interactions are more feasible. Comparable electrophilic nature with ACQ effect of Cu^{2+} with Fe^{3+} can be a possible reason for similar quenching behaviour. This is due to the fast electron transfer between Fe^{3+} and oxygenated surface groups of aloe derived c dots [57]. Remaining ions could not make a notable quenching effect towards CQDs due to their weak electrophilic ability [65], [66], [67], [68].

(iv) Photoluminescence of CQDs - Tb^{3+}- Eu^{3+} doped silica

The excitation dependent emission property of CQDs and degradation resistant blue emission of CQDs-silica were further utilized to construct CQDs-Terbium-Europium doped silica. Photoluminescence studies of CQDs-Terbium-Europium doped silica having same RE concentration but different CQDs concentration were done to investigate their applicability to construct white light emitting devices (Fig. 2.11). Emission spectra show broad blue emission bands of CQDs and narrow green-red emissions of rare ions. Due to the intra-4f-4f transitions in Eu^{3+} and Tb^{3+}, emission bands peaked at 487 nm, 542 nm, 590 nm, 616 nm 651 nm and 698 nm wavelengths are observed. Blue-green emission bands peaked at 487 nm due to the $^5D_4 \rightarrow {}^7F_{6,5}$ magnetic, electric dipole transitions of Tb^{3+} ions [32], [69], [70]. Particularly, the most intense emission of Tb^{3+} peaked at 542 nm wavelength corresponds to $^5D_4 \rightarrow {}^7F_5$ transitions having significant magnetic dipole contributions.

The remaining peaks at 590 nm ($^5D_0 \rightarrow {}^7F_1$), 616 nm ($^5D_0 \rightarrow {}^7F_2$), 651 nm ($^5D_0 \rightarrow {}^7F_3$) and 698 nm ($^5D_0 \rightarrow {}^7F_4$) can be attributed to the transitions of Europium ions [34], [71]. An evident spectral dip around 417 nm was obtained due to the spectral overlap of luminescent bands of CQDs with the excitation peak of Eu^{3+}ions which can be ascribed due to the $^7F_1 \rightarrow {}^5D_3$ transitions in Eu^{3+} ions. This is clear evidence of energy transfer between CQDs and Eu^{3+} ions. With the same concentration of RE, green-red emissions of Tb^{3+} and Eu^{3+} ions are enhanced in A1 due to the presence of higher concentration of carbon quantum dots.

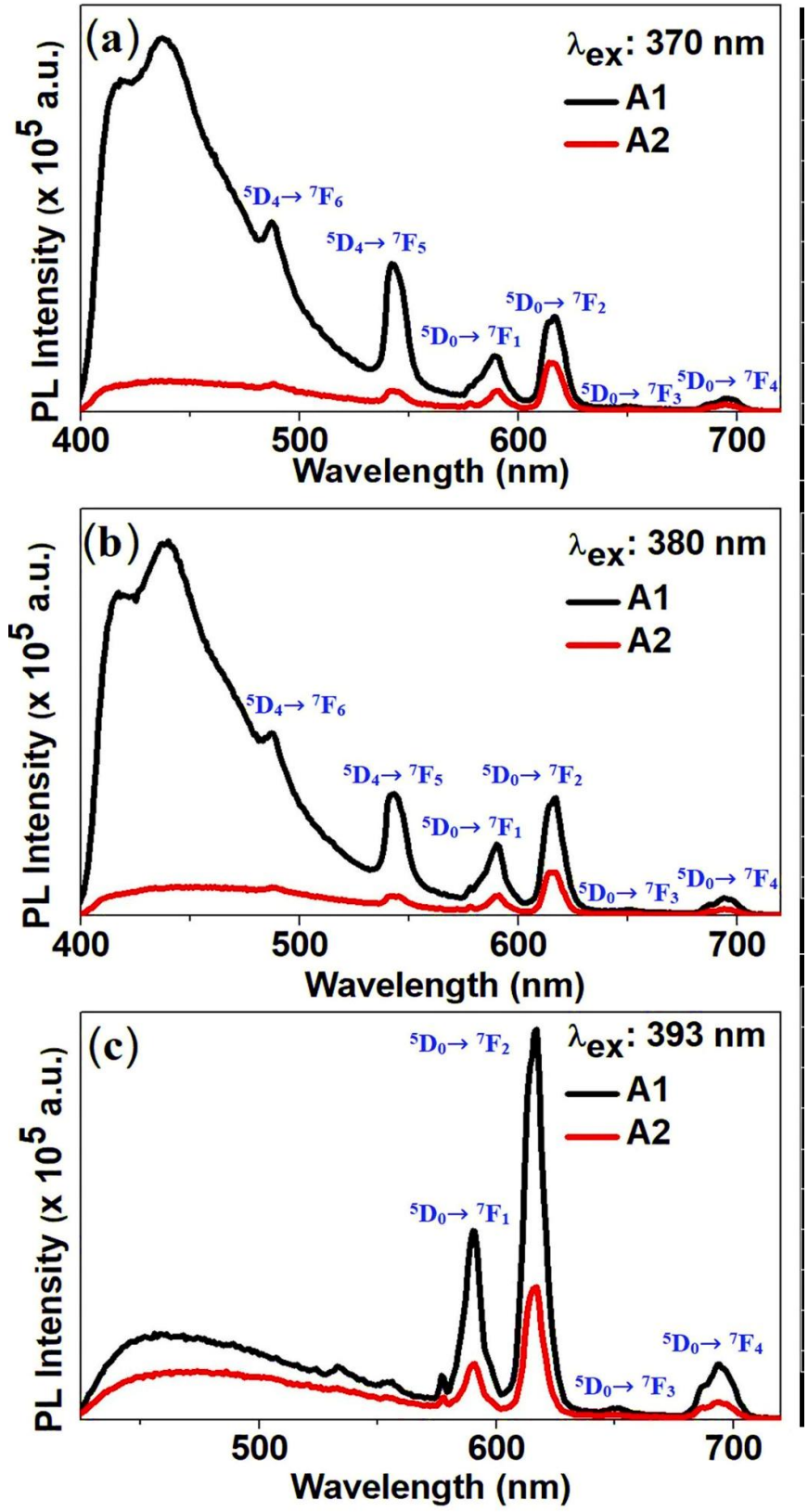

Figure 2.11: Steady state PL spectra of A1 and A2 samples of CQDs - Tb^{3+}- Eu^{3+} doped silica for excitation wavelengths (a) 370 (b) 380 and (c) 393 nm respectively.

2.3.6 Energy transfer studies

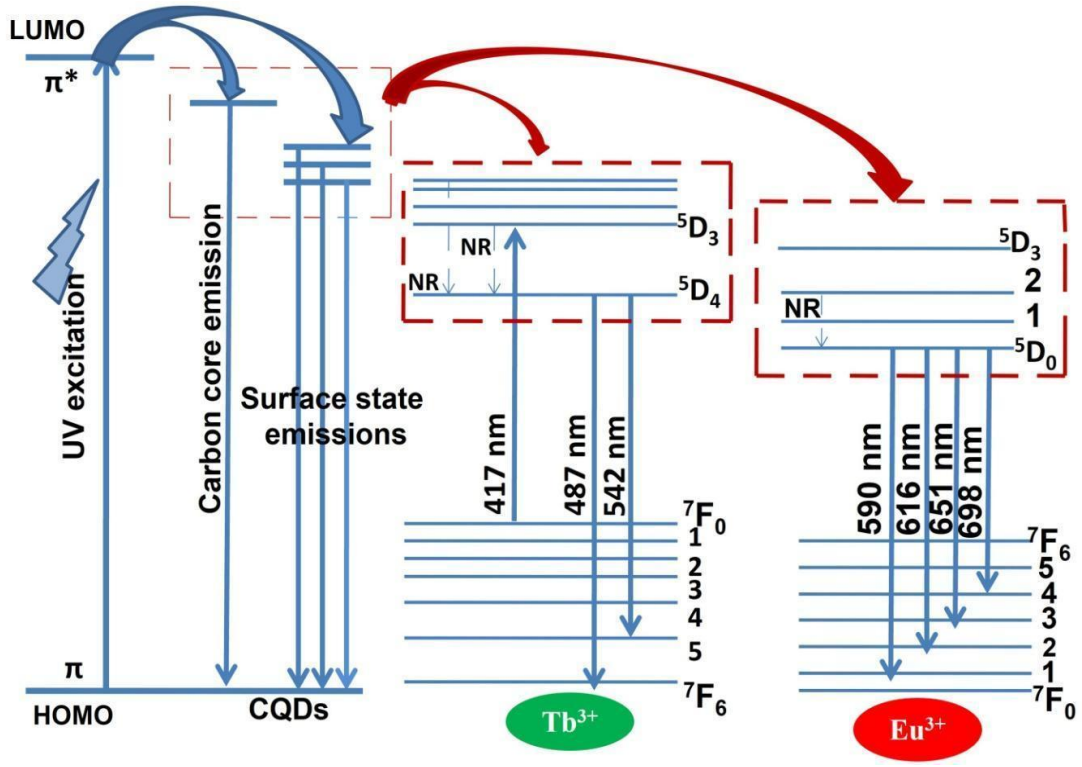

Figure 2.12: Schematic representation of energy transfer mechanism between carbon quantum dots (CQDs) and rare earth ions (RE^{3+} = Tb^{3+}, Eu^{3+}) in silica.

Significant optical amplification observed here is due to direct energy transfer from CQDs to Tb^{3+} and Eu^{3+} ions (Fig. 2.12). Thus, by varying the excitation wavelength and concentration of CQDs, a fine tuning of blue-green-red emissions is achieved. Generally, Tb^{3+} based materials glow green light due to most intense emissions ($^5D_4 \rightarrow {}^7F_5$) at 542 nm at prominent excitation wavelength of 370 nm [32]. Similarly, Eu^{3+} based materials are well known as red emitting phosphors owing to intense red color emissions (613 nm wavelength) due to $^5D_0 \rightarrow {}^7F_2$ transitions at 393 nm excitation wavelength [34]. As RE ions are known to show sharp intense emissions at only particular excitations, the existence of all Eu^{3+} emission curves at excitation wavelengths other than its prominent excitations illustrates the energy transfer between CQDs and RE. Though 380 nm wavelength is not a prominent excitation wavelength for Tb^{3+} and Eu^{3+}, green-red emissions of comparable intensity are achieved in both samples. Due to the spectral overlap and vicinity of luminescent centres efficient Forster resonance energy transfer occurs. By the incorporation into a rigid matrix, the

vicinity of the donor-acceptor (CQDs-RE^{3+}) comes to a close distance (< 10 nm) which enhances the energy transfer routes.

2.3.7 CQDs - Tb^{3+}- Eu^{3+} doped silica as WLEDs

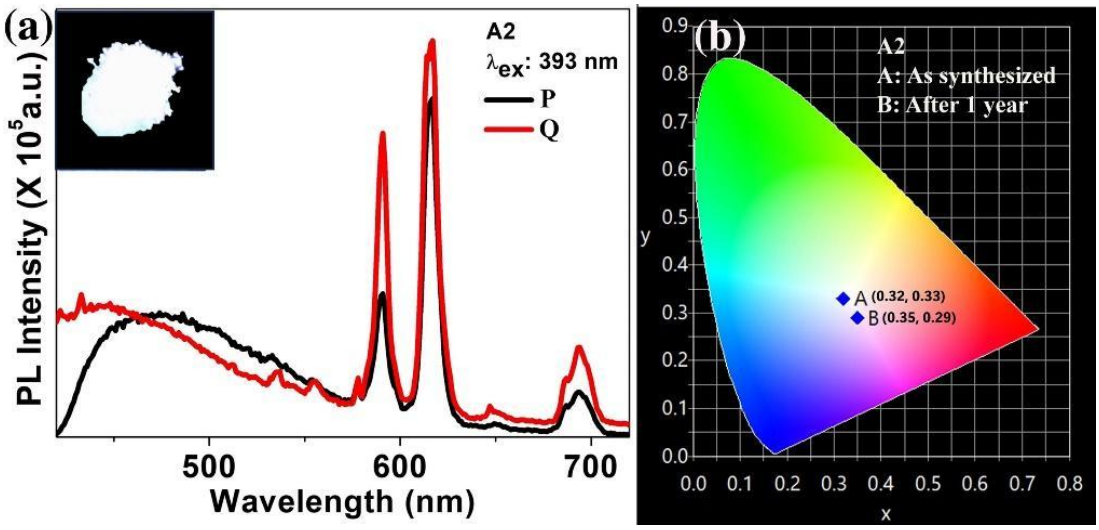

Figure 2.13: (a) Steady state PL spectra of A2, as synthesized (P) and after 1 year (Q) [inset shows photograph of sample A2 under UV excitation of 365 nm) and (b) CIE chromaticity diagram of A2, as synthesized and after one year.

In order to examine the optical stability of the WLE composite (A2) was stored for a period of 1 year and fluorescence spectrum was examined (Fig. 2.13). Even after 1 year storage period, for the excitation of 393 nm A2 has got an emission spectrum with non-shifted peak positions and comparable intensity. Under UV exposure white emissions of the obtained samples were retained as given in the photograph (inset of Fig. 2.13(a)).

2.3.8 Colorimetric analysis with CIE Chromaticity diagrams

CIE chromaticity charts displayed the color of emission for each sample excited at specific excitations. Stable multicolor emissions from an integrated RE-CQDs material are achieved here by utilizing the excitation dependent broad blue emissions of CQDs. This is further investigated from the CIE chromaticity diagram (Fig. 2.14). The CIE indices of composites for different excitations were obtained in different color domains (as in table. 2.3). The colorimetric coordinates (x, y) of pure WLE combination composite (A2) were found to be (0.27, 0.26), (0.27, 0.28) and (0.32, 0.33) for excitation wavelengths of 370 nm, 380 nm and 393 nm respectively which are located in and around the ideal white point (0.33, 0.33). Optimized composition of CQDs with Terbium and Europium ions produced white light emissions specifically under UV

exposure of 393 nm. Therefore, the fabricated tunable and white emitting flat display panels could be a best alternative for conventional lighting systems.

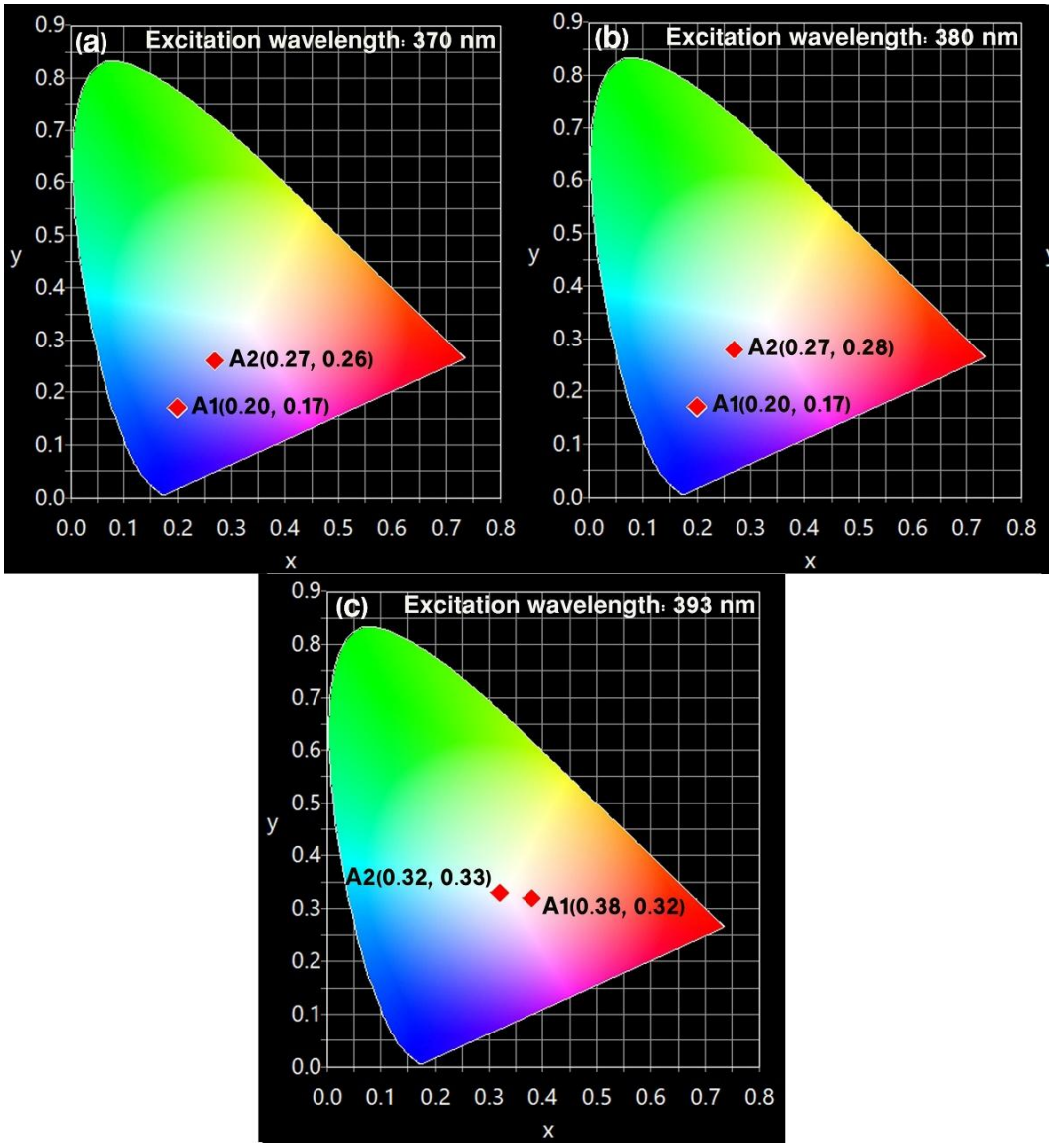

Figure 2.14: CIE diagram of A1 and A2 samples of CQDs - Tb^{3+}- Eu^{3+} doped silica for excitation wavelengths (a) 370 (b) 380 and (c) 393 nm respectively.

The colorimetric parameters of WLE composites with different carbon concentrations including correlated color temperature CCT (color correlated temperature), CIE indices for distinct excitation wavelength were tabulated in the table. 2.4. WLE systems with warm white (CCT < 4000) can be used in indoor lightings and (CCT > 4000K) cool white utilized mainly for outdoor illuminations [7].

Table 2.3: Excitation wavelength, CIE indices, color region of CQDs-Tb-Eu incorporated silica.

Sample code	Excitation wavelength (in nm)	CIE Index	Color region
A1	370	(0.20, 0.17)	Blue
A1	380	(0.20, 0.17)	Blue
A1	393	(0.38, 0.32)	White
A2	370	(0.27, 0.26)	White
A2	380	(0.27, 0.28)	White
A2	393	(0.32, 0.33)	White

Table 2.4: CIE indices, CCT, CRI values obtained for optimized compositions of white light emitting RE-CQDs silica.

Sample code	Excitation wavelength (in nm)	CIE Index	CCT (K)	CRI	Nature of white light
A1	393	(0.38, 0.32)	3508	61	Warm
A2	393	(0.32, 0.33)	6114	71	Cool

Under UV excitation of 393 nm, continuous tuning from warm white emission with CCT of 3508 K to cool white emission with CCT 6114 K can be achieved by varying the concentration of CQDs. CCT values exceed 10000K for the lower CIE coordinates (x, y). Tuning from warm to cool temperature scales may make the glassy frames as artificial lighting solutions for both indoor and outdoor applications. Moreover, for both outdoor and indoor lighting applications color rendering index (CRI) >70 is best required. Moderate CRI values of RE-CQDs silica confirmed the spectral quality of white emissions. For 393 nm excitation wavelength, the estimated color points (0.32, 0.33) with adjustable CCT (6114 K) and CRI values (71) of A2, reveals the potential WLED applications of constructed composites. Under UV excitation of 393 nm wavelength (Fig. 2.13) similar white emissions with CIE indices (0.35, 0.29) confirmed the ultra-stable nature of obtained luminescent systems. Rigid silica encapsulated CQDs and stable fluorescence from composite material is achieved even after a period of one year.

2.4 Conclusion

In summary, solid state white light emitting rare earth ions (RE^{3+})–Carbon quantum dots (CQDs) embedded silica having adjustable correlated color temperature (CCT) values (3508 -6114 K) were prepared via sol-gel route. Blue emitting CQDs were prepared by simple hydrothermal method with eco-friendly aloe as carbonaceous precursor. Polycrystalline carbon dots of average size ranging from 2-8 nm have presence of different functional groups on the surface. The CQDs exhibited excellent biocompatibility and water solubility. The excitation dependent emissions were effectively quenched with addition of Fe^{3+} ions. The optical stability of CQDs was analyzed from UV-visible absorption and photoluminescence spectra. To overcome surface oxidation and CQDs degradation, CQDs doped silica were prepared showing stable blue emission in the long run. Optically consistent white and multi-color emissions were obtained by incorporating optimized composition of CQDs and Terbium-Europium ions within the mesoporous silica network. Intense green-red emissions were obtained by increasing the concentration of CQDs due to direct energy transfer from CQDs to Tb^{3+} and Eu^{3+} ions. Additionally, by varying the excitation wavelength, a fine tuning of blue-green-red emissions was achieved. Both compositions of CQDs with Terbium and Europium ions produced white light emissions with tunable warm to cool white emission (CCT 3508 to 6114 K) under UV exposure of 393 nm wavelength. Moreover, the colorimetric coordinates (x, y) of pure WLE combination composite were found to be (0.27, 0.26), (0.27, 0.28) and (0.32, 0.33) for excitation wavelengths of 370 nm, 380 nm and 393 nm respectively. The CIE indices (0.32, 0.33) of white light emitting material have moderate CRI value of 71 and CCT (6114 K) at 393 nm wavelength excitations. This solid-state phosphor is found to have white color CIE indices (0.35, 0.29) even after 1 year of time which reveals its potential WLED applications for high-definition advanced lighting systems with high lighting prospects.

References

[1] R. Devi, R. Boddula, J. Tagare, A. B. Kajjam, K. Singh, and S. Vaidyanathan, "White emissive europium complex with CRI 95%: butterfly vs. triangle structure," *J. Mater. Chem. C*, vol. 8, no. 34, pp. 11715–11726, Sep. 2020, doi: 10.1039/D0TC02724C.

[2] X. Feng, F. Zhang, Y. Wang, Y. Zhang, Y. Yang, and X. Liu, "Fluorescent Carbon Quantum Dots as Single Light Converter for White LEDs," *J. Electron. Mater.*, vol. 45, no. 6, pp. 2784–2788, Jun. 2016, doi: 10.1007/s11664-016-4407-7.

[3] X. Liu *et al.*, "Carbon quantum dot-sensitized and tunable luminescence of $Ca_{19}Mg_2(PO_4)_{14}$:Ln^{3+} (Ln^{3+} = Eu^{3+} and/or Tb^{3+}) nanocrystalline phosphors with abundant colors via a sol–gel process," *J. Mater. Chem. C*, vol. 7, no. 8, pp. 2361–2375, Feb. 2019, doi: 10.1039/C8TC06599C.

[4] M. S. Shur and R. Zukauskas, "Solid-State Lighting: Toward Superior Illumination," *Proceedings of the IEEE*, vol. 93, no. 10, pp. 1691–1703, Oct. 2005, doi: 10.1109/JPROC.2005.853537.

[5] P. He *et al.*, "Recent advances in white light-emitting diodes of carbon quantum dots," *Nanoscale*, vol. 12, no. 8, pp. 4826–4832, Feb. 2020, doi: 10.1039/C9NR10958G.

[6] Georgakilas, Vasilios, et al. "Broad Family of Carbon Nanoallotropes: Classification, Chemistry, and Applications of Fullerenes, Carbon Dots, Nanotubes, Graphene, Nanodiamonds, and Combined Superstructures, C*hemical reviews*, vol. 115, no. 11, pp. 4744-4822, May 2015, doi: 10.1021/cr500304f

[7] S. N. Baker and G. A. Baker, "Luminescent Carbon Nanodots: Emergent Nanolights," *Angewandte Chemie International Edition*, vol. 49, no. 38, pp. 6726–6744, 2010, doi: 10.1002/anie.200906623.

[8] Z. Peng *et al.*, "Carbon dots: Biomacromolecule interaction, bioimaging and nanomedicine," *Coordination Chemistry Reviews*, vol. 343, pp. 256–277, Jul. 2017, doi: 10.1016/j.ccr.2017.06.001.

[9] Y. Wang and A. Hu, "Carbon quantum dots: synthesis, properties and applications," *Journal of Materials Chemistry C*, vol. 2, no. 34, pp. 6921–6939, 2014, doi: 10.1039/C4TC00988F.

[10] Y. Wu, P. Wei, S. Pengpumkiat, E. A. Schumacher, and V. T. Remcho, "Development of a Carbon Dot (C-Dot)-Linked Immunosorbent Assay for the Detection of Human α-Fetoprotein," *Anal. Chem.*, vol. 87, no. 16, pp. 8510–8516, Aug. 2015, doi: 10.1021/acs.analchem.5b02019.

[11] Y. Dong *et al.*, "Carbon-based dots co-doped with nitrogen and sulfur for high quantum yield and excitation-independent emission," *Angewandte Chemie International Edition*, vol. 52, no. 3, pp. 7800 –7804, July 2013, doi: 10.1002/anie.201301114

[12] N. Kiran and A. Suresh Kumar, "White light emission from Dy^{3+} doped sodium–lead borophosphate glasses under UV light excitation," *Journal of Molecular Structure*, vol. 1054–1055, pp. 6–11, Dec. 2013, doi: 10.1016/j.molstruc.2013.09.023.

[13] Y. Lin, G.-E. Wang, C.-L. Hu, J.-H. Feng, L.-N. Li, and J.-G. Mao, "White-Light Emission from a Semi-Conductive Borate-Stannate," *Angewandte Chemie*, vol. 131, no. 38, pp. 13524–13527, 2019, doi: 10.1002/ange.201907650.

[14] T. Sambasiva Rao *et al.*, "Studies on structural characterization and near white light emission through energy transfer between Ce^{3+} and Tb^{3+} in barium gallium borosilicate glasses," *Journal of Molecular Structure*, vol. 1190, pp. 184–195, Aug. 2019, doi: 10.1016/j.molstruc.2019.04.065.

[15] T. K. Mondal, S. Mondal, U. K. Ghorai, and S. K. Saha, "White light emitting lanthanide based carbon quantum dots as toxic Cr (VI) and pH sensor," *Journal of Colloid and Interface Science*, vol. 553, pp. 177–185, Oct. 2019, doi: 10.1016/j.jcis.2019.06.009.

[16] Y. Wang *et al.*, "Construction, energy transfer, tunable multicolor and luminescence enhancement of YF_3:RE^{3+}(RE=Eu,Tb)/carbon dots nanocomposites," *Journal of Luminescence*, vol. 221, p. 117072, May 2020, doi: 10.1016/j.jlumin.2020.117072.

[17] C. Wang, T. Hu, Y. Chen, Y. Xu, and Q. Song, "Polymer-Assisted Self-Assembly of Multicolor Carbon Dots as Solid-State Phosphors for Fabrication of Warm, High-Quality, and Temperature-Responsive White-Light-Emitting Devices," *ACS Appl. Mater. Interfaces*, vol. 11, no. 25, pp. 22332–22338, Jun. 2019, doi: 10.1021/acsami.9b04345.

[18] Z. Tian *et al.*, "Full-Color Inorganic Carbon Dot Phosphors for White-Light-Emitting Diodes," *Advanced Optical Materials*, vol. 5, no. 19, p. 1700416, 2017, doi: 10.1002/adom.201700416.

[19] A. Balaji *et al.*, "Biomaterials based nano-applications of Aloe vera and its perspective: a review," *RSC Adv.*, vol. 5, no. 105, pp. 86199–86213, Oct. 2015, doi: 10.1039/C5RA13282G.

[20] X. Guo and N. Mei, "Aloe vera: A review of toxicity and adverse clinical effects," *Journal of Environmental Science and Health, Part C*, vol. 34, no. 2, pp. 77–96, Apr. 2016, doi: 10.1080/10590501.2016.1166826.

[21] K. ESHUN and Q. HE, "Aloe Vera: A Valuable Ingredient for the Food, Pharmaceutical and Cosmetic Industries—A Review," *Critical Reviews in Food Science and Nutrition*, vol. 44, no. 2, pp. 91–96, Mar. 2004, doi: 10.1080/10408690490424694.

[22] T. Reynolds and A. C. Dweck, "Aloe vera leaf gel: a review update," *Journal of Ethnopharmacology*, vol. 68, no. 1, pp. 3–37, Dec. 1999, doi: 10.1016/S0378-8741(99)00085-9.

[23] S. Zhu *et al.*, "Highly Photoluminescent Carbon Dots for Multicolor Patterning, Sensors, and Bioimaging," *Angewandte Chemie International Edition*, vol. 52, no. 14, pp. 3953–3957, 2013, doi: 10.1002/anie.201300519.

[24] Z.-C. Yang *et al.*, "Intrinsically fluorescent carbon dots with tunable emission derived from hydrothermal treatment of glucose in the presence of monopotassium phosphate," *Chem. Commun.*, vol. 47, no. 42, pp. 11615–11617, Oct. 2011, doi: 10.1039/C1CC14860E.

[25] B. De and N. Karak, "A green and facile approach for the synthesis of water soluble fluorescent carbon dots from banana juice," *RSC Advances*, vol. 3, no. 22, pp. 8286–8290, 2013, doi: 10.1039/C3RA00088E.

[26] C.-L. Li *et al.*, "Carbon dots prepared from ginger exhibiting efficient inhibition of human hepatocellular carcinoma cells," *J. Mater. Chem. B*, vol. 2, no. 28, pp. 4564–4571, Jun. 2014, doi: 10.1039/C4TB00216D.

[27] S. Sahu, B. Behera, T. K. Maiti, and S. Mohapatra, "Simple one-step synthesis of highly luminescent carbon dots from orange juice: application as excellent bio-imaging agents," *Chem. Commun.*, vol. 48, no. 70, pp. 8835–8837, Aug. 2012, doi: 10.1039/C2CC33796G.

[28] V. Singh *et al.*, "Biocompatible fluorescent carbon quantum dots prepared from beetroot extract for in vivo live imaging in C. elegans and BALB/c mice," *J. Mater. Chem. B*, vol. 6, no. 20, pp. 3366–3371, May 2018, doi: 10.1039/C8TB00503F.

[29] L. G. Van Uitert and L. F. Johnson, "Energy Transfer Between Rare-Earth Ions," *The Journal of Chemical Physics*, vol. 44, no. 9, pp. 3514–3522, May 1966, doi: 10.1063/1.1727258.

[30] R. L. Amster and C. S. Wiggins, "Spectroscopic Identification of Europium-Oxygen Complexes in Calcium Fluoride," *J. Electrochem. Soc.*, vol. 116, no. 1, p. 68, Jan. 1969, doi: 10.1149/1.2411777.

[31] J. Juárez-Batalla, A. N. Meza-Rocha, G. Muñoz H., I. Camarillo, and U. Caldiño, "Luminescence properties of Tb^{3+}-doped zinc phosphate glasses for green laser application," *Optical Materials*, vol. 58, pp. 406–411, Aug. 2016, doi: 10.1016/j.optmat.2016.06.022.

[32] K. Linganna, S. Ju, Ch. Basavapoornima, V. Venkatramu, and C. K. Jayasankar, "Luminescence and decay characteristics of Tb^{3+}-doped fluorophosphate glasses," *Journal of Asian Ceramic Societies*, vol. 6, no. 1, pp. 82–87, Jan. 2018, doi: 10.1080/21870764.2018.1442674.

[33] B. M. J. Smets, "Phosphors based on rare-earths, a new era in fluorescent lighting," *Materials Chemistry and Physics*, vol. 16, no. 3, pp. 283–299, Feb. 1987, doi: 10.1016/0254-0584(87)90103-9.

[34] K. Mariselvam, R. A. Kumar, and S. Karthik, "Optical and luminescence characteristics of europium doped barium lithium fluoroborate glasses," *Chemical Physics*, vol. 525, p. 110379, Sep. 2019, doi: 10.1016/j.chemphys.2019.05.006.

[35] P. Singhal, B. G. Vats, S. K. Jha, and S. Neogy, "Green, Water-Dispersible Photoluminescent On–Off–On Probe for Selective Detection of Fluoride Ions," *ACS Appl. Mater. Interfaces*, vol. 9, no. 24, pp. 20536–20544, Jun. 2017, doi: 10.1021/acsami.7b03346.

[36] M. Zhang *et al.*, "When rare earth meets carbon nanodots: mechanisms, applications and outlook," *Chem. Soc. Rev.*, vol. 49, no. 24, pp. 9220–9248, Dec. 2020, doi: 10.1039/D0CS00462F.

[37] T. Paul, J. J. Palakulam, N. V. Unnikrishnan, R. Philip, and K. A. A. Mary, "Warm to cool tunable ultra-stable white light emissions from carbon dots -Tb^{3+} - Eu^{3+} doped silica," *Optical Materials*, vol. 138, p. 113673, Apr. 2023, doi: 10.1016/j.optmat.2023.113673.

[38] H. X. Zhao, L. Q. Liu, Z. D. Liu, Y. Wang, X. J. Zhao, and C. Z. Huang, "Highly selective detection of phosphate in very complicated matrixes with an off–on fluorescent probe of europium-adjusted carbon dots," *Chem. Commun.*, vol. 47, no. 9, pp. 2604–2606, Feb. 2011, doi: 10.1039/C0CC04399K.

[39] X. Xu *et al.*, "Construction of $NaYF_4$:Yb,Er(Tm)@CDs composites for enhancing red and NIR upconversion emission," *J. Mater. Chem. C*, vol. 7, no. 21, pp. 6231–6235, May 2019, doi: 10.1039/C9TC01346F.

[40] R. Pratap, V. Vishal, S. Chaudhary, and A. Singh Parmar, "Fabrication of white light emitting diodes via high yield surface passivated carbon quantum dots doped with terbium," *RSC Advances*, vol. 13, no. 3, pp. 1974–1984, 2023, doi: 10.1039/D2RA07890B.

[41] H. Dong, A. Kuzmanoski, D. M. Gößl, R. Popescu, D. Gerthsen, and C. Feldmann, "Polyol-mediated C-dot formation showing efficient Tb^{3+}/Eu^{3+} emission," *Chem. Commun.*, vol. 50, no. 56, pp. 7503–7506, Jun. 2014, doi: 10.1039/C4CC01715C.

[42] Y. Zhao *et al.*, "Facile Preparation of Double Rare Earth-Doped Carbon Dots for MRI/CT/FI Multimodal Imaging," *ACS Appl. Nano Mater.*, vol. 1, no. 6, pp. 2544–2551, Jun. 2018, doi: 10.1021/acsanm.8b00137.

[43] H. Xu, X. Yang, G. Li, C. Zhao, and X. Liao, "Green Synthesis of Fluorescent Carbon Dots for Selective Detection of Tartrazine in Food Samples," *J. Agric. Food Chem.*, vol. 63, no. 30, pp. 6707–6714, Aug. 2015, doi: 10.1021/acs.jafc.5b02319.

[44] K. A. A. Mary, N. V. Unnikrishnan, and R. Philip, "Cubic to amorphous transformation of Se in silica with improved ultrafast optical nonlinearity," *RSC Adv.*, vol. 5, no. 18, pp. 14034–14041, Jan. 2015, doi: 10.1039/C4RA14025G.

[45] Q. Chen *et al.*, "Biomass-derived porous graphitic carbon materials for energy and environmental applications," *J. Mater. Chem. A*, vol. 8, no. 12, pp. 5773–5811, Mar. 2020, doi: 10.1039/C9TA11618D.

[46] C. Falco, N. Baccile, and M.-M. Titirici, "Morphological and structural differences between glucose, cellulose and lignocellulosic biomass derived hydrothermal carbons," *Green Chem.*, vol. 13, no. 11, pp. 3273–3281, Jan. 2011, doi: 10.1039/C1GC15742F.

[47] I. C. Lewis, "Chemistry of carbonization," *Carbon*, vol. 20, no. 6, pp. 519–529, Jan. 1982, doi: 10.1016/0008-6223(82)90089-6.

[48] X. Li, M.-F. Li, J. Bian, B. Wang, J.-K. Xu, and R.-C. Sun, "Hydrothermal carbonization of bamboo in an oxalic acid solution: effects of acid concentration and retention time on the characteristics of products," *RSC Adv.*, vol. 5, no. 94, pp. 77147–77153, Sep. 2015, doi: 10.1039/C5RA15063A.

[49] J. Ryu, Y.-W. Suh, D. J. Suh, and D. J. Ahn, "Hydrothermal preparation of carbon microspheres from mono-saccharides and phenolic compounds," *Carbon*, vol. 48, no. 7, pp. 1990–1998, Jun. 2010, doi: 10.1016/j.carbon.2010.02.006.

[50] M.-M. Titirici and M. Antonietti, "Chemistry and materials options of sustainable carbon materials made by hydrothermal carbonization," *Chemical Society Reviews*, vol. 39, no. 1, pp. 103–116, 2010, doi: 10.1039/B819318P.

[51] M.-M. Titirici, M. Antonietti, and N. Baccile, "Hydrothermal carbon from biomass: a comparison of the local structure from poly- to monosaccharides and pentoses/hexoses," *Green Chem.*, vol. 10, no. 11, pp. 1204–1212, Nov. 2008, doi: 10.1039/B807009A.

[52] M. Li, T. Chen, J. J. Gooding, and J. Liu, "Review of Carbon and Graphene Quantum Dots for Sensing," *ACS Sens.*, vol. 4, no. 7, pp. 1732–1748, Jul. 2019, doi: 10.1021/acssensors.9b00514.

[53] V. Ţucureanu, A. Matei, and A. M. Avram, "FTIR Spectroscopy for Carbon Family Study," *Critical Reviews in Analytical Chemistry*, vol. 46, no. 6, pp. 502–520, Nov. 2016, doi: 10.1080/10408347.2016.1157013.

[54] A. Pal, A. Bhakat, and A. Chattopadhyay, "Zinc Ion-Induced Assembly of Crystalline Carbon Dots with Excellent Supercapacitor Performance," *J. Phys. Chem. C*, vol. 123, no. 32, pp. 19421–19428, Aug. 2019, doi: 10.1021/acs.jpcc.9b05820.

[55] C. Hu, F. Wang, and Z. Zheng, "Ab initio study of phase stability, thermodynamic and elastic properties of C_3N_2 derived from cubic C_{20}," *Physica B: Condensed Matter*, vol. 407, no. 17, pp. 3398–3404, Sep. 2012, doi: 10.1016/j.physb.2012.04.045.

[56] Y. Wu *et al.*, "High Quantum Yield Boron and Nitrogen Codoped Carbon Quantum Dots with Red/Purple Emissions for Ratiometric Fluorescent IO^{4-} Sensing and Cell Imaging," *ACS Sustainable Chem. Eng.*, vol. 10, no. 16, pp. 5195–5202, Apr. 2022, doi: 10.1021/acssuschemeng.1c08676.

[57] R. Kumari, K. Pal, P. Karmakar, and S. K. Sahu, "pH-Responsive Mn-Doped Carbon Dots for White-Light-Emitting Diodes, Fingerprinting, and Bioimaging," *ACS Appl. Nano Mater.*, vol. 2, no. 9, pp. 5900–5909, Sep. 2019, doi: 10.1021/acsanm.9b01335.

[58] Q. Hu *et al.*, "Green synthesis of fluorescent nitrogen/sulfur-doped carbon dots and investigation of their properties by HPLC coupled with mass spectrometry," *RSC Adv.*, vol. 4, no. 35, pp. 18065–18073, Apr. 2014, doi: 10.1039/C4RA02170C.

[59] S. Xu *et al.*, "One-step fabrication of boronic-acid-functionalized carbon dots for the detection of sialic acid," *Talanta*, vol. 197, pp. 548–552, May 2019, doi: 10.1016/j.talanta.2019.01.074.

[60] H. Ding, L.-W. Cheng, Y.-Y. Ma, J.-L. Kong, and H.-M. Xiong, "Luminescent carbon quantum dots and their application in cell imaging," *New J. Chem.*, vol. 37, no. 8, pp. 2515–2520, Jul. 2013, doi: 10.1039/C3NJ00366C.

[61] L. Li, B. Yu, and T. You, "Nitrogen and sulfur co-doped carbon dots for highly selective and sensitive detection of Hg (II) ions," *Biosensors and Bioelectronics*, vol. 74, pp. 263–269, Dec. 2015, doi: 10.1016/j.bios.2015.06.050.

[62] S. Gogoi and R. Khan, "NIR upconversion characteristics of carbon dots for selective detection of glutathione," *New J. Chem.*, vol. 42, no. 8, pp. 6399–6407, Apr. 2018, doi: 10.1039/C8NJ00567B.

[63] S. Zhu, Y. Song, X. Zhao, J. Shao, J. Zhang, and B. Yang, "The photoluminescence mechanism in carbon dots (graphene quantum dots, carbon nanodots, and polymer dots): current state and future perspective," *Nano Res.*, vol. 8, no. 2, pp. 355–381, Feb. 2015, doi: 10.1007/s12274-014-0644-3.

[64] A. Sharma, T. Gadly, A. Gupta, A. Ballal, S. K. Ghosh, and M. Kumbhakar, "Origin of Excitation Dependent Fluorescence in Carbon Nanodots," *J. Phys. Chem. Lett.*, vol. 7, no. 18, pp. 3695–3702, Sep. 2016, doi: 10.1021/acs.jpclett.6b01791.

[65] P. Wu, W. Li, Q. Wu, Y. Liu, and S. Liu, "Hydrothermal synthesis of nitrogen-doped carbon quantum dots from microcrystalline cellulose for the detection of Fe^{3+} ions in an acidic environment," *RSC Advances*, vol. 7, no. 70, pp. 44144–44153, 2017, doi: 10.1039/C7RA08400E.

[66] J. F. Y. Fong, S. F. Chin, and S. M. Ng, "Facile synthesis of carbon nanoparticles from sodium alginate via ultrasonic-assisted nano-precipitation and thermal acid dehydration for ferric ion sensing," *Sensors and Actuators B: Chemical*, vol. 209, pp. 997–1004, Mar. 2015, doi: 10.1016/j.snb.2014.12.038.

[67] W. Liu, H. Diao, H. Chang, H. Wang, T. Li, and W. Wei, "Green synthesis of carbon dots from rose-heart radish and application for Fe3+ detection and cell imaging," *Sensors and Actuators B: Chemical*, vol. 241, pp. 190–198, Mar. 2017, doi: 10.1016/j.snb.2016.10.068.

[68] G. Yang, X. Wan, Y. Su, X. Zeng, and J. Tang, "Acidophilic S-doped carbon quantum dots derived from cellulose fibers and their fluorescence sensing performance for metal ions in an extremely strong acid environment," *J. Mater. Chem. A*, vol. 4, no. 33, pp. 12841–12849, Aug. 2016, doi: 10.1039/C6TA05943K.

[69] L. Żur, J. Pisarska, and W. A. Pisarski, "Terbium-doped heavy metal glasses for green luminescence," *Journal of Rare Earths*, vol. 29, no. 12, pp. 1198–1200, Dec. 2011, doi: 10.1016/S1002-0721(10)60626-6.

[70] P. C. Ricci, C. M. Carbonaro, R. Corpino, C. Cannas, and M. Salis, "Optical and Structural Characterization of Terbium-Doped Y_2SiO_5 Phosphor Particles," *J. Phys. Chem. C*, vol. 115, no. 33, pp. 16630–16636, Aug. 2011, doi: 10.1021/jp203523s.

[71] S. J. Park *et al.*, "Green and red emitting $YBO_3:Ln^{3+}$ (Ln=Eu, Tb) phosphors for detection of latent fingerprint," *Journal of Alloys and Compounds*, vol. 789, pp. 367–374, Jun. 2019, doi: 10.1016/j.jallcom.2019.03.029.

3

Dual Emitting Carbon Nanoparticles for Tunable White Light Emission

Eco-friendly, biomass derived single component luminescent materials with dual emission bands hold immense potential in white light emitting devices (WLED). Compared to WLED fabricated from different color emitting carbon nanoparticles, self-reabsorption and degradation will be negligible in single system white light emitting materials which guarantees stability in long run. Herein, we report a facile, inexpensive and sustainable direct thermal decomposition method to synthesize carbon nanoparticles with dual emission bands. Addition of PVP could efficiently enhance the red emission band of carbon nanoparticles. The excitation dependent broad blue-green emission and excitation independent narrow red emission helps to obtain white light emitting carbon nanoparticles. Upon change in excitation wavelength from 410 nm to 370 nm, white light emissions are obtained with tunable CCT value from 2648 K to 8980 K respectively. By virtue of this tunable warm to cool white light emission, single system WLED can be designed suitable for both indoor and outdoor applications.

Graphical abstract

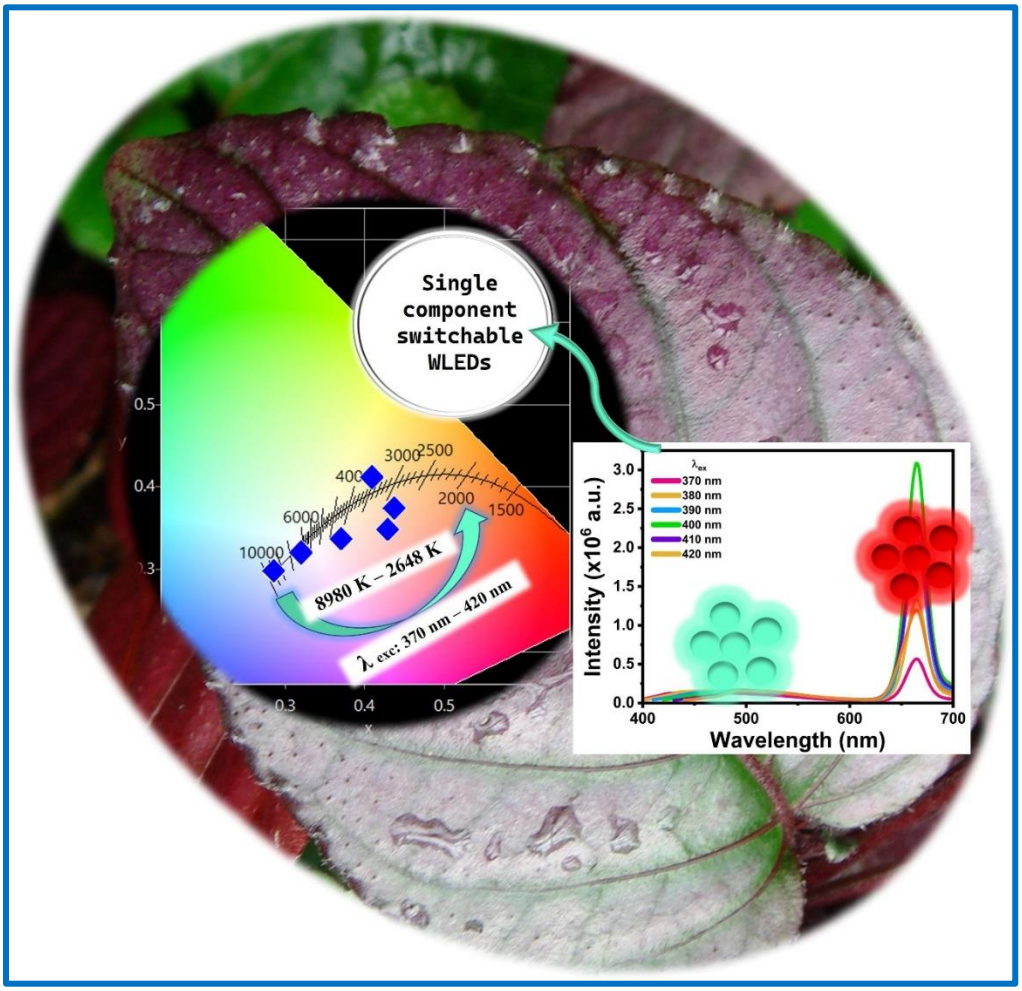

3.1 Introduction

Over the last few decades, a sudden upsurge in the research of white light emitting materials occurred owing to their application in solid state lighting [1], [2] displays [3] and fluorescent sensors [4]. Conventional white illumination systems use careful controlling of red-green-blue (RGB) color profiles of individual light emitting phosphor devices [5]. An alternate way for efficient white light perception is to coat suitable rare-earth phosphor materials on a single chip [6]. However, design, complexity, low reproducibility rate for color tuning, low color rendering index (CRI) and relatively higher color correlated temperatures (CCT) hamper with their routine applications [5], [7]. Deepening concerns regarding the depleting sources of rare earth (RE) materials, their cost effectiveness and compatibility with the environment has also triggered minds to search for suitable alternatives [8]. Currently, great deal of efforts is put into white light emitting devices (WLEDs) exploiting various photophysical properties of semiconductor quantum dots [9], [10], nanomaterials [11], [12], [13], polymers [14], metal-organic frameworks (MOFs) [15], [16], lanthanide doped systems [17] and organic-inorganic hybrids [18], [19].

Carbon based nanomaterials are often exploited for their hassle free and facile synthesis, low cost, biocompatibility, excellent photoluminescence (PL) properties and high stability in various devices [20], [21], [22]. Extensive studies are done on these materials to understand the mechanism of photoluminescence, their correlation to the structure and synergistic contribution of various optical active centers [23], [24]. Their sp^2 hybridized graphitic core with varying surface appendages has always been rigorously studied for application in catalysis [25], sensors [26], [27], imaging [28] and other optoelectronic devices. Mn doped carbon dots with strong pH responsive blue, green and orange fluorescence were utilized for white light emission (WLE) in a recent work [29]. Nitrogen and phosphorous doped carbon quantum dots synthesized by a one pot microwave route were reported to have a strong single WLE in solution as well as polymer frame [30]. Chen et.al., recently reported a double band carbon nanostructures formed from the hydrothermal synthesis of 1,3-dihydroxynaphthalene and hydrochloric

acid [31]. The single white light converter obtained was fabricated into a solid state WLED exhibiting a cold light source with CIE values (0.3122, 0.3429). However, adjustable white light emission parameters and CCT values with different excitation wavelengths from a single component material is still a matter to explore.

Nevertheless, most of these reports use complex and skill demanding synthesis procedures and even costly carbon and amine precursors [24], [32]. Natural sources being cheap, environment friendly with hassle free extraction procedures and strong fluorescence could pose as an alternative to such lab-grown inorganic luminogens [33], [34]]. An aqueous dye cocktail with pomegranate and curcumin extract in ethanol was recently used for WLE [35]. Though there are a few prior works in natural dye and dye derived quantum dots for WLE, these mostly use mixed emitter tuning [36], [37]. Stable and highly photoluminescent carbon nanoparticles synthesized by a one pot thermal degradation with panchromatic emission remains conceptual and enigmatic to date.

In this chapter, synthesis and optical properties of dual emitting carbon nanoparticles from the leaves of *Hemigraphis colorata* is discussed. A one step, facile low temperature thermal decomposition route is adopted which can ensure easy, large scale, inexpensive and sustainable synthesis. The optical properties, Commission Internationale d'Eclairage (CIE) coordinates and CCT values of the fluorescent nanoparticles were calculated. Encapsulation of the nanoparticles in a matrix like silica xerogel could inhibit undesirable aggregation induced quenching (AIQ) in the nanomaterials, prevent degradation and facilitate easy device fabrication.

3.1.1 Hemigraphis colorata

Figure 3.1: Photograph of Hemigraphis colorata leaves.

Hemigraphis colorata is known as red-flame ivy or waffle plant which is a member of acanthaceae family, native to tropical domains of globe especially tropical Asia [38]. The top face of the leaves appeared in dark green color and the lower face had a purplish green color. Appropriate moisture content, soil quality with indirect sunlight are the key factors which ensures a healthy plant growth. In particular, it is tremendously appreciated for its wound healing effects. Indonesians employed this herbal plant for promoting urination, treating hemorrhages and as a medication course for venereal diseases [39]. In India it is locally called muriyan pacha which indicates the wound healing property of the plant. Keralites called this plant with local name murikooti referred to as a component in ayurvedic medicines for wound healing treatments. These exotic perennial herbs belonging to the Acanthaceae family are often exploited for their anti-inflammatory, antibacterial and wound healing potencies [40], [41]. Its dye extract was reportedly used as a photosensitizer in combination with mesoporus TiO_2 for photovoltaic application [38]

3.1.2 Polyvinyl pyrrolidone (PVP)

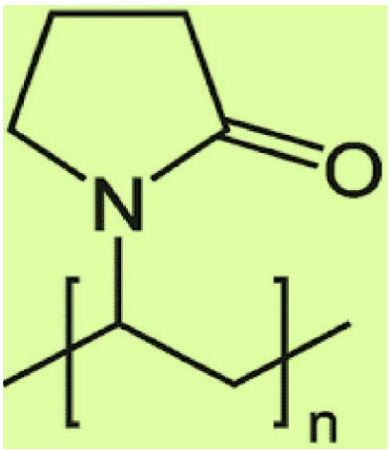

Figure 3.2: Structure of polymer poly (vinyl-pyrrolidone).

Poly vinyl-pyrrolidone (PVP) is a synthetic polymer derived from the monomer units of N-vinyl pyrrolidone. High solubility in both water and organic solvents made it applicable for fuel cells, pharmaceuticals and adhesives. Particularly, in the pharmaceutical field, PVP serves as binder in tablets, stabilizing agents in suspensions and as key components in wound healing products. The chemical structure of PVP is depicted in figure 3.2. PVP is feasible for thermal cross linking with other compounds which results in novel hybrid materials with outstanding

thermal stability and mechanical strength [42]. Unlike the flaky solid powder form, in liquid state PVP shows remarkable wetting properties which promotes easy film formation. PVP is safe, inedible which was employed as a blood plasma expander in trauma victims. On the other hand, the monomer units of PVP are highly toxic which severely affects aquatic lives.

3.1.3 Dual emissive (DE) fluorescence

Dual emissive (DE) fluorescence is commonly reported from purely light emitting compounds which was initially reported in azulene [43]. DE emitters produce emission bands at two distinct wavelengths by exciting with a single excitation source. Commonly fluorescence process involves speedy relaxation of a molecule from its excited singlet state to the stable ground state associated with the emission of energy packets as photons. So, simultaneous de-excitation from I^{st} and II^{nd} singlet excited states accompanied with luminescence is rare and significant in the case of a single molecule [44]. Generally, biomass derived dual emissive fluorescence are described as a combination of fluorescence from carbon core and the chlorophyll derived porphyrins. To the point, blue green fluorescence originated from intrinsic carbon cores with functionalized surface states which exhibit excitation dependent fluorescence. Mainly, excitation dependent fluorescence originated from functionalized surface states. Surface engineering of nanocarbon assemblies played a key role in obtaining excitation dependent luminescence [45], [46]. Meanwhile, red emissive fluorescence is generated from the chlorophyll derived porphyrins which have an excitation independent luminescence behavior [47]. Spinach, algae and many such pigment rich biomaterials are reported for their dual emissive fluorescence and they find applications in smartphone-based sensors, metal ion detectors and visual time detection [47], [48] .

DE bands are often used in cost-efficient white light emitting (WLEDs) and sensors by exploiting its ability to generate multiple optical signals. WLEDs constructed with single molecule derived DE emitters are capable in avoiding certain drawbacks of light emitting devices designed from multiple luminescent molecules such as degradation, color ageing as well as phase separation. Typically, ratiometric sensing was well performed with dual emissive luminescent systems. Other key areas

of application include data encryption, and anticounterfeiting. Easy device fabrication, stability with excellent reproducibility are the highlights of DE emitter-based lighting platforms [49], [50].

3.1.4 Chlorophyll and pheophytin

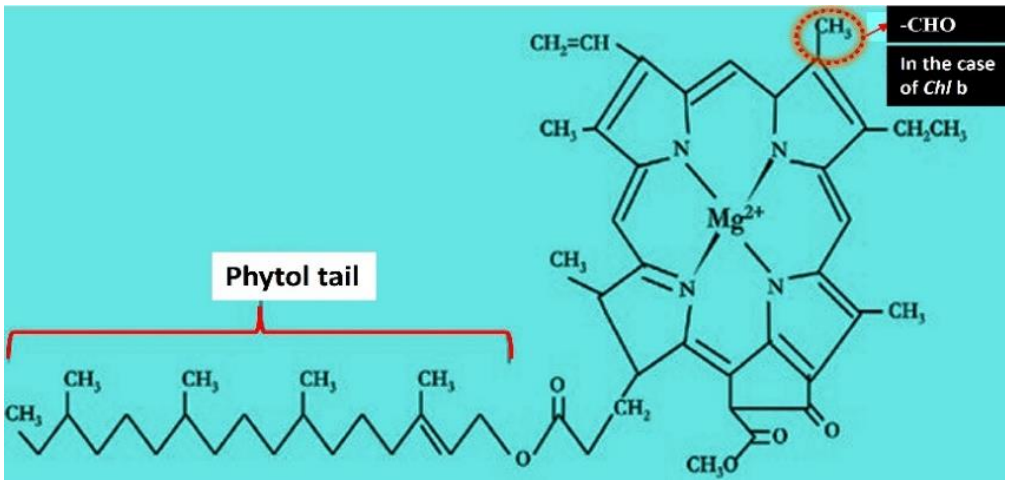

Figure 3.3: Structure of chlorophyll a and chlorophyll b molecules.

Chlorophylls (*Chl*) molecules are abundant in nature which plays a major role in photosynthesis. This compound contains porphyrin rings with one unit of reduced pyrrole ring and Mg^{2+} ions coordinated with N atoms [51]. *Chl* is a significant biopigment which commonly exists in chloroplasts of algae, cyanobacteria and other plants. In addition, *Chl* participates in photon capture, energy transfer and other related optical activities. Porphyrins are macrocyclic molecules extended with delocalized π-electrons and have shown remarkable thermal stability. Mostly, *Chl* molecule exists in two different forms called as chlorophyll a (*Chl a*) and chlorophyll b (*Chl b*). *Chl b* differs from *Chl a* by replacing the methyl (CH_3) group with formyl (CHO) group (given in figure 3.3). Meanwhile, pheophytin *(Phe)* is nothing but *Chl* molecule in which Mg^{2+} ions in the tetrapyrrole ring is substituted with H atoms [52]. It can be experimentally produced by treating chlorophyll with weak acids. Pheophytin serves as the pioneer electron carrier intermediate in the photoreaction centers of purple bacteria (RC P870) and photosystem II (RC P680). As per recent reports, *Chl* derived strong red luminescence was obtained via green synthetic

route[47]. Pheophytin a (*Phe a*) and pheophytin b (*Phe b*) are the two forms derived from *Chl a* and *Chl b* respectively.

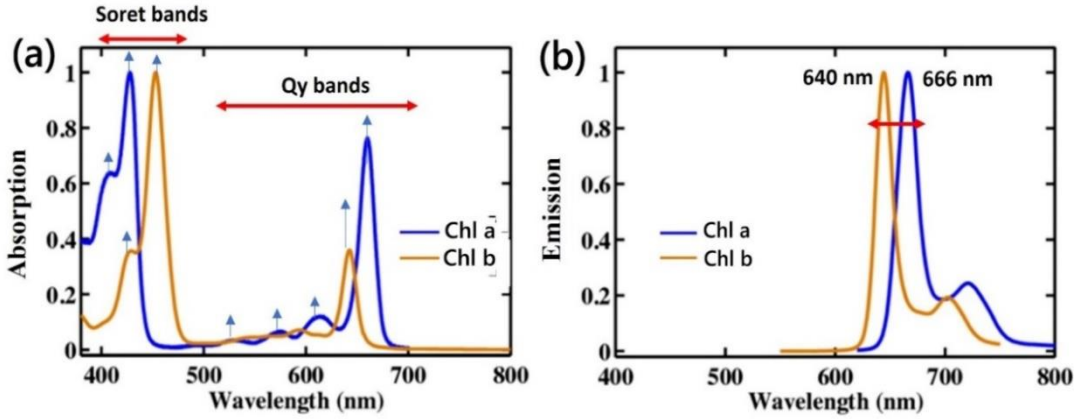

Figure 3.4: UV-Visible absorption spectra and photoluminescence spectra of chlorophyll a and chlorophyll b [53]**.**

As given in figure 3.4 (a) absorption bands of *Chl a* have peaks at 428nm and 660 nm whereas, for *Chl b* slightly shifted peaks at 453 nm and 643 nm are present. In the case of fluorescence (as shown in figure 3.4 (b)), similar spectral shift is observed. ie; *Chl a* has emission peak at 666 nm and *Chl b* emits around 640 nm [53]. In detail, two major bands namely Soret and Q_y-bands are commonly obtained in compounds with porphyrin rings. Generally, in terms of spectroscopy Soret band is referred as intense absorption bands around 400 nm and Q_y-bands are present in visible region with most intense peak at higher wavelength range of 600 to 660 nm.

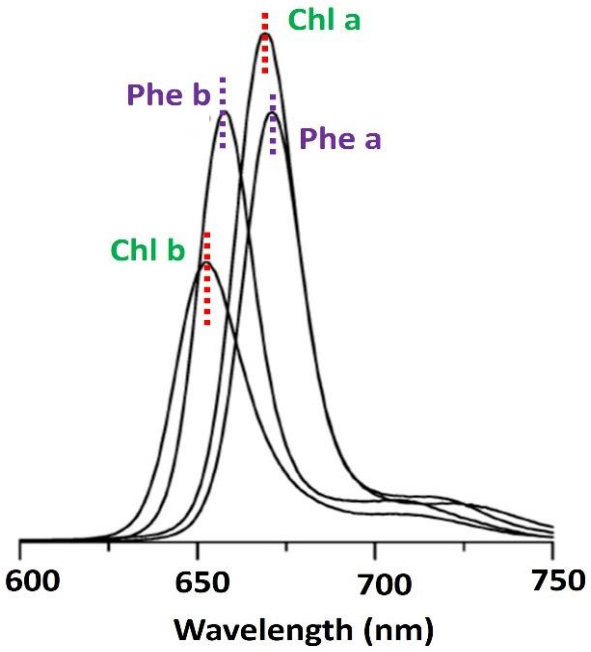

Figure 3.5: Photoluminescence spectra of chlorophyll and pheophytin in acetone/water (9:1) medium [52].

In the luminescence profiles shown in figure 3.5, *Phe* and *Chl* molecules have peaks in the red region around 650 nm. But excitation spectra for these red emissions are different in some peak positions. Particularly, *Chl a* and *Phe a* have very close luminescence peaks at 670 nm and on the other hand, *Chl b* and *Phe b* has similar red emissions centered around 650 nm [52].

3.1.5 Review on biomass derived carbon nanostructures

Biomass derived carbon nanostructures have got tremendous attention due to its versatility in structure and characteristics. Till date numerous synthesis strategies are employed in developing biomass derived carbon nano structures. Microwave method, pyrolysis, hydrothermal carbonization (HTC), ionothermal carbonization (ITC), molten salt carbonization are certain synthesis approaches for nano carbon systems [54], [55]. Even though there are many synthesis routes, HTC is most common method used to convert biomass to different nanostructures of carbon. It is usually carried out at moderate temperature ranges (< 300 ^{0}C) with self-generated pressures [56]. Song et. al. employed HTC for carbon nanoparticle synthesis by using flaxseed as the carbon source [57]. Several researchers reported microwave method on silk worm chrysalis [58], serum albumin to obtain carbon materials and in some

cases carbon materials are prepared using peanut shell and hair via pyrolysis method. Recently eutrophic algae derived luminescent nanocarbon are obtained via microwave method has been reported [54]. Diversity in the composition of biomass sources made huge differences in the finally obtained carbon materials.

By varying the sources, synthetic parameters and synthesis routes, structure and dimensions of end product varies. Thereby, their applications are also distinct like starch are excellent in cell imaging [59] but aloe derived carbon dots through the same HTC method are apt for tartrazine detection [60]. Accordingly, from similar synthesis with different carbon source itself create many changes in structure, optical profile and the key areas of application. Less expensive, easily available, eco-friendly bio sources are commonly rich in various vitamins, minerals and biopigments. Efficient panel of natural sources such as vegetables, fruits, plant parts are well explored and even the ejected waste items such as kitchen waste, egg shell, water lemon peel, waste frying oil are also found out in reports as precursors of carbonization. Due to their optical features like photoluminescence color tuning (PLCT) and up conversion luminescence, biomass derived carbon nanoparticles are utilized in various fields such as sensors for biomolecules and metal ions, bioimaging and drug delivery. Apart from this, they have inevitable role in various other fields like photovoltaics, fuel cells [55], supercapacitors [61]. Carbon based composites are another enthusiastic research topic in which novel combinations are presented. Recently, Wang and his co-workers constructed hybrid supercapacitors by bridging carbon nanosheets with MnO [62]. Meanwhile, reported UV/Visible absorption bands of nanocarbon are too short which may cause damage to DNA and proteins. So, it may arise certain limitations in their bio medical applications. In future perspective, NIR absorptions can also be achieved to widen the spectra of nanocarbon applications.

3.2 Experimental section

3.2.1. Synthesis of carbon nanoparticles (CNP)

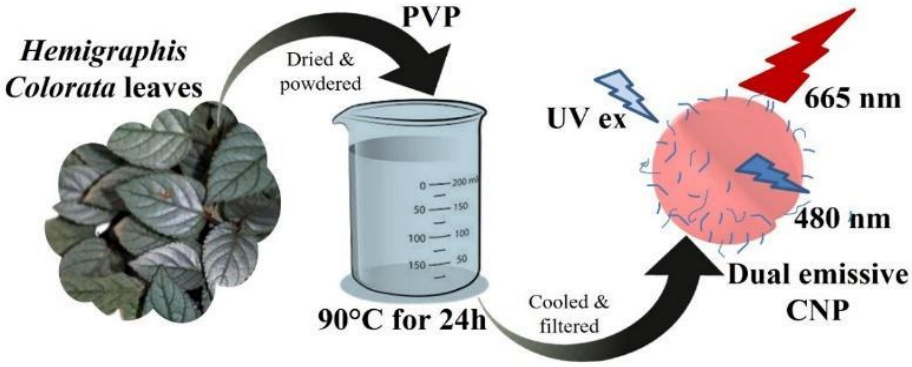

Figure 3.6: Synthesis of dual emissive CNP from *Hemigraphis colorata* leaves.

The carbon nanoparticles were synthesized through direct thermal decomposition of the precursor (shown in figure 3.6). The leaves of *Hemigraphis colorata* were washed, air-dried at room temperature and crushed using a mortar and pestle to obtain fine powder. 1 g of PVP was dissolved in 200 mL distilled water. 10 g of leaf powder was added to the above solution and agitated homogeneously. The mixture was kept in the oven at 95 °C for 24 hours and then allowed to cool naturally to room temperature. The solution was filtered using a Whatman filter paper and dark brown supernatant solution obtained (CNP) was used for further experiments. The carbon nanoparticles made in a similar manner without adding PVP was named CN. Similar synthesis route was repeated for preparing CN-60 and CN-90 by drying the leaves at 60 °C and 90 °C respectively.

3.2.2 Optical and morphological characterization

The X-Ray Diffraction (XRD) analysis was done on Aeris Research XRD Diffractometer, (PANalytical, The Netherlands) with a scanning range of $2\theta = 10-90°$ with Cu Kα radiation ($\lambda = 1.540598$ Å). The surface functional groups were identified from Fourier-transform infrared (FTIR) spectra recorded in transmission mode on a FTIR spectrometer (Thermo Nicolet, USA) at room temperature in the range 4000-400 cm-1. A high-resolution transmission electron microscopy (HRTEM) data using a TALOS F200S G2 transmission electron microscope (200 kV, FEG, CMOS Camera

4K × 4K) was used to identify the morphology of the sample. Ultraviolet/Visible (UV/Vis) absorption spectra in the range 200-700 nm were obtained from the Shimadzu UV 1800 spectrophotometer. All photoluminescence measurements were made on a Fluorolog NIR spectrofluorometer (Horiba Jobin Yvon, USA). WLED properties like color rendering index (CRI), color coordinate (CIE), and correlated color temperature (CCT) were evaluated from Color Calculator software.

3.3 Results and discussions

3.3.1 Powder X-ray diffraction (XRD)

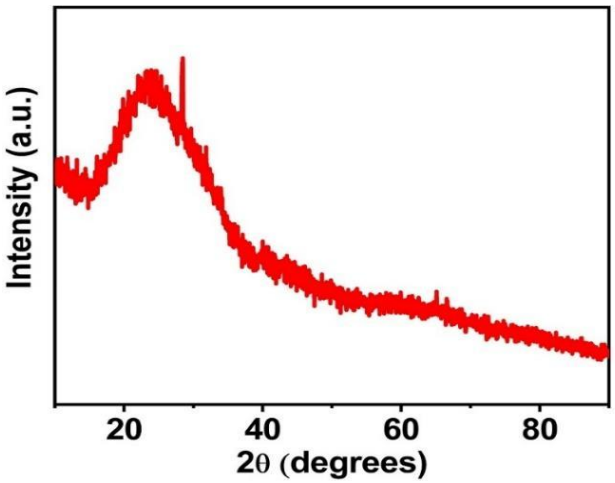

Figure 3.7: XRD pattern of CNP.

The XRD pattern (Fig. 3.7) of CNP shows a wide peak centered at 2theta value of 23°. This suggests the graphitic structure of the nanoparticles corresponding to (002) plane [63]. Absence of any other peaks suggests the purity of sample.

3.3.2 Fourier transform infrared spectroscopy (FTIR)

FTIR spectrum (figure 3.8) helps to identify the surface functional groups and moieties attached to the graphitic core. The broad band from 3050-3550 cm^{-1} can be attributed to the stretching vibrations of hydrophilic groups –OH and –NH. These surface groups are responsible for water dispersibility of the synthesized nanoparticles. The bands peaked at 580, 1636, 2080 cm^{-1} correspond to –OH bending vibration, stretching vibration of –C=O, -C-N respectively [64]. This confirms that the structural skeleton of CNP contains electron donating groups and porphyrin groups attached to the surface or core.

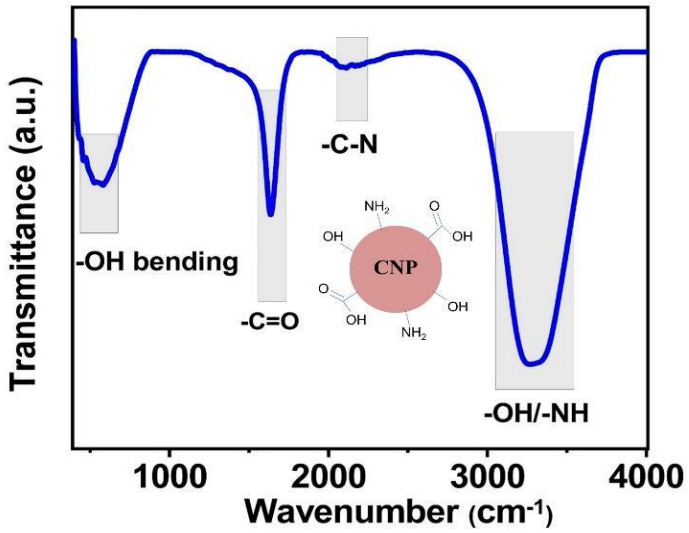

Figure 3.8: FTIR spectrum of CNP; the inset of the figure shows the structure of surface functionalized carbon nanoparticles.

3.3.3 Transmission electron microscopy (TEM)

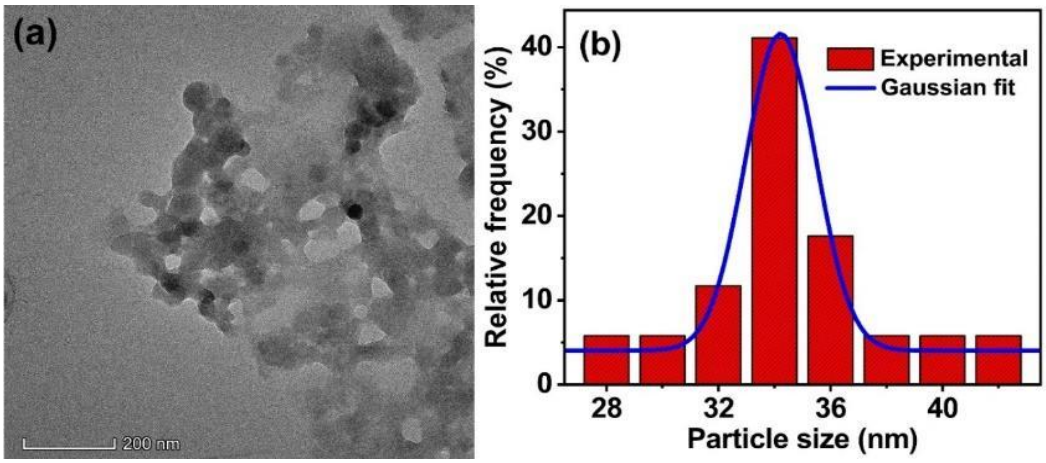

Figure 3.9: (a) TEM image of CNP and (b) corresponding particle size distribution.

The morphology of the sample was studied by TEM. Figure 3.9(a) shows monodispersed quasi spherical carbon nanoparticles in PVP polymer. The statistical particle size histogram (Fig. 3.9(b)) evaluated from the TEM image shows a distribution in the range of 28 - 42 nm.

3.3.4 Energy dispersive X-ray spectroscopy (EDX)

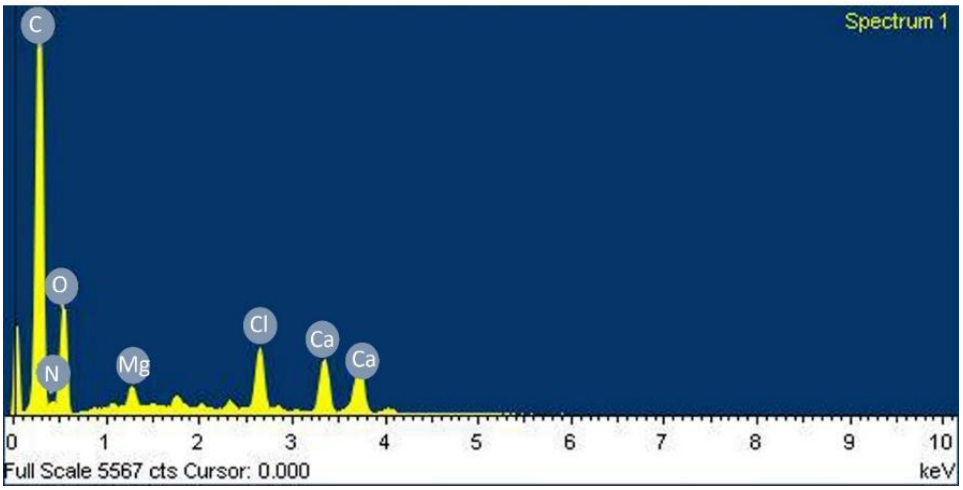

Figure 3.10: EDS spectrum of CNP.

EDX spectrum (Fig. 3.10) reveals that CNP contains C, N, O, Mg, Cl, Ca. Presence of magnesium indicates the existence of chlorophyll within the dual emissive CNPs. Also, peaks corresponding to Cl and Ca are observed due to the trace amount of elements present in the leaf.

3.3.5 UV-Visible absorption spectra

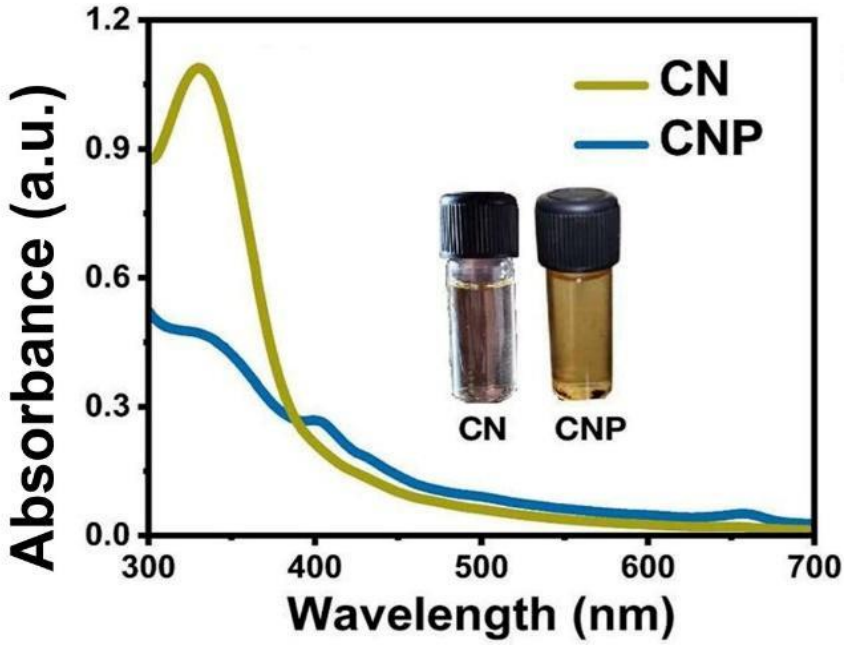

Figure 3.11: UV-visible absorption spectra of CN and CNP (inset of figure shows the photographs of CN and CNP solution in daylight.

The optical properties of CNP were studied from UV-visible (given in figure 3.11) and fluorescence spectra (3.12). The absorption spectrum of CNP has characteristic bands corresponding to the electronic transition in carbon centres and surface states. The strong band centered at 336 nm can be attributed to n→π* edge transition of the aromatic sp^2 -C=O bond in nanocarbon [65]. It is primarily responsible for surface trapping of excited energy and the blue emission mostly observed in carbon cores. To gain better insights into the role of PVP on the optical properties of synthesized nanoparticles, carbon nanoparticles were prepared without using PVP (CN). Similar to UV-visible spectrum of CNP, band peaked at 333 nm can be attributed to n→π* transitions of the aromatic sp^2 carbon system [52]. In CNP, the absorption bands in the visible region (400 to 700 nm) are mainly due to the transitions of surface groups [66]. The absorption bands at 405 and 655 nm can be ascribed to the π →π* and n→π* electron transition (Soret band and Q-band) of the -C=O and -C=N bonds in the chlorophyll-derived porphyrin [48], [67]. For CN, weak absorption band in the visible region suggests that lack of PVP results in less surface passivation with nitrogen-containing molecules.

3.3.6 Photoluminescence spectra

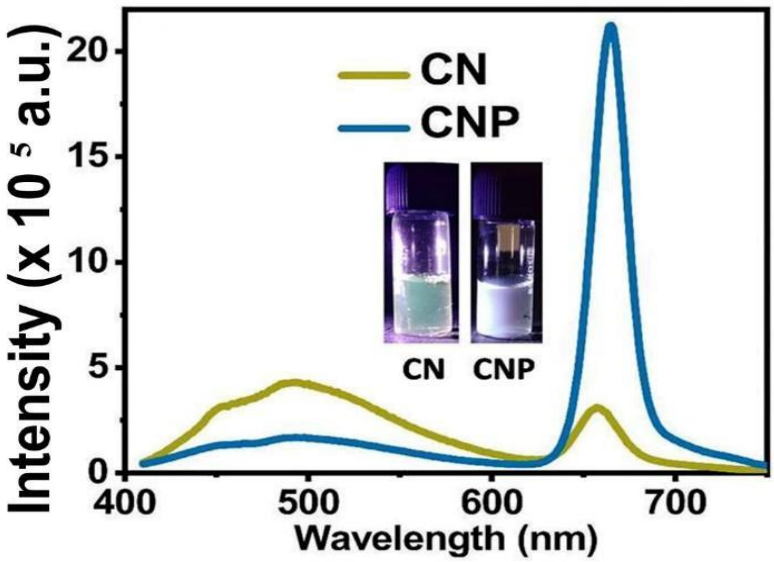

Figure 3.12: Fluorescence spectra of CN and CNP at 390 nm excitation wavelength (inset shows the photographs of CN and CNP solution in daylight and under UV excitation respectively).

The fluorescence spectra of CN and CNP exhibit dual and distinct emission bands at ~480 nm and 665 nm upon UV excitations (Fig. 3.12). The broad emission band observed in the blue-green region is due to surface states and trapping centers for electron hole pairs which originated from O-, N-, and S- containing groups of CQDs. The cluster luminescence responsible for the blue green emission bands of CNP is formed by the aggregation of heteroatoms containing functional groups attached to the surface states via weak forces [68], [69]. While carbon core with cluster of surface states acts as the center of blue green luminescence, the strong red luminescence observed can be ascribed to the molecular state transitions associated with chlorophyll and pheophytin [48], [52]. Addition of PVP enhanced the red emission intensity by about 8 times in carbon nanoparticles due to molecular state transitions. Increase in red emission is accompanied by decrease in blue emission which indicates energy transfer from carbon core to porphyrin rings. Due to the presence of intense red emission, the blue-green emitting CN could turn into a good white light emitter as shown in the inset of Fig. 3.12.

3.3.7 Energy transfer studies

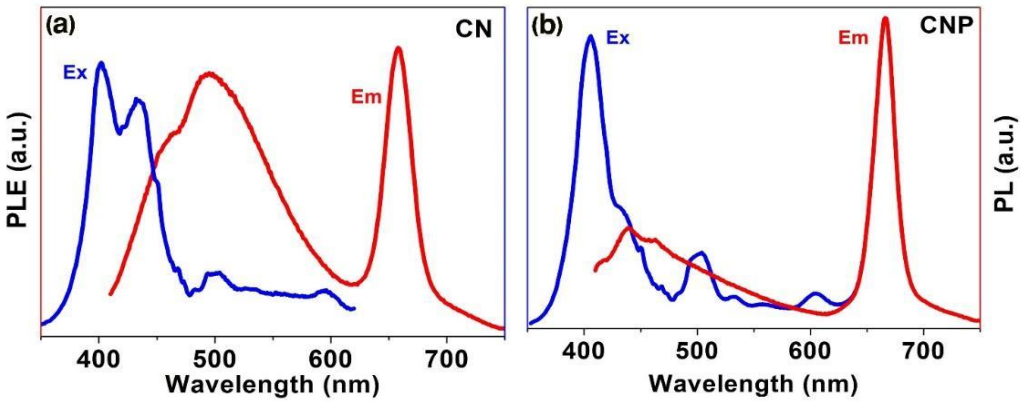

Figure 3.13: Photoluminescence excitation spectra (Blue line) and Photoluminescence emission spectra (red line) of (a) CN and (b) CNP respectively.

From the figure 3.13, it can be observed that excitation spectrum of CN and CNP overlaps with blue-green emission and a donor-acceptor pair is established between carbon nuclei and porphyrin. Additionally, it can be inferred that characteristic excitation peaks of pheophytin are enhanced in CNP which suggests the interaction between PVP and pheophytin. Moreover, in presence of PVP, the average exciton life

time of blue green emission peaked at 480 nm is decreased while average decay time of red emission peaked at 665 nm is increased (Table. 2.1). This confirms the energy transfer between carbon nuclei and porphyrin from chlorophyll/ pheophytin to obtain enhanced red emission.

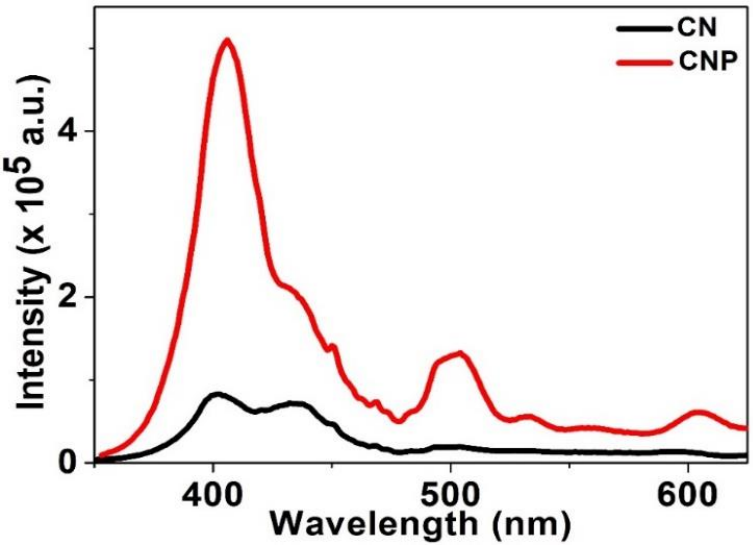

Figure 3.14: Photoluminescence excitation spectra of CN and CNP.

From the excitation spectrum (figure 3.14) it is clear that addition of PVP causes partial conversion of chlorophyll to pheophytin. Moreover, the presence of characteristic peaks at 505 nm and 535 nm suggests the absence of any other metal substituted derivatives of chlorophyll. Even though chlorophyll and pheophytin has characteristic red emission peaked at 665 nm wavelength [52] excitation spectra for chlorophyll and pheophytin for 665 nm has different characteristic absorption peaks. While absorption band peaked at 405 nm, 435 nm and 604 nm is characteristic excitations of chlorophyll, the peaks at 405 nm 505 nm and 534 nm can be attributed to prominent excitation peaks pheophytin emission. This confirms the existence of porphyrin containing chlorophyll and pheophytin on CNP. Thus, direct thermal decomposition of organics from dried leaves in the presence of PVP gives carbon nanoparticles with surface functionalized with porphyrins from chlorophyll and pheophytin. The schematic representation depicting the synthesis of such dual emissive carbogenic nanoparticles has been shown in Fig. 3.6. The presence of PVP effectively functionalizes the CNP surface with more porphyrin groups to absorb

more in the visible region (400 to 700 nm). Moreover, these molecular states are predominantly responsible for the enhanced bright red emission in CNPs under UV excitation [47], [70]. It was reported that carbon quantum dots synthesized from withered leaves emit blue color while those prepared from green leaves exhibit dual blue-red emission [47]. Here, the leaves are air dried at room temperature using a hairdryer, which causes degradation of chlorophyll compared to fresh leaves. This results in less surface modification of CN by chlorophyll derived porphyrin groups.

Table. 3.1. The fluorescence lifetime decay parameters of CNP monitored for blue green (B-G) and red (R) peak.

Sample code	α_1	τ_1 (ns)	α_2	τ_2 (ns)	α_3	τ_3 (ns)	T_{avg} (ns)
CN - (B-G peak)	1.23	0.67	0.24	2.58	0.03	0.58	0.97
CN - (R peak)	0.42	3.97	0.37	4.08	0.36	0.83	3.02
CNP- (B-G peak)	0.71	0.73	0.68	0.36	0.32	1.62	0.75
CNP – (R peak)	0.30	3.07	0.26	4.71	0.23	5.74	4.40

3.3.8 Influence of leaf drying temperature on dual luminescence

To investigate dependence of leaf drying temperature, PL spectra of carbon nanoparticles prepared by air dried leaves (~40 ℃) (CN), with leaves dried at oven at 60 ℃ (CN-60) and at 90 ℃ (CN-90) respectively are studied.

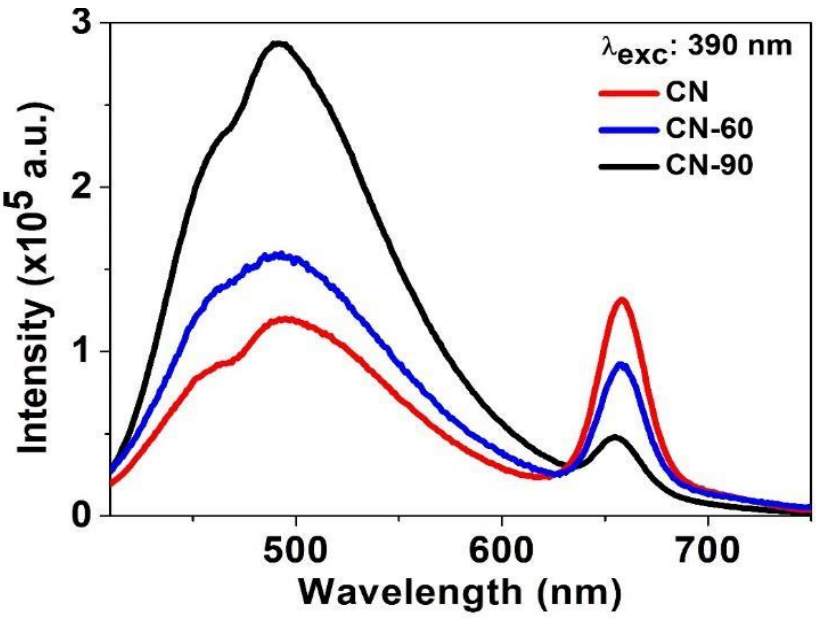

Figure 3.15: Emission spectra of CN by varying the leaf drying temperature. (CN: Air dry, 60 ℃ and 90 ℃).

As the leaf drying temperature increases, chlorophyll/pheophytin content in the leaves decreases remarkably which is accompanied with the reduction in red luminescence (shown in figure 3.15). Additionally, as drying temperature increases, high degree of carbonization occurs which helps CN-90 to exhibit greater blue green emission intensity. However, PVP could form complexes with porphyrin compounds through hydrogen bonds or coordination bonds which are capable of photoinduced electron transfer [71].

The room-temperature photoluminescence QY is obtained as 0.81 which can be attributed occurrence of less passivated surface states and defects in prepared CNP at low pyrolysis temperature. This results in defect-mediated nonradiative recombination from surface states and trap sites [72]. Increase in the pyrolysis temperature can increase the QY of nanoparticles, but temperature beyond 100 ^{o}C cause degradation of chlorophyll and pheophytin. Similar QY values have been reported for certain carbon nanoparticles [73] due to the presence of surface states and defects.

3.3.9 Influence of concentration on dual luminescence

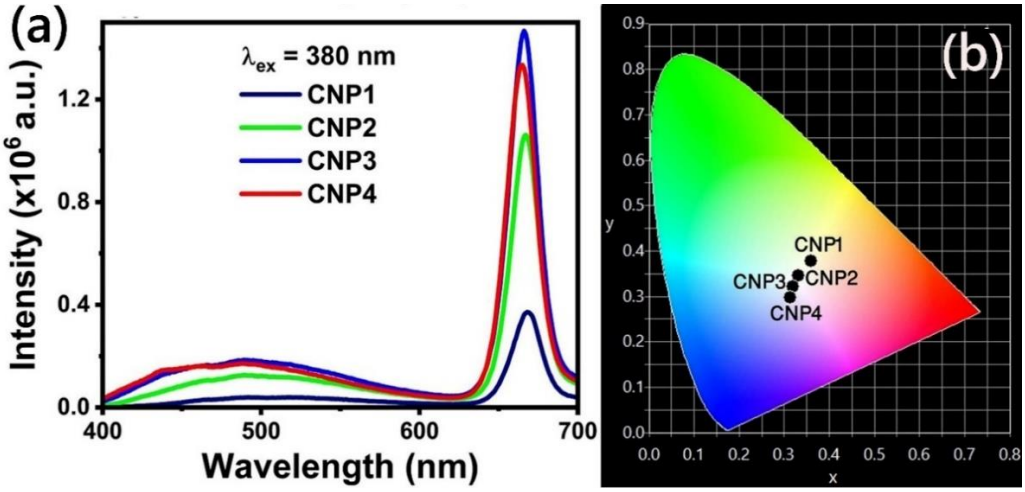

Figure 3.16: (a) Fluorescence spectra of CNP at varying volume % (1 to 4) of carbon nanoparticles (CNP1 to CNP4) at 380 nm excitation and (b) corresponding CIE 1931 chromaticity chart.

As nanoparticles suffer aggregation induced quenching, the concentration effect of the nanoparticles is studied by analyzing the fluorescence spectra of CNP at varying volume % (1 to 4) of carbon nanoparticles (Fig. 3.16(a)). According to Chen, the fluorescence band is red shifted at higher concentrations of nanoparticles [74]. It is evident that there is no discernible shift in major peak position of both fluorescence bands, upon varying concentration of the nanoparticles. This is due to the effective wrapping of nanoparticles with PVP. The intensity of the PL spectral peak is maximum for an intermediate concentration (3 volume % carbon nanoparticles) and decreases slightly with increase of concentration. As concentration is increased there will be higher number of particles and spacing between the particles will be less than the Förster distance (R_0). This might cause reabsorption of emission which results in self-quenching of the fluorescence. Moreover, an increase in the number of particles results in aggregation induced quenching which can also affect the fluorescence efficiency.

3.3.10 Influence of excitation wavelength on dual luminescence

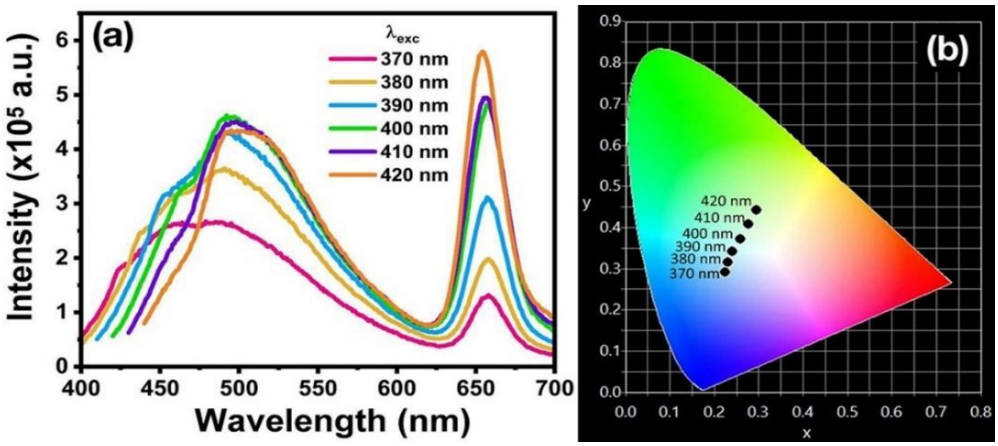

Figure 3.17: (a) Excitation wavelength dependent emission spectra and (b) CIE 1931 chromaticity chart of CN.

The Fig. 3.17(a) shows the fluorescence of the CN upon varying excitation wavelength. Interestingly, the blue peak has an apparent excitation dependent emission with peak center varying from 475 nm to 510 nm while the red peak shows an excitation independent emission peak centered at 665 nm. Also, the intensity of the peak centered at 480 nm is almost the same with the peak centered at 665 nm wavelength. Upon different excitation wavelengths, blue-green emission together with the narrow red emission band could exhibit color varying from light blue to greenish yellow as obtained from CIE 1931 chromaticity chart of CN.

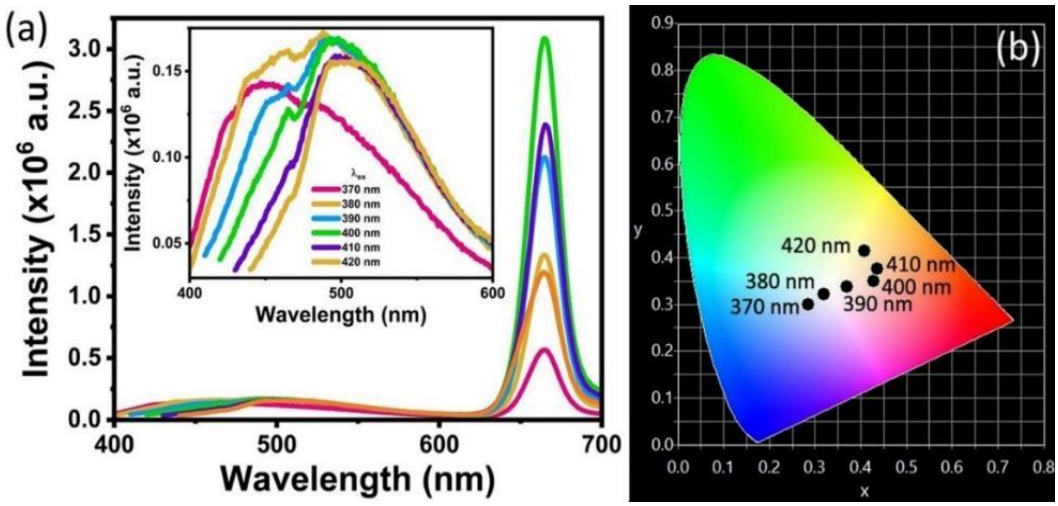

Figure 3.18: (a) Excitation wavelength dependent emission spectra of CNP (b) CIE 1931 chromaticity chart of CNP,

Subsequently, as observed for CN, the low energy emission peak at 655 nm wavelength is narrow and excitation independent (figure 3.18) for PVP capped carbon nanoparticles. As seen from the inset of figure 3.18 (a), the blue- green emission is broad and excitation dependent like exhibited by CN. Upon different excitation wavelengths from 370 nm to 420 nm, tunable dual-band emission gives white to yellow color as obtained from the CIE 1931 chromaticity chart of CNP. The CIE chromaticity coordinates obtained for all excitations from 370 nm to 420 nm confirms that the fluorescence obtained from CNP under broad excitation wavelengths lies in white light trajectory (Table 3.2).

Table 3.2. List of Excitation wavelengths, CIE indices, CCT values of CNP.

Excitation wavelength (nm)	CIE	CCT (K)
370	(0.2860, 0.2983)	8980
380	(0.3202, 0.3208)	6154
390	(0.3706, 0.3376)	3982
400	(0.4289, 0.3492)	2648
410	(0.4369, 0.3745)	2750
420	(0.4089, 0.4131)	3602

3.3.11 CNPs as tunable WLEDs

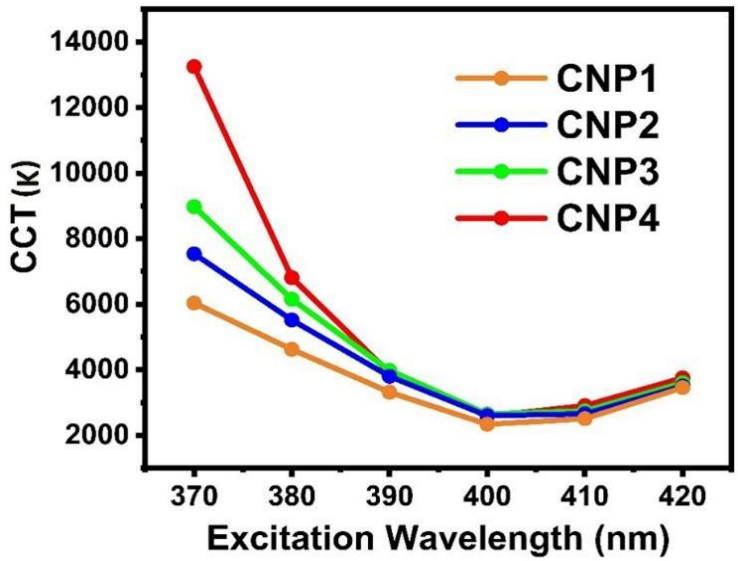

Figure 3.19: CCT values of CNP at varying volume % (1 to 4) of carbon nanoparticles (CNP1 to CNP4) at varying excitations (370 nm to 420 nm).

Tunable correlated color temperature (CCT) values from warm to cool emission are obtained upon different excitation wavelengths (Figure 3.19).

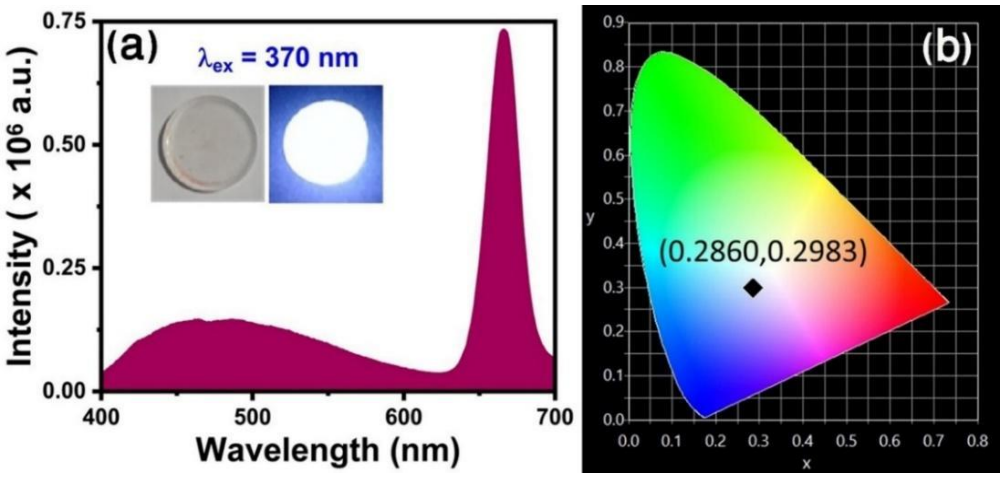

Figure 3.20: (a) PL spectra of CNP at excitation wavelength of 370 nm showing dual emission at 480 nm and 665 nm; the inset shows the photograph of silica glass dipped in CNP under daylight and UV illumination (b) CIE plot of PL emission from CNP exhibiting indices values (0.2860, 0.2983).

At 400 nm excitation wavelength, all concentrations give warm white color emission (∼2500 K) which changes to cool white color emission at UV excitations (4623 K to 8117 K). Inspired by the excellent tunability for CCT and CIE color coordinates, cool white emissions are obtained for CNP (figure 3.20(a)) at 370 nm excitation wavelength. White emissions having CIE color coordinates (0.2860, 0.2983) with CCT of 8980 K and CRI value of 68 are achieved for CNP (3 volume % carbon nanoparticles) and is marked in CIE 1931 color space (figure 3.20 (b)). The color point lies on the black body Planckian locus. For the sake of overcoming the agglomeration of nanoparticles, solid matrix of CNP - silica xerogels were fabricated and white emissions are observed (inset of figure 3.20 (a)).

3.3.12 Optical stability of CNPs with storage time interval

To check the stability of CNP solutions in normal room temperature, the temporal stability of the PL intensity of CNP was evaluated for an interval of one week (figure 3.21(a)). It can be identified that the intensity of the blue peak at 480 nm stays relatively constant. Even though the peak at 665 nm shows a slight decrease in PL intensity, it remains almost the same after the second week of storage.

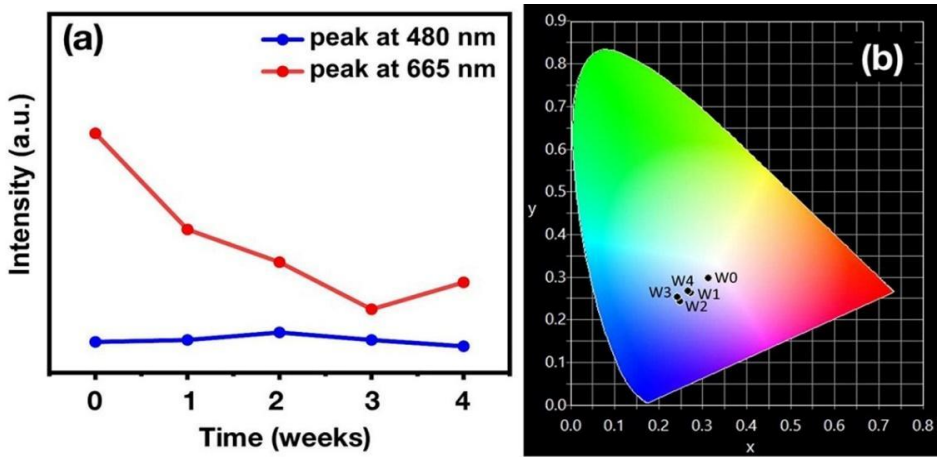

Figure 3.21: (a) Plot of PL intensity maximum of CNP solution and storage time. (b) corresponding CIE plot.

From the CIE 1931 color space, it is evident that the white emission remains unchanged for a period of 4 weeks. All the results demonstrate the enormous potential applications of the biomass derived CQD-based phosphors in high-performance WLEDs.

3.4 Conclusion

Dual emitting carbon nanoparticles were prepared through one step, facile, low temperature thermal degradation of *Hemigraphis colorata* leaves. Detailed characterizations proved that nanoparticles have an average size range of 28 - 42 nm. The surface states of nanoparticles are rich in electron donating groups and porphyrin groups, ultimately determining the dual color of their PL, which peaked at 480 nm and 665 nm wavelengths. With the addition of PVP, the intensity of red emission enhances sharply. While the blue emission band was excitation dependent, the red emission band was excitation independent. This strategy elucidates the design of efficient white light emitting devices with broad band excitation. Upon different excitation wavelengths, dual emissive carbon nanoparticles could show tunable correlated color temperature (CCT) values from warm to cool emission which promises for environment-friendly, indoor, and outdoor lighting application

References

[1] E. F. Schubert and J. K. Kim, "Solid-State Light Sources Getting Smart," *Science*, vol. 308, no. 5726, pp. 1274–1278, May 2005, doi: 10.1126/science.1108712.

[2] B. W. D'Andrade and S. R. Forrest, "White Organic Light-Emitting Devices for Solid-State Lighting," *Advanced Materials*, vol. 16, no. 18, pp. 1585–1595, 2004, doi: 10.1002/adma.200400684.

[3] A. K. Bedyal, V. Kumar, and H. C. Swart, "Charge compensated derived enhanced red emission from Sr3(VO4)2:Eu3+ nanophosphors for white light emitting diodes and flat panel displays," *Journal of Alloys and Compounds*, vol. 709, pp. 362–372, Jun. 2017, doi: 10.1016/j.jallcom.2017.03.139.

[4] J. Wang, W. Lin, and W. Li, "Three-channel fluorescent sensing via organic white light-emitting dyes for detection of hydrogen sulfide in living cells," *Biomaterials*, vol. 34, no. 30, pp. 7429–7436, Oct. 2013, doi: 10.1016/j.biomaterials.2013.06.013.

[5] Y.-P. Xia *et al.*, "Utilizing an effective framework to dye energy transfer in a carbazole-based metal–organic framework for high performance white light emission tuning," *Inorg. Chem. Front.*, vol. 5, no. 11, pp. 2868–2874, Nov. 2018, doi: 10.1039/C8QI00747K.

[6] H. Chen *et al.*, "Chromaticity-tunable phosphor-in-glass for long-lifetime high-power warm w-LEDs," *J. Mater. Chem. C*, vol. 3, no. 31, pp. 8080–8089, Jul. 2015, doi: 10.1039/C5TC01057H.

[7] T. Wang, V. Chirmanov, W. H. M. Chiu, and P. V. Radovanovic, "Generating Tunable White Light by Resonance Energy Transfer in Transparent Dye-Conjugated Metal Oxide Nanocrystals," *J. Am. Chem. Soc.*, vol. 135, no. 39, pp. 14520–14523, Oct. 2013, doi: 10.1021/ja407013z.

[8] Q.-L. Chen, C.-F. Wang, and S. Chen, "One-step synthesis of yellow-emitting carbogenic dots toward white light-emitting diodes," *J Mater Sci*, vol. 48, no. 6, pp. 2352–2357, Mar. 2013, doi: 10.1007/s10853-012-7016-8.

[9] Y. Zhang *et al.*, "Employing Heavy Metal-Free Colloidal Quantum Dots in Solution-Processed White Light-Emitting Diodes," *Nano Lett.*, vol. 11, no. 2, pp. 329–332, Feb. 2011, doi: 10.1021/nl1021442.

[10] X. Feng and Y. Zhang, "A simple and green synthesis of carbon quantum dots from coke for white light-emitting devices," *RSC Advances*, vol. 9, no. 58, pp. 33789–33793, 2019, doi: 10.1039/C9RA06946A.

[11] V. Revuri, K. Cherukula, M. Nafiujjaman, K. Jae cho, I.-K. Park, and Y.-K. Lee, "White-Light-Emitting Carbon Nano-Onions: A Tunable Multichannel Fluorescent Nanoprobe for Glutathione-Responsive Bioimaging," *ACS Appl. Nano Mater.*, vol. 1, no. 2, pp. 662–674, Feb. 2018, doi: 10.1021/acsanm.7b00143.

[12] K.-J. Chen *et al.*, "White light emitting diodes with enhanced CCT uniformity and luminous flux using ZrO_2 nanoparticles," *Nanoscale*, vol. 6, no. 10, pp. 5378–5383, Apr. 2014, doi: 10.1039/C3NR06894C.

[13] S. Bose *et al.*, "Synthesis of Silicon Nanoparticles from Rice Husk and their Use as Sustainable Fluorophores for White Light Emission," *ACS Sustainable Chem. Eng.*, vol. 6, no. 5, pp. 6203–6210, May 2018, doi: 10.1021/acssuschemeng.7b04911.

[14] H. T. Nicolai, A. Hof, and P. W. M. Blom, "Device Physics of White Polymer Light-Emitting Diodes," *Advanced Functional Materials*, vol. 22, no. 10, pp. 2040–2047, 2012, doi: 10.1002/adfm.201102699.

[15] Y. Tang, W. Cao, L. Yao, Y. Cui, Y. Yu, and G. Qian, "Polyurethane-coated luminescent dye@MOF composites for highly-stable white LEDs," *J. Mater. Chem. C*, vol. 8, no. 35, pp. 12308–12313, Sep. 2020, doi: 10.1039/D0TC02887H.

[16] C.-Y. Sun *et al.*, "Efficient and tunable white-light emission of metal–organic frameworks by iridium-complex encapsulation," *Nat Commun*, vol. 4, no. 1, Art. no. 1, Nov. 2013, doi: 10.1038/ncomms3717.

[17] Y. Ledemi *et al.*, "White light and multicolor emission tuning in triply doped Yb3+/Tm3+/Er3+ novel fluoro-phosphate transparent glass-ceramics," *J. Mater. Chem. C*, vol. 2, no. 25, pp. 5046–5056, Jun. 2014, doi: 10.1039/C4TC00455H.

[18] W. Ki, J. Li, G. Eda, and M. Chhowalla, "Direct white light emission from inorganic–organic hybrid semiconductor bulk materials," *J. Mater. Chem.*, vol. 20, no. 47, pp. 10676–10679, Nov. 2010, doi: 10.1039/C0JM02213F.

[19] S. Wang *et al.*, "A semi-conductive organic–inorganic hybrid emits pure white light with an ultrahigh color rendering index," *J. Mater. Chem. C*, vol. 5, no. 19, pp. 4731–4735, May 2017, doi: 10.1039/C7TC00279C.

[20] H. Li, Z. Kang, Y. Liu, and S.-T. Lee, "Carbon nanodots: synthesis, properties and applications," *J. Mater. Chem.*, vol. 22, no. 46, pp. 24230–24253, Nov. 2012, doi: 10.1039/C2JM34690G.

[21] J. Liu, R. Li, and B. Yang, "Carbon Dots: A New Type of Carbon-Based Nanomaterial with Wide Applications," *ACS Cent. Sci.*, vol. 6, no. 12, pp. 2179–2195, Dec. 2020, doi: 10.1021/acscentsci.0c01306.

[22] M. Semeniuk *et al.*, "Future Perspectives and Review on Organic Carbon Dots in Electronic Applications," *ACS Nano*, vol. 13, no. 6, pp. 6224–6255, Jun. 2019, doi: 10.1021/acsnano.9b00688.

[23] M. J. Krysmann, A. Kelarakis, P. Dallas, and E. P. Giannelis, "Formation Mechanism of Carbogenic Nanoparticles with Dual Photoluminescence Emission," *J. Am. Chem. Soc.*, vol. 134, no. 2, pp. 747–750, Jan. 2012, doi: 10.1021/ja204661r.

[24] A. Nandy, A. Kumar, S. Dwivedi, S. K. Pal, and D. Panda, "Connecting the Dots of Carbon Nanodots: Excitation (In)dependency and White-Light Emission in One-Step," *J. Phys. Chem. C*, vol. 123, no. 33, pp. 20502–20511, Aug. 2019, doi: 10.1021/acs.jpcc.9b02428.

[25] C. Testa, A. Zammataro, A. Pappalardo, and G. T. Sfrazzetto, "Catalysis with carbon nanoparticles," *RSC Advances*, vol. 9, no. 47, pp. 27659–27664, 2019, doi: 10.1039/C9RA05689K.

[26] R. Santonocito, M. Intravaia, I. Maria Caruso, A. Pappalardo, G. T. Sfrazzetto, and N. Tuccitto, "Fluorescence sensing by carbon nanoparticles," *Nanoscale Advances*, vol. 4, no. 8, pp. 1926–1948, 2022, doi: 10.1039/D2NA00080F.

[27] E. Asadian, M. Ghalkhani, and S. Shahrokhian, "Electrochemical sensing based on carbon nanoparticles: A review," *Sensors and Actuators B: Chemical*, vol. 293, pp. 183–209, Aug. 2019, doi: 10.1016/j.snb.2019.04.075.

[28] H. Li *et al.*, "Recent advances in carbon dots for bioimaging applications," *Nanoscale Horizons*, vol. 5, no. 2, pp. 218–234, 2020, doi: 10.1039/C9NH00476A.

[29] R. Kumari, K. Pal, P. Karmakar, and S. K. Sahu, "pH-Responsive Mn-Doped Carbon Dots for White-Light-Emitting Diodes, Fingerprinting, and Bioimaging," *ACS Appl. Nano Mater.*, vol. 2, no. 9, pp. 5900–5909, Sep. 2019, doi: 10.1021/acsanm.9b01335.

[30] K. Ahmad, A. Pal, U. N. Pan, A. Chattopadhyay, and A. Paul, "Synthesis of single-particle level white-light-emitting carbon dots via a one-step microwave method," *J. Mater. Chem. C*, vol. 6, no. 25, pp. 6691–6697, Jun. 2018, doi: 10.1039/C8TC01276H.

[31] X. Chen *et al.*, "Blue and green double band luminescent carbon quantum dots: Synthesis, origin of photoluminescence, and application in white light-emitting devices," *Applied Physics Letters*, vol. 118, no. 15, p. 153102, Apr. 2021, doi: 10.1063/5.0046495.

[32] H. Qi *et al.*, "Synthesis of multiple-color emissive carbon dots towards white-light emission," *Nanotechnology*, vol. 31, no. 24, p. 245001, Mar. 2020, doi: 10.1088/1361-6528/ab7b08.

[33] T. C. Wareing, P. Gentile, and A. N. Phan, "Biomass-Based Carbon Dots: Current Development and Future Perspectives," *ACS Nano*, vol. 15, no. 10, pp. 15471–15501, Oct. 2021, doi: 10.1021/acsnano.1c03886.

[34] X. Zhang *et al.*, "Natural-Product-Derived Carbon Dots: From Natural Products to Functional Materials," *ChemSusChem*, vol. 11, no. 1, pp. 11–24, 2018, doi: 10.1002/cssc.201701847.

[35] V. Singh and A. K. Mishra, "White light emission from vegetable extracts.," *Scientific Reports*, vol. 5, no. 1, 2015, Accessed: Apr. 15, 2023.

[36] J. Mathew, J. Joy, A. Kumar S, and J. Philip, "White light emission by energy transfer from areca nut husk extract loaded with carbon dots synthesized from the same extract," *Journal of Luminescence*, vol. 208, pp. 356–362, Apr. 2019, doi: 10.1016/j.jlumin.2018.10.110.

[37] V. Singh and A. K. Mishra, "White light emission from a mixture of pomegranate extract and carbon nanoparticles obtained from the extract," *J. Mater. Chem. C*, vol. 4, no. 15, pp. 3131–3137, Apr. 2016, doi: 10.1039/C6TC00480F.

[38] V. G. Nandakumar, S. Suresh, C. O. Sreekala, S. K. Sudheer, and V. P. Mahadevan Pillai, "Hemigraphis colorata as a natural dye for solar energy conversion," *Materials Today: Proceedings*, vol. 4, no. 2, Part C, pp. 4358–4365, Jan. 2017, doi: 10.1016/j.matpr.2017.04.006.

[39] C. Wiart, Christophe, *Medicinal Plants of The Asia-pacific: Drugs For The Future?* World Scientific, Jan. 2006. doi: 10.1142/5834

[40] B. Kumar, M. Vijayakumar, R. Govindarajan, and P. Pushpangadan, "Ethnopharmacological approaches to wound healing—Exploring medicinal plants of India," *Journal of Ethnopharmacology*, vol. 114, no. 2, pp. 103–113, Nov. 2007, doi: 10.1016/j.jep.2007.08.010.

[41] M. I. Safna, U. V. Visakh, and A. Gangadharan, "Biological activity of hexane extract of Hemigraphis colorata, an indigenous wound healing plant," *Materials*

Today: Proceedings, vol. 25, pp. 294–297, Jan. 2020, doi: 10.1016/j.matpr.2020.01.461.

[42] Z.-J. Zhang, H.-H. Chen, X.-X. Yang, and J.-T. Zhao, "Preparation and luminescent properties of Eu^{3+} and Tb^{3+} ions in the host of $CaMoO_4$," *Materials Science and Engineering: B*, vol. 145, no. 1, pp. 34–40, Dec. 2007, doi: 10.1016/j.mseb.2007.09.091.

[43] G. Eber, F. Grüneis, S. Schneider, and F. Dörr, "Dual fluorescence emission of azulene derivatives in solution," *Chemical Physics Letters*, vol. 29, no. 3, pp. 397–404, Dec. 1974, doi: 10.1016/0009-2614(74)85131-6.

[44] N. A. Kukhta and M. R. Bryce, "Dual emission in purely organic materials for optoelectronic applications," *Materials Horizons*, vol. 8, no. 1, pp. 33–55, 2021, doi: 10.1039/D0MH01316A.

[45] Li, Xiaoming, et al., "Engineering surface states of carbon dots to achieve controllable luminescence for solid-luminescent composites and sensitive Be^{2+} detection", Scientific *Reports*", vol. 4, no. 1, pp. 4976, May 2014, doi: 10.1038/srep04976

[46] Yan, Fanyong, et al., "The fluorescence mechanism of carbon dots, and methods for tuning their emission color: a review, *Microchimica Acta*. vol. 186, no. 583, July 2019, doi: 10.1007/s00604-019-3688-y

[47] H. Rao *et al.*, "Smartphone-Based Fluorescence Detection of Al3+ and H2O Based on the Use of Dual-Emission Biomass Carbon Dots," *ACS Sustainable Chem. Eng.*, vol. 8, no. 23, pp. 8857–8867, Jun. 2020, doi: 10.1021/acssuschemeng.0c03354.

[48] X. Xu *et al.*, "Red-emissive carbon dots from spinach: Characterization and application in visual detection of time," *Journal of Luminescence*, vol. 227, p. 117534, Nov. 2020, doi: 10.1016/j.jlumin.2020.117534.

[49] C. Li *et al.*, "An Organic Emitter Displaying Dual Emissions and Efficient Delayed Fluorescence White OLEDs," *Advanced Optical Materials*, vol. 7, no. 10, p. 1801667, 2019, doi: 10.1002/adom.201801667.

[50] T. Ishi-i *et al.*, "White-light emission from a pyrimidine–carbazole conjugate with tunable phosphorescence–fluorescence dual emission and multicolor emission switching," *Chem. Commun.*, vol. 56, no. 29, pp. 4051–4054, Apr. 2020, doi: 10.1039/D0CC00251H.

[51] A. P. Gerola, T. M. Tsubone, A. Santana, H. P. M. de Oliveira, N. Hioka, and W. Caetano, "Properties of Chlorophyll and Derivatives in Homogeneous and Microheterogeneous Systems," *J. Phys. Chem. B*, vol. 115, no. 22, pp. 7364–7373, Jun. 2011, doi: 10.1021/jp201278b.

[52] T. Galeano Díaz, I. Durán Merás, C. A. Correa, B. Roldán, and M. I. Rodríguez Cáceres, "Simultaneous Fluorometric Determination of Chlorophylls a and b and Pheophytins a and b in Olive Oil by Partial Least-Squares Calibration," *J. Agric. Food Chem.*, vol. 51, no. 24, pp. 6934–6940, Nov. 2003, doi: 10.1021/jf034456m.

[53] Mammadov, Gulmammad, "Measurement of the Membrane Electric Field and the Swimming Behavior of *Chlamydomonas reinhardtii*: Experiments and Analytical Modeling Diss. Syracuse University, 2015.

[54] W. Meng, X. Bai, B. Wang, Z. Liu, S. Lu, and B. Yang, "Biomass-Derived Carbon Dots and Their Applications," *Energy & Environmental Materials*, vol. 2, no. 3, pp. 172–192, 2019, doi: 10.1002/eem2.12038.

[55] J. Deng, M. Li, and Y. Wang, "Biomass-derived carbon: synthesis and applications in energy storage and conversion," *Green Chem.*, vol. 18, no. 18, pp. 4824–4854, Sep. 2016, doi: 10.1039/C6GC01172A.

[56] A. Abbas, L. T. Mariana, and A. N. Phan, "Biomass-waste derived graphene quantum dots and their applications," *Carbon*, vol. 140, pp. 77–99, Dec. 2018, doi: 10.1016/j.carbon.2018.08.016.

[57] Y. Song *et al.*, "Highly photoluminescent carbon dots derived from linseed and their applications in cellular imaging and sensing," *J. Mater. Chem. B*, vol. 6, no. 19, pp. 3181–3187, May 2018, doi: 10.1039/C8TB00116B.

[58] J. Feng, W.-J. Wang, X. Hai, Y.-L. Yu, and J.-H. Wang, "Green preparation of nitrogen-doped carbon dots derived from silkworm chrysalis for cell imaging," *J. Mater. Chem. B*, vol. 4, no. 3, pp. 387–393, Jan. 2016, doi: 10.1039/C5TB01999K.

[59] W. Chen *et al.*, "Synthesis of graphene quantum dots from natural polymer starch for cell imaging," *Green Chem.*, vol. 20, no. 19, pp. 4438–4442, Oct. 2018, doi: 10.1039/C8GC02106F.

[60] H. Xu, X. Yang, G. Li, C. Zhao, and X. Liao, "Green Synthesis of Fluorescent Carbon Dots for Selective Detection of Tartrazine in Food Samples," *J. Agric. Food Chem.*, vol. 63, no. 30, pp. 6707–6714, Aug. 2015, doi: 10.1021/acs.jafc.5b02319.

[61] Y. Wang and Y. Xia, "Recent Progress in Supercapacitors: From Materials Design to System Construction," *Advanced Materials*, vol. 25, no. 37, pp. 5336–5342, 2013, doi: 10.1002/adma.201301932.

[62] H. Wang *et al.*, "Hybrid Device Employing Three-Dimensional Arrays of MnO in Carbon Nanosheets Bridges Battery–Supercapacitor Divide," *Nano Lett.*, vol. 14, no. 4, pp. 1987–1994, Apr. 2014, doi: 10.1021/nl500011d.

[63] T. N. J. I. Edison, R. Atchudan, M. G. Sethuraman, J.-J. Shim, and Y. R. Lee, "Microwave assisted green synthesis of fluorescent N-doped carbon dots: Cytotoxicity and bio-imaging applications," *Journal of Photochemistry and Photobiology B: Biology*, vol. 161, pp. 154–161, Aug. 2016, doi: 10.1016/j.jphotobiol.2016.05.017.

[64] A. Dager, A. Baliyan, S. Kurosu, T. Maekawa, and M. Tachibana, "Ultrafast synthesis of carbon quantum dots from fenugreek seeds using microwave plasma enhanced decomposition: application of C-QDs to grow fluorescent protein crystals," *Sci Rep*, vol. 10, no. 1, Art. no. 1, Jul. 2020, doi: 10.1038/s41598-020-69264-9.

[65] J. Song, Q. Ma, Y. Liu, Y. Guo, F. Feng, and S. Shuang, "Novel single excitation dual-emission carbon dots for colorimetric and ratiometric fluorescent dual mode detection of Cu^{2+} and Al^{3+} ions," *RSC Advances*, vol. 9, no. 66, pp. 38568–38575, 2019, doi: 10.1039/C9RA07030C.

[66] K. J. Mintz, Y. Zhou, and R. M. Leblanc, "Recent development of carbon quantum dots regarding their optical properties, photoluminescence mechanism, and core structure," *Nanoscale*, vol. 11, no. 11, pp. 4634–4652, 2019, doi: 10.1039/C8NR10059D.

[67] L. Tang *et al.*, "Deep Ultraviolet Photoluminescence of Water-Soluble Self-Passivated Graphene Quantum Dots," *ACS Nano*, vol. 6, no. 6, pp. 5102–5110, Jun. 2012, doi: 10.1021/nn300760g.

[68] S. Wang *et al.*, "Cluster-luminescent polysiloxane nanomaterials: adjustable full-color ultralong room temperature phosphorescence and a highly sensitive response to silver ions," *Inorg. Chem. Front.*, vol. 9, no. 14, pp. 3619–3626, Jul. 2022, doi: 10.1039/D2QI00914E.

[69] H. Qi *et al.*, "Rationally Designed Matrix-Free Carbon Dots with Wavelength-Tunable Room-Temperature Phosphorescence," *Chemistry – An Asian Journal*, vol. 18, no. 6, p. e202201284, 2023, doi: 10.1002/asia.202201284.

[70] W. Li *et al.*, "Enhanced Biological Photosynthetic Efficiency Using Light-Harvesting Engineering with Dual-Emissive Carbon Dots," *Advanced Functional Materials*, vol. 28, no. 44, p. 1804004, 2018, doi: 10.1002/adfm.201804004.

[71] Y. Cao, T. Takasaki, S. Yamashita, Y. Mizutani, A. Harada, and H. Yamaguchi, "Control of Photoinduced Electron Transfer Using Complex Formation of Water-Soluble Porphyrin and Polyvinylpyrrolidone," *Polymers*, vol. 14, no. 6, Art. no. 6, Jan. 2022, doi: 10.3390/polym14061191.

[72] S. Wang *et al.*, "A 200-fold Quantum Yield Boost in the Photoluminescence of Silver-Doped Ag_xAu_{25-x} Nanoclusters: The 13^{th} Silver Atom Matters," *Angewandte Chemie*, vol. 126, no. 9, pp. 2408–2412, 2014, doi: 10.1002/ange.201307480.

[73] H. Kim, D.-H. Lien, M. Amani, J. W. Ager, and A. Javey, "Highly Stable Near-Unity Photoluminescence Yield in Monolayer MoS_2 by Fluoropolymer Encapsulation and Superacid Treatment," *ACS Nano*, vol. 11, no. 5, pp. 5179–5185, May 2017, doi: 10.1021/acsnano.7b02521.

[74] J. Zhu *et al.*, "Carbon dots with efficient solid-state red-light emission through the step-by-step surface modification towards light-emitting diodes," *Dalton Trans.*, vol. 47, no. 11, pp. 3811–3818, Mar. 2018, doi: 10.1039/C7DT04579D.

4

Se-Tb^{3+} Doped Silica for Multicolor Emitting Applications

In this chapter, we describe formation of RE-QD composites by tailoring the concentration of Se QDs via sol-gel method. Nanosized Se undergoes allotropic transition from cubic to amorphous phase via annealing at 200 ^{o}C. The structure and thermal stability of the composites are confirmed from TEM, FTIR, SAED and TGA curves. Reduced band gap values of Se-Tb^{3+} doped silica than the pure Se-SiO_2 is due to the formation of energy levels associated with defective states upon Tb^{3+} doping. Under UV excitations, Se-Tb^{3+} doped SiO_2 composites exhibited broad blue emissions along with enhanced narrow green emissions from Tb^{3+} ions. Herein, the Se QDs acts as sensitizer in its cubic phase, boosting Tb^{3+} fluorescence whereas it played the role of a quencher in its amorphous phase. Delayed lifetimes and enhanced excitation-emission bands of Tb^{3+} obtained in the presence of cubic Se evidences strong ET channels in the c-Se-Tb^{3+} silica composites. Besides, fluorescence profile of the composites could be easily tuned from white (0.2233, 0.3113) to green (0.3245, 0.4923) upon increase in Se concentration. Allotropy based spectral characteristics of the Se-Tb^{3+}-SiO_2 composites will be beneficial in realizing solid color tunable lighting devices and advanced optical accessories.

Graphical abstract

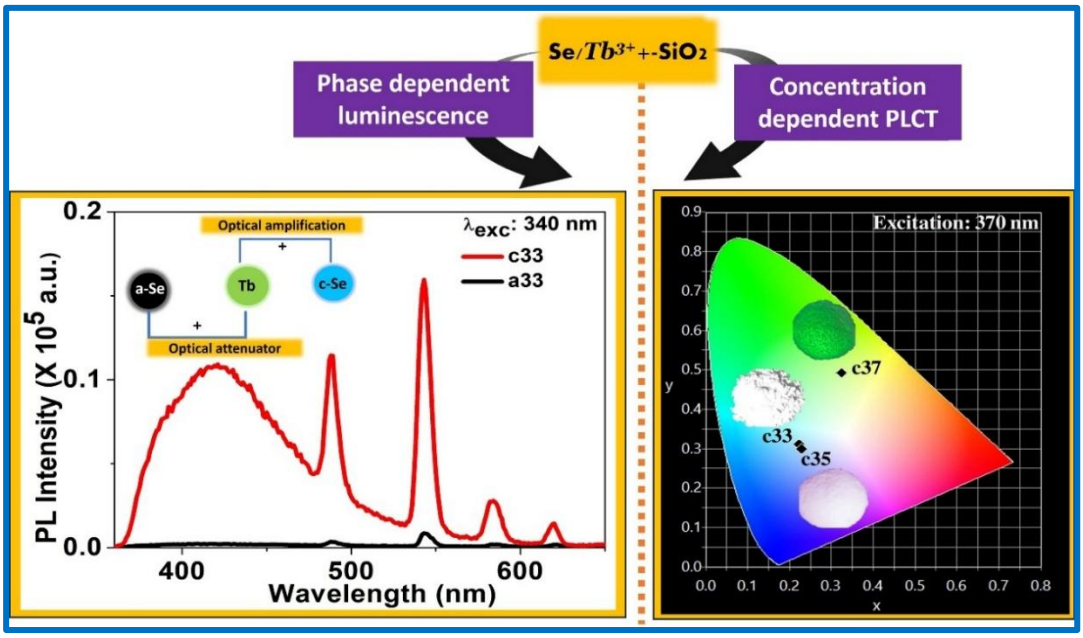

4.1 Introduction

Semiconducting quantum dots (QDs) with inherent optical excellence and their exciting features have been widely exploited for optoelectronic, photovoltaic applications with high conversion efficiency [1]. Among extensively studied elemental QDs, Selenium QDs stands out due to its polymorphism based distinctive structural and optical characteristics. Elemental Se exists in both crystalline and amorphous forms of nanostructures with different morphology. In particular, it has two amorphous forms which appears in red and black color can be found as chains, rings or their mixtures. For crystalline Se, orthorhombic (o-Se), monoclinic (m-Se), trigonal (t-Se), cubic (c-Se) are the four major forms in which t-Se exhibits highest stability [2] [3]. Thermally unstable elemental forms of Se have shown rapid transitions into stable allotropic structures with entirely different properties [4]. Cubic to amorphous transition of Se doped silica under certain thermal conditions are recently studied [5]. Different Se nanostructures with similar allotropy such as t-Se nano spheres, t-Se nanorods, a-Se nanospheres and crystalline nanospheres are synthesised by various research groups [2]. Commonly a-Se appears in the form of spheres with minimum interfacial free energy and reduced anisotropic features. Even though the element remains same, optical characteristics of Se polymorphs are quite different in itself due to the diverse atomic level arrangements. From prior optical studies of Se allotropes, strong blue fluorescence peaked at 421 nm [5] and 434 nm [3] are obtained for c-Se and t-Se respectively via direct inter band transitions with similar k-vector space while there was no reported emissions for a-Se [5]. At nanoscale, reported band gap energies of a-Se, c-Se, t-Se are 2.4 eV, 3.5 eV, 2 eV respectively and have shown noticeable blue shift from their bulk counterparts due to the quantum confinement effects [5].

Nowadays efficient fluorescent materials were realized by integrating luminescent RE ions that can create abundant fluorescence bands owing to their rich 4f electron configurations. Owing to their prolonged fluorescence lifetimes, photostability and spectral shifts (stokes/anti-stokes) [6], [7] RE based materials finds potential applications in various fields like sensors, optical fibres, optical thermometry, display and anticounterfeiting devices [8], [9]. The luminescent stability observed in lanthanides is attributed to the effective shielding of 4f electron by the outer $5s^2$, $5p^6$

orbitals that prevents the energy loss via environmental interactions and crystal fields. Among luminescent rare earths, Tb^{3+}, Eu^{3+} are mostly explored activator ions due to their unparalleled green and red emissions at 543 nm ($5D_4 \rightarrow 7F_5$) and 616 ($^5D_0 \rightarrow ^7F_2$) nm respectively. Despite of these, their thin absorption bands, precise excitations and small absorption coefficients originated from the parity forbidden intra 4f transitions severely minimized its utilization in tunable lighting devices [6], [10]. Interestingly, it is urge to combine a suitable fluorescent dopant that can widen the spectral distribution and boost the optical performance of activator ions. Certain investigations on this notion leads to the designing of sensitizer-activator pairs involving two RE ions ($Ce^{3+} - Eu^{3+}$). However, due to the inter metallic charge transfer among the pairs alters the oxidation states ($Ce^{4+} - Eu^{2+}$) which results in quenching of fluorescence intensity. Instead of making compositions with different RE ions, currently researchers focused on composites of luminescent sources such as elemental QDs, polymer dots, perovskite QDs, inert metal based nano assemblies with RE ions [6], [13], [14], [15]. To analyse the tunable emission bands for WLEDs Junjie Zhang and his team designed an Eu-doped $CsPbX_3$(Cl, Br, I) quantum dots glasses [13]. However, complex structured perovskite QDs can be replaced with simple elemental QDs. By changing the radiative recombination process, more easier fluorescence tuning can be attained by the incorporation of elemental QDs with RE ions (Eu^{3+}, Tb^{3+}, Ce^{3+}) of tailorable optical features [1], [16], [17]. Due to the spectral overlap and the faster decay lifetime in presence of QDs, FRET occurs in some RE-QD composites while in some pairs, QD sensitizes the fluorescence of lanthanides via efficient ET channels [6], [18], [19]. P. T. Tho and co-workers have investigated ET mechanisms among the CdS/Eu incorporated composites for their tuned optical behaviours [1]. RE-QD based phosphors like ZnSe: Eu^{3+} [20] CdTe:Eu^{3+} [21] are certain multi-elemental RE/QD combinations that contributes in photonic applications due to their mechanical and thermal stability.

For past several years considerable interest was paid on developing host matrices. Among various host lattices used in lighting platforms like barium orthosilicate, silica, gelatin, strontium orthosilicate, PVA [12], [23], [24] mesoporous silica holds an inimitable position due to their unique characteristics such as optical window from UV to near IR, thermal expansion coefficient, feeble nonlinear refractive index, mechanical strength and chemical durability [25]. Effective preparation methods are also necessary in ensuring fluorescence generation from both luminescent centres.

However, till date allotropic forms of Se QDs co-doped with luminescent Tb^{3+} ions, and their potential in achieving distinct optical behaviours are not yet explored. Although scientific community explored the combinations of RE ions with allotropic forms of carbon such as CNTs, CQDs, fullerene their *in-situ* mode of phase transitions is less reported. Herein, we designed solid fluorescent Se-RE^{3+}- SiO_2 nanocomposites with peculiar optical features. We prepared a series of xSe-Tb^{3+} (x = 3, 5, 7 w %) doped silica and the allotropic transitions of Se are achieved via annealing process. We examined PLCT behaviour by varying the dopant concentration and excitation wavelengths. Phase dependent ET between Se QDs and Tb^{3+} ions are also studied in detail.

4.1.1 Review on rare earth (RE) ions /selenide composites

Selenium have got profound interest due to their fascinating allotropy-based features. Among Se polymorphs, amorphous QDs and trigonal nanowires are well explored due to their stability and ease of growth. Even though Se-RE compositions are rarely found in reports elemental selenides are frequently studied in combination with RE ions. When RE ions meet elemental selenides, optical profiles are significantly modified via various ET mechanisms. By combining nano crystallites of CdSe with Eu^{3+} ions, phonon mediated ET from CdSe to RE^{3+} ions leading to enhanced optical features as a combined result of electron-hole recombination and multi-phonon relaxation. In this case, de-excitation process of RE ions are analyzed by using the phonon side band spectrum recorded for the excitation transition $7F_0 \rightarrow 5D_2$ [26], [27]. Radiative parameters of CdSe/RE^{3+} composites are evaluated using JO theory which supports the experimentally obtained luminescence enhancement [28]. N.V. Unnikrishnan and his research group prepared CdSe/Dy^{3+}doped silica matrices via sol-gel technique. In the presence of CdSe nanoparticles, excitation bands of Dy^{3+} are evidently enhanced via different ET mechanisms. Optically enhanced luminescence bands are well explained on the basis of non-radiative ET from CdSe to Dy^{3+} ions which promotes electron-hole recombination pathways [29]. In addition to that, Siby. et. al, utilized wide band gap of zinc selenides in combination with europium ions. Characteristic emissions from Eu^{3+} ions show considerable hike in their intensity which are attributed to the non-radiative ET from ZnSe to Eu^{3+}ions by means of electron-hole recombination. Adsorption of ZnSe on silica matrix allows strong interactions between

ZnSe and Eu^{3+} ions and branching ratios from JO analysis supports the experimental results [30].

4.2 Experimental section

4.2.1 Fabrication of Selenium-Terbium doped silica

Se-Tb^{3+} doped silica glasses were prepared via sol gel route at room temperature [5]. 3.9 ml of ethanolic solution of terbium (III) nitrate pentahydrate (3 w %) was mixed with 7.4 ml tetraethyl orthosilicate (TEOS) and stirred continuously for one hour to get homogenous solution. To this, 4 ml of aqueous selenous acid solution of suitable w % (3 %) was added and stirred well for 1 hour. Two drops of concentrated nitric acid were added as a catalyst and the molar ratio of TEOS/H_2O/HNO_3 was maintained as 1:12:0.01 throughout the synthesis. Final clear solutions kept in small polypropylene containers were sealed with paraffin wax and stored for a month to allow gelation process. Samples heated in the hot air oven at 60 °C for one week to remove water and other organics present and were named as c33. Similar synthesis route was repeated with varying w % (5 % and 7 %) of Se and were named as c35 and c37. Pure Tb^{3+} doped silica (3 w %) was obtained through same synthesis route which was named as T3 and heated at 200 ^{0}C in muffle furnace for two hours to obtain T3$^{'}$. To prepare amorphous Se and Tb^{3+} doped silica, c33, c35 and c37 were annealed at 200 ^{0}C in muffle furnace for two hours. The deep orange-colored glasses were named as a33, a35, a37 respectively. Synthesised samples with corresponding compositions, heated temperatures are listed in Table 4.1.

Table 4.1: Compositions of the prepared samples and annealing temperatures.

Sample code	w % Tb	w % Se	Annealing Temperature
c33	3	3	60 ^{0}C
c35	3	5	60 ^{0}C
c37	3	7	60 ^{0}C
a33	3	3	200 ^{0}C
a35	3	5	200 ^{0}C
a37	3	7	200 ^{0}C
T3	3	0	60 ^{0}C
T3$^{'}$	3	0	200 ^{0}C

4.2.2 Optical and morphological characterization

A model TALOS F200S G2 transmission electron microscope (200 kV, FEG, CMOS Camera 4K × 4K) with an attachment of energy dispersive X-ray (EDX) spectrometer was used to analyse the morphology and crystallinity of Se-Tb3+ doped silica glasses. Fourier Transform Infrared Spectroscopy (FTIR) was carried out with the Perkin Elmer spectrum TWO FTIR spectrometer. The optical absorption spectrum was recorded using UV-vis spectrophotometer, (Shimadzu UV-2600) and fluorescence measurements were acquired from Fluoromax Spectrofluorometer (Horiba Jobin Yvon, USA). Time-resolved fluorescence decay analysis was carried out using fluorescence spectrometer (Horiba Fluorolog, USA). The colorimetric parameters were found out from the CIE (Commission Internationale de L'Eclairage1931) chromaticity diagram using

Color Calculator software. All these experiments were conducted at room temperature. Thermal decomposition studies of prepared composites were performed with PerkinElmer STA 8000. TGA-DTA and DSC curves were recorded using a nitrogen purge system at the heating rate of 10 °C/min.

4.3 Results and discussions

4.3.1 Transmission electron microscopy (TEM)

The crystallinity and morphology of the Se- Tb^{3+} doped silica was confirmed from TEM micrographs and SAED patterns.

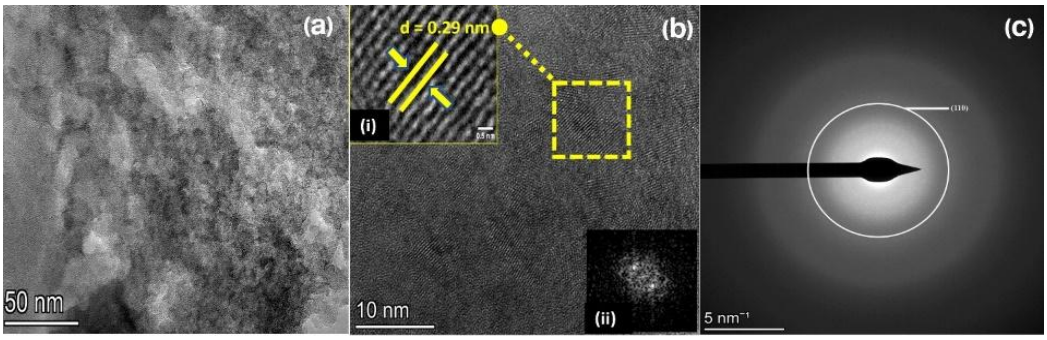

Figure 4.1: TEM (a) and HRTEM (b) of c33. [Inset (i) shows a plane with interlayer spacing d-value for the crystalline assembly was found to be 0.29 nm corresponds to (100) plane and inset (ii) shows the corresponding FFT pattern] (c) SAED pattern of c33.

TEM image (Fig. 4.1 (a)) shows the nano crystallites agglomerated together within the silica network. From HRTEM micrograph (Fig. 4.1 (b)), clear, equi-spaced lattice planes were observed. The well resolved lattice fringes having d-spacing of 0.29 nm, and can be indexed to (100) plane of cubic Se (ICDD no. 38-0768). The fast Fourier transform (FFT) corresponding to the HRTEM image gives inter planar spacing value (d) of 0.291 nm (inset of Fig. 4.1 (b)) which is in good agreement with the values obtained from HRTEM images. Furthermore, the bright spots in the selected area electron diffraction (SAED) pattern of c33 (given in fig. 4.1(c) confirmed the crystalline array with measured lattice spacing value d = 0.22 nm attributed to (110) plane of cubic selenium (ICDD no. 38-0768) [5]**.**

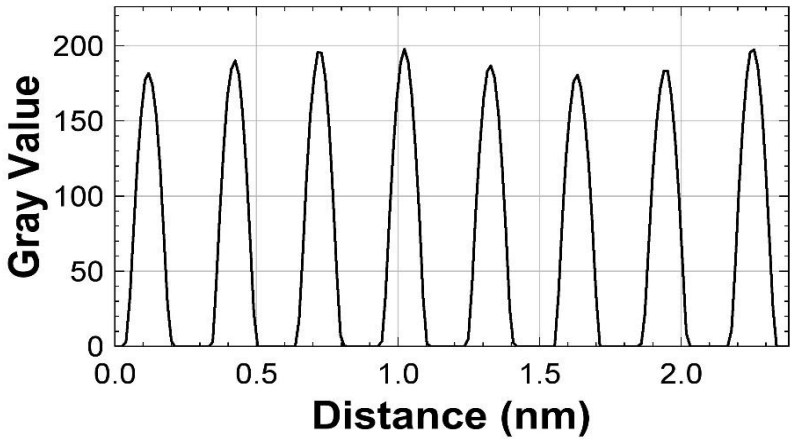

Figure 4.2: Surface plot obtained from corresponding HRTEM of c33.

By processing the parallel lattice fringes in HRTEM images using image J software, surface plots (Fig. 4.2) with respective inter planar spacings were found out as 0.297 nm.

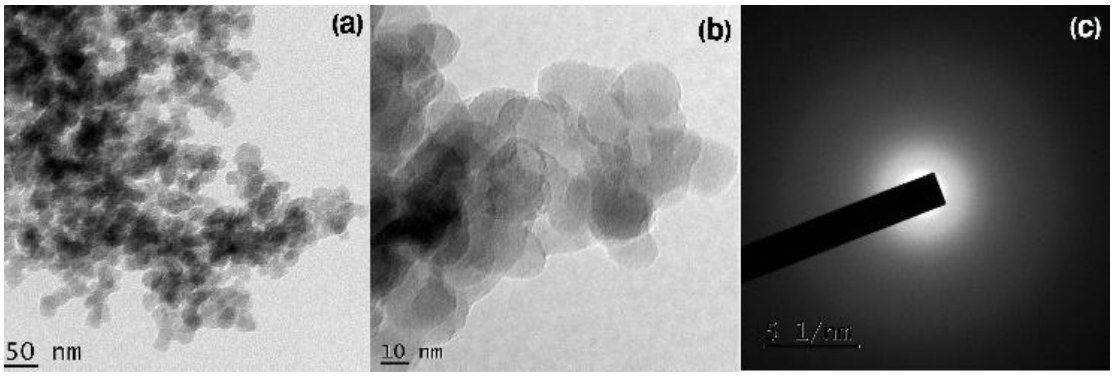

Figure 4.3: TEM (a) and (b) HRTEM (c) SAED pattern of a33.

The TEM and HRTEM image of a33 (Fig. 4.3(a-b), does not contain any lattice fringes and confirms the non- crystalline assemblies of selenium (a-Se). Nearly spherical a-Se

QDs was formed in the silica network. SAED pattern (Fig. 4.3(c), does not show any bright spots, which reaffirms the occurrence of allotropic transition from cubic to amorphous phase in a33. This is in accordance with the phase transition observed in Se-SiO_2 [5], [31].

4.3.2 Energy dispersive X-ray spectroscopy (EDX)

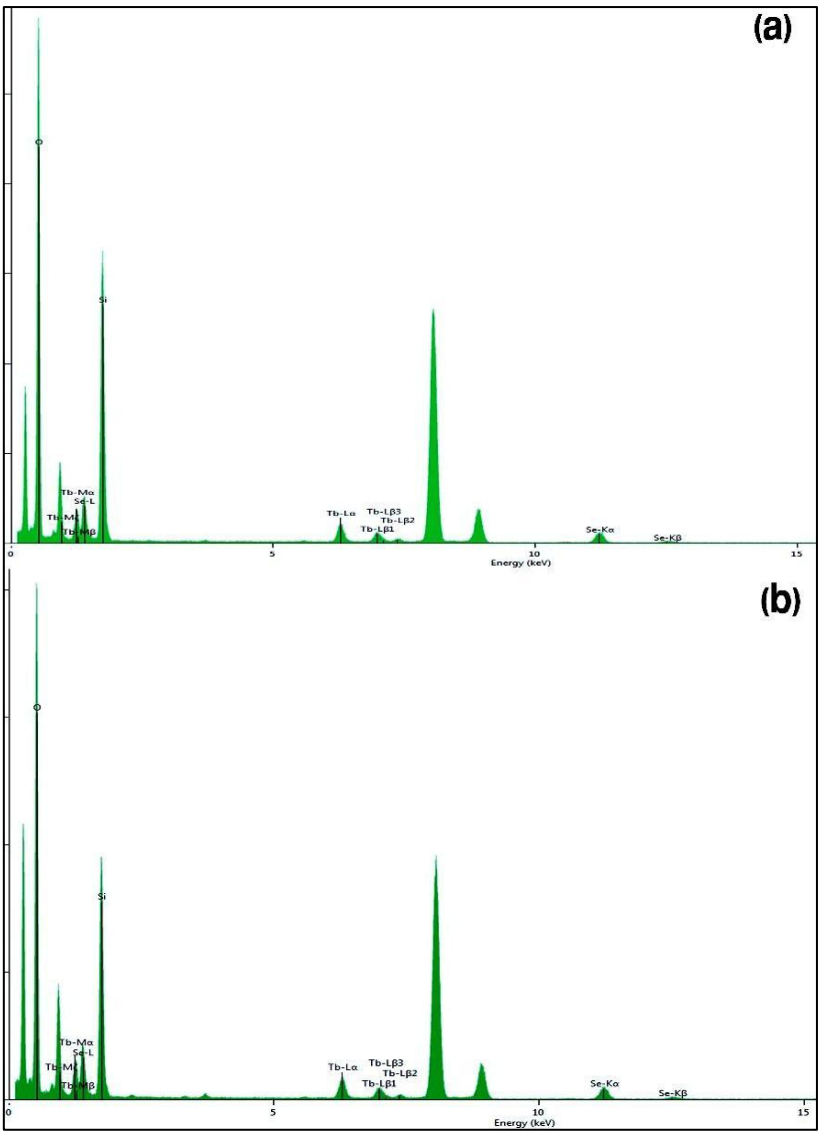

Figure 4.4: EDX spectra of (a) c33 (b) a33.

The elemental composition of c33 and a33 were confirmed with EDX spectrum (Fig. 4.4) which comprises Si, O, Tb, Se. The EDX spectrum of c33 is almost identical to the EDX observations of a33. Three unlabelled peaks located at 0.85, 8.0, 8.9 keV can be assigned as characteristic peak positions associated with the copper [32], [33]with which the TEM grids are fabricated.

4.3.3 Fourier transform infrared spectroscopy (FTIR)

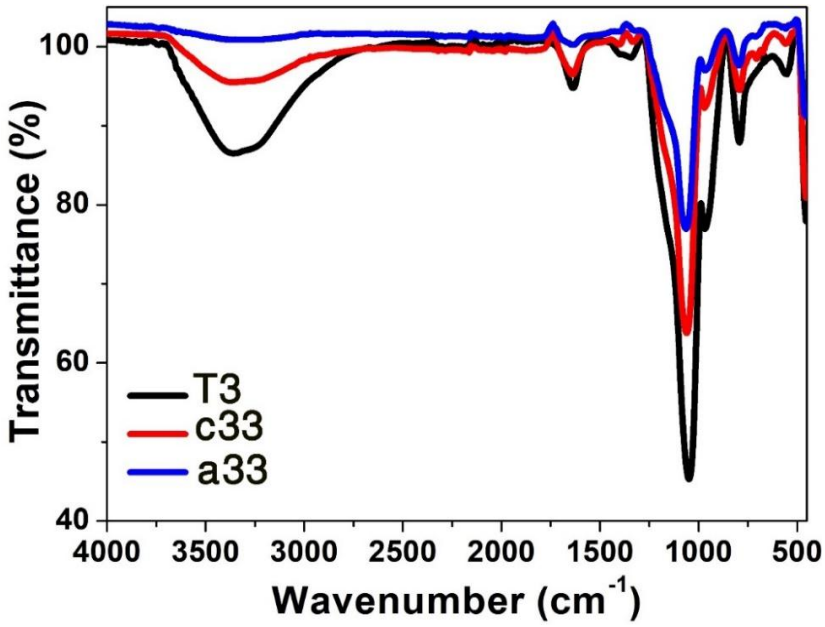

Figure 4.5: FTIR spectra of T3, c33 and a33.

The FT-IR spectra of Se-Tb^{3+} doped SiO_2 composites (as in Fig. 4.5) of 3 w % Se was attained in the wavenumber range of 500−4000 cm^{-1}. FT-IR spectrum resemble with pure SiO_2 spectrum having strong Si–O stretching and bending vibrations [34]. But the intensity of bands fluctuated with the introduction of dopants and thermal treatments of prepared composites. Intense bands occurred at 792 cm^{-1} and 1048 cm^{-1} can be assigned to Si-O symmetric stretching and bending vibrations [3], [35] The broad absorption around 3363 cm^{-1} corresponds to the stretching vibrations of hydroxyl groups. Weak absorption bands at 1644 and 968 cm^{-1} reveals the existence of an oxyethyl group and a feeble peak at 551 cm^{-1} is associated with four membered siloxane ring vibrations within the silica network. Narrow peaks around 1343 cm-1 can be ascribed due to H-O-H bonding [5]. Furthermore, a reduction in the band intensity was remarkably noted with heat treatment. Particularly, bands located at 3363, 1644, 1343, 1048 cm^{-1} have shown a notable dip in intensity with increasing temperature which indicates gradual strengthening via cross linking. Due to the low water content, intensity of broad bands around 3363 cm^{-1} substantially decreased to minimum in a33-silica. After thermal treatments of c33-silica, moisture free a33-silica composites with strong cross-linking forms a tough matrix [5].

4.3.4 Thermal decomposition studies

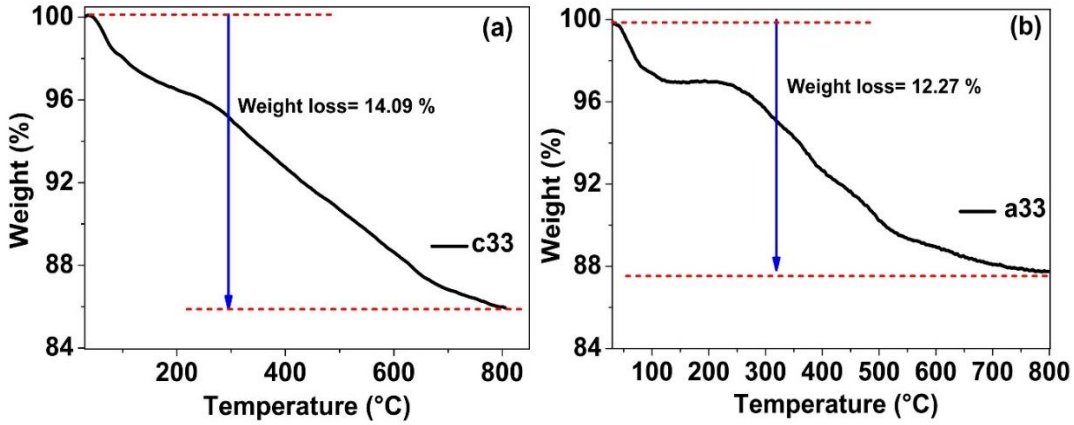

Figure 4.6: TGA curves of (a) c33 (b) a33.

The thermal stability of the Se-Tb^{3+} doped silica were investigated via thermogravimetric analysis (TGA) and differential thermal analysis (DTA). The TGA was performed from room temperature to a maximum of 800 °C at a heating rate of 10 °C/min in the nitrogen atmosphere. TGA thermograms of Se-Tb^{3+} doped silica are given in Fig. 4.6. Initial minor weight loss in c33 and a33 around 100 °C can be due to the removal of moisture content within the composites [36]. TGA curves of the composites revealed that at lower temperatures (100 °C -200 °C), c-Se in c33 begins to decompose while a33 exhibits exceptional thermal stability up to 237 °C. Meanwhile, a33 contains a-Se which decompose only after 235 °C [37]. Furthermore, decomposition process continued in a slow linear path up to 800 ^{0}C in both c33 and a33. When the temperature reached around 800 ^{0}C, 14.09 % of c33 is decomposed whereas, for a33 weight loss percentage at 800 ^{0}C recorded as 12.27 %. Comparatively lower weight loss in a33 is due to the prior loss of water and other volatile components during annealing at 200 ^{0}C. As the reported melting point of Se is around 217 ^{0}C [37] and the TGA analysis performed up to 800 ^{0}C, weight loss in the composites may be mainly due to vaporization than melting. In comparison to previous thermal studies of Se nanoparticles [36], [38] weight loss is minimum for the presented composites due to the encapsulation of dopants within the silica network.

4.3.5 UV-Visible absorption spectra

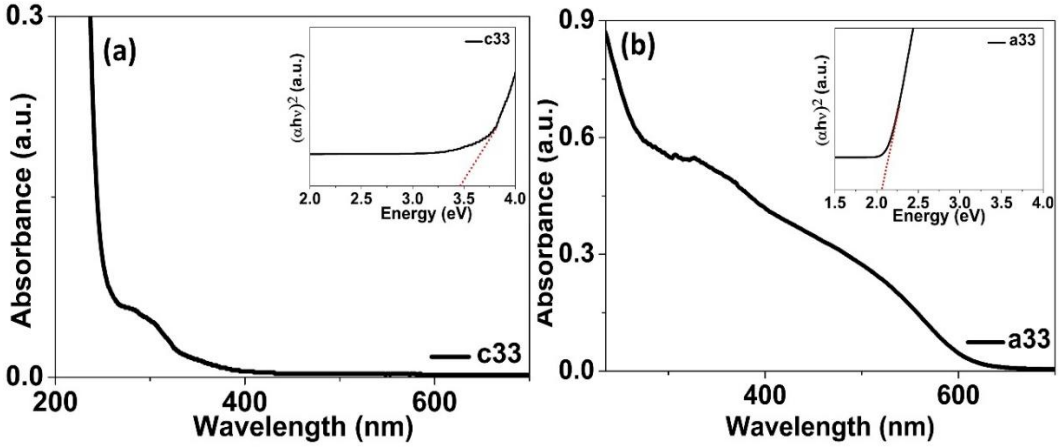

Figure 4.7: UV−visible absorption spectra of (a) c33 (b) a33. The tauc plots given in the insets give bandgaps of 3.46 eV and 2.06 eV respectively.

The absorption spectra of Se-Tb^{3+} doped silica annealed at 60 ^{0}C and 200 ^{0}C are depicted in Fig. 4.7 while c33 composites exhibits feeble absorption at higher wavelength region, a33 composites absorbs wavelength upto 600 nm. Absorption occurs via transitions from LUMO to HOMO levels of the material by absorbing an energy corresponds to the band gap. Herein, the direct band gap of Se-Tb^{3+} composites estimated from tauc plots (insets of Fig. 4.7) are 3.46 eV and 2.06 eV for c33 and a33 respectively which are consistent with the reported band gap energies of c-Se (3.5 eV) and a-Se (2.4 eV) doped silica [5], [39]. Slight decrease in the Eg values can be ascribed to the formation of additional energy levels within the band gap accompanied with defect states induced by Tb^{3+} doping [40]. Also, it is interesting to note that while considering the bulk energy band gap values of crystalline (1.85 eV) and amorphous (1.99 eV) Se, very clear blue shift is originated due to the quantum confinement effect at nanometric scales [41].

4.3.6 Photoluminescence spectra

(i) Phase dependent energy transfer studies

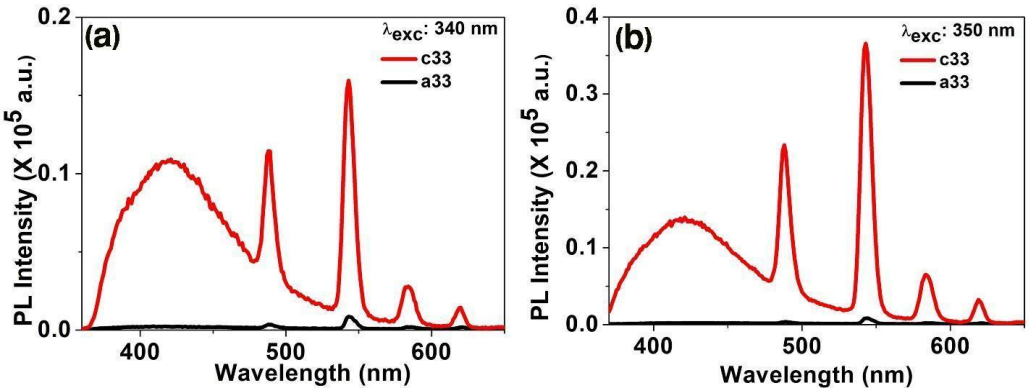

Figure 4.8: PL spectra of c33 and a33 under UV excitation of (a) 340 nm and (b) 350 nm.

Studies regarding the effect of phase transition in Se on fluorescence of composites are conducted in detail. As given in figure 4.8, under UV exposure multiple visible fluorescence bands are originated from Se QDs and RE ions. Bright broad blue fluorescence from c-Se peaked at 421 nm are obtained in combination with narrow luminescence of Tb^{3+} ions at 488 ($5D_4 \rightarrow 7F_6$), 543 ($5D_4 \rightarrow 7F_5$), 584 ($5D_4 \rightarrow 7F_4$), 620 nm ($5D_4 \rightarrow 7F_3$) nm [42]. The most dominant emission band at 543 nm can be assigned as a magnetic dipole transition which can be spotted in the vivid green domain of CIE chart. As per the PL spectra recorded under similar conditions, intense blue green emissions in c33 are not observed in a33. According to literatures, a-Se with a wide absorption band in the visible region has no reported photoluminescence. As absorption band of a-Se overlaps over the emissions of Tb^{3+} ions, intensive emission peaks [5], [41] of Se-Tb^{3+} silica were quenched. As c-Se has a band gap of 3.46 eV and Tb^{3+} ions have prominent excitation from 378 nm to 303 nm. When c-Se absorbs an Energy (E) > 3.46 eV, valence band electrons getting excited via band-to-band transitions and reaches the excited states. Deexcitation process sensitizes the ET to Tb^{3+} ions that results enhanced multiple emissions (given in Fig. 4.10). Distinct optical responses in c33 and a33 strongly supports the phase dependent ET phenomenon among Se QDs and Tb^{3+} ions.

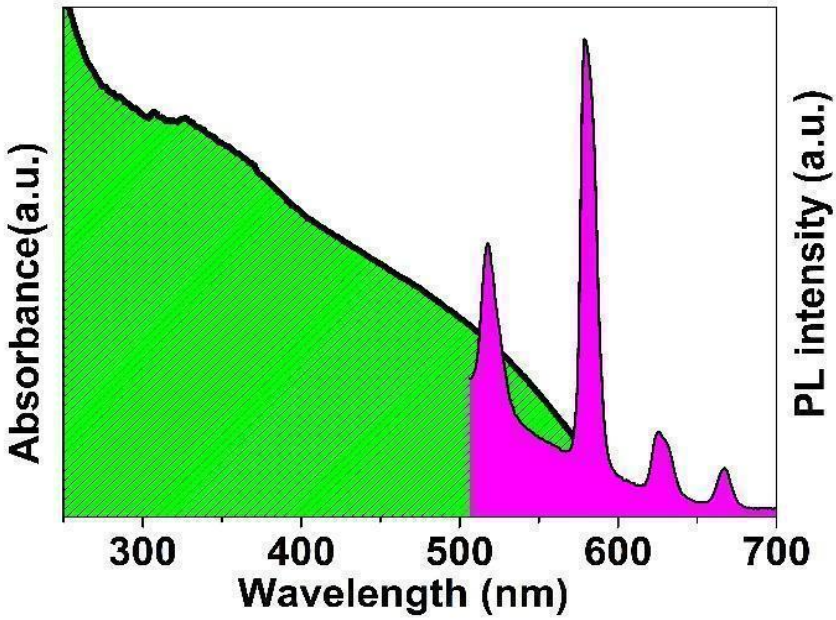

Figure 4.9. Spectral overlap between the absorption spectra of a-Se and emission spectrum of T3.

Fluorescence quenching exhibited by a33 can be further studied from the Fig. 4.9. Absorption curve of a-Se which spans over the entire visible window has an overlap with the characteristic blue-green emissions of Tb^{3+} ions. Then band to band transition in c-Se triggers intense Tb^{3+} emission in c33 while band to band transition of a-Se induces quenching of Tb^{3+}emission intensity in a33. Hence fluorescence of Tb^{3+} ions in a33 is suppressed by the strong absorption of a-Se.

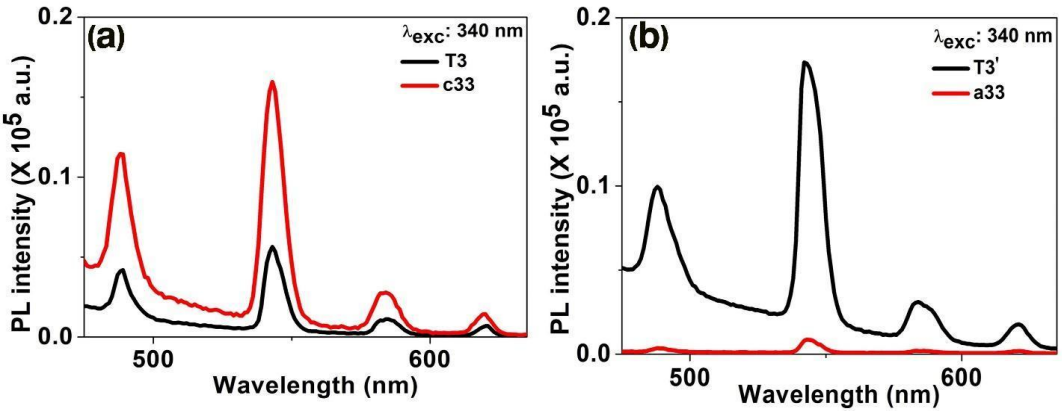

Figure 4.10: PL spectra of Tb^{3+} and Se-Tb^{3+}doped silica (a) heated at 60 ^{0}C (b) heated at 200 ^{0}C under UV excitation of 340 nm.

To analyze the enhancement and quenching of Tb^{3+} emission in a more detailed investigation was done. In comparison to T3 composites, T3$^{'}$ have intense fluorescence bands at 488 nm, 543 nm, 584 nm, 620 nm wavelengths. Fluorescence enhancements of RE ions at higher temperatures are commonly reported which can be ascribed due to

increase in the excitation-deexcitation rates via thermal activation [44]. In contrast, c-Se amplifies the emission bands of c33 at 488 nm, 543 nm, 584 nm, 620 nm in c33. (shown in Fig. 4.10). Interestingly, for c33 the Tb^{3+} fluorescence bands are enhanced while, for a33 the intense Tb^{3+} bands are observed to be quenched. While c-Se amplifies the emission bands of Tb^{3+} at 488 nm, 543 nm, 584 nm, 620 nm a33 attenuates the intensity of Tb^{3+}emission.

(ii) Photoluminescence excitation spectra

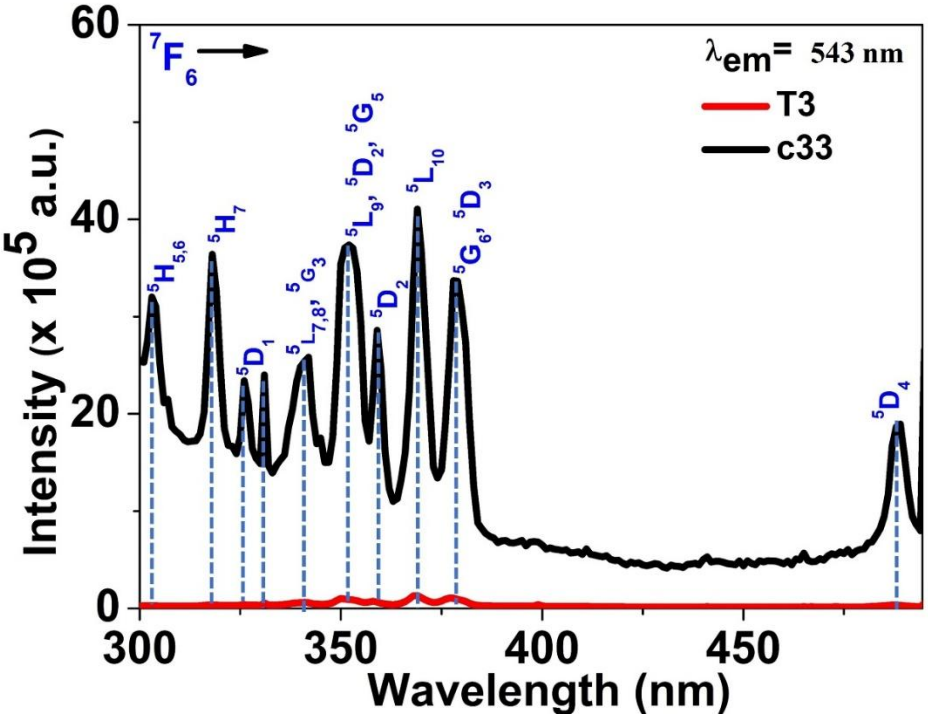

Figure 4.11: Photoluminescence excitation spectra (λ_{em}:543 nm) of T3 and c33.

Furthermore, photoluminescence excitation (PLE) spectra of Tb^{3+}-SiO_2 and Se-Tb^{3+}-SiO_2 was (given in Fig. 4.11) monitored for the characteristic green emission line of Tb^{3+} ion at 543 nm. PLE spectra of Tb-SiO_2 have prominent excitation peaks of Tb^{3+} ions as seen in literatures [43] which are decreasingly ordered in their intensity as 369 nm, 378 nm, 350 nm, 359 nm, 340 nm, 489 nm. Interestingly, upon Se addition, excitation peaks of Tb^{3+} ions are enhanced without any significant spectral shifts. The boosted excitation bands of Tb^{3+} in c33 composites confirmed that Se serves as sensitizer that initiates ET from c-Se QDs to Tb^{3+} ions. For c33, the excitation peaks of Tb^{3+} ions follows the order of decreasing intensity as 369 nm, 350 nm, 378 nm, 318 nm, 303 nm, 359 nm, 340 nm, 331 nm, 325 nm, 489 nm. Furthermore, even the feeble excitation peaks in T3, particularly, at 303 nm and 318 nm, 326 nm, 331 nm now

becomes prominent peaks in c33. By introducing an effective sensitizer c-Se, even the weak far UV excitation bands become highly intense. Simply, excitation probability of RE ions are enormously enhanced in the presence of a suitable sensitizer c-Se. Furthermore broadened excitation band of c-Se at 350 nm in PLE spectrum of c33 is another indication of the role of c-Se as sensitizer [6], [18].

(iii) Energy transfer diagram

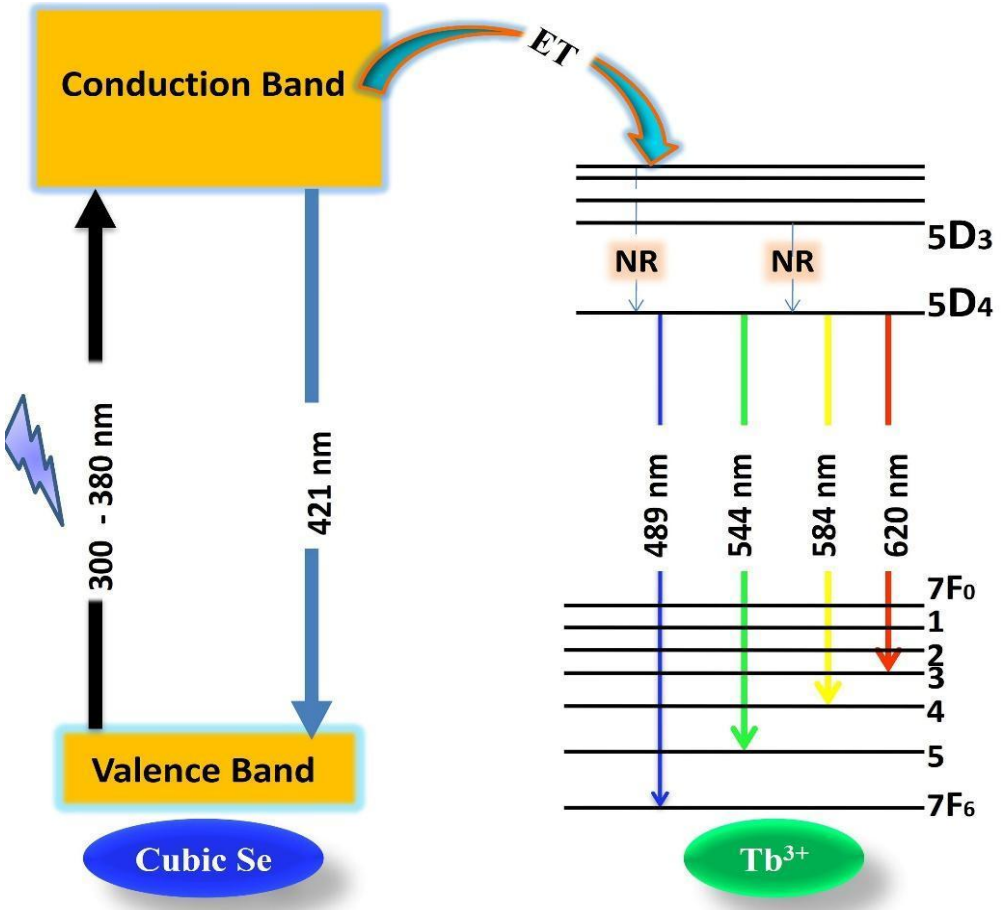

Figure 4.12: Schematic representation of possible energy transfer mechanism between c-Se and Tb^{3+} ions.

Possible ET process within the Se-Tb^{3+}-SiO_2 nanocomposites is depicted in Figure 4.12. The band gap of c-Se is 3.46 eV with absorption edge around 350 nm. When the composites excited at an energy higher than the band gap, inter band transition in c-Se occurs. Along with the blue luminescence from Se QDs and it sensitizes the excited energy levels of Tb^{3+} ions. Thus, strong multicolor Tb^{3+} centred visible emissions are exuded from c33. Apart from this, certain non-radiative transitions like internal conversion occurs within picosecond time scales from various levels to $5D_4$ also take part in the de-excitation process [34].

4.3.7 Fluorescence lifetime decay curves

Fluorescence decay curves of Se-Tb^{3+}-SiO_2 are recorded for the better understanding of ET mechanism among dopants. To investigate how the incorporation of Se QDs influences the Tb^{3+} luminescence, the time correlated single photon counting method (TCSPC) is performed.

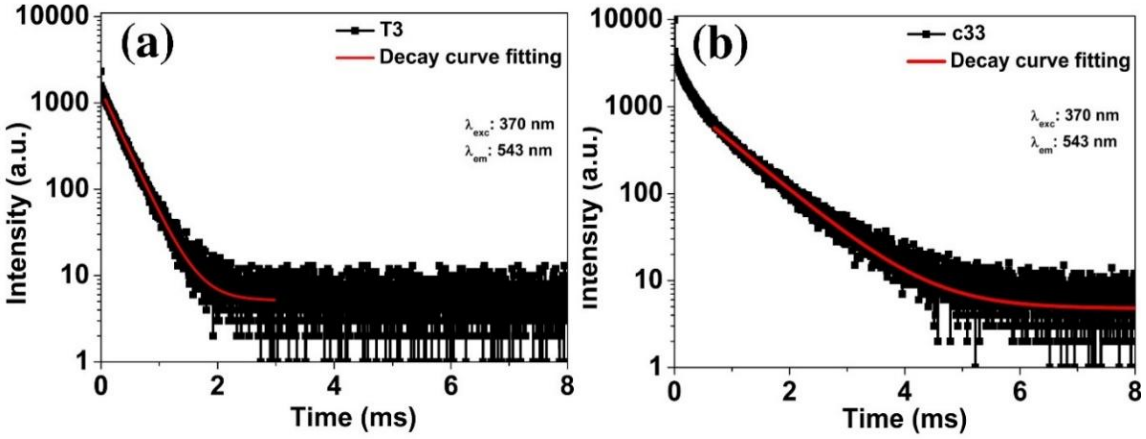

Figure 4.13: Fluorescence lifetime decay curves of T3 and c33.

Obtained decay curves (Fig. 4.13) are successfully fitted with a single exponential law for the two sets of samples (T3, c33) [25], [34]. Decay measurements are performed for the most intense emission located at 543 nm ($5D_4 \rightarrow 7F_5$) by exciting the T3, c33 composites with 370 nm diode laser. The average lifetime of luminescence decay process in T3 is obtained as $\tau_{av} = 0.30$ ms which is much faster than the lifetime of c33 ($\tau_{av} = 0.79$ ms) composites. Comparatively prolonged lifetime values of c33 reveals that c-Se act as sensitizer for enhanced luminescence [18]. In presence of sensitizer, excited states will be highly populated due to the continuous energy flow from sensitizer (Se QDs) to activator (Tb^{3+}) ions. That results in slower decay. Disruptions in the non-radiative decay pathways also contributes in obtaining slow decay for c33.

4.3.8 Colorimetric analysis with CIE Chromaticity diagrams

(i) Excitation dependent photoluminescence studies

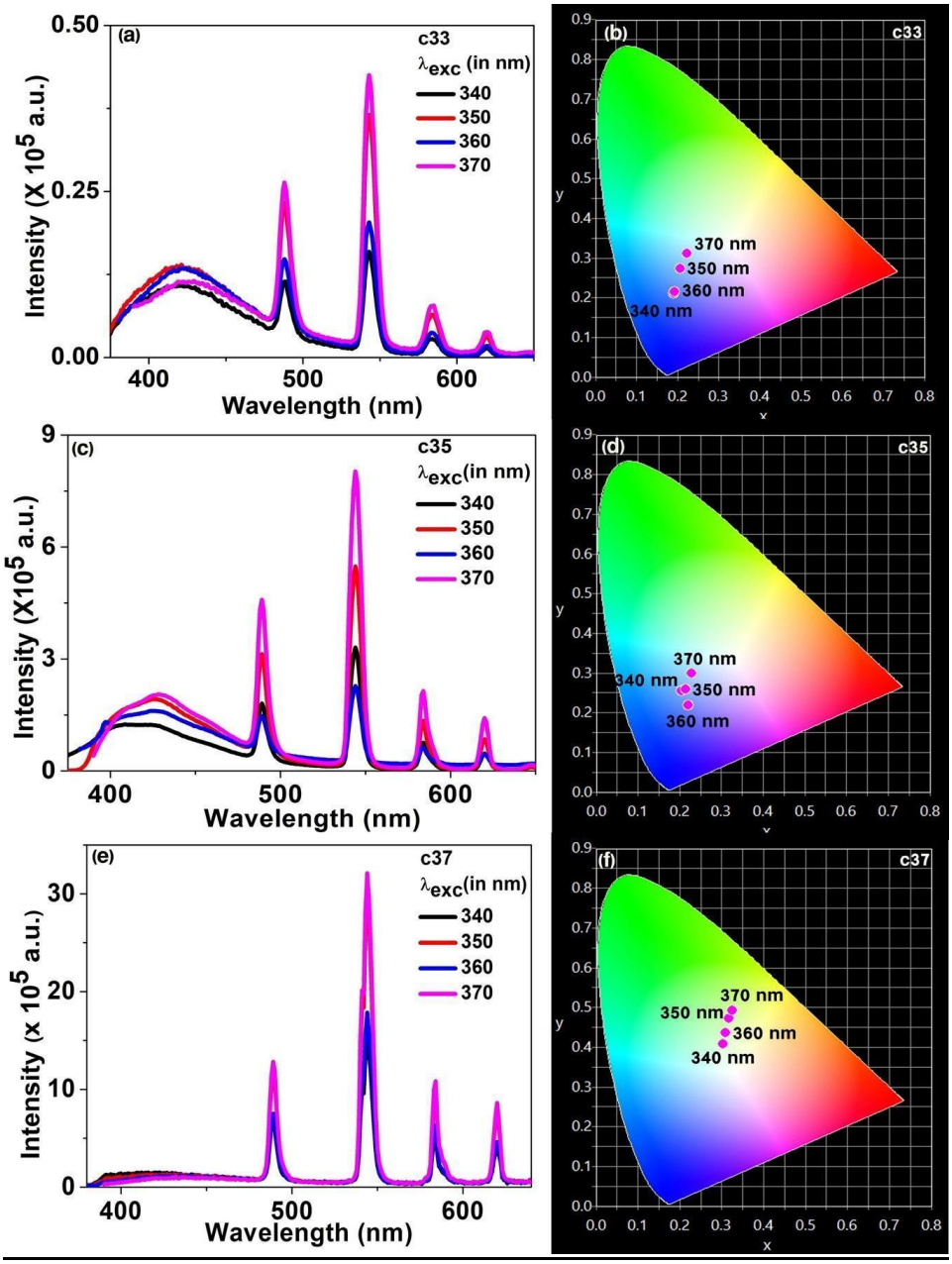

Figure 4.14: Excitation dependent PL spectra and CIE diagrams of c33 (a, b), c35 (c, d), c37 (e, f) under UV excitation vary from 340 nm to 370 nm.

Excitation dependent fluorescence spectra of c33, c35, c37 given in Figure 4.14 shows enhanced emissions with a maximum intensity occurring at 370 nm excitation and no evident spectral shift is observed. Most intense luminescence observed at λ_{exc}= 370 nm are consistent with the dominant excitation band obtained in PLE spectra (Fig. 4.12). As the excitation wavelength varies from 340 nm to 370 nm with an increment of 10

nm, progressive shift in the colorimetric coordinates is obtained. The CIE coordinates of composites for distinct composites and varying excitations were located in different color regions (given in table 4.2). Photoluminescence color tuning (PLCT) is observed in c33 and c35 due to blue to near white emission upon changing the excitation wavelengths. On the other hand, c37 exhibited a PLCT from white to green region due to the highly enhanced Tb^{3+} emissions at higher Se content (3 w%). Under UV excitation of 340 nm c37 shows a cool white emission with CCT value of 6426 K.

Table 4.2: Excitation wavelength, CIE indices, color region of Se-Tb^{3+} doped silica.

Sample code	Excitation wavelength (in nm)	CIE Index	Color region
c33	340	(0.1913, 0.2109)	Blue
c33	350	(0.2073, 0.2731)	Cyan
c33	360	(0.1918, 0.2142)	Blue
c33	370	(0.2233, 0.3113)	Near white
c35	340	(0.2043, 0.2550)	Light blue
c35	350	(0.2148, 0.2596)	Light blue
c35	360	(0.2211, 0.2185)	Blue
c35	370	(0.2291, 0.2995)	Near white
c37	340	(0.3040, 0.4074)	White
c37	350	(0.3169, 0.4720)	Near white
c37	360	(0.3100, 0.4350)	Near white
c37	370	(0.3245, 0.4923)	Green

(ii) Concentration dependent photoluminescence studies

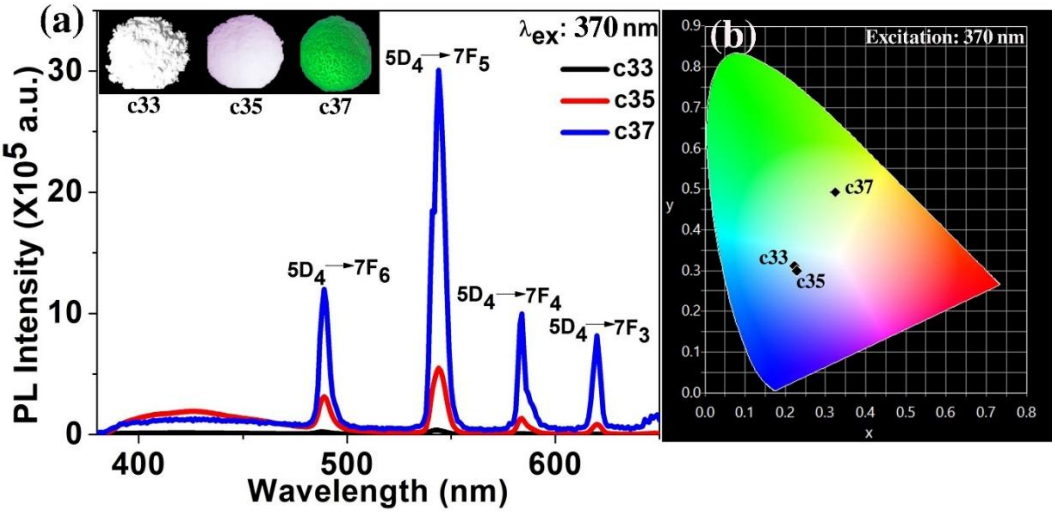

Figure 4.15. (a) PL spectra of Se-Tb^{3+}doped silica with varying concentrations of Se (c33, c35, c37) under UV excitation of 370 nm (inset image: the photograph of c33, c35, c37 kept under UV light of 365 nm) (b) corresponding CIE chromaticity diagrams.

Figure 4.15 shows PL spectra of composites having similar RE content with increasing concentration of Se. ET pathways directed from c-Se QDs to Tb^{3+} ions are clearly understood from the PL spectra of composite series when (c33, c35, c37) excited at 370 nm wavelength. The narrow emission peaks of Tb^{3+} ions are intensified with the increase of c-Se concentration. Enhanced Tb^{3+} luminescence exhibited in the composites (c33, c35, c37) having fixed Tb^{3+} ion concentration implies that efficient ET occurs from c-Se in an ordered manner with increasing Se concentration. Proportional increase in the sensitizer (c-Se) concentration resulted in shifted fluorescence from near white (0.2233, 0.3113) to alluring green (0.3245, 0.4923) region with respective CIE indices. Additionally, from photographs given in the inset of Fig. 4.15 (a) visual color difference achieved upon increasing the sensitizer concentration are clearly presented. Thus, the sensitizer c-Se act as energy donor and the activator Tb^{3+} ions plays the role of an acceptor in the ET process. All the composites show increase in Tb^{3+}emission without increase in the RE concentration. This is highly appreciable in both economic and environmental point of view as RE ions are expensive and toxic at large amounts.

4.4 Conclusion

In summary, we studied Se-Tb^{3+} based SiO_2 nanocomposites that exhibit unique phase dependent optical features with switchable spectral characteristics. Cubic to amorphous

phase transition of Se in the composites achieved via annealing process determine the spectral characteristics of the composites. For cubic Se-Tb^{3+} composites, intensive Tb^{3+} luminescence is obtained due to the presence of c-Se. Enhanced ET channels is affirmed from the increased fluorescence lifetime values in c33 (τ_{av} = 0.79 ms) than T3 (τ_{av} = 0.30 ms). Meanwhile, when Se exists in amorphous phase, it results in fluorescence quenching of Tb^{3+} ions. For composites with same RE concentration (c33, c35, c37), a dramatic increase in the PL intensity of Tb^{3+} ions are observed at elevated Se concentrations. Under UV excitation of 370 nm wavelength, tunable fluorescence from white to green region observed can be further utilized in designing multicolor emitting devices.

References

[1] P. M. Tan *et al.*, "New insights on the energy transfer mechanisms of Eu-doped CdS quantum dots," *Phys. Chem. Chem. Phys.*, vol. 22, no. 11, pp. 6266–6274, Mar. 2020, doi: 10.1039/C9CP06778G.

[2] M. A. Ruiz-Fresneda, L. C. Staicu, G. Lazuén-López, and M. L. Merroun, "Allotropy of selenium nanoparticles: Colorful transition, synthesis, and biotechnological applications," *Microbial Biotechnology*, vol. n/a, no. n/a, doi: 10.1111/1751-7915.14209.

[3] K. Anupama, T. Paul, and K. A. Ann Mary, "Solid-State Fluorescent Selenium Quantum Dots by a Solvothermal-Assisted Sol–Gel Route for Curcumin Sensing," *ACS Omega*, vol. 6, no. 33, pp. 21525–21533, Aug. 2021, doi: 10.1021/acsomega.1c02441.

[4] L. Properzi, A. Polian, P. Munsch, and A. Di Cicco, "Investigation of the phase diagram of selenium by means of Raman spectroscopy," *High Pressure Research*, vol. 33, no. 1, pp. 35–39, Mar. 2013, doi: 10.1080/08957959.2013.769048.

[5] K. A. A. Mary, N. V. Unnikrishnan, and R. Philip, "Cubic to amorphous transformation of Se in silica with improved ultrafast optical nonlinearity," *RSC Adv.*, vol. 5, no. 18, pp. 14034–14041, Jan. 2015, doi: 10.1039/C4RA14025G.

[6] M. Zhang *et al.*, "When rare earth meets carbon nanodots: mechanisms, applications and outlook," *Chem. Soc. Rev.*, vol. 49, no. 24, pp. 9220–9248, Dec. 2020, doi: 10.1039/D0CS00462F.

[7] K. Binnemans, "Lanthanide-Based Luminescent Hybrid Materials," *Chem. Rev.*, vol. 109, no. 9, pp. 4283–4374, Sep. 2009, doi: 10.1021/cr8003983.

[8] P. Du, X. Wan, L. Luo, W. Li, and L. Li, "Thermally Stable Tb^{3+}/Eu^{3+}-Codoped $K_{0.3}Bi_{0.7}F_{2.4}$ Nanoparticles with Multicolor Luminescence for White-Light-Emitting Diodes," *ACS Appl. Nano Mater.*, vol. 4, no. 7, pp. 7062–7071, Jul. 2021, doi: 10.1021/acsanm.1c01072.

[9] Pushpendra, R. K. Kunchala, S. N. Achary, and B. S. Naidu, "$NaBi_{0.9}Eu_{0.1}(MoO_4)_2$ Nanomaterials: Tailoring the Band Gap and Luminescence by La^{3+} Substitution for Light-Emitting Diodes," *ACS Appl. Nano Mater.*, vol. 2, no. 9, pp. 5527–5537, Sep. 2019, doi: 10.1021/acsanm.9b01111.

[10] P. Du, W. Ran, Y. Hou, L. Luo, and W. Li, "Eu^{3+}-Activated $NaGdF_4$ Nanorods for Near-Ultraviolet Light-Triggered Indoor Illumination," *ACS Appl. Nano Mater.*, vol. 2, no. 7, pp. 4275–4285, Jul. 2019, doi: 10.1021/acsanm.9b00743.

[11] M. A. van de Haar, A. C. Berends, M. R. Krames, L. Chepyga, F. T. Rabouw, and A. Meijerink, "Eu^{3+} Sensitization via Nonradiative Interparticle Energy Transfer Using Inorganic Nanoparticles," *J. Phys. Chem. Lett.*, vol. 11, no. 3, pp. 689–695, Feb. 2020, doi: 10.1021/acs.jpclett.9b03764.

[12] A. G. Bispo-Jr, S. A. M. Lima, and Ana. M. Pires, "Energy transfer between terbium and europium ions in barium orthosilicate phosphors obtained from sol-gel route," *Journal of Luminescence*, vol. 199, pp. 372–378, Jul. 2018, doi: 10.1016/j.jlumin.2018.03.057.

[13] P. Li *et al.*, "Nanocrystalline structure control and tunable luminescence mechanism of Eu-doped $CsPbBr_3$ quantum dot glass for WLEDs," *Nanoscale*, vol. 12, no. 12, pp. 6630–6636, Mar. 2020, doi: 10.1039/D0NR01207F.

[14] L. J. Charbonnière, N. Hildebrandt, R. F. Ziessel, and H.-G. Löhmannsröben, "Lanthanides to Quantum Dots Resonance Energy Transfer in Time-Resolved Fluoro-Immunoassays and Luminescence Microscopy," *J. Am. Chem. Soc.*, vol. 128, no. 39, pp. 12800–12809, Oct. 2006, doi: 10.1021/ja062693a.

[15] Q. Wang, G. Chen, Z. Yu, X. Ouyang, J. Tian, and M. Yu, "Photoluminescent Composites of Lanthanide-Based Nanocrystal-Functionalized Cellulose Fibers for Anticounterfeiting Applications," *ACS Sustainable Chem. Eng.*, vol. 6, no. 11, pp. 13960–13967, Nov. 2018, doi: 10.1021/acssuschemeng.8b02307.

[16] A. A. Ansari, A. K. Parchur, B. Kumar, and S. B. Rai, "Highly aqueous soluble CaF_2:Ce/Tb nanocrystals: effect of surface functionalization on structural, optical band gap, and photoluminescence properties," *J Mater Sci: Mater Med*, vol. 27, no. 12, p. 178, Oct. 2016, doi: 10.1007/s10856-016-5791-5.

[17] M. Odziomek, F. Chaput, F. Lerouge, M. Sitarz, and S. Parola, "Highly luminescent YAG:Ce ultra-small nanocrystals, from stable dispersions to thin films," *J. Mater. Chem. C*, vol. 5, no. 47, pp. 12561–12570, Dec. 2017, doi: 10.1039/C7TC03504G.

[18] T. Samanta, C. Hazra, and V. Mahalingam, "C-dot sensitized Eu^{3+} luminescence from Eu^{3+} -doped LaF_3 –C dot nanocomposites," *New Journal of Chemistry*, vol. 39, no. 1, pp. 106–109, 2015, doi: 10.1039/C4NJ01647E.

[19] H. Dong, A. Kuzmanoski, D. M. Gößl, R. Popescu, D. Gerthsen, and C. Feldmann, "Polyol-mediated C-dot formation showing efficient Tb^{3+}/Eu^{3+} emission," *Chem. Commun.*, vol. 50, no. 56, pp. 7503–7506, Jun. 2014, doi: 10.1039/C4CC01715C.

[20] J. Y. Park *et al.*, "Structural and optical properties of ZnSe:Eu/ZnS quantum dots depending on interfacial residual europium," *Applied Surface Science*, vol. 429, pp. 225–230, Jan. 2018, doi: 10.1016/j.apsusc.2017.09.018.

[21] J.-F. Gao, J.-H. Yang, X.-Y. Zhang, J. Zhao, X.-W. Liu, and B.-F. Shi, "Synthesis and fluorescence properties of CdTe:Eu^{3+} nanocrystals and core–shell SiO_2-coated CdTe:Eu^{3+} nanospheres," *Rare Met.*, vol. 38, no. 10, pp. 989–995, Oct. 2019, doi: 10.1007/s12598-018-1180-1.

[22] Q. Huo, W. Tu, and L. Guo, "Enhanced photoluminescence property and broad color emission of $ZnGa2O_4$ phosphor due to the synergistic role of Eu^{3+} and carbon dots," *Optical Materials*, vol. 72, pp. 305–312, Oct. 2017, doi: 10.1016/j.optmat.2017.06.013.

[23] M. A. Tshabalala, H. C. Swart, and O. M. Ntwaeaborwa, "TOF SIMS analysis and generation of white photoluminescence from strontium silicate codoped with europium and terbium," *Journal of Vacuum Science & Technology A*, vol. 32, no. 2, p. 021401, Mar. 2014, doi: 10.1116/1.4862752.

[24] V. Singh and A. K. Mishra, "White light emission from vegetable extracts.," *Scientific Reports*, vol. 5, no. 1, June 2015, doi: 10.1038/srep111182015.

[25] C. Armellini, M. Ferrari, M. Montagna, G. Pucker, C. Bernard, and A. Monteil, "Terbium(III) doped silica-xerogels: effect of aluminium(III) co-doping," *Journal of Non-Crystalline Solids*, vol. 245, no. 1, pp. 115–121, Apr. 1999, doi: 10.1016/S0022-3093(98)00856-4.

[26] G. Jose, T. Teddy Fernandez, C. Joseph, and M. Ittyachen, "Display Application of CdSe Nanocrystallites/Eu^{3+},Tb^{3+} Ions in Sol-Gel Glasses". *Photonics-2004:* 7th International Conference on Fiber Optics and Photonics. 2004

[27] G. Jose, G. Jose, V. Thomas, C. Joseph, M. A. Ittyachen, and N. V. Unnikrishnan, "Optical Characterization of Eu^{3+} Ions in CdSe Nanocrystal Containing Silica Glass," *Journal of Fluorescence*, vol. 14, no. 6, pp. 733–738, Nov. 2004, doi: 10.1023/B:JOFL.0000047223.82811.4c.

[28] G. Jose *et al.*, "Radiative parameters of Eu^{3+} ions in CdSe nanocrystal containing silica matrices," *Physica B: Condensed Matter*, vol. 357, no. 3, pp. 270–276, Mar. 2005, doi: 10.1016/j.physb.2004.11.075.

[29] Jyothy, P. V., et al., "Optical characterization of CdSe/Dy^{3+}-doped silica matrices", *Pramana*, pp. 999-1004, Dec. 2010, doi: 10.1007/s12043-010-0187-4

[30] S. Mathew, P. R. Rejikumar, X. Joseph, and N. V. Unnikrishnan, "Optical studies on Eu^{3+}/ZnSe nanocrystal in silica hosts," *Optical Materials*, vol. 29, no. 12, pp. 1689–1692, Aug. 2007, doi: 10.1016/j.optmat.2006.09.014.

[31] V. S. Minaev, S. P. Timoshenkov, and V. V. Kalugin, "Structural and phase transformations in condensed selenium". *Journal of Optoelectronics and Advanced Materials,* vol. 7, no. 4, pp.1717, Aug. 2005.

[32] M. A. Amin, "Weight loss, polarization, electrochemical impedance spectroscopy, SEM and EDX studies of the corrosion inhibition of copper in aerated NaCl solutions," *J Appl Electrochem*, vol. 36, no. 2, pp. 215–226, Feb. 2006, doi: 10.1007/s10800-005-9055-1.

[33] X. W. Ang, V. S. Sethu, J. M. Andresen, and M. Sivakumar, "Copper(II) ion removal from aqueous solutions using biosorption technology: thermodynamic and SEM–EDX studies," *Clean Techn Environ Policy*, vol. 15, no. 2, pp. 401–407, Apr. 2013, doi: 10.1007/s10098-012-0523-0.

[34] S. Gopi *et al.*, "Tunable green to red emission via Tb sensitized energy transfer in Tb/Eu co-doped alkali fluoroborate glass," *Journal of Luminescence*, vol. 192, pp. 1288–1294, Dec. 2017, doi: 10.1016/j.jlumin.2017.09.009.

[35] M. Epifani, G. De, A. Licciulli, and L. Vasanelli, "Preparation of uniformly dispersed copper nanocluster doped silica glasses by the sol–gel process," *J. Mater. Chem.*, vol. 11, no. 12, pp. 3326–3332, Nov. 2001, doi: 10.1039/B101059J.

[36] M. Safaei, H. R. Mozaffari, H. Moradpoor, M. M. Imani, R. Sharifi, and A. Golshah, "Optimization of Green Synthesis of Selenium Nanoparticles and Evaluation of Their Antifungal Activity against Oral Candida albicans Infection," *Advances in Materials Science and Engineering*, vol. 2022, no. 1, p. 1376998, 2022, doi: 10.1155/2022/1376998.

[37] A. A. Jadhav and P. K. Khanna, "Impact of microwave irradiation on cyclo-octeno-1,2,3-selenadiazole: formation of selenium nanoparticles and their polymorphs," *RSC Adv.*, vol. 5, no. 56, pp. 44756–44763, May 2015, doi: 10.1039/C5RA05701A.

[38] N. O. San Keskin, O. Akbal Vural, and S. Abaci, "Biosynthesis of Noble Selenium Nanoparticles from Lysinibacillus sp. NOSK for Antimicrobial, Antibiofilm Activity, and Biocompatibility," *Geomicrobiology Journal*, vol. 37, no. 10, pp. 919–928, Oct. 2020, doi: 10.1080/01490451.2020.1799264.

[39] K. A. Ann Mary, N. V. Unnikrishnan, and R. Philip, "Ultrafast optical nonlinearity in nanostructured selenium allotropes," *Chemical Physics Letters*, vol. 588, pp. 136–140, Nov. 2013, doi: 10.1016/j.cplett.2013.09.069.

[40] I. Apostolova, A. Apostolov, and J. Wesselinowa, "Band Gap Tuning in Transition Metal and Rare-Earth-Ion-Doped TiO_2, CeO_2, and SnO_2 Nanoparticles," *Nanomaterials*, vol. 13, no. 1, Art. no. 1, Jan. 2023, doi: 10.3390/nano13010145.

[41] A. K. Bhatnagar, K. V. Reddy, and V. Srivastava, "Optical energy gap of amorphous selenium: effect of annealing," *J. Phys. D: Appl. Phys.*, vol. 18, no. 9, p. L149, Sep. 1985, doi: 10.1088/0022-3727/18/9/001.

[42] P. C. Ricci, C. M. Carbonaro, R. Corpino, C. Cannas, and M. Salis, "Optical and Structural Characterization of Terbium-Doped Y_2SiO_5 Phosphor Particles," *J. Phys. Chem. C*, vol. 115, no. 33, pp. 16630–16636, Aug. 2011, doi: 10.1021/jp203523s.

[43] I. Koseva, P. Tzvetkov, P. Ivanov, A. Yordanova, and V. Nikolov, "Terbium and europium co-doped $NaAlSiO_4$ nano glass-ceramics for LED application," *Optik*, vol. 137, pp. 45–50, May 2017, doi: 10.1016/j.ijleo.2017.02.098.

[44] X. Wang, Q. Liu, Y. Bu, C.-S. Liu, T. Liu, and X. Yan, "Optical temperature sensing of rare-earth ion doped phosphors," *RSC Advances*, vol. 5, no. 105, pp. 86219–86236, 2015, doi: 10.1039/C5RA16986K.

[45] H. Sahoo, "Förster resonance energy transfer – A spectroscopic nanoruler: Principle and applications," *Journal of Photochemistry and Photobiology C: Photochemistry Reviews*, vol. 12, no. 1, pp. 20–30, Mar. 2011, doi: 10.1016/j.jphotochemrev.2011.05.001.

[46] R. Pratap, V. Vishal, S. Chaudhary, and A. Singh Parmar, "Fabrication of white light emitting diodes via high yield surface passivated carbon quantum dots doped with terbium," *RSC Advances*, vol. 13, no. 3, pp. 1974–1984, 2023, doi: 10.1039/D2RA07890B.

5

Carbon Quantum Dots-Tb^{3+} Doped Silica for Multicolor Emitting Applications

We synthesized carbon quantum dots (CQDs) showing excitation dependent emission through environmentally- friendly one-step solvothermal route. TEM micrographs confirmed the formation of carbon quantum dots with graphitic cores with an average core size of 3.5 nm. At 370 nm excitation wavelength, significant luminescence quenching is produced by Fe^{3+} and Cu^{2+} ions. Besides, optical profiles of CQDs opens up its possibility in anti-counterfeiting and data storage applications as invisible security ink. Moreover, CQD-Tb^{3+} embedded silica are fabricated with efficient spectral tuning over the entire visible spectrum. Under broad UV excitation wavelengths, CQD-Tb^{3+} glasses exhibit color tuning from blue (0.1952, 0.2328) to near white region (0.2201, 0.3106) which illustrates the photo luminescence color tuning (PLCT) behavior. The results facilitate the potential application of multicolor-emissive CQDs to develop solid multicolor emitting displays and panels.

Graphical abstract

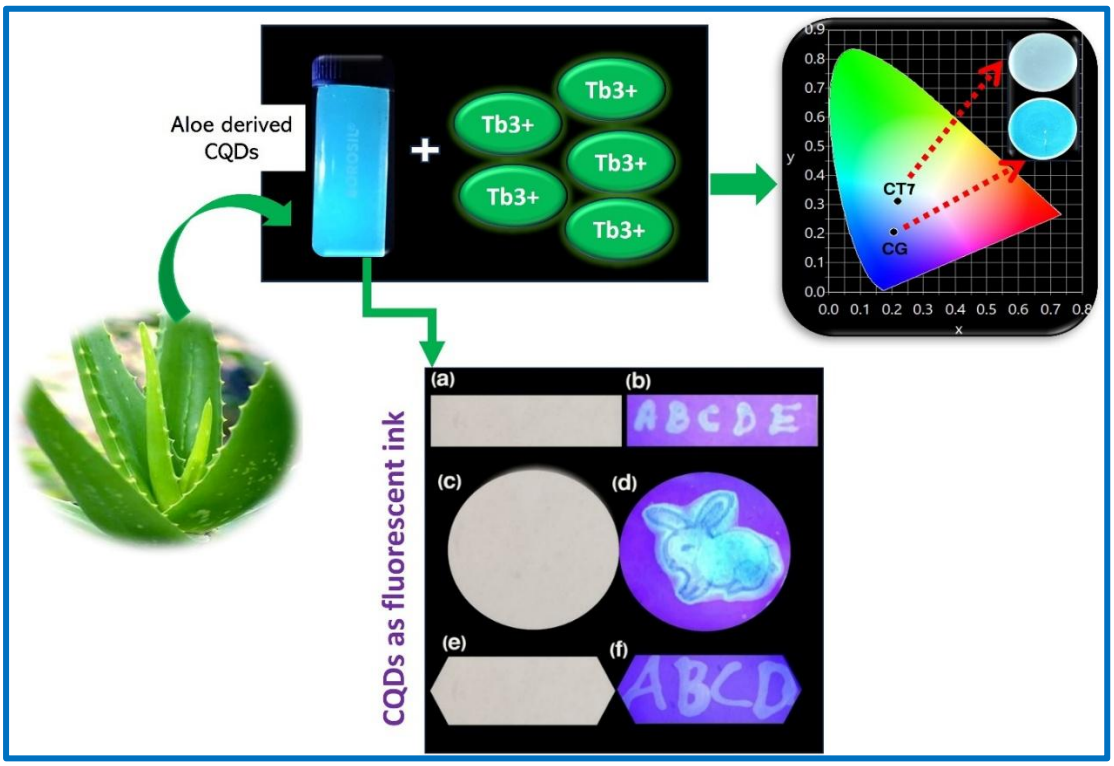

5.1 Introduction

For last few decades, rare earth (RE) based luminescent materials having sharp visible emissions due to discrete 4f-4f transitions excelled in applications such as LEDs, bioanalysis platforms, solar cell light converters, fluorescent sensing probes [1]. However, their spectrum of applications is limited to a narrow regime due to weak absorption cross sections (10^{-18} cm^2) linked with intra-4f transitions and thin, precise excitation bands [1]. Establishing energy transfer channels by the introduction of a donor-acceptor (D-A) pair is a key way to vanish those parity limitations [2], [3]. To widen the spectral window of luminescence, RE ions are combined with conventional QDs (quantum dots) having broader energy band gaps associated with respective energy level transitions. Numerous efforts are already reported on preparation of multicolor emissive materials combining inorganic QDs, rare-earth ions and organic luminescent dyes [4]. RE-QD compositions of Gd^{3+} - Ag_2S luminescent material shows enhanced IR fluorescence [5]. Moreover, RE -PbS QDs are reported for their enhanced up conversion efficiency [6]. Furthermore, attempts to broaden the excitation bands of RE ions resulted in enhanced luminescence in $YVO_4:Eu^{3+}$ by the presence of CdTe QDs [1]. Expensive synthesis routes with potential toxicity of selenium and cadmium necessitate the replacement of QDs like CdTe, CdSe with alternate solutions [7], [8]. Apart from their wide spectrum tunability, high toxicity and water insolubility, traditional QDs reduces its success rate in their practical application and commercial production [4].

Carbon based nanostructures became a thriving topic of discussion for the research community due to its embracing structural and optical diversity with multifunctional applications. Weak fluorescence with low solubility of carbon at macroscale completely reversed in the nano carbon world. Diverse carbon nanostructures, such as carbon nanotubes (CNTs) [9], fullerenes [10], nanodiamonds [11] and carbon quantum dots (CQDs) [12] acquired tremendous attention due to their unique structural and optical characteristics. Typically, carbon quantum dots are adorned with a list of exceptional qualities such as high solubility, easy surface functionalization, and strong resistance towards photobleaching [13]. Importantly, large two photon cross section areas of CQDs open up their applications in light

emitting platforms. On the other hand, CQDs are also reliable for bio applications due to their low toxicity and excellent biocompatibility [12]. Favorable optical parameters of CQDs like excitation wavelength dependent photoluminescence [14], prolonged lifetimes and good quantum yield (QY) are utilized commonly in the designing of sensors and bioimaging platforms [15], [16].

Notably, enthusiastic research efforts in designing RE-CQD hybrid materials progressed considerably for a broad range of application [17], [18]. According to literatures, mere physical mixing of RE ions with CQDs could not generate intense RE emissions. To explore energy transfer studies in RE-CQD solutions, strategic ways have to be considered to minimize nonradiative transition. Otherwise, quenching of RE^{3+} emission occurs due to high-energy vibration of O–H in aqueous solution [2]. Luminescence quenching can also explainable on the basis of coupling between -OH groups within CQD solutions and excitonic states of RE ions [19]. Other severe drawbacks such as gradual ageing associated with self- absorption loss, non-portability, low thermal stability hinders its potential applications. This can be overcome by creating rigid environment by incorporating RE^{3+} ions incorporated in solid PVA, PMMA films and glassy matrices. Enhanced Eu emissions were achieved via $ZnGa_2O_4:Eu^{3+}$ based fabrication routes affirms the necessity of solid matrix that assures excellent fluorescence performance [20]. Optimized compositional ratios of rare earth dopants (Eu^{3+} and Tb^{3+}) and carbon nanoparticles in PMMA matrix results excellent white light emitting films [21]. RE-CQD (RE = Eu^{3+}, Tb^{3+}) silica hybrid material for white light emissions with adjustable CCTs was recently reported from our group [14]. Appreciable shelf life of white light emitting material over 1 year affirms the stable optical performance of RE-CQD-SiO_2 composites over solution mixtures [14]. By combining the surface passivated CQDs with RE ions (Eu^{3+}, $Sm^{3+,}$ Yb^{3+}) shift in the emission chromaticity up to NIR region was acquired with photoluminescence color tuning (PLCT) [2].

Herein, we strategize to achieve a cost effective, easy to process, solid multicolor emitting platform from CQD: xTb^{3+} (x = 3, 5, 7 w %) based compositions @silica. The luminescence of CQDs is exploited to design fluorescent security ink for data storage and anticounterfeit application. Photoluminescence color tuning (PLCT) for CQD-Tb^{3+}glasses is obtained upon broad range of UV excitations. The CQD-RE silica hybrids act as a potential candidate for color display and solid lighting applications.

5.2 Experimental section

5.2.1 Synthesis of carbon quantum dots (CQDs)

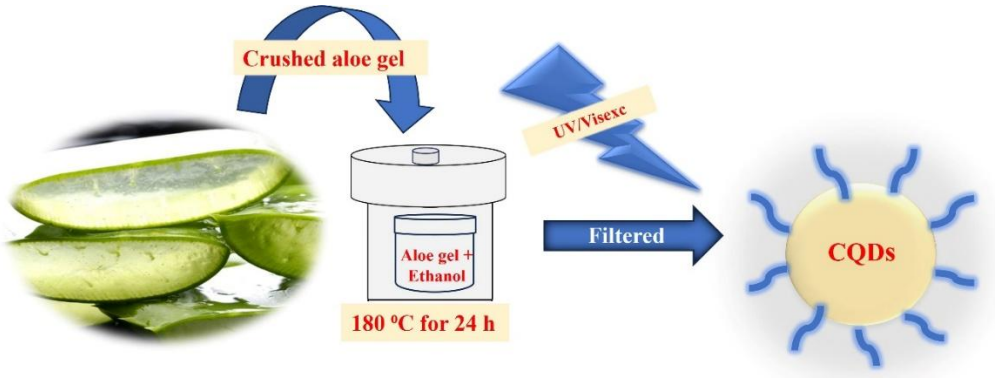

Figure 5.1: Synthesis diagram of aloe derived carbon quantum dots (CQDs).

The CQDs were synthesized by the solvothermal treatment of ethanolic aloe vera gel solutions. Synthesis process was performed as depicted in Figure 5.1. Well cleaned aloe vera leaves were chopped into small pieces and the jelly portion was scratch out. 15 g of solid gel pieces were crushed into a juicy form and mixed with 25 ml of ethanol. The mixture is stirred well and then transferred in a 50 ml Teflon lined autoclave. The autoclave was placed in a hot air oven at 180 °C for 24 h. After naturally cooling down to room temperature, the obtained brownish solution was filtered to avoid the presence of unreacted organic moieties.

5.2.2 Preparation of metal ion solutions

Solutions of various metal ions (Cd^{2+}, Co^{2+}, Cu^{2+}, Fe^{3+}, Mn^{2+}, Pb^{2+}, Zn^{2+}) of 10 mM concentration were prepared by dissolving corresponding precursors in known volume of distilled water. Few microliters of metal ion solutions were added into the obtained CQD solution and their optical absorption and emission bands were recorded.

5.2.3 Fabrication of CQDs-Tb^{3+} incorporated silica

The CQDs-silica were prepared through sol gel method at room temperature. The whole synthesis was carried out by keeping the molar ratio of TEOS – water − ethanol as 1:2:2. Initially, a mixture of tetraethyl orthosilicate (TEOS) of 7.4 ml and appropriate amount of distilled water was stirred magnetically for 1 h. To this, ethanolic solution

of 21 mg of CQDs were added and continued stirring for 1 more hour to obtain a homogeneous solution. Two drops of concentrated nitric acid were added as a catalyst. The resultant solution was poured into bottom flattened polypropylene containers which were wrapped with paraffin wax and kept undisturbed for about a month to form a stiff gel. Glassy sample was then placed in the hot air oven at 60 ^{0}C for 48 h to eliminate moisture content and other organics present [22]. Finally collected highly transparent glassy CQDs were named as CG (21 mg CQDs, in 2 g of silica). Tb^{3+}-CQDs co-doped silica at different terbium contents [0 wt%, 3 wt%, 5 wt% and 7 wt% Tb^{3+} in 2 g of silica] were fabricated using terbium nitrate as Tb^{3+} precursor and are named as T3, CT3, CT5 and CT7 respectively (as given in table 5.1). Additionally, 3 w% of Tb^{3+} ions were combined with lower contents of CQDs (10.5 mg) to obtain C·T3 named glassy samples.

Table 5.1: Compositions of the prepared samples.

Sample code	w % Tb	CQDs (mg)	Matrix/State
CG	0	21	Silica
T5	5	21	Silica
CT3	3	21	Silica
CT5	5	21	Silica
CT7	7	21	Silica
CDT3	3	10.5	Silica

5.2.4 Optical and morphological characterization

The X-ray diffraction spectrum of CQDs were collected by a benchtop powder X-ray diffractometer (Aeris Research, PANalytical, The Netherlands) with Cu Kα radiation of λ = 1.540598 Å. The morphology and crystallinity of CQDs were studied from high-resolution transmission electron microscopy, (HRTEM) on JEM 2100 operated at 200 kV. Fourier transform infrared (FTIR) spectrum was recorded in the region 4000 cm^{-1}-500 cm^{-1} with FTIR spectrometer (Perkin Elmer spectrum two FTIR spectrometer) by using ATR (attenuated total reflection) method. Optical absorption spectrum of CQDs was obtained by using UV-vis spectrophotometer, (Shimadzu UV-2600) and fluorescence emission spectra were acquired on Fluoromax spectrofluorometer (Horiba Jobin Yvon, USA). The color of emitting radiation was marked with the CIE chromaticity diagram (Commission Internationale de L'Eclairage1931) using *color*

calculator software. Time-resolved fluorescence decay curves were evaluated using fluorescence spectrometer (Horiba Fluorolog, USA). Optical photographs were captured with normal mobile camera. All the measurements were carried out at room temperature.

5.3 Results and discussions

5.3.1 Powder X-ray diffraction (XRD)

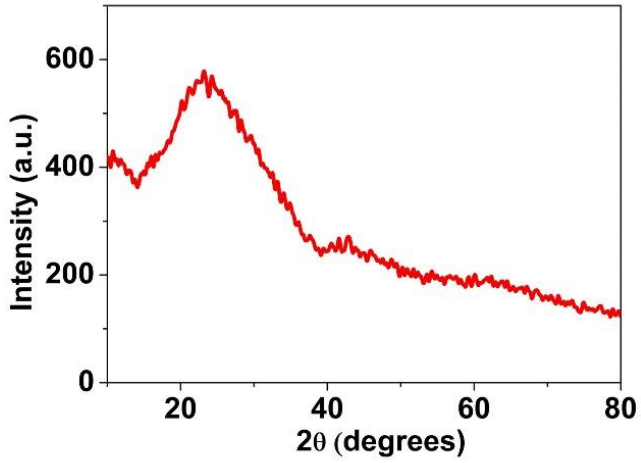

Figure 5.2: XRD pattern of CQD solution.

The X-Ray diffraction spectrum of CQDs measured is shown in Figure 5.2. The broad peak around 2theta value of 23.5° and 42° corresponds to the (002) and (100) plane of graphitic carbon core respectively [23].

5.3.2 Fourier transform infrared spectroscopy (FTIR)

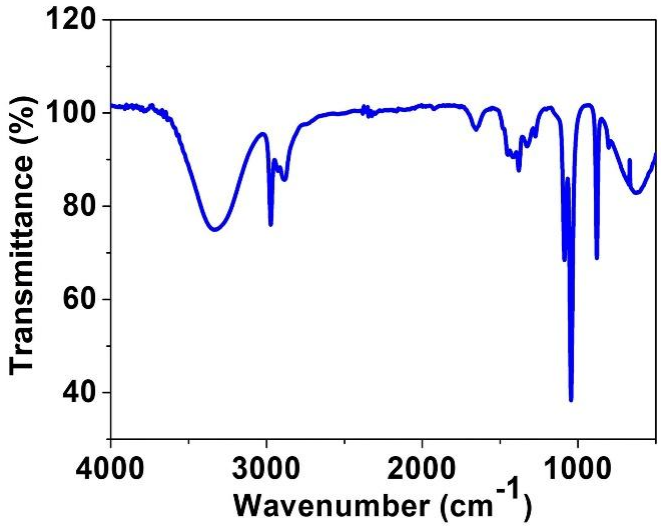

Figure 5.3: FTIR spectrum of CQD solution.

To examine the presence of surface groups, FTIR spectroscopy was employed. Figure 5.3 depicts that the aloe derived CQDs composed of functional groups containing carbon, oxygen and hydrogen. The characteristic absorption bands at 3332 and 1087 cm^{-1} corresponds to the stretching vibrational mode of hydroxyl groups (−OH) [24]. The C=C vibrational modes are responsible for the bands observed at 2973 and 1634 cm^{-1} [25]. Strong band observed at 2888 cm^{-1} suggests the presence of C-H stretching vibration mode. Meanwhile bands at 1559, 1380 cm^{-1} may be due to the asymmetric and symmetric stretching vibration of COO− respectively [24]. Bands at 1044 cm^{-1} can be ascribed to the stretching vibration mode of C-O bonds. All those hydroxyl and carboxyl surface groups originated from the carbonized aloe vera gel which was rich in carbohydrates [26], [27]. Due to the abundance of hydroxyl surface groups, CQDs have shown high solvent solubility which would be beneficial in designing optoelectronic devices [28].

5.3.3 Transmission electron microscopy (TEM)

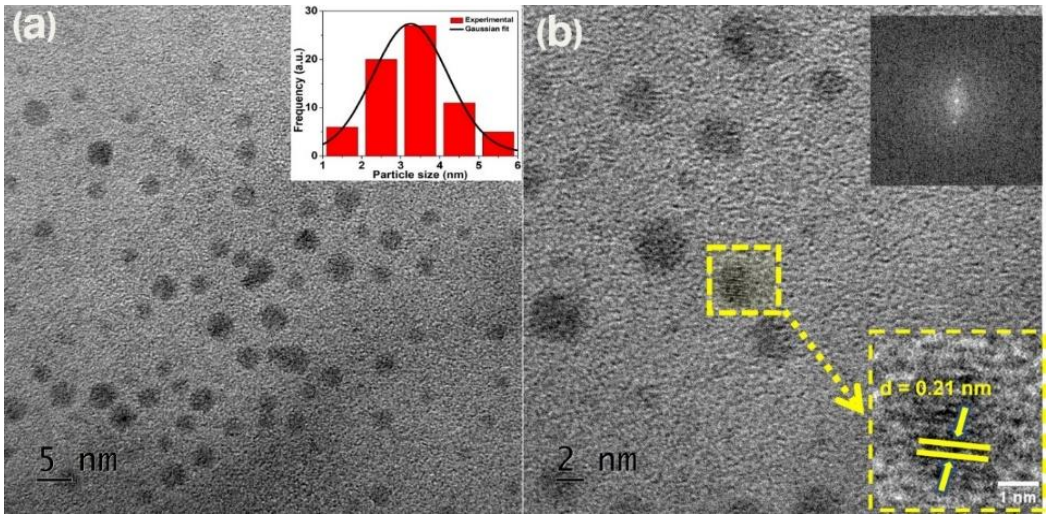

Figure 5.4: (a) TEM image of CQDs [inset of (a) shows particle size distribution profiles of CQDs] and (b) HRTEM image of CQDs. [Inset shows plane with interlayer spacing of 0.21 nm and corresponding FFT pattern].

The morphology, crystallinity and the core size distribution of the prepared CQDs are analyzed from transmission electron microscopy (TEM) images (Fig. 5.4). The CQDs are homogeneous and almost spherical in shape having a narrow size distribution of 1-6 nm (inset of Fig. 5.4(a)). The HRTEM image (Fig. 5.4(b)) reveals the presence of a single plane with lattice spacing of 0.21 nm which corresponds to the (101) graphitic carbon facets [4]. Controlled carbonization at constant temperature and constant volume for 24 h develops nanocarbon assemblies with graphitic cores.

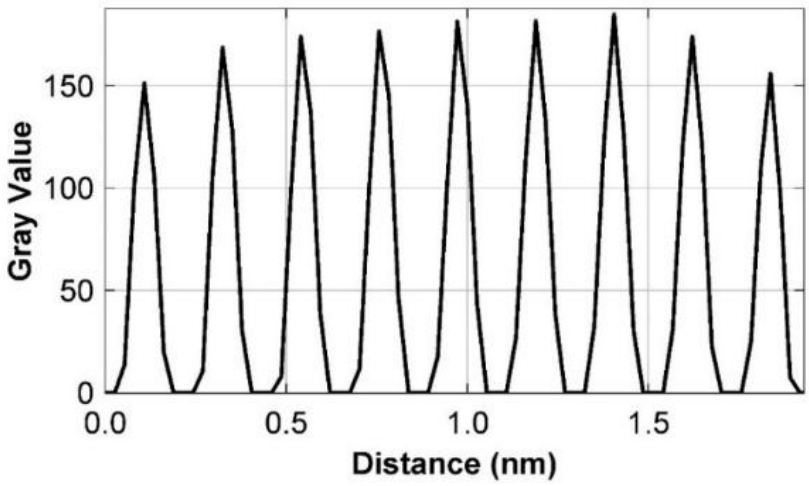

Figure 5.5: Surface plot obtained from HRTEM of CQDs.

Surface plot (Fig. 5.5) analysis was done using image-J software by processing selected regions of TEM images with equi-spaced parallel lattice fringes. The d value calculated from the surface plot closely matches with the results from HRTEM and the corresponding FFT pattern (given in the inset of Fig. 5.5(b)).

5.3.4 UV-Visible absorption spectra

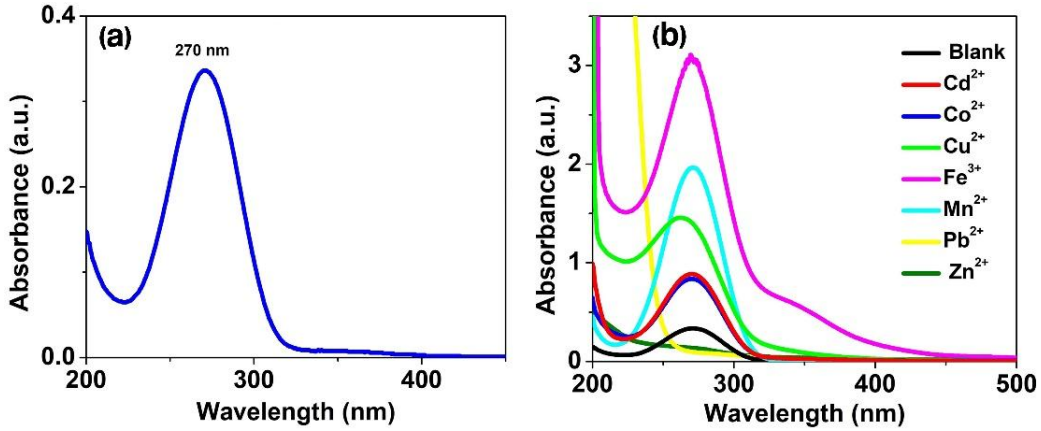

Figure 5.6: UV-visible absorption spectra of (a) CQDs and (b) in the presence and absence of different metal ions.

UV-visible absorption spectrum (Fig. 5.6(a)), exhibits a strong absorption band around 270 nm and 350 nm, which can be assigned to n→π* transitions of C=N and C=O respectively [4], [29], [30]. The observed absorption bands can be attributed to electron transition occurring within intrinsic carbonic core and surface states of CQDs [31], [32]. UV-visible absorption of CQD solution is measured in the presence of various metal ions reveals the influence of various metal ions on the surface states of CQDs (Fig. 5.6(b)). The absorption band peaked at 270 nm is assigned to n→π*

transitions of the surface group C=N. Enhanced optical absorption is observed 270 nm wavelength for all ions except Pb^{2+}, Zn^{2+} can be attributed to their complex formation with surface groups on CQDs. Upon addition of $Pb^{2+}$and Zn^{2+} ions the absorption band vanishes as the complexes formed didn't facilitates n→π* transitions of group C=N. Additionally, the absorption band observed around 350 nm is enhanced upon addition of Cu^{2+} and Fe^{3+} ions which suggests their influence on n→π* transitions of C=O.

5.3.5 Photoluminescence spectra

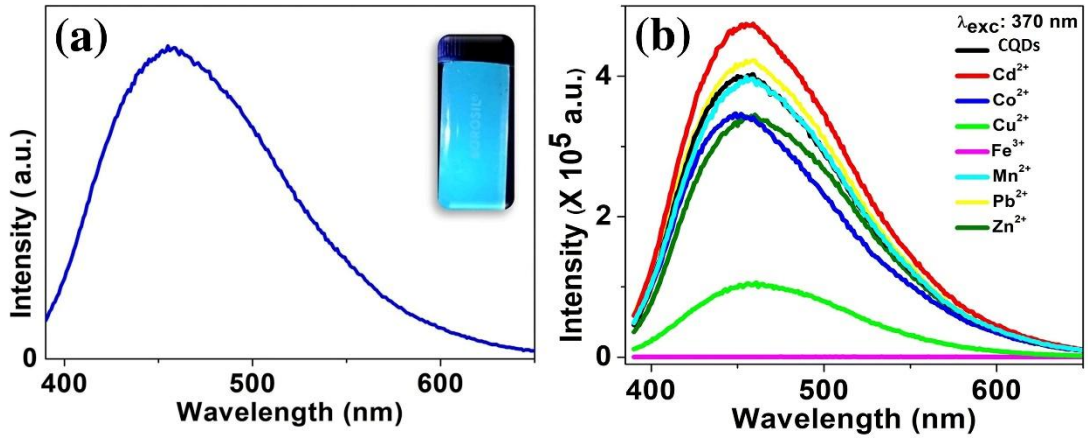

Figure 5.7: PL spectra of (a) aqueous CQD solution [The inset of (a) shows corresponding photographs under 365 nm] and (b) in the presence of different metal ions.

Upon UV excitation wavelength of 370 nm, a strong blue emission peak centered at 455 nm was observed (Fig. 5.7(a)). This can be ascribed to the energy transfer among sp^2 carbon cores and surface functional groups [32]. Moreover, drastic reduction in the luminescence intensity (Fig. 5.7(b)) upon 370 nm excitation wavelength occurs in the presence of Fe^{3+} and Cu^{2+} ions which confirms the complex formation between the oxygenated surface groups on CQDs. These ions exhibits strong affinity towards electron donating surface functional groups such as -OR, -OH [33]. Specific metal ion interactions on luminescence of CQDs are exploited in designing *in-vitro* sensors for Fe^{3+} ions [28].

5.3.6 Fluorescence lifetime decay curves

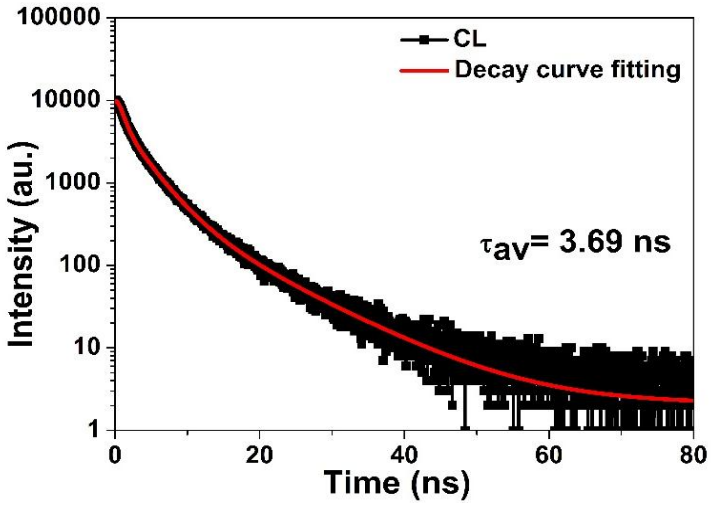

Figure 5.8: The fluorescence lifetime decay curve of CQDs.

The average fluorescence lifetime for broad blue emission was measured using nano LED with 330 nm excitation wavelength (Fig. 5.8). From the tri-exponential function fitted fluorescence decay curve, obtained average lifetime value of 3.69 ns is comparable with other biomass derived CQDs [34].

5.3.7 CQDs as fluorescent ink

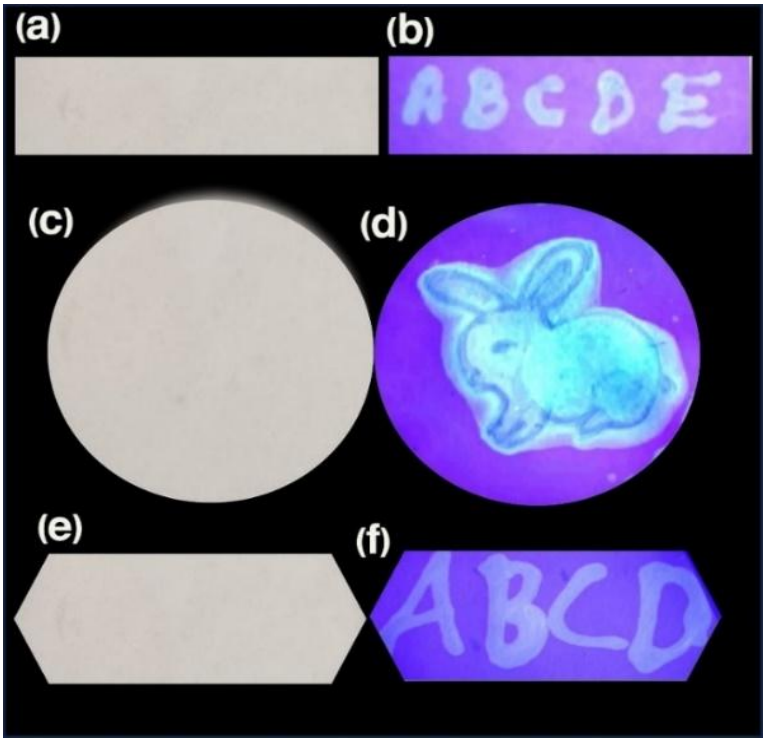

Figure 5.9: Information loaded on commercial filter paper using CQDs invisible ink under daylight (a, c, e) and 365 nm UV light (b, d, f).

CQDs can be employed as fluorescent ink which make it possible for secure data storage and advanced anti-counterfeiting applications [35,36]. The filler of ink pen was cleaned and filled with obtained light brown colored CQD solution to load certain data on commercially available filter paper. The encrypted data was allowed to dry for a few minutes in air. Then the filter paper loaded with certain characters was exposed to UV light. Optical images of the patterns in filter paper kept under day light and UV exposure (365 nm) were captured with a mobile camera. The optical images of various characters and patterns in the filter paper were displayed in Figure. 5.9. Invisible images under daylight appears fluorescent under UV illumination which assures the security of the loaded data. Stable non-polluting nature of CQDs can be considered as a perfect alternative for conventional inks [23,28].

5.3.8 Photoluminescence studies of CQDs-Tb^{3+} incorporated silica

(i) Photoluminescence studies of CQDs incorporated silica

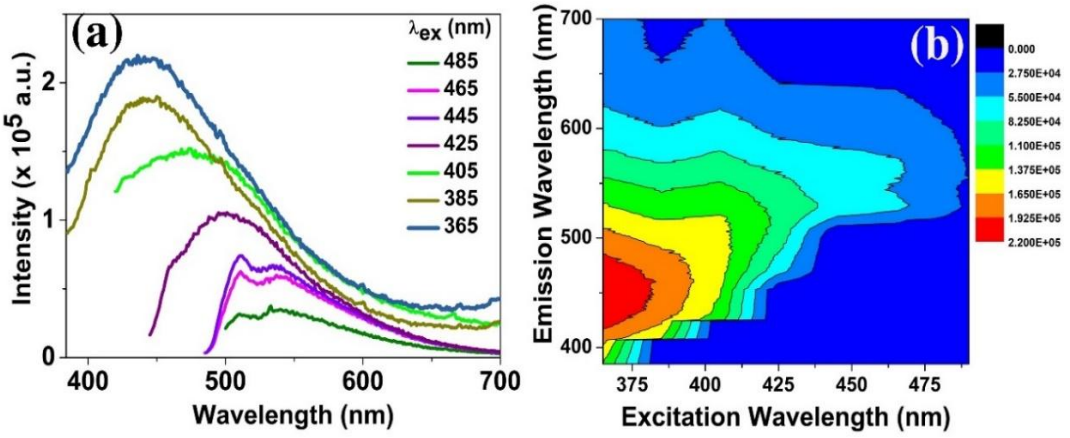

Figure 5.10: (a) PL spectra of CG at different excitation wavelengths (b) corresponding contour plot of the excitation/emission map.

The excitation dependent luminescence behaviour of CG is illustrated in Figure 5.10(a). With the increase of excitation wavelength, noticeable spectral redshift is observed, which can be ascribed to the multiple emissive states on the CQDs surfaces [37].

(ii) Energy transfer studies of CQDs-Tb^{3+} incorporated silica

To know more about the spectral transitions and energy transfer pathways, deep rooted investigations were carried out at (i) varying concentrations of RE & CQDs and

(ii) varying excitation wavelengths. Concentration dependent luminescence studies of CQD-Tb^{3+} encapsulated silica glasses were depicted in Figure 5.11 & Figure 5.12.

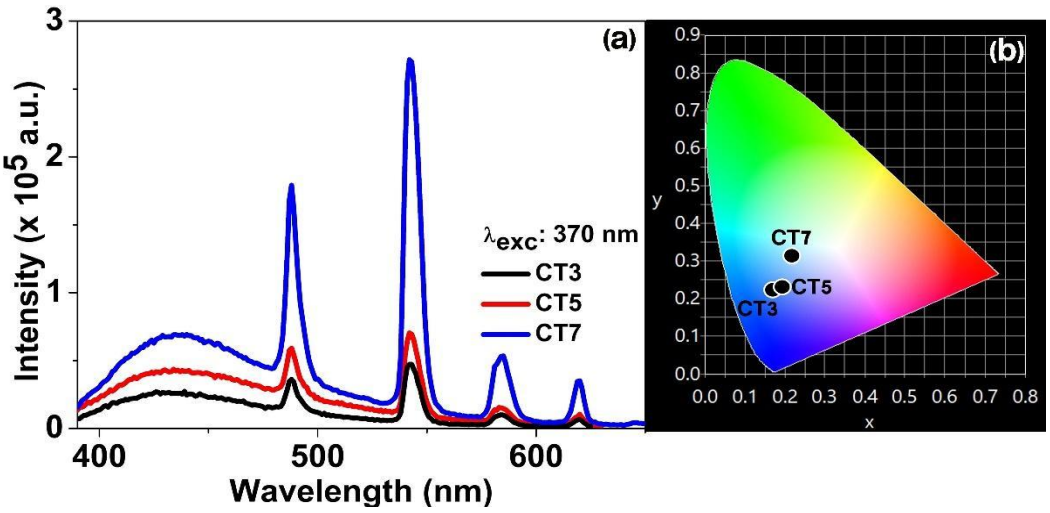

Figure 5.11: (a) PL spectra of CT3, CT5 and CT7 at 370 nm excitation wavelength (b) corresponding CIE chromaticity diagram.

To know more about the spectral transitions and energy transfer pathways, deep rooted investigations were carried out at (i) varying concentrations of RE & CQDs and (ii) varying excitation wavelengths. Concentration dependent luminescence studies of CQD-Tb^{3+} incorporated silica glasses at two different UV excitation wavelengths are studied. For 370 nm excitation wavelength, intensity of apparent peaks of terbium ions at 488 nm, 543 nm, 584 nm, 620 nm are prominent due to transitions from various crystal field levels of distinct metastable multiplets ($^5D_4 \rightarrow {}^7F_J$ (with J = 3, 4, 5, 6) [38]. Specifically, in terms of colors, blue-green emission bands peaked at 488 nm are due to the $^5D_4 \rightarrow {}^7F_6$ magnetic, electric dipole transitions of Tb^{3+} ion. The most intense green emission at 543 nm can be ascribed due to the $^5D_4 \rightarrow {}^7F_5$ magnetic dipole transitions [38]. From the chromaticity charts (Fig. 5.11(b)), the spectral tuning from blue (0.1952, 0.2328) to cyan (0.1995, 0.2310) and then to near white (0.2201, 0.3106) luminescence can be achieved upon 370 nm excitations. Upon increase in Tb^{3+} ion concentrations in rigid porous environment, surface binding sites may not be accessible as in liquid state and thereby prevents the luminescence quenching of CQDs. As presented in several previous reports of RE-CQD, luminescence from donor QDs is enhanced in the vicinity of increased RE acceptor concentration [39]. CQD acts as a sensitizer to open several energy transition pathways through more efficient emissions from $^5D_4 \rightarrow {}^7F_J$ (J = 3, 4, 5, 6) energy levels of Tb^{3+}.

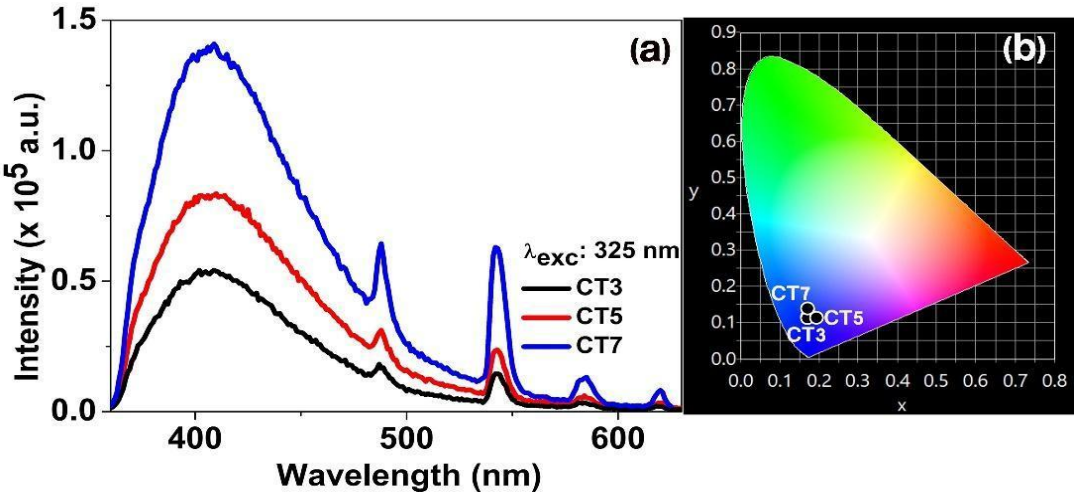

Figure 5.12: (a) PL spectra of CT3, CT5 and CT7 at 325 nm excitation wavelength (b) the corresponding CIE chromaticity diagram.

Though characteristic excitation wavelength of terbium ions is at 370 nm, intense emissions from $^5D_4 \rightarrow {}^7F_J$ (J = 3, 4, 5, 6) of Tb^{3+} is observed at non-prominent excitation wavelength of 325 nm (Fig. 5.11(a)). As blue emission bands are comparatively more intense than remaining peaks all the CIE indices appear in the blue region irrespective of the dopant concentration (Fig. 5.12(b)).

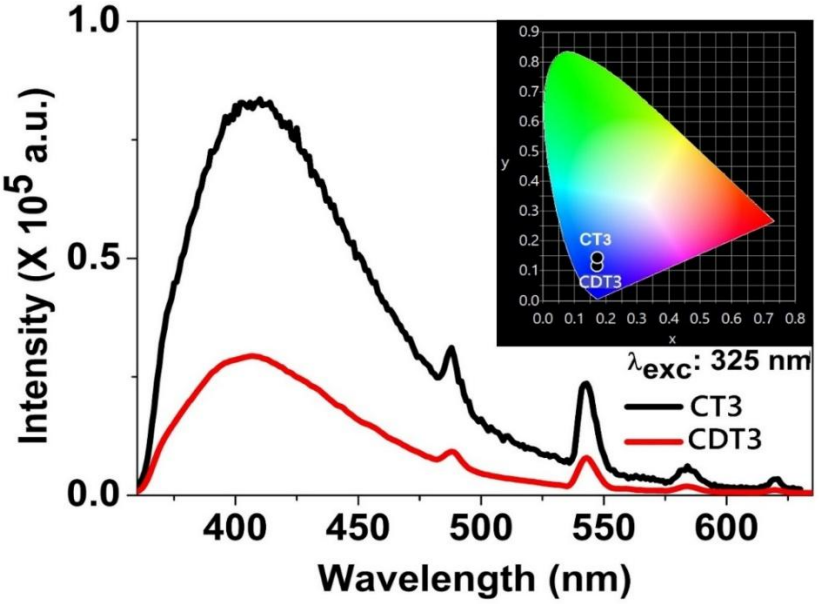

Figure 5.13: PL spectra of CQDs-Tb^{3+}incorporated silica containing different CQD concentrations (inset shows corresponding CIE chromaticity diagram).

Moreover, by reducing the CQD content to half, the intensity of CQD fluorescence attenuated to 1/3rd (Fig. 5.13). Due to the reduction of donor concentrations, optical quenching for acceptor luminescence is observed which confirmed the energy transfer among donor-acceptor (D-A) pairs.

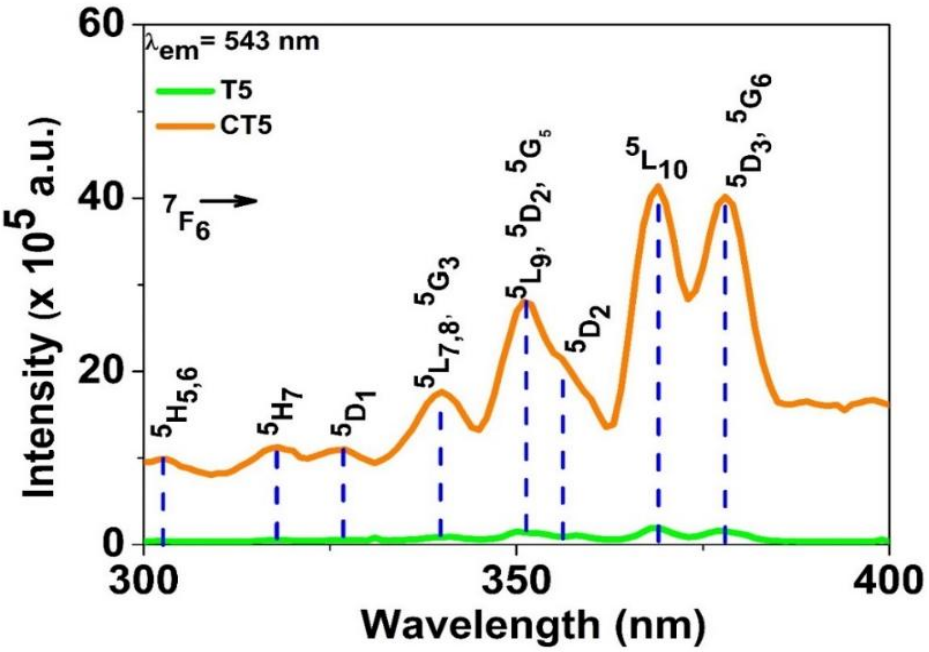

Figure 5.14: Photoluminescence excitation spectra (λ_{em} = 543 nm) of T5 and CT5.

The excitation spectrum (Fig. 5.14) presents multiple excitation bands at 317 nm, 325 nm, 340 nm, 350 nm, 358 nm, 368 nm, 378 nm which can be assigned due to the transitions from the $^7F_6$ ground state to various excited levels. The most intense excitation band at 369 nm generated from the intrinsic transition $^7F_6 \rightarrow ^5 L_{10}$ [40] was remarkably enhanced (~ 10 fold) in the presence of CQDs which strongly supports the energy transfer channels from CQDs (donor) to terbium ions (acceptor). No additional peaks were obtained in the CT5 sample other than in T5. Furthermore, the possible photoluminescence and energy transfer pathways established between CQDs and Tb^{3+}ions can be explained as described below.

By exposing the synthesized RE-CQD hybrids (CT series) with UV excitations, CQDs with comparable optical band gap absorbs photons and thereby electrons were excited from π to π* levels of CQDs. Then some electrons get de-excited to π state accompanied with a blue luminescence. Remaining electrons were transferred to $^5D_4$ levels of terbium ions and strong multicolor emissions were triggered. Hence $^5D_4$ level is populated with a greater number of electrons which catalyzes the de-excitation process accompanied with significant enhancement in characteristic luminescence of Tb^{3+} [2,39].

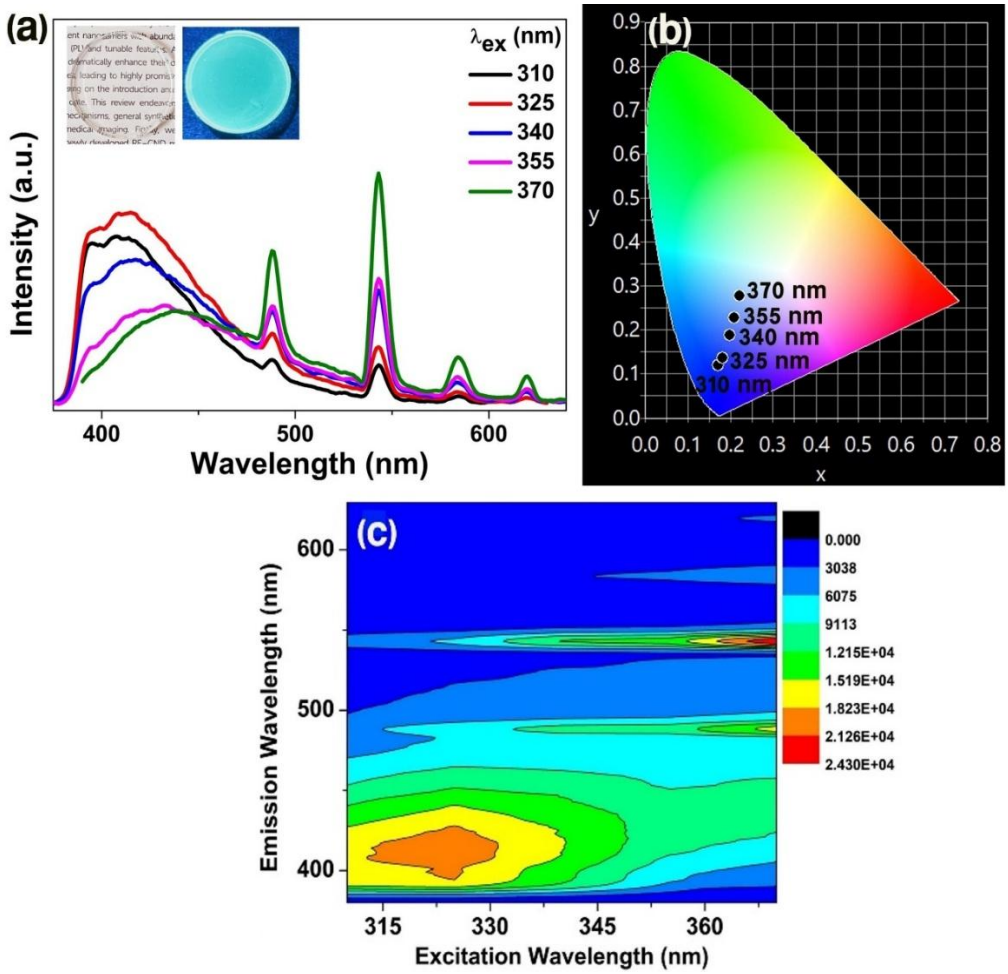

Figure 5.15:(a) Excitation dependent PL spectra CT5 [inset; photograph of CT5 in daylight and kept under UV source of 365 nm wavelength (b) corresponding CIE diagram (c) contour plot of the excitation/emission map of CT5.

An ordered increase in the peak intensity of terbium ions, at 488 nm, 543 nm, 584 nm, 620 nm is observed in excitation dependent emission of CQD-RE SiO_2 hybrids (Fig. 5.15 (a)). Multiple emissions associated with terbium ions exhibited highest intensity for 370 nm excitation. Progressive color point tuning in CIE charts (Fig. 5.15(b)) from blue to near white illustrates the tunability of obtained CT5 glasses. Figure 5.15(c) displays corresponding contour plots for excitation/emission map confirms that tunable emissions are obtained under broad excitations. At far UV excitations (310 nm, 325 nm), broad intense blue emissions from CQDs dominate and while narrow emissions from terbium ions are more intense for near UV excitations (370 nm). Besides, sharp emissions of RE ions at 488 nm lies within the contour region of blue emitting CQDs which extends up to 500 nm. Moreover, regulated luminous colors by adjusting the dopant concentrations may be further utilized in designing novel high-definition lighting platforms.

5.3.9 CQDs-Tb^{3+} silica for tunable solid state lighting applications

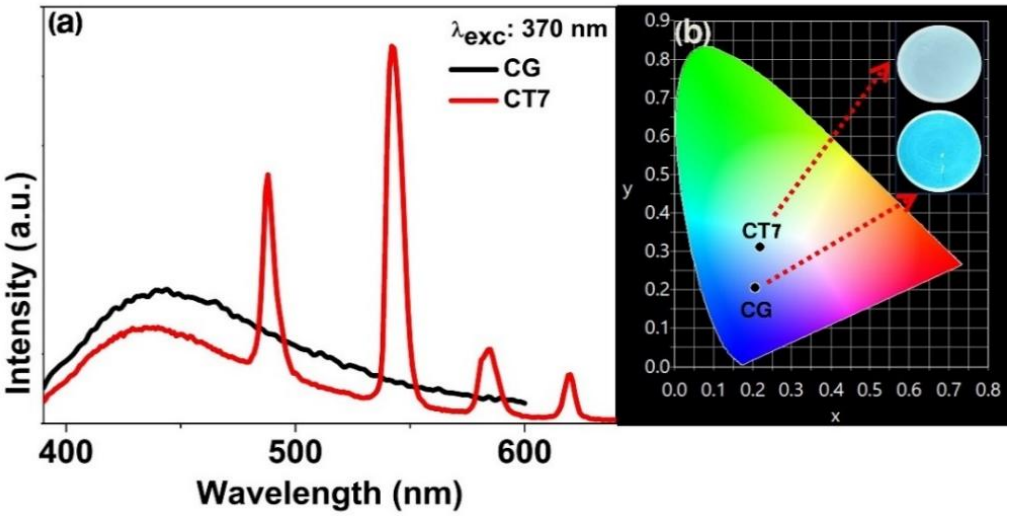

Figure 5.16: (a) PL spectra of CG and CT7 at 370 nm excitation (b) corresponding CIE chromaticity diagram [inset; photographs of CG, CT7 kept under 365 nm UV light].

Photoluminescence spectra of multicolor emitting CQD-RE silica matrix is analysed to explore the energy transfer mechanisms between CQDs and Tb^{3+}. it can be inferred that upon addition of Tb^{3+} ions, the blue emitting CQD-SiO_2 changes to near white emitting glasses under excitation of 370 nm (Fig. 5.16). Decrease in fluorescence intensity of CQD suggests possible energy transfer to Tb^{3+} ions. UV illuminated CG glasses were tuned from blue to the white point in the CIE chart due to the neighbouring terbium ions in CT7. Particularly, from the captured photographs and corresponding color points, tuning of emission chromaticity from intense blue (0.1809, 0.1992) to near white (0.2201, 0.3106) domain was observed.

5.4 Conclusion

In this study, a series of CQD: xTb^{3+} (x = 3, 5, 7 w %) were prepared at room temperature via sol-gel method. Aloe derived CQDs with excellent excitation dependent luminescence were utilized in fabricating luminescent silica glasses. Surface passivated CQDs owned with numerous emissive traps shows excitation dependent emissions. A notable optical quenching is exhibited for CQDs in presence of Fe^{3+} and Cu^{2+} ions. Solid silica networks retain the spectral tuning of CQDs. Peculiar 'visible-invisible' spectral features of CQDs can be explored in anti-counterfeiting, data loading

and figure print formation applications. Bright tunable fluorescence achieved by combining CQD with (Tb^{3+}) terbium ions unveiled its potential applications in tunable fluorescent displays. High optical performance of Tb^{3+} in presence of CQDs is explained by the energy transfer routes from the donor CQDs to acceptor (Tb^{3+}) ions. Under UV excitations, while CQD - SiO_2 glasses exhibited blue emissions (0.1952, 0.2328) and CQD-Tb^{3+}-SiO_2 glasses shows a near white (0.2201, 0.3106) luminescence. Tail orable compositional features of CT glasses can be further developed as solid tunable fluorescent developers and displays.

References

[1] Y. Zhu *et al.*, "Efficient energy transfer from inserted CdTe quantum dots to $YVO_4:Eu^{3+}$ inverse opals: a novel strategy to improve and expand visible excitation of rare earth ions," *Nanoscale*, vol. 6, no. 14, pp. 8075–8083, Jun. 2014, doi: 10.1039/C4NR01845A.

[2] M. Zhang *et al.*, "When rare earth meets carbon nanodots: mechanisms, applications and outlook," *Chem. Soc. Rev.*, vol. 49, no. 24, pp. 9220–9248, Dec. 2020, doi: 10.1039/D0CS00462F.

[3] J. Xie *et al.*, "Wide range color tunability and efficient energy transfer of novel $NaCaGd(WO_4)_3:Tb^{3+},Eu^{3+}$ phosphors with excellent thermal stability for pc-WLEDs," *Inorg. Chem. Front.*, vol. 8, no. 20, pp. 4517–4527, Oct. 2021, doi: 10.1039/D1QI00831E.

[4] W. Cai *et al.*, "Full color carbon dots through surface engineering for constructing white light-emitting diodes," *J. Mater. Chem. C*, vol. 7, no. 8, pp. 2212–2218, Feb. 2019, doi: 10.1039/C9TC00274J.

[5] C. Ding, X. Cao, C. Zhang, T. He, N. Hua, and Y. Xian, "Rare earth ions enhanced near infrared fluorescence of Ag_2S quantum dots for the detection of fluoride ions in living cells," *Nanoscale*, vol. 9, no. 37, pp. 14031–14038, Sep. 2017, doi: 10.1039/C7NR04436D.

[6] A. C. Pan, C. del Cañizo, E. Cánovas, N. M. Santos, J. P. Leitão, and A. Luque, "Enhancement of up-conversion efficiency by combining rare earth-doped phosphors with PbS quantum dots," *Solar Energy Materials and Solar Cells*, vol. 94, no. 11, pp. 1923–1926, Nov. 2010, doi: 10.1016/j.solmat.2010.06.028.

[7] K.-T. Yong *et al.*, "Nanotoxicity assessment of quantum dots: from cellular to primate studies," *Chem. Soc. Rev.*, vol. 42, no. 3, pp. 1236–1250, Jan. 2013, doi: 10.1039/C2CS35392J.

[8] X. Michalet *et al.*, "Quantum Dots for Live Cells, in Vivo Imaging, and Diagnostics," *Science*, vol. 307, no. 5709, pp. 538–544, Jan. 2005, doi: 10.1126/science.1104274.

[9] S. Iijima, "Helical microtubules of graphitic carbon," *Nature*, vol. 354, no. 6348, Art. no. 6348, Nov. 1991, doi: 10.1038/354056a0.

[10] W. Krätschmer, L. D. Lamb, K. Fostiropoulos, and D. R. Huffman, "Solid C60: a new form of carbon," *Nature*, vol. 347, no. 6291, pp. 354–358, Sep. 1990, doi: 10.1038/347354a0.

[11] H. Ding, L.-W. Cheng, Y.-Y. Ma, J.-L. Kong, and H.-M. Xiong, "Luminescent carbon quantum dots and their application in cell imaging," *New J. Chem.*, vol. 37, no. 8, pp. 2515–2520, Jul. 2013, doi: 10.1039/C3NJ00366C.

[12] H. Liu, L. Zhang, M. Yan, and J. Yu, "Carbon nanostructures in biology and medicine," *J. Mater. Chem. B*, vol. 5, no. 32, pp. 6437–6450, Aug. 2017, doi: 10.1039/C7TB00891K.

[13] B. Wang *et al.*, "Rational Design of Multi-Color-Emissive Carbon Dots in a Single Reaction System by Hydrothermal," *Advanced Science*, vol. 8, no. 1, p. 2001453, 2021, doi: 10.1002/advs.202001453.

[14] T. Paul, J. J. Palakulam, N. V. Unnikrishnan, R. Philip, and K. A. A. Mary, "Warm to cool tunable ultra-stable white light emissions from carbon dots -Tb^{3+} - Eu^{3+} doped silica," *Optical Materials*, vol. 138, p. 113673, Apr. 2023, doi: 10.1016/j.optmat.2023.113673.

[15] J. Yang, Y. Liu, J. Wang, S. Wang, X. Zhou, and H. Li, "Visual multiple color emission of solid-state carbon dots," *J. Mater. Chem. C*, vol. 7, no. 25, pp. 7806–7811, Jun. 2019, doi: 10.1039/C9TC01638D.

[16] T. Feng *et al.*, "Color-Tunable Carbon Dots Possessing Solid-State Emission for Full-Color Light-Emitting Diodes Applications," *ACS Photonics*, vol. 5, no. 2, pp. 502–510, Feb. 2018, doi: 10.1021/acsphotonics.7b01010.

[17] A. B. Bourlinos *et al.*, "Gd(III)-doped carbon dots as a dual fluorescent-MRI probe," *J. Mater. Chem.*, vol. 22, no. 44, pp. 23327–23330, Oct. 2012, doi: 10.1039/C2JM35592B.

[18] P. Verwilst, S. Park, B. Yoon, and J. S. Kim, "Recent advances in Gd-chelate based bimodal optical/MRI contrast agents," *Chem. Soc. Rev.*, vol. 44, no. 7, pp. 1791–1806, Mar. 2015, doi: 10.1039/C4CS00336E.

[19] Y. Haas and G. Stein, "Pathways of radiative and radiationless transitions in europium(III) solutions. Role of solvents and anions," *ACS Publications*, vol. 75, no. 24, pp. 3668–3677, Nov. 1971, doi: 10.1021/j100693a005

[20] Q. Huo, W. Tu, and L. Guo, "Enhanced photoluminescence property and broad color emission of $ZnGa_2O_4$ phosphor due to the synergistic role of Eu3+ and carbon dots," *Optical Materials*, vol. 72, pp. 305–312, Oct. 2017, doi: 10.1016/j.optmat.2017.06.013.

[21] B. Chen and J. Feng, "White-Light-Emitting Polymer Composite Film Based on Carbon Dots and Lanthanide Complexes," *J. Phys. Chem. C*, vol. 119, no. 14, pp. 7865–7872, Apr. 2015, doi: 10.1021/acs.jpcc.5b00208.

[22] K. A. A. Mary, N. V. Unnikrishnan, and R. Philip, "Cubic to amorphous transformation of Se in silica with improved ultrafast optical nonlinearity," *RSC Adv.*, vol. 5, no. 18, pp. 14034–14041, Jan. 2015, doi: 10.1039/C4RA14025G.

[23] T. N. J. I. Edison, R. Atchudan, M. G. Sethuraman, J.-J. Shim, and Y. R. Lee, "Microwave assisted green synthesis of fluorescent N-doped carbon dots: Cytotoxicity and bio-imaging applications," *Journal of Photochemistry and Photobiology B: Biology*, vol. 161, pp. 154–161, Aug. 2016, doi: 10.1016/j.jphotobiol.2016.05.017.

[24] H. Xu, X. Yang, G. Li, C. Zhao, and X. Liao, "Green Synthesis of Fluorescent Carbon Dots for Selective Detection of Tartrazine in Food Samples," *J. Agric. Food Chem.*, vol. 63, no. 30, pp. 6707–6714, Aug. 2015, doi: 10.1021/acs.jafc.5b02319.

[25] V. Ţucureanu, A. Matei, and A. M. Avram, "FTIR Spectroscopy for Carbon Family Study," *Critical Reviews in Analytical Chemistry*, vol. 46, no. 6, pp. 502–520, Nov. 2016, doi: 10.1080/10408347.2016.1157013.

[26] A. Balaji *et al.*, "Biomaterials based nano-applications of Aloe vera and its perspective: a review," *RSC Adv.*, vol. 5, no. 105, pp. 86199–86213, Oct. 2015, doi: 10.1039/C5RA13282G.

[27] T. Reynolds and A. C. Dweck, "Aloe vera leaf gel: a review update," *Journal of Ethnopharmacology*, vol. 68, no. 1, pp. 3–37, Dec. 1999, doi: 10.1016/S0378-8741(99)00085-9.

[28] B. De and N. Karak, "A green and facile approach for the synthesis of water soluble fluorescent carbon dots from banana juice," *RSC Advances*, vol. 3, no. 22, pp. 8286–8290, 2013, doi: 10.1039/C3RA00088E.

[29] P. Raj, S. Lee, and T. Y. Lee, "Carbon Dot/Naphthalimide Based Ratiometric Fluorescence Biosensor for Hyaluronidase Detection," *Materials*, vol. 14, no. 5, Art. no. 5, Jan. 2021, doi: 10.3390/ma14051313.

[30] S. Wang, I. S. Cole, D. Zhao, and Q. Li, "The dual roles of functional groups in the photoluminescence of graphene quantum dots," *Nanoscale*, vol. 8, no. 14, pp. 7449–7458, Mar. 2016, doi: 10.1039/C5NR07042B.

[31] J. Yu *et al.*, "Luminescence Mechanism of Carbon Dots by Tailoring Functional Groups for Sensing Fe^{3+} Ions," *Nanomaterials*, vol. 8, no. 4, Art. no. 4, Apr. 2018, doi: 10.3390/nano8040233.

[32] K. J. Mintz, Y. Zhou, and R. M. Leblanc, "Recent development of carbon quantum dots regarding their optical properties, photoluminescence mechanism, and core structure," *Nanoscale*, vol. 11, no. 11, pp. 4634–4652, 2019, doi: 10.1039/C8NR10059D.

[33] L. Li, B. Yu, and T. You, "Nitrogen and sulfur co-doped carbon dots for highly selective and sensitive detection of Hg (II) ions," *Biosensors and Bioelectronics*, vol. 74, pp. 263–269, Dec. 2015, doi: 10.1016/j.bios.2015.06.050.

[34] R. Pratap, V. Vishal, S. Chaudhary, and A. Singh Parmar, "Fabrication of white light emitting diodes via high yield surface passivated carbon quantum dots doped with terbium," *RSC Advances*, vol. 13, no. 3, pp. 1974–1984, 2023, doi: 10.1039/D2RA07890B.

[35] R. Bandi, N. P. Devulapalli, R. Dadigala, B. R. Gangapuram, and V. Guttena, "Facile Conversion of Toxic Cigarette Butts to N,S-Codoped Carbon Dots and Their Application in Fluorescent Film, Security Ink, Bioimaging, Sensing and Logic Gate Operation," *ACS Omega*, vol. 3, no. 10, pp. 13454–13466, Oct. 2018, doi: 10.1021/acsomega.8b01743.

[36] R. Atchudan, T. N. Jebakumar Immanuel Edison, S. Perumal, and Y. R. Lee, "Indian Gooseberry-Derived Tunable Fluorescent Carbon Dots as a Promise for In Vitro/In Vivo Multicolor Bioimaging and Fluorescent Ink," *ACS Omega*, vol. 3, no. 12, pp. 17590–17601, Dec. 2018, doi: 10.1021/acsomega.8b02463.

[37] A. Sharma, T. Gadly, A. Gupta, A. Ballal, S. K. Ghosh, and M. Kumbhakar, "Origin of Excitation Dependent Fluorescence in Carbon Nanodots," *J. Phys. Chem. Lett.*, vol. 7, no. 18, pp. 3695–3702, Sep. 2016, doi: 10.1021/acs.jpclett.6b01791.

[38] P. C. Ricci, C. M. Carbonaro, R. Corpino, C. Cannas, and M. Salis, "Optical and Structural Characterization of Terbium-Doped Y_2SiO_5 Phosphor Particles," *J. Phys. Chem. C*, vol. 115, no. 33, pp. 16630–16636, Aug. 2011, doi: 10.1021/jp203523s.

[39] Y. Wang *et al.*, "Construction, energy transfer, tunable multicolor and luminescence enhancement of YF_3:RE^{3+}(RE=Eu, Tb)/carbon dots nanocomposites," *Journal of Luminescence*, vol. 221, p. 117072, May 2020, doi: 10.1016/j.jlumin.2020.117072.

[40] J. Juárez-Batalla, A. N. Meza-Rocha, G. Muñoz H., I. Camarillo, and U. Caldiño, "Luminescence properties of Tb^{3+}-doped zinc phosphate glasses for green laser application," *Optical Materials*, vol. 58, pp. 406–411, Aug. 2016, doi: 10.1016/j.optmat.2016.06.022.

6

Nanocarbon Doped Silica for WLE Applications

Achieving a single component WLE from nano assemblies is still a challenging strategy in the solid-state lighting (SSL) systems. Herein, solid state luminescent graphitic and non-graphitic crystalline nano carbon were synthesized through sol-gel assisted thermal route by changing the carbon content in the materials. Morphology and the degree of crystallinity were confirmed with the aid of TEM, SAED and FTIR. At lower carbon content, graphitic carbon nano crystallites were obtained. Polycrystalline spherical, non-graphitic carbon nanoparticles were obtained at higher concentration of carbon in silica. Silica confines the growth and crystallization of carbon nanoparticles. Upon graphitic to non-graphitic transformation, a reduction in band gap values from 3.35 eV to 2.65 eV are exhibited. Interestingly, under UV exposure graphitic carbon nano crystallites exhibited strong blue luminescence whereas non-graphitic crystalline nanoparticles show broad luminescent band. Non-graphitic carbon nanoparticles with wide emissions yielded cool white CCTs (> 6000 K), good CRI value (~80) with favorable CIE coordinates. This solid fluorescent composites with concentration mediated optical and structural tunability are potential candidate for high-definition multicolor emitting display panels and advanced lighting applications.

Graphical abstract

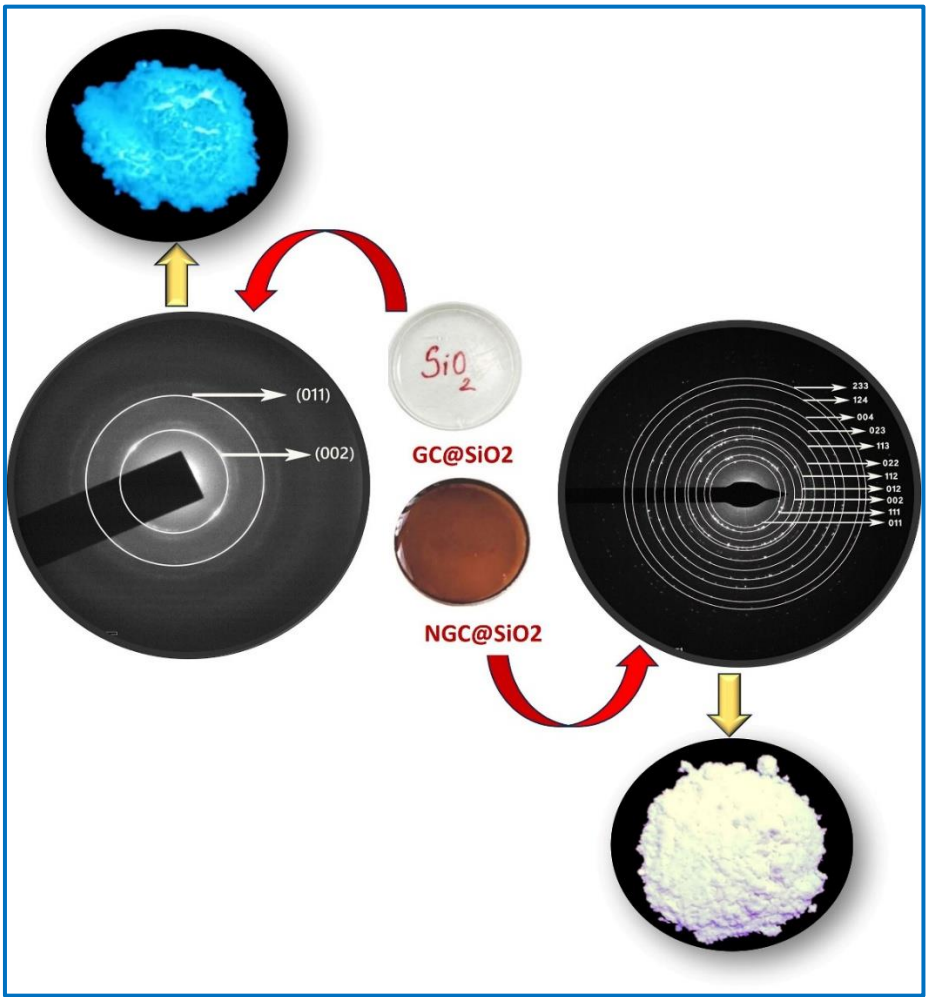

6.1 Introduction

Solid fluorescent materials are merited with peculiar attention in recent years towards distinct applications including sensors, white light emitting diodes (WLEDs) data encryption, barcoding and patterning etc. [1]. Till date, diverse strategies were presented in literatures to fabricate efficient color tunable platforms. Stable but complex networks such as lanthanide organic hybrids [2] and organic-dye-based complexes [3] are certain photoluminescence color tunable (PLCT) materials reported in recent years. Excitation wavelength dependent spectral tuning is obtained in some materials including $(Ba, Sr)_5(PO_4)_3Br: Eu^{2+}$ phosphors [4]. On the other hand, $Cd_{(1-x)}Zn_xS$ nanomaterials are illustrated as a rare compositional variation dependent PLCT due to FRET between the donor-acceptor (D-A) pair of (ZnS- CdS) [5]. In addition, concentration dependent PLCT in N-CQDs [6] and the wide range PLCT from $NaCaGd(WO_4)_3:Tb^{3+}$, Eu^{3+} [7] are also reported. Usually, desired chromaticity points are achieved by blending individual discrete chromatic emitters in multiphase or in composite forms. Nevertheless, using multiphase chromatic emitters raises preparation costs while varying degradation rates of components alters their stability and shelf life. Consequently, single component PLCT materials are to be developed with ultimate importance and consideration.

In addition to PLCT materials, solid state WLE materials are also a topic of great interest in which plenty of research works are done. Optimized integration of RGB or YB chromophores of comparable luminescence intensity are necessary to obtain WLE materials. White light emissions are generally characterized with certain colorimetric parameters like color rendering index (CRI), correlated color temperature (CCT) and Commission Internationale de I'Eclairage (CIE) indices. CRI value is a measure of realizing the exact color of an object in comparison with the same kept under reference sources. Wider the spectral distributions, higher the CRI values which usually rated from 0 to 100. While warm WLE materials have CCT > 6000 K, cool white luminescence accompanied with lower CCTs (3200–6000 K) [8], [9], [10]. The CIE indices quantify the emitting color from the designed light source with two coordinates (x, y). Quality of white emissions are generally confirmed with CCTs as

mentioned in above ranges. WLE color coordinates are around (0.33, 0.33) with desirable CRI (~80) values. Even though certain solid fluorescent materials like $BaY_2ZnO_5:Dy^{3+}$ [11] and $YAG:Ce^{3+}$[8] have favorable CIE coordinates, invalid CCTs with poor CRI values hinders it from future lighting applications. Certain phosphors like, $BaSrMg(PO_4)_2:Eu^{2+}$ [12] have good CRI values and CIE coordinates. But lack of stable CCTs prevents it from perfect white light generation with desired spectral quality. Additionally, self-absorption among various components impairs the effectiveness of multicomponent phosphors, and distinct degradation trajectories impact their long-term uses.

Among nontoxic, green, biocompatible solid state fluorescent materials, nano carbon has drawn tremendous attention in recent years owing to their diverse structural and optical characteristics. In comparison to the bulk counterparts, elemental carbon exhibits strong blue fluorescence at nanometric scales. So far, owing to the self-quenching in solid state, most of the research focused on luminescence from aqueous solution of carbon quantum dots (CQDs) or nanoparticles and solid-state fluorescent nano carbon remains as a less explored area of research. Earlier, CQDs were considered as amorphous nanodots and modified synthesis strategies led to the generation of graphitic and non- graphitic crystalline domains. Amorphous carbon cores are confirmed by the absence of sharp peaks in XRD with no bright spots in SAED pattern. Single crystalline, graphitic carbon exhibits well resolved lattice fringes from TEM micrographs (0.28, 0.32 nm) which corresponds to (020) and (002) planes of graphitic cores [13], [14]. Besides, non-graphitic polycrystalline carbon forming cubic C_8 structure is studied for their blue luminescence capable of sensing Cu^{2+} ions [15]. Furthermore, blue emitting N-doped non graphitic CQDs functionalized with L-valine is recently reported for tetracycline detection [16]. Polycrystalline, non- graphitic CQDs achieved via heteroatom doping find applications in sun light mediated saline water purification whereas zinc ion induced crystalline nanocarbon exhibits appreciable supercapacitor performances [17], [18]. Though some studies focused on crystalline non-graphitic carbon nanostructures, experimental evidences are very rare for nanostructures with carbon C_{20} crystal structure. Moreover, though solid state carbon nano systems are studied for their blue

[19] yellow [20], orange [21] and red [22] luminescence, carbon based single component WLEDs are still demanding.

Herein, we study the influence of structural transformation from graphitic to non-graphitic crystalline carbon on their optical properties. By varying the carbon content in mesoporous silica, luminescence shift from blue to cool white was observed. To best of our knowledge, studies on solid state fluorescent carbon nano assemblies @silica are rarely found in literatures, which is a key lighting candidate in the rapidly growing optoelectronic industry.

6.2 Experimental section

6.2.1 Synthesis of C@SiO_2 nanocomposites

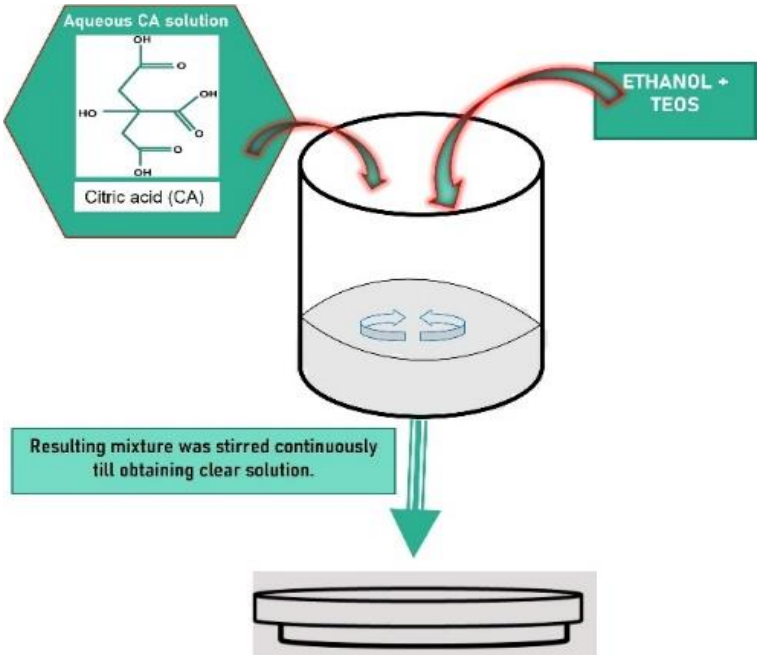

Figure 6.1: Schematic representation of synthesis of C@ SiO_2.

10 wt% C and 40 wt% C doped silica glasses were synthesized through sol gel route as shown in schematic representation given in figure. 6.1. Appropriate amount of ethanol was added to 7.4 ml tetraethyl orthosilicate (TEOS) and the mixture was continuously stirred for 1 h. To this, aqueous citric acid solution was added and continued stirring to obtain a homogeneous solution. The molar ratio of TEOS – water − ethanol was maintained as 1:2:2. Two drops of concentrated nitric acid was added as a catalyst. The final clear solution obtained was transferred into polypropylene

containers, sealed using paraffin wax and kept for about a month to form a stiff gel. Samples were then heated in the hot air oven at 60 ^{0}C for 2 days to eliminate water and other organics present.

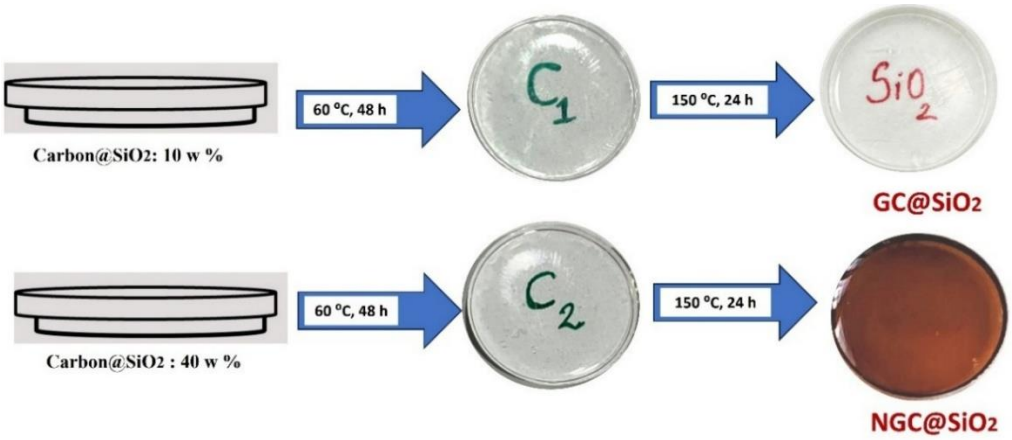

Figure 6.2: Schematic representation of synthesis of carbon@ SiO_2.

Obtained glassy samples with excellent transparency are allowed to undergo thermal annealing at 150 °C for 24 h (given in Fig. 6.2). The composites are ground into fine powder and further used for various measurements. The samples are named as [GC@SiO_2 [10 wt% C in 2 g of silica], NGC@SiO_2 [40 wt% C in 2 g of silica]].

Table 6.1: Compositions and annealing temperatures of samples.

Sample code	w % C	Weight of silica (in g)	Annealing Temperature (^{0}C)
GC@SiO_2	10	2	150 ^{0}C
NGC@SiO_2	40	2	150 ^{0}C

6.2.2 Structural and Optical characterization

The morphology and crystallinity of nanocomposites were analysed using TALOS F200S G2 transmission electron microscope (200 kV, FEG, CMOS Camera 4K × 4K). For TEM analysis, ethanolic dispersion of finely powdered sample drop-casted and dried in air. Fourier Transform Infrared Spectroscopy (FTIR) was performed on a Perkin-Elmer FTIR spectrophotometer. Prepared nanocomposites were thermally analyzed with PerkinElmer STA 8000. TGA, DTA thermographs were procured in nitrogen atmosphere at a heating rate of 10 °C/min. The optical absorption spectrum was recorded using UV-vis spectrophotometer (Shimadzu UV-2600) and fluorescence profiles were recorded using Fluoromax Spectrofluorometer (Horiba Jobin Yvon,

USA). Time-resolved fluorescence decay profiles were obtained using fluorescence spectrometer (Horiba Fluorolog, USA). Optical photographs were recorded using normal mobile camera. The color of the light and other colorimetric parameters was identified by the CIE (Commission Internationale de L'Eclairage1931) chromaticity charts provided by the color calculator software.

6.3 Results and discussions

6.3.1 Transmission electron microscopy (TEM)

The morphology and crystallinity of nanocarbon embedded silica were investigated via transmission electron microscopy (TEM) and selected area electron diffraction (SAED) pattern.

(i) GC@SiO₂

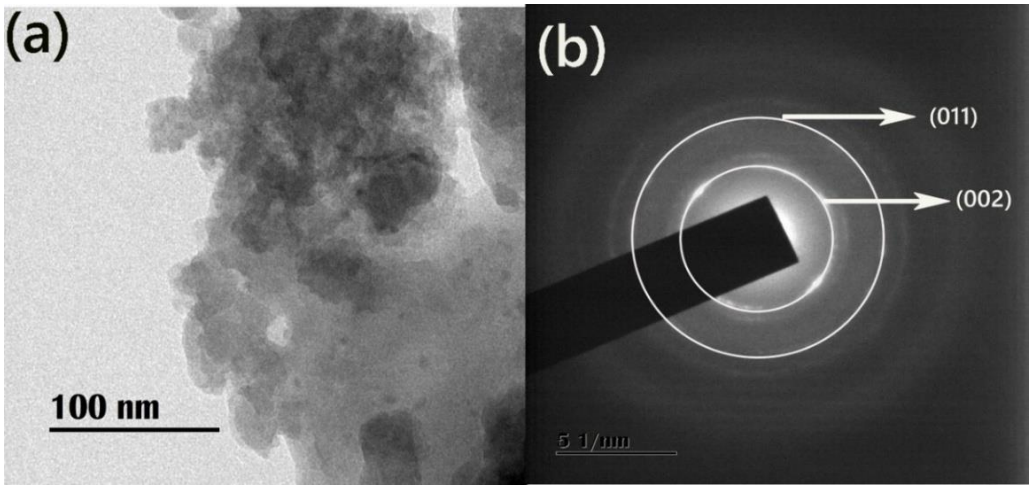

Figure 6.3: (a) TEM image and (b) SAED image of GC@SiO_2.

TEM micrograph displayed in Figure 6.3 (a) shows clusters of carbon nano assemblies. Presence of bright spots in selected area electron diffraction (SAED) pattern (Fig. 6.3(b)) indicates crystallinity of graphitic carbon entrapped within mesoporous silica. Brightest ring in the SAED pattern of GC@SiO_2 can be indexed to crystalline graphitic carbon cores. Obtained d-spacing at 0.32 nm, 0.19 nm corresponds to the (002), (011) lattice planes of the graphitic carbon (ICSD:31170) [23].

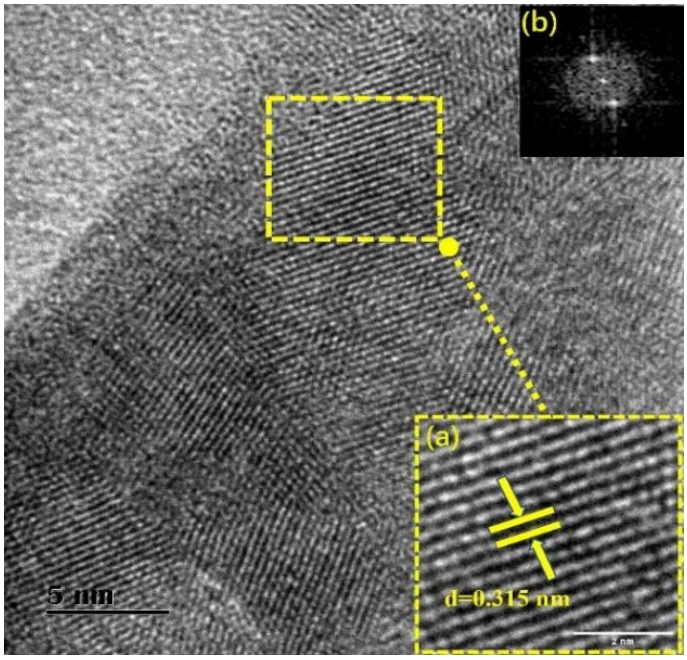

Figure 6.4: HRTEM image of GC@ SiO_2. [Inset (a) shows plane with d- value 0.315 nm and (b) shows corresponding FFT pattern].

The HRTEM image (Figure 6.4) shows that the GC@SiO_2 has assemblies of nano crystallites. The interlayer spacing d-value of well-defined lattice fringes were obtained as 0.315 nm, which corroborates with previously reported (002) graphitic cores of carbon.

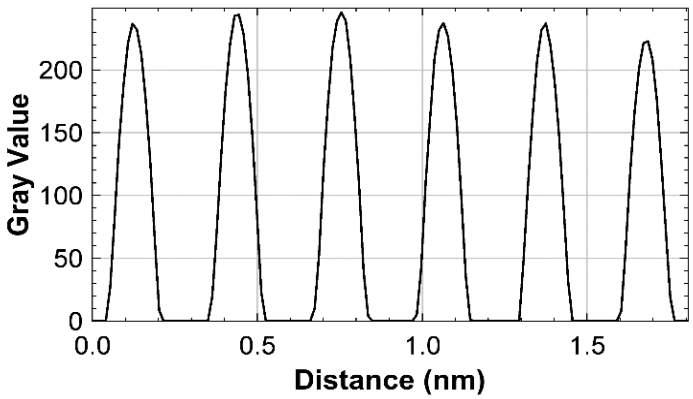

Figure 6.5: Surface plot obtained from HRTEM of GC@ SiO_2.

In depth investigations on d-spacing value was carried out with the aid of image J software. Surface plot was obtained by processing selected areas of TEM micrographs with equal spaced parallel lattice fringes. From the surface plot (Fig. 6.5), d value was found to be 0.306 nm which is in accordance with the results from HRTEM and

SAED pattern. A comparison of d spacing values obtained from different analysis method is given in table 6.2.

Table 6.2: Comparison of the d-spacing of the (002) plane of graphitic carbon obtained from SAED, HRTEM, FFT, and surface plot analysis for GC@ SiO_2.

Sample	d_{SAED} (nm)	d_{HRTEM} (nm)	d_{FFT} (nm)	$d_{surface\ plot}$(nm)	$d_{reference\ data}$ (nm)
GC@SiO_2	0.317	0.315	0.320	0.306	0.32

(ii) NGC@SiO_2

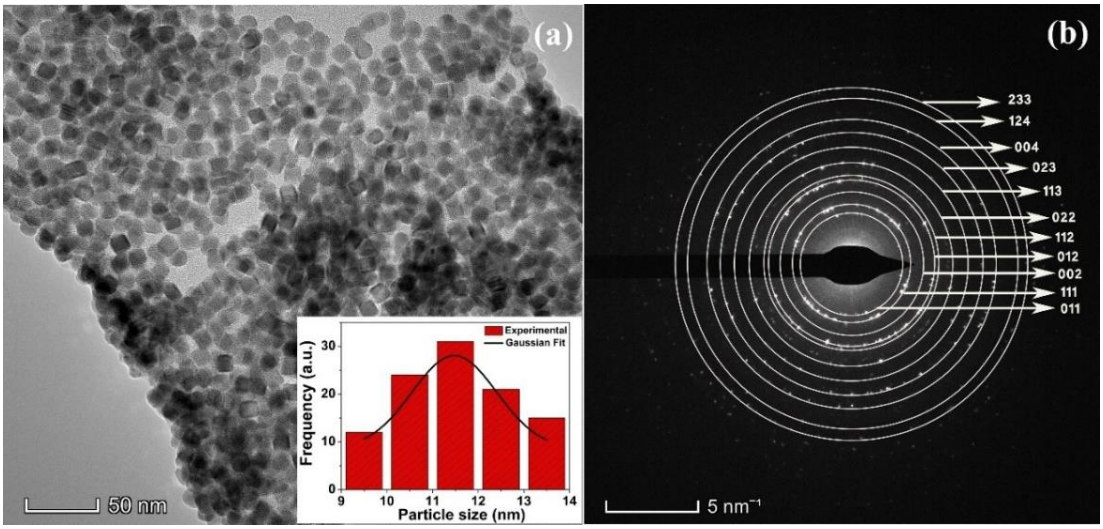

Figure 6.6: (a) TEM image of NGC@SiO_2 [inset shows corresponding particle size distribution] (b) SAED image of NGC@SiO_2.

TEM micrographs displayed in Figure 6.6 (a) shows a quasi-spherical morphology of carbon nanoparticles with particle size ranges from 9-14 nm. Moreover, the existence of bright spots with multiple rings in selected area electron diffraction (SAED) pattern (Fig. 6.6(b)) implies high degree of poly crystallinity of the obtained carbon-silica network. Measured inter planar spacing values are well consistent with the reported values of polycrystalline C_{20} structure (ICSD No-185973).

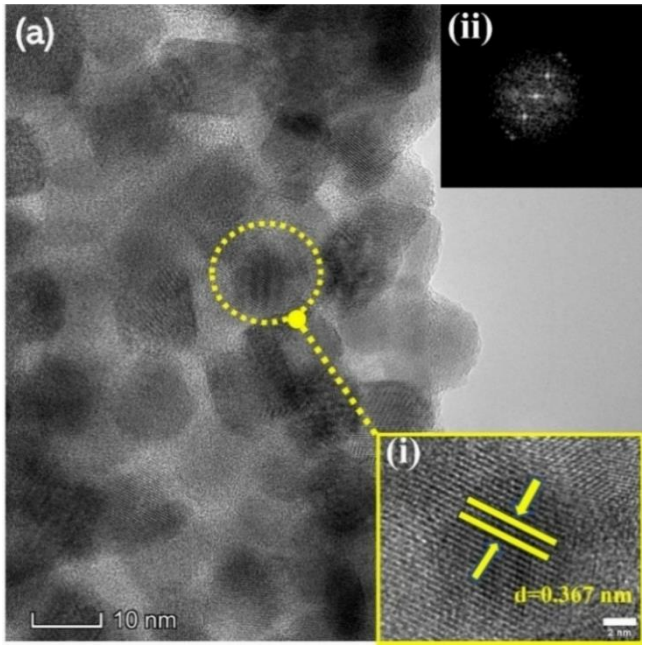

Figure 6.7: (a) HRTEM-I image of NGC@SiO_2 [Inset (i) shows plane with d-spacing as 0.367 nm and (ii) shows corresponding FFT pattern].

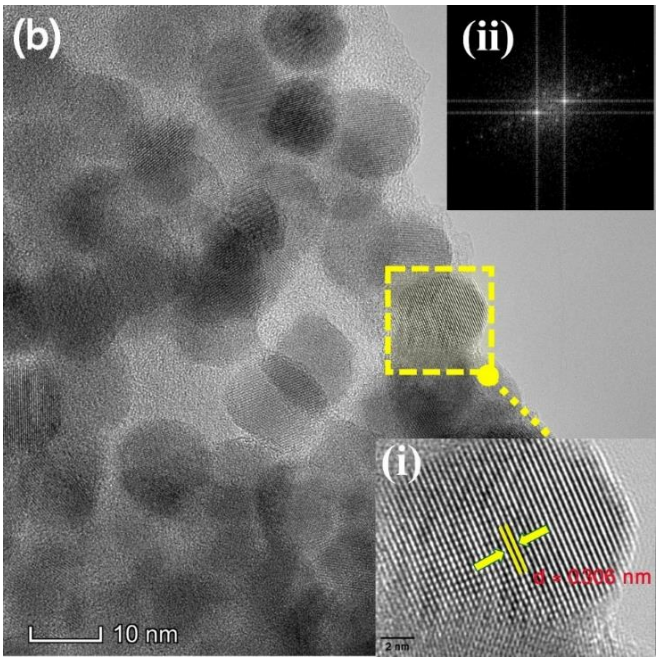

Figure 6.8: HRTEM-II image of NGC@SiO_2. [Inset (i) shows plane with d-spacing as 0.306 nm and (ii) shows corresponding FFT pattern].

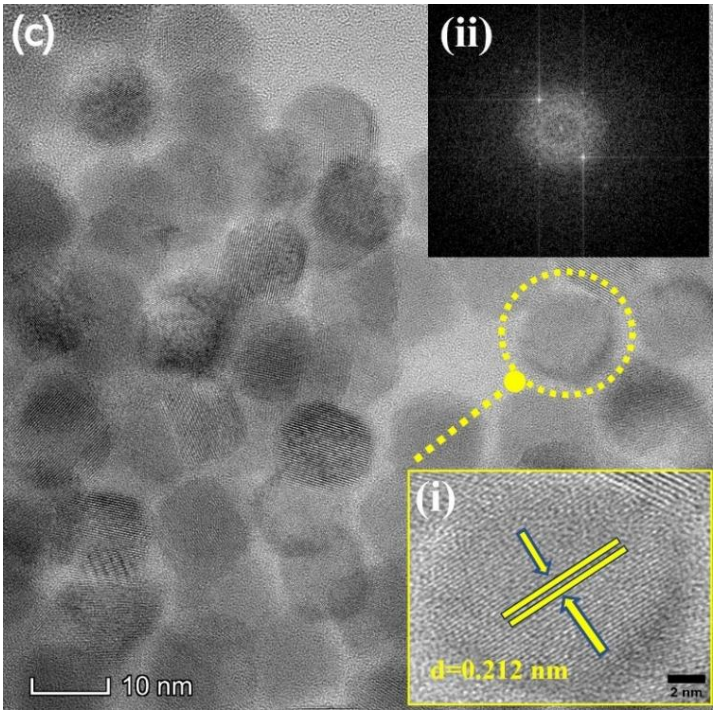

Figure 6.9: HRTEM-III image of NGC@ SiO_2 [Inset (i) shows plane with d-spacing as 0.212 nm and (ii) shows corresponding FFT pattern].

Besides, the HRTEM images (Fig. 6.7, 6.8 & 6.9) clearly shows well defined equi-distant lattice fringes. Quasi spherical morphology of the synthesized non-graphitic carbon nanoparticles is affirmed from the TEM micrographs at high resolution. Inset (i) of Fig 6.7 shows nanoparticle having d spacing value of 0.367 nm. Corresponding FFT analysis (inset (ii) of Fig 6.7) gives d-spacing value of 0.36 nm. Additionally, inset (i) of Fig. 6.8 shows crystalline nanoparticles with interplanar spacing value of 0.306 nm and corresponding FFT (inset (ii) of Fig 6.8) gives d-spacing of 0.31 nm. Inset (i) of Fig 6.9 shows nanoparticle having d spacing value of 0.217 nm. Corresponding FFT pattern (inset (ii) of Fig 6.9) gives d-spacing value of 0.21 nm.

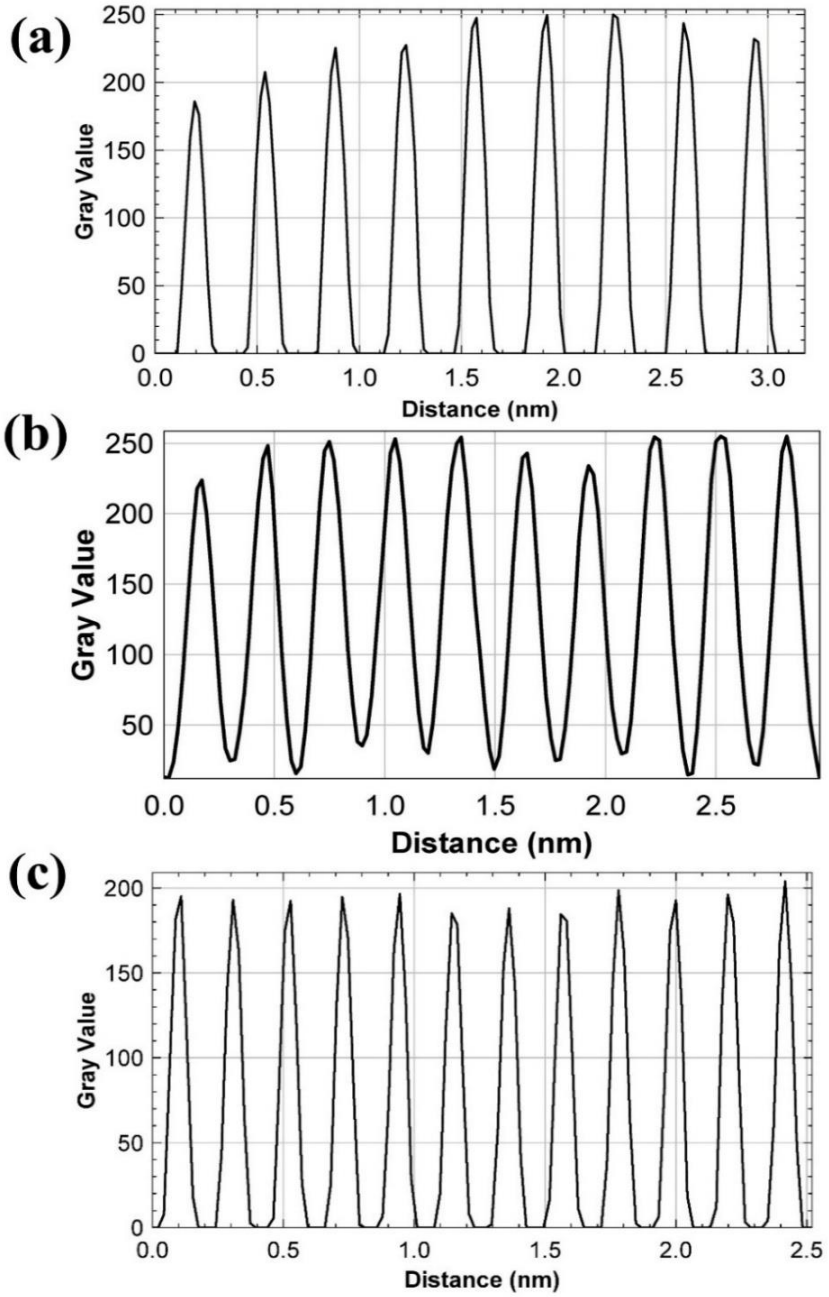

Figure 6.10: Surface plots obtained from (a) HRTEM-I b) HRTEM-II c) HRTEM-III of NGC@ SiO_2.

Surface plots (Fig. 6.10) are generated from the respective HRTEM planes (inset (i) of Fig 6.7, 6.8 & 6.9). From the analysis, the d spacing values of corresponding planes are obtained as 0.367 nm, 0.306 nm, 0.212 nm for (011), (111) and (112) planes. Crystalline nature of the composites is further confirmed through comparison of d values measured from HRTEM, SAED, FFT and surface plots. From Table 6.3, d values obtained from HRTEM are almost similar with SAED and are consistent with

the d-values calculated from corresponding FFT patterns and surface plots. Obtained d-spacing values are in good agreement with polycrystalline, non-graphitic (C_{20}) structure. HRTEM analysis implies that NGC@SiO_2 composed of non-graphitic carbon nano assemblies with multiple crystalline domains.

Table 6.3: Comparison of the d-spacing of the (011), (111), (112) planes of C_{20} obtained from SAED, HRTEM-I, HRTEM-II and HRTEM-III with corresponding FFT, and surface plot analysis of NGC@SiO_2

Sample	d_{SAED} (nm)	d_{HRTEM} (nm)	d_{FFT} (nm)	$d_{surface\ plot}$ (nm)	$d_{reference\ data}$ (nm)
NGC@SiO_2	0.361	0.367	0.36	0.354	0.3681
NGC@SiO_2	0.316	0.306	0.31	0.299	0.3006
NGC@SiO_2	0.217	0.212	0.21	0.211	0.2125

From HRTEM and SAED analysis, it is clear that a transition from graphitic to non-graphitic crystalline carbon occurs, with an increase in wt% of carbon in silica. The degree of crystallinity rises with increasing carbon concentration. Moreover, assemblies of nano crystallites transform to nanoparticles with well-defined morphology. Nanocarbon in silica have a tendency to form a spherical shape. The symmetrical growth in all directions produced particles with exceptional homogeneity inside the silica network. Notably, the (002) plane, with a d-spacing value of 0.32 nm, is the major plane in graphitic carbon. For lower carbon content, nano crystallites with a graphitic structure are formed. As the carbon concentration increases, the nano crystallites have a tendency to assemble in a preferred orientation across their major crystallographic planes with a d-spacing value of 0.32 nm. They undergo transformation to nanoparticles having a C_{20} crystal structure where (111) planes with 0.30 nm are major crystalline planes. As the amount of carbon increases, the crystal structure transforms to energetically favorable structure along this coherent interface since the interplanar spacings of the graphitic (002) - C_{20} (111) and graphitic (100) - C_{20} (112) planes are nearly similar.

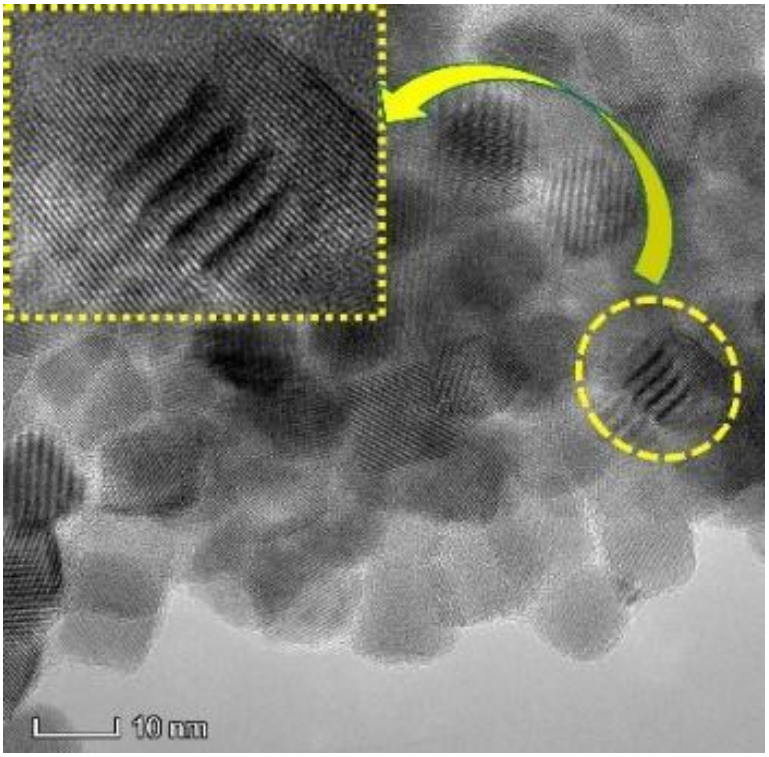

Figure 6.11: HR-TEM image with Moire's fringes in the NGC@ SiO_2.

As observed in Fig. 6.11, stacking one plane over another with different d values generates Moire interference. The highly crystalline nanoparticles in NGC@ SiO_2 are stacked one over other and Moire's fringes are obtained in different regions (inset of Fig. 6.11). This effect has been previously reported in various crystalline carbon nano structures such as carbon dots (CQDs), carbon nanotubes (CNTs) [24].

6.3.2 Fourier transform infrared spectroscopy (FTIR)

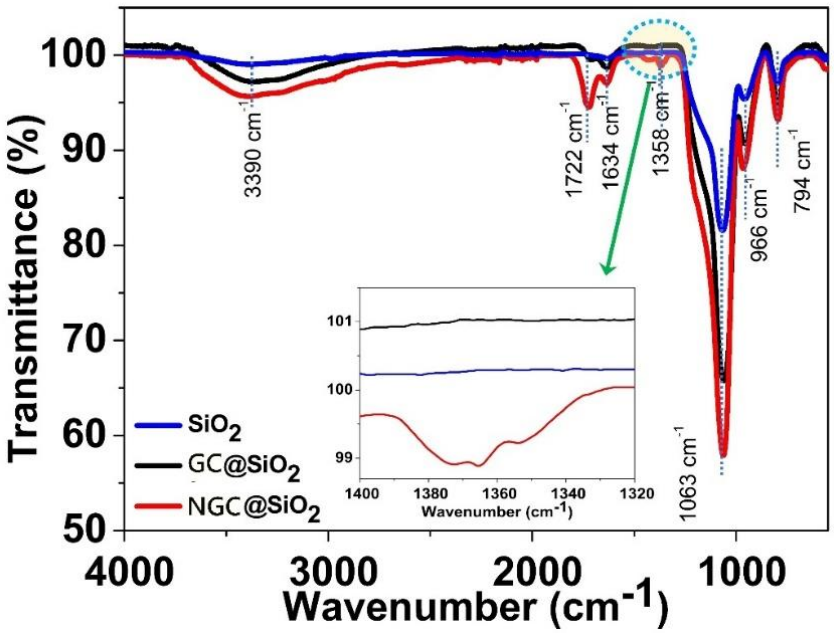

Figure 6.12: FT-IR spectra of carbon@SiO_2.

FT-IR spectra was analyzed to better understand the presence of different functional groups formed in the prepared nanocomposites. Spectra of carbon@SiO_2 depicted in Figure 6.12, exhibits with distinct IR bands ranging from 500-4000 cm^{-1}. The broad absorption around 3390 cm^{-1} indicate the stretching vibrations of hydroxyl group and band at 1722 cm^{-1} can be assigned to C=O groups [25]. The band observed due the carboxyl functional group is more intense in NGC@SiO_2 due to the higher carbon content present. The band identified at 1634 cm^{-1} can be attributed to the existence of C=C vibrational bands around 1600-1650 cm^{-1} [25]. The band occurring at 966 cm^{-1} and 468 cm^{-1} [27] is produced by symmetric stretching modes of Si-O bonds in SiO_4 tetrahedra having multiple numbers of oxygen. Vibrational bands around 1063 cm^{-1} and 794 cm^{-1} clearly indicate the presence of Si-O stretching. Interestingly, exclusive broadening of certain IR bands at 794, 1063, 3390 cm^{-1} in the composites can be ascribed due to the overlapping of multiple bands in the same region. Typically, stretching mode vibrations of Si-C (770-800 cm^{-1}), wagging mode vibrational bands in of C-H in (CH_2)-Si and (CH_3)-Si (980-1000 cm^{-1}) and bands due to bending mode vibrations of Si-(CH_3) (1250-1260 cm^{-1}) contributes in the widening of abovementioned IR bands [28], [29]. Additionally, symmetric-asymmetric stretching mode vibrations of C-H (3110 & 3085 cm^{-1}) [25], [30], vibrational bands of (=C-H)

ranges from 3000-3100 cm^{-1} [31] and C=O (3085 cm^{-1}) [30] take part in the spectral widening IR band around 3000 cm^{-1}. Furthermore, exclusive tiny band at 1358 cm^{-1} in NGC@SiO_2 can be assigned to the C_{20} structure with D_{2h} symmetry as depicted in theoretical reports [25].

6.3.3 Thermal decomposition studies

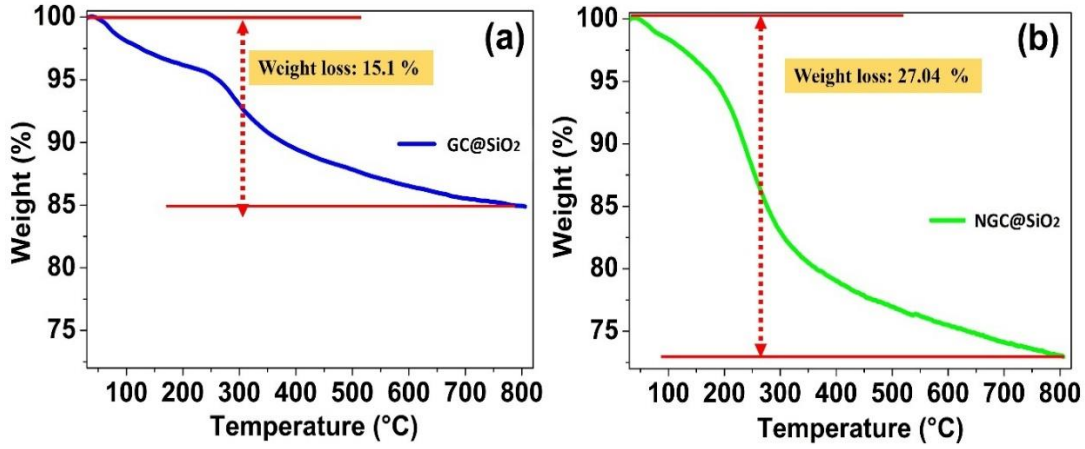

Figure 6.13: TGA curve of (a) GC@ SiO_2 (b) NGC@ SiO_2.

The thermal decomposition studies of the nanocarbon doped silica were performed with thermogravimetric analysis (TGA). The analysis was carried out in nitrogen atmosphere at a range of room temperature to a maximum of 800 °C by keeping a heating rate of 10 °C/min (Fig. 6.13). From thermograms, initial weight loss (~3 %) observed at temperature scales below 130 °C was similar for both composites which was accompanied with the desorption of water molecules within the composites [24]. In the temperature range from 150°C-350°C NGC@SiO_2 shows a more rapid decomposition. In comparison to GC@SiO_2 low residual weight in NGC@SiO_2 can be ascribed due to the burning of relatively high amount of organic matter. As per reports, the reduced weight in TGA curves of carbon-silica composites around 150 - 350 °C were mainly accompanied with the decomposition of COOH and OH groups [33]. From 400^0C to 800 ^{0}C, almost a linear curve is obtained in both composites that contributes nearly 7 % to the total weight loss. As the temperature reaches to a maximum of 800 ^{0}C, 84.88 % of GC@SiO_2 retains whereas residual w% of NGC@SiO_2 is 72.96 %. In comparison with GC@SiO_2, NGC@SiO_2 has higher carbon content, and hence an additional weight reduction of ~12 % occurs due to the increased breakdown rates of functional groups.

6.3.4 UV-Visible absorption spectra

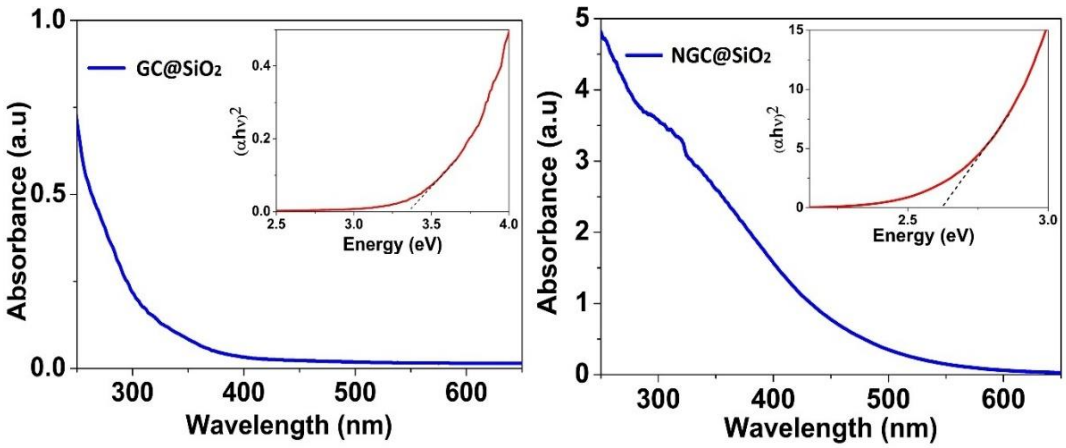

Figure 6.14: UV-visible absorption spectra of (a) GC@ SiO_2 (b) NGC@ SiO_2. The tauc plots given in the insets give bandgaps of 3.34 eV and 2.62 eV respectively.

As shown in Figure 6.14, for GC@SiO_2 absorption band extend up to 400 nm, which was widened up to 600 nm for NGC@SiO_2. From graphitic to non-graphitic crystalline transformation, energy bands became broader which subsequently reduce the band gap values from 3.34 eV to 2.62 eV (inset of Fig. 6.14). For graphitic carbon nanocrystallites, the observed band gap is in accordance with the reported values of graphitic carbon quantum dots and nanoparticles [34], [35]. Hence the shift in band gap is due to the change in crystal structure rather than the change in morphology.

6.3.5 Photoluminescence spectra

Photoluminescence studies of GC@SiO_2 and NGC@SiO_2 are done under varying UV excitations and visible emissions from 400-700 nm was recorded. The solid-state fluorescence of both composites exhibited distinct optical features.

(i) GC@SiO₂

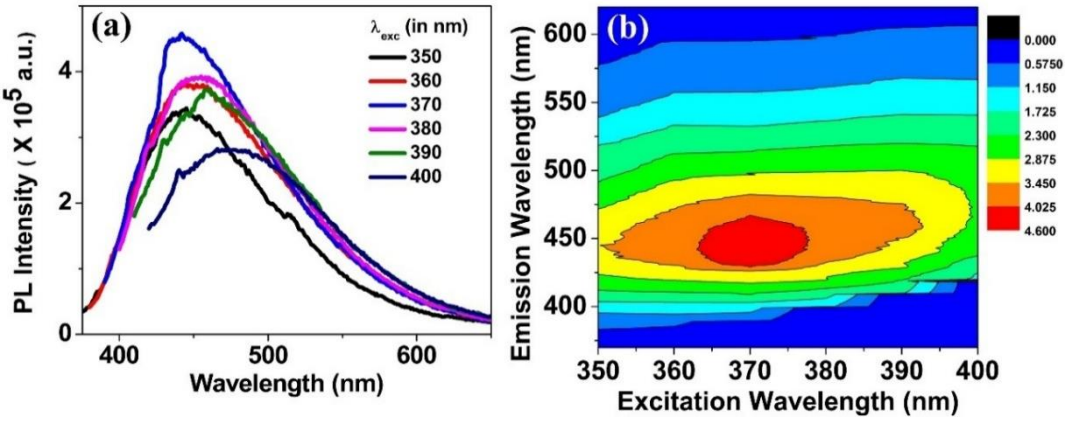

Figure 6.15: (a) PL spectra of GC@ SiO_2 at different excitation wavelengths (b) corresponding contour plot of the excitation/emission map.

Excitation dependent luminescence spectra of GC@SiO_2 is depicted in Figure 6.15(a). The strong blue luminescence of GC@SiO_2 generated is similar to the widely reported fluorescence characteristics from graphitic core of carbon quantum dots. As per literature, blue emissions are dominantly produced from sp^2 carbon cores of nanocarbon [36], [37]. When excited with UV radiation of λ_{ex}= 370 nm wavelength, maximum intensity obtained was peaked at 442 nm. Noticeable spectral red shift was observed with change in excitation wavelength. Figure 6.15 (b) displays the PL contour plots of GC@SiO_2 for varying excitation wavelengths, and the color domains associated with PL intensity are given in the color bar scale. The GC@SiO_2 show the emission bands ranges from 400 nm to 600 nm. The silica network encapsulated the luminescent nanocarbon cores and prevents aggregation induced quenching in solid state. Thus, *in situ* synthesized nanocarbon in SiO_2 generates solid intense blue emissions which can be effectively utilized in display devices.

(ii) NGC@SiO$_2$

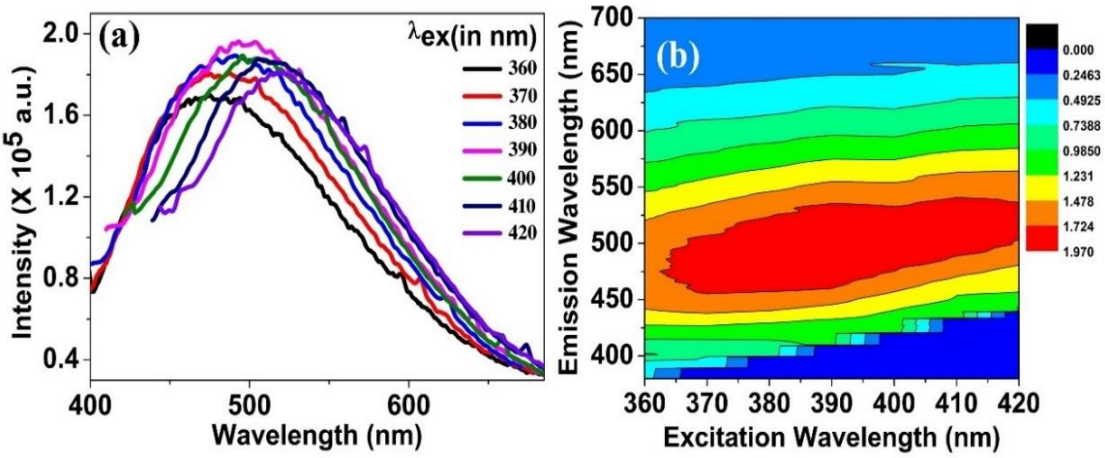

Figure 6.16: (a) PL spectra of NGC@ SiO_2 at different excitation wavelengths (b) corresponding contour plot of the excitation/emission map.

Excitation dependent luminescence studies of NGC@ SiO_2 was performed by recording the emission spectra for excitation wavelengths ranging from 360 nm to 420 nm (shown in Fig. 6.16(a)). Similar to GC@SiO_2, excitation dependent spectral red shift was observed in NGC@SiO_2 and under 390 nm excitations, a maximum fluorescence intensity centered at 493 nm is obtained. Origin of excitation dependent luminescence can be attributed to the existence of multiple surface emissive states within the carbon nanoparticle assemblies. Single broad intense fluorescence extends from 400 nm to 700 nm are clearly demonstrated in the contour plots (shown in Fig. 6.16 (b)) of the composites. Compared to GC@ SiO_2 the maximum intensity region (red color) is broad and remains as such for entire excitation wavelengths. Thus, for broad excitation wavelengths of NGC@SiO_2 exhibits broad emission spectrum from 400 nm to 700 nm which covers the entire visible region.

6.3.6 Fluorescence lifetime decay curves

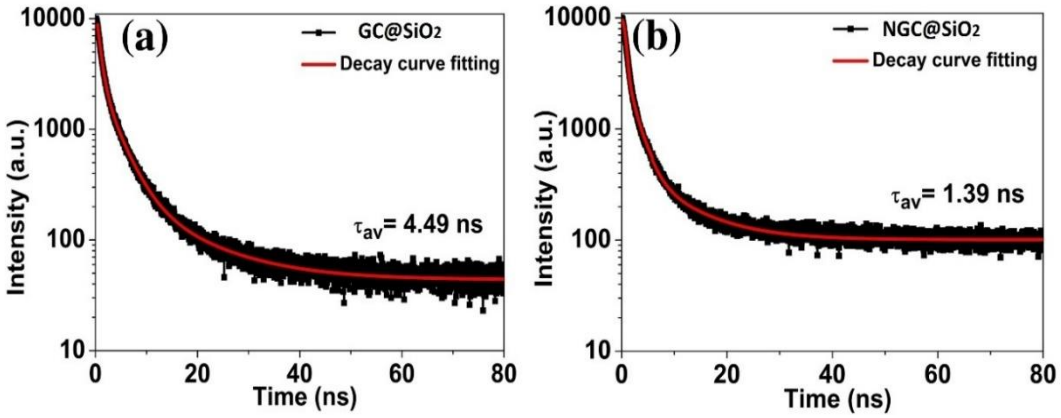

Figure 6.17: The lifetime decay curve of (a) GC@SiO_2 (b) NGC@SiO_2.

Time-resolved fluorescence lifetime experiments were also conducted (Fig. 6.17). The fluorescence decays were fitted with a triexponential equation (eq (1)). Average lifetime values were calculated using eq (2).

$$R(t) = A_1e^{(-t/\tau_1)} + A_2e^{(-t/\tau_2)} + A_3e^{(-t/\tau_3)} \quad \text{---------- (1)}$$

$$\langle\tau\rangle = (A_1\,\tau_1 + A_2\,\tau_2 + A_3\,\tau_3) / (A_1 + A_2 + A_3) \quad \text{---------- (2)}$$

For both materials the decay time is of the order of nanoseconds which is in accordance with the reported lifetime decay values for carbon nano systems [38], [39]. For non-graphitic crystalline carbon, decay process is faster. As the carbon content increases, distance between the particles reduces and thereby non radiative energy transfer among them will be more feasible. Modified surface states of obtained carbon nanoparticles significantly contribute in the speedy fluorescence decay in NGC@SiO_2 by means of enhanced radiative recombination [40].

Table 6.4: Fluorescence lifetime parameters of carbon@SiO_2.

Sample code	α_1	τ_1 (ns)	α_2	τ_2 (ns)	α_3	τ_3 (ns)	τ_{av} (ns)
GC@SiO_2	51.52	3.25	27.48	0.76	21	12.41	4.49
NGC@SiO_2	67.09	0.02	22.32	1.90	10.60	8.98	1.39

6.3.7 Colorimetric analysis with CIE Chromaticity diagrams

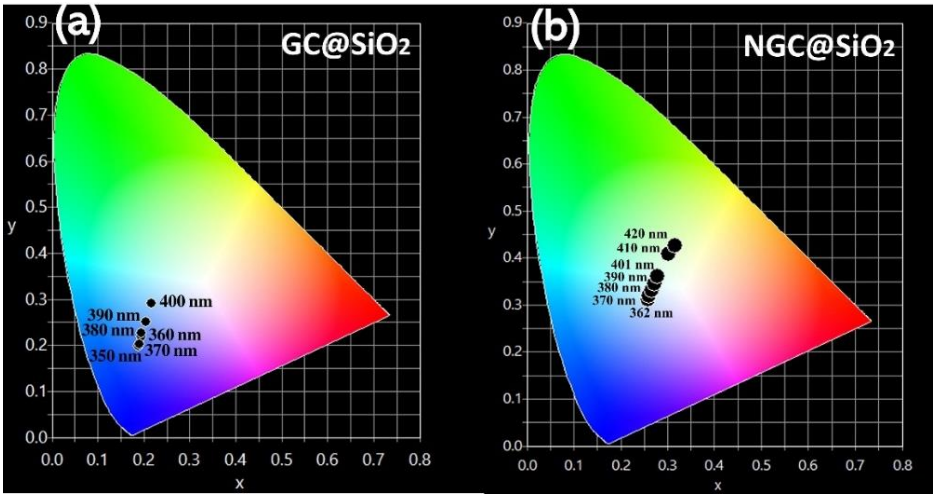

Figure 6.18: CIE diagram of $GC@SiO_2$ and $NGC@SiO_2$ for varying excitation wavelengths.

The CIE chromaticity diagrams (shown in Fig. 6.18) of the composites demonstrate color of emission from the composites excited at distinct wavelengths. Obtained CIE indices of both composites strongly agree with the recorded PL spectra. In common, upon increasing the excitation wavelengths, a progressive shift in CIE coordinates is observed in graphitic ($GC@SiO_2$) and non-graphitic ($NGC@SiO_2$) carbon nano assemblies. Upon different excitation wavelengths, exhibited color shifts from dark blue to light blue for graphitic carbon nanocrystallites. For non-graphitic carbon nanoparticles, the color shifts from light blue to light yellow through a trajectory near to perfect white coordinates (0.33, 0.33) where white emissions were generated from $NGC@SiO_2$ with the color points progressively shifted upon increasing the excitation wavelength.

Table 6.5: Excitation wavelength and CIE indices of GC@ SiO_2.

Sample code	Excitation wavelength (in nm)	CIE Index
GC@SiO_2	350	(0.1876, 0.1978)
GC@SiO_2	360	(0.1947, 0.2193)
GC@SiO_2	370	(0.1898, 0.2027)
GC@SiO_2	380	(0.1952, 0.2258)
GC@SiO_2	390	(0.2042, 0.2498)
GC@SiO_2	400	(0.2176, 0.2916)

Visual contrast in the luminescence of composites is consistent with the corresponding CIE indices and color points spotted in CIE 1931 chromaticity diagram. From table 6.5, CIE indices move from dark to light blue color. The colorimetric WLE parameters of NGC@SiO_2 composites including correlated color temperature (CCT), CIE indices and CRI for distinct excitation wavelength are tabulated in the table. 6.6. For all the excitation wavelengths studied, the cool white emissions are obtained for 380 nm and 390 nm with CRI values 79 and 77 respectively. A maximum value of CRI is obtained at 360 nm and 370 nm excitation.

Table 6.6: Excitation wavelengths, CIE indices, CCT, CRI, FWHM of NGC@ SiO_2.

Sample code	Excitation wavelength (nm)	CIE Index	CCT (in K)	CRI	FWHM
NGC@SiO_2	360	(0.2581, 0.3118)	10836	82	130.86
NGC@SiO_2	370	(0.2606, 0.3195)	10246	82	132.94
NGC@SiO_2	380	(0.2655, 0.3312)	9428	79	141.03
NGC@SiO_2	390	(0.2724, 0.3453)	8590	77	143.04
NGC@SiO_2	400	(0.2780, 0.3601)	7989	76	127.23
NGC@SiO_2	410	(0.3021, 0.4076)	6506	70	118.31
NGC@SiO_2	420	(0.3143, 0.4256)	6013	69	104.61

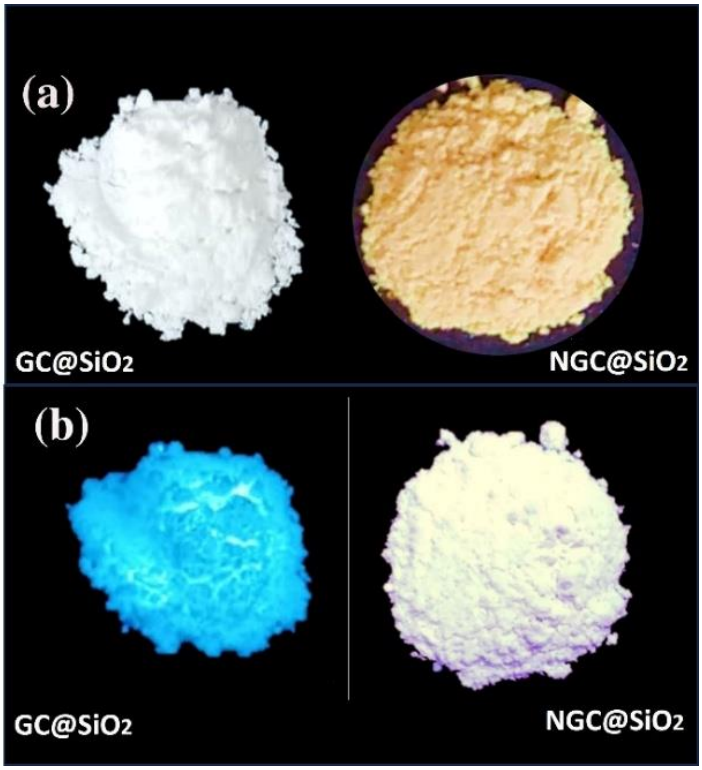

Figure 6.19: The solid-state (powder) photographs of GC@SiO_2 and NGC@SiO_2 under (a) daylight and (b) UV lamp.

The optical images of carbon@SiO_2 composites (shown in Fig. 6.19) were captured under daylight and UV light of 365 nm. C@SiO_2 composites show a concentration-mediated color tuning from blue to white region. While graphitic carbon gives a blue fluorescence, non- graphitic C_{20} crystalline carbon gives white emissions. Furthermore, as the carbon content is more in NGC@SiO_2, more functionalized surface states can contribute in exhibiting a broad luminescence.

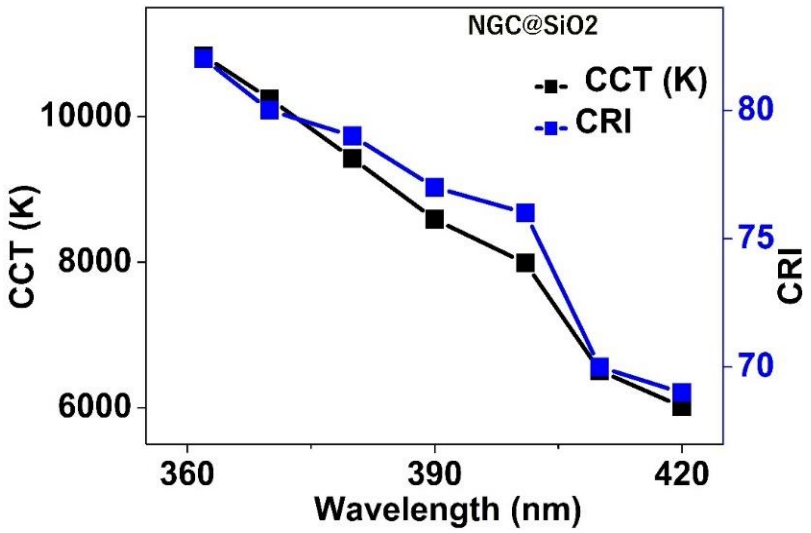

Figure 6.20: Plot of (a) CCT Vs excitation wavelength (b) CRI Vs excitation wavelength of NGC@ SiO_2.

Yellow colored powder sample in day light generated intense white emissions under UV exposure of 365 nm. This is perfectly consistent with the calculated CIE indices of NGC@SiO_2 (0.2724, 0.3453) which lie around ideal white point (0.33, 0.33). CCT values found with CIE indices revealed that the prepared WLE systems with (CCT > 5000K) are potential candidates for outdoor lighting platforms which require cool white domains. Trends observed in CCT, CRI values of NGC@SiO_2 with varying excitations are plotted in Figure 6.20. Single phase solid WLE systems with CRI values ranges from 70-80 and adjustable CCT values are potential candidates in lighting platforms. Moreover, as the material exhibit cool white light emissions for a wide range of excitation wavelengths, NGC@SiO_2 can have potential applications for broad band white light emitting devices.

6.4 Conclusion

To summarize, solid state fluorescent C@SiO_2 was synthesized via in situ, sol-gel assisted thermal route. Under identical thermal conditions, graphitic to non-graphitic transitions are achieved at distinct carbon concentrations within silica network. While graphitic nanocrystallites were formed at low carbon content, non-graphitic

polycrystalline carbon nanoparticles were obtained at high carbon content. Morphologically different composites exhibit distinct optical characteristics which were strongly controlled by the carbon concentration. An aggregation induced band gap tuning from 3.34 eV to 2.62 eV was accompanied with the graphitic to non-graphitic transition. Intense blue fluorescence obtained from GC@SiO_2 and WLE characteristics of NGC@SiO_2 were confirmed with the CIE indices in respective color domains. Cool white CCTs (> 6000 K), with consistent CIE coordinates and good color rendering properties CRI (~ 80) of NGC@SiO_2 could make it beneficial for solid WLE applications.

References

[1] M. Pan, W.-M. Liao, S.-Y. Yin, S.-S. Sun, and C.-Y. Su, "Single-Phase White-Light-Emitting and Photoluminescent Color-Tuning Coordination Assemblies," *Chem. Rev.*, vol. 118, no. 18, pp. 8889–8935, Sep. 2018, doi: 10.1021/acs.chemrev.8b00222.

[2] R. L. I. Ayscue, C. P. Verwiel, J. A. Bertke, and K. E. Knope, "Excitation-Dependent Photoluminescence Color Tuning in Lanthanide-Organic Hybrid Materials," *Inorg. Chem.*, vol. 59, no. 11, pp. 7539–7552, Jun. 2020, doi: 10.1021/acs.inorgchem.0c00405.

[3] M. Gutiérrez, F. Sánchez, and A. Douhal, "Efficient multicolor and white light emission from Zr-based MOF composites: spectral and dynamic properties," *J. Mater. Chem. C*, vol. 3, no. 43, pp. 11300–11310, Oct. 2015, doi: 10.1039/C5TC02357B.

[4] R. Li *et al.*, "Multispectral tunability in single Eu^{2+}-doped $(Ba,Sr)_5(PO_4)_3Br$ phosphor," *Inorg. Chem. Front.*, vol. 7, no. 13, pp. 2515–2522, Jun. 2020, doi: 10.1039/D0QI00399A.

[5] L. Kumari and A. K. Kar, "Compositional variation dependent color tuning and observation of Förster resonant energy transfer in $Cd_{(1-x)}Zn_xS$ nanomaterials," *New J. Chem.*, vol. 44, no. 3, pp. 870–883, Jan. 2020, doi: 10.1039/C9NJ05199F.

[6] C. Wang *et al.*, "Concentration-dependent color tunability of nitrogen-doped carbon dots and their application for iron(III) detection and multicolor bioimaging," *Journal of Colloid and Interface Science*, vol. 521, pp. 33–41, Jul. 2018, doi: 10.1016/j.jcis.2018.03.021.

[7] J. Xie *et al.*, "Wide range color tunability and efficient energy transfer of novel $NaCaGd(WO_4)_3:Tb^{3+},Eu^{3+}$ phosphors with excellent thermal stability for pc-WLEDs," *Inorg. Chem. Front.*, vol. 8, no. 20, pp. 4517–4527, Oct. 2021, doi: 10.1039/D1QI00831E.

[8] M. Shang, C. Li, and J. Lin, "How to produce white light in a single-phase host?," *Chem. Soc. Rev.*, vol. 43, no. 5, pp. 1372–1386, Feb. 2014, doi: 10.1039/C3CS60314H.

[9] S. Ye, F. Xiao, Y. X. Pan, Y. Y. Ma, and Q. Y. Zhang, "Phosphors in phosphor-converted white light-emitting diodes: Recent advances in materials, techniques and properties," *Materials Science and Engineering: R: Reports*, vol. 71, no. 1, pp. 1–34, Dec. 2010, doi: 10.1016/j.mser.2010.07.001.

[10] P. F. Smet, A. B. Parmentier, and D. Poelman, "Selecting Conversion Phosphors for White Light-Emitting Diodes," *J. Electrochem. Soc.*, vol. 158, no. 6, p. R37, Apr. 2011, doi: 10.1149/1.3568524.

[11] C.-H. Liang, L.-G. Teoh, K. T. Liu, and Y.-S. Chang, "Near white light emission of BaY_2ZnO_5 doped with Dy^{3+} ions," *Journal of Alloys and Compounds*, vol. 517, pp. 9–13, Mar. 2012, doi: 10.1016/j.jallcom.2011.11.088.

[12] Z.-C. Wu, J. Liu, W.-G. Hou, J. Xu, and M.-L. Gong, "A new single-host white-light-emitting $BaSrMg(PO_4)_2$: Eu^{2+} phosphor for white-light-emitting diodes," *Journal of Alloys and Compounds*, vol. 498, no. 2, pp. 139–142, May 2010, doi: 10.1016/j.jallcom.2010.03.136.

[13] A. Pal, M. Palashuddin Sk, and A. Chattopadhyay, "Recent advances in crystalline carbon dots for superior application potential," *Materials Advances*, vol. 1, no. 4, pp. 525–553, 2020, doi: 10.1039/D0MA00108B.

[14] M. L. Liu, L. Yang, R. S. Li, B. B. Chen, H. Liu, and C. Z. Huang, "Large-scale simultaneous synthesis of highly photoluminescent green amorphous carbon nanodots and yellow crystalline graphene quantum dots at room temperature," *Green Chem.*, vol. 19, no. 15, pp. 3611–3617, Jul. 2017, doi: 10.1039/C7GC01236E.

[15] T. Paul, J. J. Palakulam, N. V. Unnikrishnan, R. Philip, and K. A. A. Mary, "Warm to cool tunable ultra-stable white light emissions from carbon dots -Tb^{3+} - Eu^{3+} doped silica," *Optical Materials*, vol. 138, p. 113673, Apr. 2023, doi: 10.1016/j.optmat.2023.113673.

[16] K. Bisht and R. K. Dutta, "l-valine functionalized nitrogen doped non-graphitic carbon dots as a photoluminescent probe for detection of tetracycline," *Dyes and Pigments*, vol. 208, p. 110823, Jan. 2023, doi: 10.1016/j.dyepig.2022.110823.

[17] A. Pal, A. Bhakat, and A. Chattopadhyay, "Zinc Ion-Induced Assembly of Crystalline Carbon Dots with Excellent Supercapacitor Performance," *J. Phys. Chem. C*, vol. 123, no. 32, pp. 19421–19428, Aug. 2019, doi: 10.1021/acs.jpcc.9b05820.

[18] A. Pal, G. Natu, K. Ahmad, and A. Chattopadhyay, "Phosphorus induced crystallinity in carbon dots for solar light assisted seawater desalination," *J. Mater. Chem. A*, vol. 6, no. 9, pp. 4111–4118, Feb. 2018, doi: 10.1039/C7TA10224K.

[19] Chen, Yonghao, et al. , "A Self-Quenching-Resistant Carbon-Dot Powder with Tunable Solid-State Fluorescence and Construction of Dual-Fluorescence Morphologies for White Light-Emission", *Advanced Materials* 2, vol. 2, no. 28, Nov. 2016, pp. 312-318, DOI: 10.1002/adma.201503380.

[20] J. Guo *et al.*, "Yellow-Emissive Carbon Dots with High Solid-State Photoluminescence," *Advanced Functional Materials*, vol. 32, no. 20, p. 2110393, 2022, doi: 10.1002/adfm.202110393.

[21] J. Wang, Q. Li, J. Zheng, Y. Yang, X. Liu, and B. Xu, "N, B-Codoping Induces High-Efficiency Solid-State Fluorescence and Dual Emission of Yellow/Orange Carbon Dots," *ACS Sustainable Chem. Eng.*, vol. 9, no. 5, pp. 2224–2236, Feb. 2021, doi: 10.1021/acssuschemeng.0c07992.

[22] J. He *et al.*, "Solid-State Carbon Dots with Red Fluorescence and Efficient Construction of Dual-Fluorescence Morphologies," *Small*, vol. 13, no. 26, p. 1700075, 2017, doi: 10.1002/smll.201700075.

[23] Y.-L. Zhang *et al.*, "Graphitic carbon quantum dots as a fluorescent sensing platform for highly efficient detection of Fe^{3+} ions," *RSC Advances*, vol. 3, no. 11, pp. 3733–3738, 2013, doi: 10.1039/C3RA23410J.

[24] Vuong, Amanda, "Nanocarbon: Defect Architectures and Properties, *Nanocarbon: Defect Architectures and Properties*. University of Surrey (United Kingdom), 2017.

[25] V. Ţucureanu, A. Matei, and A. M. Avram, "FTIR Spectroscopy for Carbon Family Study," *Critical Reviews in Analytical Chemistry*, vol. 46, no. 6, pp. 502–520, Nov. 2016, doi: 10.1080/10408347.2016.1157013.

[26] K. A. A. Mary, N. V. Unnikrishnan, and R. Philip, "Cubic to amorphous transformation of Se in silica with improved ultrafast optical nonlinearity," *RSC Adv.*, vol. 5, no. 18, pp. 14034–14041, Jan. 2015, doi: 10.1039/C4RA14025G.

[27] M. Epifani, G. De, A. Licciulli, and L. Vasanelli, "Preparation of uniformly dispersed copper nanocluster doped silica glasses by the sol–gel process," *J. Mater. Chem.*, vol. 11, no. 12, pp. 3326–3332, Nov. 2001, doi: 10.1039/B101059J.

[28] A. V. Vasin *et al.*, "Structure, paramagnetic defects and light-emission of carbon-rich a-SiC:H films," *Journal of Applied Physics*, vol. 103, no. 12, p. 123710, Jun. 2008, doi: 10.1063/1.2946446.

[29] F. Shariatmadar Tehrani, B. T. Goh, M. R. Muhamad, and S. A. Rahman, "Pressure dependent structural and optical properties of silicon carbide thin films deposited by hot wire chemical vapor deposition from pure silane and methane gases," *J Mater Sci: Mater Electron*, vol. 24, no. 4, pp. 1361–1368, Apr. 2013, doi: 10.1007/s10854-012-0934-z.

[30] P. K. Chu and L. Li, "Characterization of amorphous and nanocrystalline carbon films," *Materials Chemistry and Physics*, vol. 96, no. 2, pp. 253–277, Apr. 2006, doi: 10.1016/j.matchemphys.2005.07.048.

[31] V. A. Chhabra, A. Deep, R. Kaur, and R. Kumar, "Functionalization of graphene using carboxylation process," *Int. J. Sci. Emerg. Technol*, vol. 4, pp. 13–19, 2012.

[32] S. Najafi-Shoa, H. Roghani-Mamaqani, M. Salami-Kalajahi, R. Azimi, and M. Gholipour-Mahmoudalilou, "Incorporation of epoxy resin and carbon nanotube into silica/siloxane network for improving thermal properties," *J Mater Sci*, vol. 51, no. 19, pp. 9057–9073, Oct. 2016, doi: 10.1007/s10853-016-0158-3.

[33] A. Abdollahi, H. Roghani-Mamaqani, M. Salami-Kalajahi, A. Mousavi, B. Razavi, and S. Shahi, "Preparation of organic-inorganic hybrid nanocomposites from chemically modified epoxy and novolac resins and silica-attached carbon nanotubes by sol-gel process: Investigation of thermal degradation and stability," *Progress in Organic Coatings*, vol. 117, pp. 154–165, Apr. 2018, doi: 10.1016/j.porgcoat.2018.01.001.

[34] J. Yu *et al.*, "Luminescence Mechanism of Carbon Dots by Tailoring Functional Groups for Sensing Fe^{3+} Ions," *Nanomaterials*, vol. 8, no. 4, Art. no. 4, Apr. 2018, doi: 10.3390/nano8040233.

[35] K. J. Mintz, Y. Zhou, and R. M. Leblanc, "Recent development of carbon quantum dots regarding their optical properties, photoluminescence mechanism, and core structure," *Nanoscale*, vol. 11, no. 11, pp. 4634–4652, 2019, doi: 10.1039/C8NR10059D.

[36] X. Li, S. Zhang, S. A. Kulinich, Y. Liu, and H. Zeng, "Engineering surface states of carbon dots to achieve controllable luminescence for solid-luminescent composites and sensitive Be^{2+} detection," *Sci Rep*, vol. 4, no. 1, p. 4976, May 2014, doi: 10.1038/srep04976.

[37] F. Yan, Z. Sun, H. Zhang, X. Sun, Y. Jiang, and Z. Bai, "The fluorescence mechanism of carbon dots, and methods for tuning their emission color: a review," *Microchim Acta*, vol. 186, no. 8, p. 583, Jul. 2019, doi: 10.1007/s00604-019-3688-y.

[38] R. Pratap, V. Vishal, S. Chaudhary, and A. Singh Parmar, "Fabrication of white light emitting diodes via high yield surface passivated carbon quantum dots doped with terbium," *RSC Advances*, vol. 13, no. 3, pp. 1974–1984, 2023, doi: 10.1039/D2RA07890B.

[39] J.-Y. Wei *et al.*, "Scalable Synthesis of Green Fluorescent Carbon Dot Powders with Unprecedented Efficiency," *Advanced Optical Materials*, vol. 8, no. 7, p. 1901938, 2020, doi: 10.1002/adom.201901938.

[40] G. Hu *et al.*, "Rational synthesis of silane-functionalized carbon dots with high-efficiency full-color solid-state fluorescence for light emitting diodes," *Carbon*, vol. 203, pp. 1–10, Jan. 2023, doi: 10.1016/j.carbon.2022.11.048.

7

Conclusion

In this chapter we summarized the overall conclusion of the thesis. Chapter wise key points with individual characteristics of developed composites are briefly discussed. Major outcomes of the research work are focused on achieving different RE/EN combinations for solid lighting applications.

The entire thesis focused on structural and optical investigations of different RE/EN based silica composites with diverse optical features. Scope of RE/EN doped silica composites in solid state lighting platforms are well explored on the basis of energy transfer pathways with tunable optical profiles.

Chapter 1 dealt with general concepts and basics of rare earth ions, elemental nanoparticles, the synthesis of RE/EN composites and white light emission and CIE chromaticity diagram. Typically, various nanostructures, synthesis approaches, energy transfer mechanisms, RE spectroscopy with different electronic transitions are discussed in detail. Apart from this, literature reviews on relevant topics are also included.

Chapter 2 presented a trichromatic approach for generating WLE in which the prepared CQDs-Tb^{3+}-Eu^{3+}- doped silica exhibited remarkable optical stability of 1 year. Aloe derived CQDs showed selective optical responses towards Fe^{3+}, Cu^{2+} ions. Continuous tuning from warm to cool white emission (CCT 3508 to 6114 K) at 393 nm excitation is well explained with colorimetric analysis. Tunable optical behaviour with adjustable CCTs made it possible for solid WLE platforms.

Chapter 3 discussed the synthesis of dual emissive carbon nanoparticles via direct thermal decomposition of *Hemigraphis colorata* leaves. It presented the WLE capability of obtained nanocarbon with adjustable CCTs. This biomass derived carbon nano assemblies are well suited for environment-friendly, indoor and outdoor lighting application.

Chapter 4 dealt with peculiar phase dependent spectral profiles of Se-Tb^{3+} doped silica from cubic to amorphous transition of selenium nanodots. Phase transition-based energy transfer hints toward its dual facets of applications as optical attenuator and optical amplifier. Concentration dependent luminescence of these composites points towards multicolor emitting applications.

In ***Chapter 5*** presented optical studies of CQDs-Tb^{3+} for solid state lighting applications. By integrating CQDs in combination with terbium ions, color tunable glasses are obtained.

Chapter 6 presented synthesis of nanocarbon doped silica via sol-gel route. Concentration mediated tuning in structure and luminescence of prepared silica-based composites are discussed in detail. Ultrabroad luminescent band of non-graphitic polycrystalline carbon nanoparticles merited with cool white CCTs and good CRI, which are well suited for outdoor lighting applications.

In summary, the thesis present distinct silica based RE/EN composites for lighting applications by utilizing the luminescence from RE ions (Eu^{3+}, Tb^{3+}) and elemental nanoparticles. From the colorimetric analysis, certain WLE and photoluminescence color tunable composites are successfully achieved with tailorable optical features.

8

Recommendations

Future scope of our research work is presented in the chapter. It points out the possible extensions that can mold the developed RE/EN combinations as lighting candidates for upcoming years.

Fluorescent nanomaterials in combination with RE ions are significant in achieving enhanced luminescence profiles to realize advanced lighting systems. In the current research work, we attempted in developing various RE/EN based silica composites with tunable optical features for solid lighting applications. Even though the achieved RE/EN compositions have remarkable optical characteristics, certain unexplored areas can be identified. So, on the basis of thesis, certain key ideas of future scope can be given below:

- Studies on temperature mediated structural and optical tuning of nanocarbon doped silica.
- In depth studies on decay pathways within nanocarbon doped silica via transient absorption spectroscopy.
- Exploring modified synthetic conditions for achieving solid dual emissive fluorescence with excellent white lighting features with good CRI values.
- Explore phase dependent luminescence on other RE/Se silica composites
- Temperature dependent luminescence studies on RE/EN doped silica.
- Excitation dependent and concentration dependent fluorescence studies of other RE/EN combinations for WLE applications.

UNIVERSITY OF CALICUT

CERTIFICATE ON PLAGIARISM CHECK

1.	Name of the Research Scholar	TESSY PAUL	
2.	Title of thesis / dissertation	RARE-EARTH IONS/ELEMENTAL NANOPARTICLES BASED SILICA COMPOSITES FOR SOLID STATE LIGHTING APPLICATIONS	
3.	Name of the Supervisor	DR. ANN MARY K A	
4.	Department/Institution	RESEARCH SCHOLAR DEPARTMENT OF PHYSICS ST.THOMAS COLLEGE (AUTONOMOUS) THRISSUR, KERALA	
5.	Similar content (%) identified	Non Core	Core
		Introduction/ Theoretical overview/Review of literature/ Materials & Methods/ Methodology	**Analysis/Result/Discussion/ Summary/Conclusion/ Recommendations**
		6	**3**
	Acceptable maximum limit (%)	10	10
6.	Software used	**iThenticate**	
7.	Date of verification	17th February, 2025	

**Report on plagiarism check, specifying included/excluded items with % of similarity to beattached.*

Checked by (with name, designation & signature) Name Dr. Nasirudheen. T
Assistant Librarian
University of Calicut, Kerala

and signature of the Researcher Tessy Paul

Name and signature of the Supervisor. DR. ANN MARY K.A.

The Doctoral Committee* has verified the report on plagiarism check with the contents of the thesis, as summarized above and appropriate measures have been taken to ensure originality of the Research accomplished herein.

Dr. Martin K. A.
Principal-in-Charge
St Thomas College (Autonomous)
Thrissur - 680 001

Name & Signature of the HoD/HoI (Chairperson of the Doctoral Committee)

**In case of languages like Malayalam, Tamil etc..on which no software is available for plagiarism check, a manual check shall be made by the Doctoral Committee, for which an additional certificate has to be attached.*